Experimentelle Physik

Exploring Neutrino Production in the Scotogenic Dark Matter Model and Testing it with Data from the IceCube Neutrino Observatory

Inaugural-Dissertation
zur Erlangung des Doktorgrades Dr. rer. nat.
der Naturwissenschaften im Fachbereich Physik
der Mathematisch-Naturwissenschaftlichen Fakultät
der Westfälischen Wilhelms-Universität Münster

vorgelegt von

Raffaela Solveig Busse

aus Essen

—2022—

Dekan:	**Prof. Dr. Michael Rohlfing**
Erster Gutachter:	**Prof. Dr. Alexander Kappes**
Zweiter Gutachter:	**Priv. Doz. Dr. Karol Kovařík**
Tag der mündlichen Prüfung:	Freitag, 13. Januar 2023
Tag der Promotion:	Freitag, 13. Januar 2023

Abstract

Dark Matter remains one of the major unresolved mysteries of physics. The observational evidence for its existence is overwhelming, yet its nature is still unknown. In the quest for the discovery of Dark Matter, minimal models shift more and more into focus: Theoretical models that add only very few fields to the Standard Model of particle physics. Often, these minimal models provide interesting phenomenology despite the relatively simple field content. The Scotogenic Model studied in this work belongs to the class of radiative seesaw minimal models, and offers a solution to the Dark Matter problem in terms of scalar WIMPs (weakly interacting massive particles), whilst also featuring a neutrino mass generation process.

Scalar WIMPs in the galactic Dark Matter halo can scatter with nuclei in celestial objects like the Sun. If loosing sufficient energy through scattering, they can become captured in the gravitational potential, and eventually accumulate in the core. The local Dark Matter over-density in this region then leads to enhanced annihilation. The WIMPs annihilate into Standard Model particle pairs that produce a flux of neutrinos upon decay. In this work, the mechanisms of neutrino production in the Scotogenic Model were explored theoretically, and it was found that inelastic WIMP-nuclei scattering processes can greatly enhance the capture rate in some scenarios of the model, in which the expected flux of neutrinos is boosted substantially. Large portions of the parameter space have been probed to find regions in which inelastic scattering is supported, and to identify scenarios that are viable in light of various theoretical and experimental constraints. The increased neutrino flux from WIMP annihilation in the Sun could be measured with neutrino telescopes.

The IceCube Neutrino Observatory at the South Pole is the largest neutrino telescope ever built. It is equipped with over 5,000 optical sensors in one gigaton of instrumented ice, to detect Cherenkov light induced by scattering interactions of neutrinos. The invaluable amount of data the experiment has taken since its completion in 2010 could be the key to finding neutrinos from Dark Matter annihilation inside the Sun. The scenarios of the Scotogenic Model were tested in a maximum likelihood statistical analysis with nine years of IceCube data. Previously unconstrained scenarios were excluded in this manner.

Zusammenfassung

Dunkle Materie bleibt eines der größten ungelösten Mysterien der Physik. Hinweise auf ihre Existenx gibt es viele, und dennoch ist ihre Zusammensetzung weiterhin unbekannt. Auf der Suche nach der Lösung des Rätsels rücken dabei sogenannte "minimale Dunkle-Materie-Modelle" immer mehr in den Fokus. Diese Modelle bieten oft eine sehr interessante Phänomenologie, bei einer überschaubaren Anzahl an neuen Feldern, die dem Standardmodell der Teilchenphysik hinzugefügt werden müssen. Das Scotogenic-Modell gehört zur Klasse dieser minimalen Modelle, und bietet neben einer Lösung des Dunkle-Materie-Problems beruhend auf skalaren WIMPs (schwach wechselwirkende massive Teilchen) auch einen Prozess zur Erzeugung von Neutrinomassen.

Skalare WIMPs im galaktischen Halo können durch Streureaktionen z.B. in der Sonne genügend Energie verlieren, sodass sie dem Gravitationspotential nicht mehr entkommen können. Sie sammeln sich im Kern der Sonne an, in dem dann eine höhere Dichte an Dunkle-Materie-Teilchen herrscht. Diese erhöhte Dichte führt zu einer verstärkten WIMP-Paarvernichtung in Standardmodellteilchen, die dann weiter in Neutrinos zerfallen. Teil dieser Arbeit war die Untersuchung solcher WIMP-Einfangreaktionen und die daraus folgende Produktion von Neutrinos. Es konnte festgestellt werden, dass in einigen Szenarien des Scotogenic-Modells inelastische Streuprozesse von WIMPs mit Nukleonen in der Sonne zu einem extrem verstärkten Neutrinofluss führen können. Der Parameterraum des Modells wurde systematisch auf Region untersucht, die solche inelastischen Streuprozesse ermöglichen, und im Hinblick auf theoretische und experimentelle Beschränkungen realisierbar sind. Der verstärkte Neutrinofluss solcher Szenarien kann prinzipiell mit Neutrino-Teleskopen gemessen werden.

Das IceCube Neutrino-Observatorium am geografischen Südpol ist das größte Neutrino-Teleskop seiner Art. Es ist mit über 5.000 optischen Sensoren in einem ein-Kubikkilometer großen Volumen instrumentiertem Eis ausgestattet, um Cherenkov-Strahlung zu detektieren, die durch Streuwechselwirkungen von Neutrinos mit dem antarktischen Eis induziert wird. Die riesige Menge an Daten, die das Experiment seit seiner Fertigstellung im Jahr 2010 gesammelt hat, könnte der Schlüssel zum Auffinden der aus Dunkler-Materie-Paarvernichtung in der Sonne entstandenden Neutrinos sein. Die Szenarien des Scotogenic-Modells wurden in einer Maximum-Likelihood-Analyse mit einem neun Jahre umfassendenden IceCube-Datensatz getestet. Auf diese Weise konnten zuvor unbeschränkte Szenarien ausgeschlossen werden.

Publications

Parts of the work presented in this thesis have been published in the following articles and proceedings:

- T. de Boer, R. Busse, A. Kappes, M. Klasen, S. Zeinstra: *New constraints on radiative seesaw models from IceCube and other neutrino detectors*, Phys. Rev. D 103 (2021) 12, 123006, Preprint (arXiv) 2103.06881, DOI 10.1103/PhysRevD.103.123006.
- T. de Boer, R. Busse, A. Kappes, M. Klasen, S. Zeinstra: *Indirect detection constraints on the scotogenic dark matter model*, JCAP 08 (2021) 038, Preprint (arXiv) 2105.04899, DOI 10.1088/1475-7516/2021/08/038.
- T. de Boer, R. Busse, A. Kappes, M. Klasen, S. Zeinstra: *Neutrino constraints to scotogenic dark matter interacting in the Sun*, in: 55th Rencontres de Moriond on Electroweak Interactions and Unified Theories (Moriond EW 2021), Preprint (arXiv) 2105.05613, ISBN 979-10-96879-13-7.

Table of Contents

Data: "Sir, our sensors are showing this to be the absence of everything. It is a void without matter or energy of any kind."

Riker: "Yet this hole has a form, Data; it has height, width, ..."

Data: "Perhaps. Perhaps not, Sir."

Picard: "That's hardly a scientific observation, Commander."

Data: "Captain, the most elementary and valuable statement in science, the beginning of wisdom, is, *I do not know*. I do not know what that is, Sir."

The Bridge of the Enterprise, stardate 42193.6

Chapter 1
Introduction

Not many mysteries in this universe are keeping the scientific society in similar suspense as Dark Matter. There is substantial evidence that only a tiny fraction of the matter in the world is made of atoms, the material that can be seen and felt all around. The vast majority consists of Dark Matter, and yet its nature is unknown. The largest human-made colliders failed to lift the secret fairly recently, when the long-thought messiah of Supersymmetry could not be experimentally confirmed. Ever since, more humble approaches to the problem are shifting into focus, in the form of *minimal Dark Matter models*. The models consist of rather gentle extensions to the Standard Model of particle physics, the theory that describes visible matter with immense accuracy. Adding only a few new components results in more manageable predictions, which can more easily be tested experimentally, and allow greater margins for corrections.

The minimal model studied in this work is the *Scotogenic Model*, belonging to a class of models called *radiative seesaw models*. It introduces a naturally occurring scalar Dark Matter candidate. Even though the Scotogenic Model is a simple extension, there are still plenty of parameters that require accounting. The multi-dimensional space spanned by the parameters can lead to a sheer infinite amount of possible scenarios. The basic idea, however, is the same in all of them: The Dark Matter candidate of the model can gravitationally accumulate via scattering processes in celestial bodies like the Sun, where it attracts enhanced attention than elsewhere in the low-density interstellar medium. Dark Matter in the Sun reveals itself by means of annihilation, which produces a flux of neutrinos — neutrinos that can be measured by Earth-bound neutrino telescopes like the IceCube South Pole Neutrino Observatory.

Different aspects of the Scotogenic Model have been studied before. In this work, the focus is on the specific phenomenology of inelastic scattering of Dark Matter with nuclei inside the Sun, on the investigation of neutrino production possibilities, and on studying the impact on indirect detection with IceCube.

Neutrinos are another mystery of present day physics. They are incredibly abundant — several billion pass through the area of a thumb nail every second — but they do not quite fit the margins of the Standard Model. Their masses, for instance, can not be explained by means of the Standard Model alone. The Scotogenic Model offers a solution to this problem, explaining the existence of neutrinos masses through interactions with the new dark particles. For a while, neutrinos were thought to *be* the Dark Matter, but predictions say that even their combined mass can not possibly suffice to account for all of Dark Matter. They only interact weakly with other particles, which makes them very evasive and difficult to study. Still, neutrinos can help to solve the Dark Matter riddle. Since neutrinos could be generated in Dark Matter annihilation processes, one can search for fluxes of neutrinos from regions of suspected enhanced Dark Matter density. Present-day neutrino telescopes therefore play an important role in research targeting beyond the Standard Model.

IceCube is the largest neutrino detector in the world. With over 5,000 sensors distributed in one cubic-kilometer of instrumented ice at the geographic South Pole, it can detect neutrinos from the Sun, the atmosphere, and outer space. IceCube has collected data from neutrino interactions for over ten years; an invaluable treasure of information that can be searched for neutrinos from Dark Matter annihilation.

This work is organized as follows: Neutrino astrophysics and measurement principles are explained in Chp. 2, as well as the layout and functionality of the IceCube detector. An introduction to the Standard Model of particle physics is given in Chp. 3, alongside different theories of Dark Matter. The Scotogenic Model is described in Chp. 4. Here, the implementation of the model building process is explained in detail, along with current theoretical and experimental constraints, and it is described how viable scenarios can be identified by means of scans of the parameter space. The viable scenarios are tested in an IceCube data analysis that is detailed in Chp. 5, including descriptions of the data sets and statistical analysis methods, and a discussion of the results. A summary of this work and a short outlook is given in Chp. 6.

Chapter 2
Neutrino astrophysics

This first chapter introduces the reader to neutrino astrophysics, its history, and its importance to the understanding of our universe. The sections are organized as follows: A brief introduction to neutrinos and their role in multi-messenger astronomy is given in Sec. 2.1. The following Sec. 2.2 is about cosmic rays, different neutrino sources and basic properties like oscillation and interaction mechanisms. Experimental approaches to the detection of neutrinos are covered in Sec. 2.3. One of these approaches is the IceCube South Pole Neutrino Observatory, the instrument that provided the data used in this work, which will be explained in much detail in the last subsection.

2.1 The role of neutrinos in multi-messenger astronomy

Neutrinos are elementary particles that surround us in an abundance unmet by any other massive particle species. They originate from wherever radioactive processes are at work — which is, basically, everywhere. Each second on this planet, 60 billion neutrinos pass through an area the size of a thumb nail. Most of them originate in the Sun, some in the atmosphere, others come out of nuclear power plant reactors and a few might even be generated inside the reader's fruit basket (by the natural radioactive decay of potassium in bananas).

But, from an astrophysical point of view, the far more interesting sources of neutrinos lie beyond the solar system; in distant stars, super nova remnants, black holes, merging binaries, active galactic cores. A rule of thumb regarding such objects is: The further away, the more mysterious. Optical telescopes can reach very far, but the amount of information that is accessible to detection concepts based on electromagnetic radiation is limited. The ever-growing human horizon called for alternatives to the classic telescopes. This is how *multi-messenger astronomy* was born — the term "multi-messenger" refers to the concept of not only using light for astronomical observations, but other particles as well. Neutrinos can be those other particles.

Neutrinos are the three electrically neutral counterparts to the charged leptons, namely the electron-, muon-, and tau neutrinos ν_e, ν_μ, and ν_τ. Compared to the other particles in the Standard Model, their masses are incomprehensibly tiny. In fact, the Standard Model does not budget any mass to them at all, because for the mass generation process known as the *Higgs mechanism*, a particle of right-handed chirality is required. For neutrinos, no such right-handed partner is known (more about this in Chp. 3). The eventual proof that the neutrinos do have small, but very much existing masses, was only given recently, by the discovery of *neutrino oscillation*, for which T. Kajita and A. McDonald were awarded the Nobel Prize in physics in 2015, with their experiments Super-Kamiokande [1] and SNO [2]. But the riddle remains: How, if not by means of the Higgs mechanism, do neutrinos gain their masses? Or is the mechanism still the same, and there *is* a mysterious right-handed neutrino out there, waiting to be discovered?

You see, neutrinos are about as mysterious as the distant objects that can be investigated by their means. It is quite difficult to study them, because they are so notoriously evasive. Besides gravity, neutrinos engage only in the weak force, meaning they can travel hundreds of millions of light years completely unhindered by any obstacles that might lie in their path (which is the reason one does not feel a tingle in the presence of bananas). Neutrinos move through space, clouds, atmosphere, cosmic dust and even lead easier than light falls through glass.

This lack of interaction attitude bears a unique potential. If neutrinos cannot be bothered by even the densest concentration of material, what they carry with them is the purest form of information about whatever process initially created them. In other words: They are messengers directly from their source. For instance, a photon created by fission processes deep inside the Sun's core needs millions of years of "bumping around" through scattering, absorption and re-emission processes, before it even reaches the photosphere. A neutrino, on the other hand, needs about two seconds. That makes neutrinos the *ideal cosmic messengers*. But because the precious information comes at the price of exorbitant elusiveness, scientists needed to come up with some pretty bizarre plans to catch neutrinos; a few of them are described in Sec. 2.3. But first, a closer look is taken at the different sources of neutrinos.

2.2 Neutrinos

2.2.1 Extraterrestrial sources

Some of the many origins of neutrinos have been briefly mentioned in the last section already. Here, the focus is on the extraterrestrial ones. The graph in Fig. 2.1 summarizes the neutrino fluxes from the different extraterrestrial neutrino sources known today (plus spectra of terrestrial and reactor neutrinos). The reader can see that the neutrino energies range from a few millionths of an eV to approximately 10^{20} eV; and some of the sources apparently produce neutrinos with energies over several orders of magnitude. In the following, the individual neutrino sources are briefly explained, starting at lowest energies and concluding with the most powerful neutrinos ever measured; where many portions of this section are based on Ref. [3].

Cosmological neutrinos

The lowest of all neutrino energies are attributed to the cosmological or *relic neutrinos*. The generation of these neutrinos dates back to the Big Bang, when neutrinos were produced thermally, like all other elementary particles. They existed in thermal equilibrium until the cosmological expansion rate outgrew the neutrino interaction rate, which "stranded" the existing neutrinos (hence the term "relic"). The further expansion of the universe has cooled them from a few MeV to a few μeV, which corresponds to a temperature of about 2 K. This neutrino decoupling is similar to the photon decoupling as the cause for the Cosmic Microwave Background. Since the cosmological neutrino background decoupled before the photons, it holds information about the beginning of the universe that dates even further back; however, to this day there is no experimental way of detecting it. At energies in the order of μeV, interaction

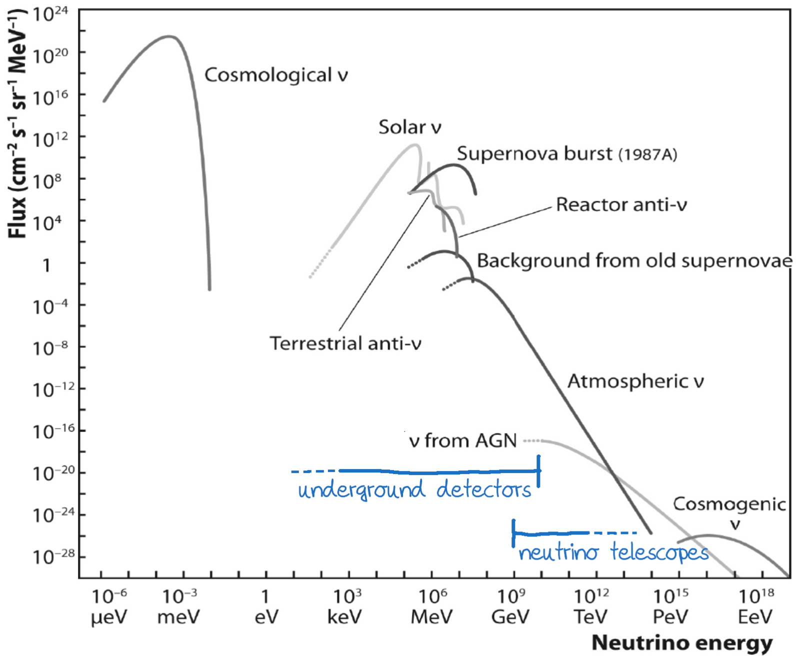

Figure 2.1: The measured and theoretical neutrino fluxes on Earth from different neutrino sources, as a function of energy. In the keV – GeV energy range, the flux can be measured with underground detectors. Large scale neutrino telescopes take over for higher energies. Taken from Ref. [4], modified.

cross sections are even smaller than they already are for neutrinos of more "manageable" energies. [3]

Solar neutrinos

The second to lowest energy spectrum belongs to solar neutrinos. Since neutrinos are produced in radioactive processes, the Sun is a massive neutrino factory, mainly due to the hydrogen fusion process

$$p + p \longrightarrow d + e^+ + \nu_e. \tag{2.1}$$

The Sun produces exclusively electron neutrinos that oscillate into different flavors, which gave rise to the "Solar Neutrino Problem" (more on neutrino oscillation in Sec. 2.2.2). [3]

Supernova neutrinos

Heavy stars at the end of their lifetimes explode in supernovae, hurling massive amounts of matter and energy into space. A vast majority of that energy is carried away by neutrinos. These neutrinos are generated in two major processes of supernova development. The first one is called *neutronization*, which begins when the iron core of the dying star reaches the critical *Chandrasekhar Mass* and kinetically enables the contained electrons to undergo electron capture: [3]

$$p + e^- \longrightarrow n + \nu_e. \tag{2.2}$$

Unlike electrons, the thereby generated electron neutrinos can leave the core unhindered, extracting so much energy that the core is no longer stable and collapses. The collapse leads to an immense compression of matter. The thermal photons in this phase undergo pair production, which results in the second and major neutrino production process: [3]

$$\gamma + \gamma \longrightarrow e^+ + e^- \longrightarrow \nu_\alpha + \bar{\nu}_\alpha, \qquad \alpha \in \{e, \mu, \tau\}. \tag{2.3}$$

Through these reactions, neutrinos of all flavors are generated, exceeding the number of formerly created electron neutrinos by orders of magnitude.

Energetically, supernova neutrinos are in the MeV region. Based on the number of stars in the universe that must have already gone supernova, the existence of an MeV diffuse supernova neutrino background (DSNB) can be assumed, although so far it has evaded experimental confirmation.

Cosmic rays and atmospheric neutrinos

Two separate neutrino fluxes are part of the *cosmic rays*: The astrophysical neutrinos and the atmospheric neutrinos. The latter flux has special relevance to this study, as will be seen in Chp. 5. The two fluxes are produced as the result of separate processes, which correspond to the two components of the cosmic rays:

- **Primary cosmic rays** include the entirety of matter particles and radiation striking Earth that is of cosmic origin. Next to photons and neutrinos, the primary cosmic bombardment consists predominantly of charged particles. The charged cosmic ray chemical composition is well known; it is made of mostly protons (~ 74 %), helium nuclei (~ 18 %), a few percent of heavier nuclei, and some trace amounts anti-protons, electrons, and positrons [5].
- **Secondary cosmic rays** are particles produced as a result of the impact of the primaries.[1]

The energy spectrum of the primary cosmic rays has been measured extensively; the left panel of Fig. 2.2 shows a composition of data from different experiments, targeting different energy regions and particle types. The sources of the primary cosmic rays are not fully understood, neither are the processes that accelerate the particles to such incredible energies. Possible sources include active galactic nuclei. These objects, along with neutrinos as a primary cosmic ray component, are described in more detail in a later subsection.

For now, the focus is on the secondary cosmic rays, where the descriptions follow Refs. [8, 9]. Neutrinos play a major role in secondary cosmic rays. This is best explained by looking at the processes that get in motion when a primary, high-energy cosmic ray proton hits the Earth's atmosphere: Upon collision with an atmospheric atom, exotic mesons are generated (plus some new protons or neutrons). These mesons are mostly charged or neutral pions and kaons, but, depending on the energy of the incident proton, can turn out as charmed mesons like the D-meson. Sticking with the pions and kaons for now, they inherit most of the primary proton's massive energy, which leads to cascades of new interactions which create so-called *air showers*. These showers can be of different nature; either hadronic (creating more hadrons and mesons), electro-magnetic (creating leptons and photons) or muonic (creating muons), and usually consist of millions of secondary cosmic ray particles. The charged pions mainly undergo the following decays:

$$\begin{aligned}\pi^+ &\longrightarrow \mu^+ + \nu_\mu \longrightarrow e^+ + \nu_e + \bar{\nu}_\mu + \nu_\mu,\\ \pi^- &\longrightarrow \mu^- + \bar{\nu}_\mu \longrightarrow e^- + \bar{\nu}_e + \nu_\mu + \bar{\nu}_\mu.\end{aligned} \tag{2.4}$$

[1]The reader should be aware that there exist different conventions for the terms "primary-" and "secondary cosmic rays", and that it is not consistent throughout literature whether neutral particles (photons, neutrinos) are part of the cosmic rays.

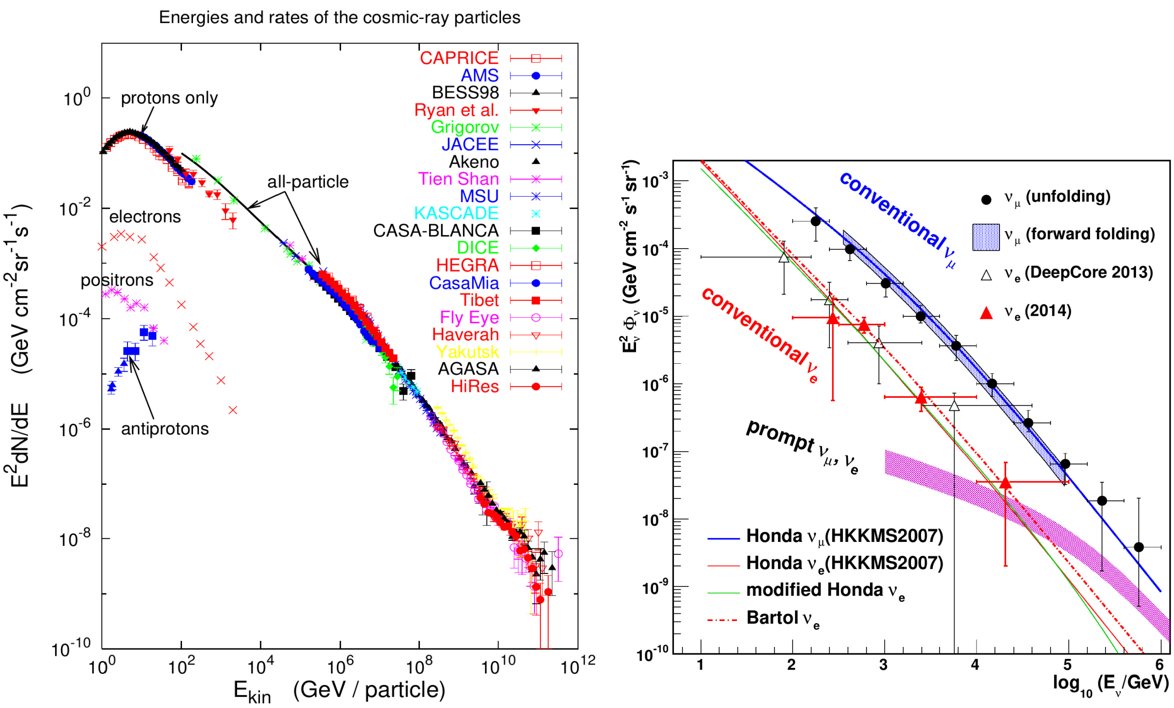

Figure 2.2: **Left:** The cosmic ray fluxes for different particle types, as measured by different experiments. Taken from Ref. [6]. **Right:** The conventional and prompt atmospheric neutrino fluxes. Taken from Ref. [7].

Similar equations hold for charged kaons, which become increasingly important for the production of atmospheric neutrinos for higher energies, and dominate for the TeV region and above [9]. Charged and neutral kaons can further decay as in [5]

$$\begin{aligned} K^0_{L,S} &\longrightarrow \pi^\pm + e^\mp + \bar{\nu}_e(\nu_e), \\ K^\pm &\longrightarrow \pi^0 + e^\pm + \nu_e(\bar{\nu}_e), \end{aligned} \tag{2.5}$$

with very small branching fractions compared to Eq. (2.4). (The K^0_L and K^0_S refer to the physical particles of the $K^0(\bar{K}^0)$ meson that have significantly different life times, and are therefore labeled with S for "short" and L for "long". The K^0_S contribution can be neglected at energies below several hundred TeV [9]). Neutrinos from the above processes are summarized under the term **conventional flux**. In the right panel of Fig. 2.2, the spectra of the conventional electron and muon neutrinos are shown.

Besides the conventional fluxes, there is also a **prompt flux**, generated from the decay of heavier mesons like D-mesons. The prompt flux is harder, but also suppressed for lower energies, so that it can usually be neglected at neutrino energies below 10^6 GeV. The name "prompt" arises from the fact that most of the heavier mesons decay very quickly, and without further energy loss. The prompt energy spectrum therefore resembles the primary cosmic ray spectrum better than the spectrum of the conventional flux.

The spacial distribution of the atmospheric neutrino flux is not isotropic. While in azimuth direction it is homogeneous when averaged over time, a significant zenith dependency arises from the decay "competition" of muons: The development of atmospheric showers, and subsequently the decay of muons, depend on the amount of atmosphere between the point of primary cosmic ray incidence and the surface of the Earth or the underground detector. The atmospheric slant depth is smallest for an incident angle of 0° (perpendicular to the surface). Small slant depths allow for only short trajectories and leave less time to decay for highly energetic muons, resulting in a lower electron neutrino flux from muon decay for larger energies. The prompt neutrino flux remains isotropic, because of the much shorter lifetimes of the involved mesons. [8]

The (initial) flavor composition of the conventional atmospheric neutrino flux can be predicted from the main production process in Eq. (2.4): The charged pion/kaon decay chain would produce the ratio

$$\frac{\nu_\mu + \bar{\nu}_\mu}{\nu_e + \bar{\nu}_e} = 2. \tag{2.6}$$

This holds under the condition that all muons decay in the atmosphere. For larger energies above a few GeV [8], this is not the case anymore, again because the muon decay lengths exceeds the distance from production point to the surface or underground detector due to time dilation[2]. For high energies, the $\nu_e + \bar{\nu}_e$ flux is therefore suppressed, and the only contribution comes from the rare processes in Eq. (2.4), or even less dominant decay modes.

In contrast to the conventional flux, the prompt atmospheric flavor composition of electron neutrinos and muon neutrinos is roughly 1 : 1, with an additional small fraction of tau neutrinos as a result of the decay modes of D-mesons [9, 8].

However, measurements of the atmospheric neutrino flux can reveal significant deviations from the above discussed ratios, due to neutrino oscillation, which is covered in more detail in Sec. 2.2.2. At medium energies (GeV region), oscillation mainly affects muon- and tau neutrinos. At lower energies, ν_e oscillation effects inside the Earth medium play a role as well. The effect depends on the neutrino energy and incident angle, and can be calculated e.g. using the tools nuflux, MCEq and NUSQuIDS [10, 9, 11].

For further reading on cosmic rays and the atmospheric neutrino flux, Refs. [3, 8, 6, 12, 7] are recommended.

Solar atmospheric neutrinos

Not only the fusion of hydrogen to heavier elements is a source of solar neutrinos — the Sun's atmosphere is assumed to generate neutrinos as a result of the bombardment with cosmic rays. This process is briefly described in the following, based on Refs. [13, 14].

The production mechanism of these solar atmospheric neutrinos is similar to that of Earth atmospheric neutrinos, so the initial flavor ratio is also $\nu_e : \nu_\mu : \nu_\tau \approx 1 : 2 : 0$ (in contrast to the "regular" solar neutrino flux, which initially consists exclusively of electron neutrinos). However, at Earth or in an underground detector, the ratio is predicted to measure $\sim 1 : 1 : 1$, due to vacuum oscillation effects between the Sun and Earth that average over a large production volume. Oscillation effects inside the solar material do play a role, but are subdominant (and not resolvable with current neutrino telescopes).

The spectrum of the solar atmospheric flux is slightly harder than the Earth atmospheric flux, due to the lower coronal particle density, which prevents especially the lighter mesons from loosing much energy prior to decay.

[2]The "classical" decay length of a muon with a mean lifetime of 2.2 μs [5] and a velocity $v \approx c$ would only be ~ 660 m.

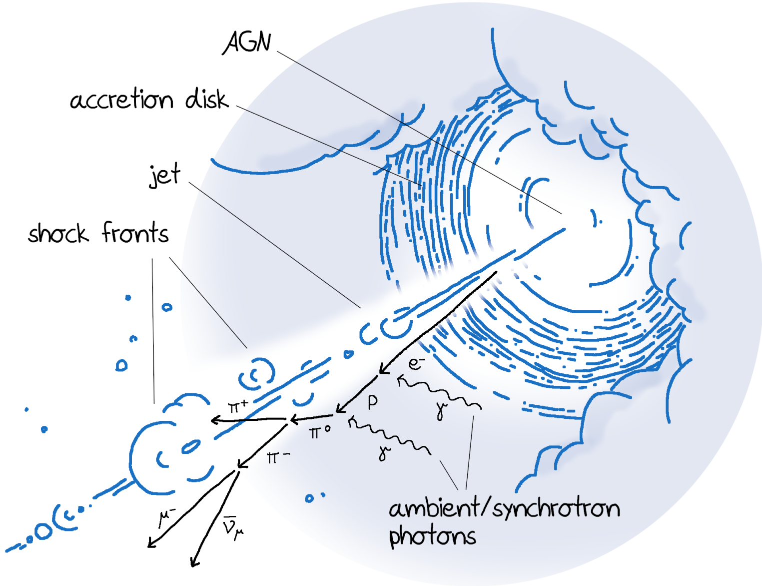

Figure 2.3: An active galactic nucleus (supermassive black hole inside the center of a galaxy), and a process of hadronic acceleration in the jet. The neutrinos produced in such objects have the highest energies ever measured.

Astrophysical neutrinos

Even though in much smaller abundance than in the secondary cosmic rays, neutrinos are also part of the primary cosmic rays. This astrophysical neutrino flux reaches the by far highest energies with a relatively hard spectrum compared to other fluxes in Fig. 2.1. Their sources are imagined to lie in the most powerful objects: Supermassive black holes in the center of galaxies, called *active galactic nuclei* (AGNs). These objects translate parts of their immense gravitational energy into kinetic energy, blasting surrounding particles into outer space in violent streams, so-called *jets*, as depicted in Fig. 2.3. Fed with energy from the object's accretion disc, the particles inside the jets are accelerated to relativistic velocities. Should protons be among those particles, then one talks of *hadronic acceleration*, a process that leads to the creation of mesons which decay into charged leptons and neutrinos, similar to the processes responsible for the secondary cosmic rays. It was long theorized that hadronic acceleration in the vicinity of AGNs could be one source of ultra high-energy astrophysical neutrinos, and only recently evidence was found that indeed it is: In a multi-collaboration and multi-messenger effort, a $\sim 300\,\mathrm{TeV}$ neutrino detected by the IceCube South Pole Neutrino Observatory could be associated with the blazar[3] TXS 0506+056, an object roughly 6 billion light years away, in consistency with gamma-ray observations by Fermi-LAT, MAGIC and several other experiments [15, 16].

One can see that astrophysical neutrinos cover distances which are, quite literally, astronomical; not rarely significant fractions of the known universe. Said TXS neutrino had to be almost half as old as the universe itself to travel that far. Nonetheless, astrophysical neutrinos are ideal cosmic messengers, and they are the key witnesses in the case of all those powerful objects at the far ends of the universe. Several neutrinos measured by IceCube pointed towards other astrophysical sources, including a tidal disruption event[4] [17], and a supermassive black hole in the active galaxy Messier 77, that a recently published IceCube study associates with about 80 TeV-neutrinos [18].

[3] A blazar is an active galactic nucleus with a jet pointing in the direction of the observer.

[4] A tidal disruption event is a star being "torn apart" by a black hole; the consumption of the star's matter results in the emission of a flare of electromagnetic radiation.

2.2.2 Oscillation

The reader has learned in Sec. 2.2.1 that the Sun produces exclusively electron neutrinos (neglecting the flavors in the flux of solar atmospheric neutrinos which is many orders of magnitude weaker). These neutrinos have first been measured in 1967 by Raymond Davis et al. and the HOMESTAKE Experiment [19], which captured solar neutrinos with a threshold energy of $\sim 0.8\,\mathrm{MeV}$ with the radio-chemical reaction

$$\nu_e + {}^{37}\mathrm{Cl} \longrightarrow e^- + {}^{37}\mathrm{Ar}. \tag{2.7}$$

The unstable ^{37}Ar decayed back into ^{37}Cl, emitting X-ray photons and Auger electrons which could be detected in gas counters. The overall neutrino count of the HOMESTAKE experiment accounted for only about 33 % of the expected solar neutrino flux — the "Solar Neutrino Problem" was born. This two thirds solar neutrino deficiency was first attributed to the high threshold energy of the experiment that did not allow for the measurement of neutrinos from the Sun's main fusion channel. Therefore, deviating parameters of the solar model could still be the explanation. When these hypothesis could not be proven correct by other radio-chemical counting experiments including GALLEX, GNO and SAGE [20, 21, 22], with much lower threshold energies, the theory of neutrino oscillation shifted into focus: If the solar electron neutrinos would change their properties on the way from the Sun to Earth, they might evade detectors that are only sensitive to a certain kind of neutrino. This was eventually confirmed by the SNO and KAMLAND [2, 23] collaborations, whose experiments were sensitive to all neutrino flavors and therefore able to measure the total solar neutrino flux.

A similar neutrino deficiency was measured in the flux of atmospheric neutrinos, which was identified to be another result of neutrino oscillation by SUPER-KAMIOKANDE [1]. In 2015, the Nobel Prize in physics was awarded to Takaaki Kajita of the SUPER-KAMIOKANDE and Arthur B. McDonald of the SNO collabroations for the discovery of neutrino oscillations. A short description of the prize-winning machines is given at the end of Sec. 2.2.3.

The theory behind neutrino oscillation described here mainly follows Refs. [3, 24]. It starts out on the fact that the neutrinos are actually a *mix*. What has been called electron-, muon-, and tau neutrinos so far are the *flavor eigenstates* of the neutrinos, which do not coincide with the three different *mass eigenstates*. The flavor eigenstates ($\alpha \in \{e, \mu, \tau\}$) and mass eigenstates ($i \in \{1, 2, 3\}$) are connected as in

$$|\nu_\alpha\rangle \quad = \quad \sum_{i=1}^{3} U_{\alpha i} |\nu_i\rangle \tag{2.8}$$

by the unitary mixing matrix $U_{\alpha i}$, the Pontecorvo–Maki–Nakagawa–Sakata (PMNS) matrix. It is easier to approach this rather complicated mixing matrix from the two-flavor case, which is done in the following.

For only two neutrino flavors α and β and two mass eigenstates k and l, Eq. (2.8) simplifies to

$$\begin{pmatrix} \nu_\alpha \\ \nu_\beta \end{pmatrix} = \begin{pmatrix} \cos\theta_{kl} & \sin\theta_{kl} \\ -\sin\theta_{kl} & \cos\theta_{kl} \end{pmatrix} \cdot \begin{pmatrix} \nu_k \\ \nu_l \end{pmatrix}. \tag{2.9}$$

The probability of flavor α to oscillate into flavor β in vacuum is given by [3]

$$P_{\alpha\to\beta}(t) \quad = \quad \sin^2(2\theta_{kl})\sin^2\left(\frac{\Delta m^2 t}{4E}\right), \tag{2.10}$$

in natural units $c = \hbar = 1$, with the mixing angle θ_{kl}, the neutrino energy E, and the squared mass difference between the two mass eigenstates, $\Delta m^2 = \left(m_k^2 - m_l^2\right)$. Under the assumption of relativistic neutrinos, the oscillation length is $L \approx T \cdot c = \left(2\pi \cdot 2E/\Delta m^2\right)$ with the oscillation period T. One can see that the oscillation probability vanishes for $m_k = m_l$, meaning that neutrino oscillation is a direct consequence of massive neutrinos with different mass eigenstates.

The PMNS matrix can be broken down into three simpler matrices of the form used in Eq. (2.9), by approximating the three-flavor mixing case with three two-flavor mixing cases. This approximation is actually well justified, since, depending on neutrino energy and distance from the source, one eigenstate can usually be neglected if the experimental conditions are chosen accordingly. For instance, in measurements of the solar oscillation parameters as conducted with SNO, Super-Kamiokande, and KamLAND [25, 26, 23], only oscillation between ν_e and ν_μ is relevant (to good approximation) — interesting here is that the solar oscillation parameters can be determined by means of solar as well as reactor neutrinos, with oscillation lengths of 1 AU and a few hundred km, respectively, in the MeV and sub-MeV energy range. The Double-Chooz, RENO and Daya-Bay [27, 28, 29] experiments investigate(d) neutrinos from nuclear power plants, also in the MeV energy region, but at much smaller oscillation lengths in the order of 1 km, and measure only the transition from ν_e to ν_τ. Lastly, experiments conducted with Super-Kamiokande and IceCube [30, 31] aiming at GeV atmospheric neutrinos, observe only oscillation between ν_μ and ν_τ.

Hence, the PMNS matrix can be conveniently parameterized by three two-flavor mixing angles θ_{12}, θ_{23}, θ_{13}: [3]

$$\begin{pmatrix} \nu_e \\ \nu_\mu \\ \nu_\tau \end{pmatrix} = \overbrace{\underbrace{\begin{pmatrix} 1 & 0 & 0 \\ 0 & c_{23} & s_{23} \\ 0 & -s_{23} & c_{23} \end{pmatrix}}_{\text{atmospheric}} \underbrace{\begin{pmatrix} c_{13} & 0 & s_{13}e^{i\delta_{\mathrm{CP}}} \\ 0 & 1 & 0 \\ -s_{13}e^{i\delta_{\mathrm{CP}}} & 0 & c_{13} \end{pmatrix}}_{\text{reactor}} \underbrace{\begin{pmatrix} c_{12} & s_{12} & 0 \\ -s_{12} & c_{12} & 0 \\ 0 & 0 & 1 \end{pmatrix}}_{\text{solar}}}^{\text{PMNS matrix}} \cdot \begin{pmatrix} \nu_1 \\ \nu_2 \\ \nu_3 \end{pmatrix}, \tag{2.11}$$

with the abbreviations $c_{ij} = \cos\theta_{ij}$ and $s_{ij} = \sin\theta_{ij}$. The phase angle δ_{CP} implies a violation of charge-parity in the lepton sector should it be non-zero, which has not yet been proven.

Besides the mixing angles, the squared mass differences of the three neutrino mass eigenstates can also be accessed experimentally, as additional atmospheric and solar oscillation parameters. Even though they are measured with good precision, the order of the absolute masses can not be inferred from these measurements. After $m_1 < m_2$ had been pinned down by the solar neutrino experiments, two kinds or "hierarchies" remain: The *normal hierarchy* with $m_1 < m_2 < m_3$, oriented at the masses of the charged leptons (since each mass eigenstate is a different mixture of the flavor eigenstates, one could say that m_1 corresponds mostly to ν_e, m_3 mostly to ν_τ, and hence m_2 to ν_μ). The other possibility is the *inverted hierarchy* with $m_3 < m_1 < m_2$. Both mass ordering options are visualized in Fig. 2.4.

Matter, specifically electrons in matter, can change the parameters of neutrino oscillation.

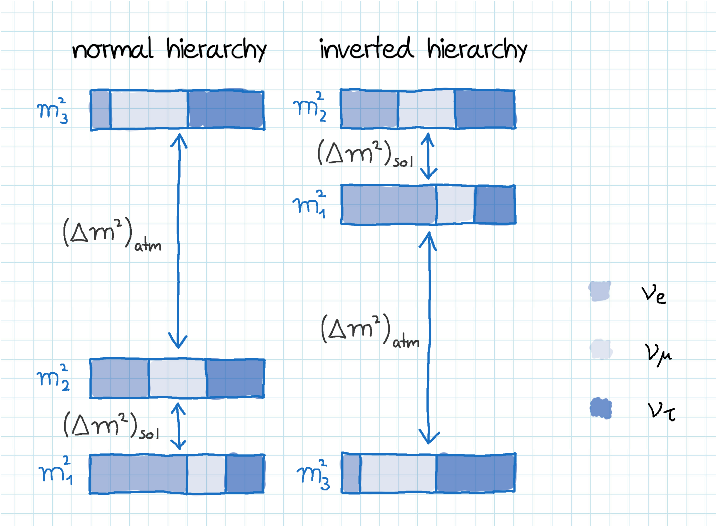

Figure 2.4: Visualization of the two possible neutrino mass hierarchies, governed by the experimentally determined squared mass differences $(\Delta m^2)_{\text{sol/atm}}$. The mass eigenstates $m_{1,2,3}$ are shown as compositions of the flavor eigenstates $\nu_{e,\mu,\tau}$, represented by the different shades of blue.

This is known as the Mikheyev–Smirnov–Wolfenstein (MSW) effect [32, 33]. The neutrinos undergo a *coherent forward scattering* with electrons inside a medium. This can be compared to the refractive index in optics: Similar to light having different velocities in matter and vacuum, so do neutrinos have slightly different effective masses in a medium than they would have in void space. The strength of the effect depends on the electron density of the medium, and the neutrino energy. Only electron neutrinos can forward-scatter with electrons in matter, but neutral-current forward-scattering with nuclei happens for all flavors in the same way. This leads to a dissonance in the oscillation parameters of ν_e compared to $\nu_{\mu,\tau}$. The effect is most significant for medium-energy (MeV – GeV) neutrinos in electron-dense media like the Sun or the Earth, so it affects the solar neutrino flux, as well as the lowest-energy atmospheric neutrino flux coming from below the horizon of the respective detector.

It is specifically the MSW effect that predicts $\Delta m^2_{12} > 0$, leading to the aforementioned relation of $m_1 < m_2$ and the two possible mass hierarchies. [3]

2.2.3 Basic interactions

Neutrinos basically never interact with matter — except when they do. The interaction cross section of a neutrino with a nucleus inside some material is (energy dependent, and generally) small, but not zero. That means neutrino interactions do happen, they are just notoriously rare when compared to interaction rates of other particles. So to catch a neutrino, one needs patience, luck, and the right machine. A few of those machines have already been mentioned in the last section.

Neutrino scattering processes can occur as a weak *charged current* (CC) or *neutral current* (NC) interaction. The two basic vertices of these interactions are shown in Fig. 2.5. Charged current interactions happen via the exchange of a W^+ or W^-. They invoke a transfer of electric charge (hence the name) and with it a transition between lepton states, e.g. from a neutrino into the corresponding lepton of the same flavor, as is shown in diagram (a). Neutral current interactions, as shown in diagram (b), are mediated by the electrically neutral Z^0. No electric charge is transferred, and the quantum numbers of the in- and outbound particles are the same.

Depending on the transferred energy, the scattering processes are further categorized in the following manner, following Ref. [3]:

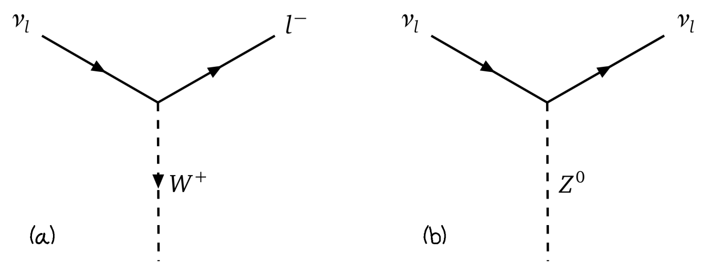

Figure 2.5: Feynman diagrams of the basic charged current (a) and neutral current (b) vertices of neutrino weak interaction, for the lepton flavors $l \in \{e, \mu, \tau\}$, with time progressing from left to right. The diagrams are valid for the respective anti-particles as well.

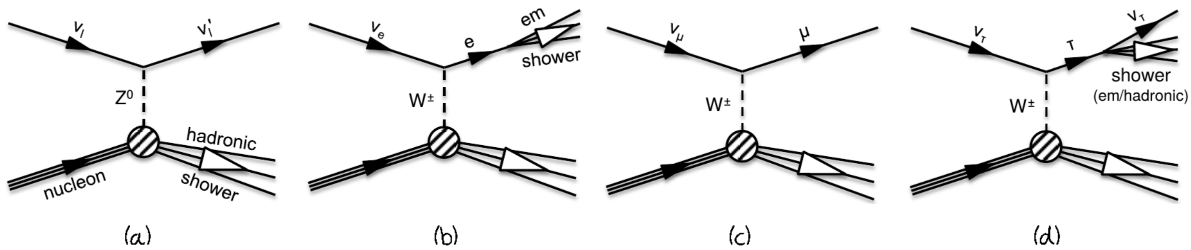

Figure 2.6: Schematic diagrams of deep inelastic scattering of high-energy neutrinos with nucleons, compare Eq. (2.14), with time progressing from left to right. (a): NC reaction of a neutrino of flavor l scattering off a nucleon exchanging a Z^0, producing a hadronic shower. (b) - (d): CC reactions for the flavors e, μ and τ, producing hadronic and/or electromagnetic showers. All reactions are valid for the respective anti-neutrinos. Taken from Ref. [12], modified.

– **Elastic scattering with electrons**, according to

$$\nu_l + e^- \longrightarrow \nu_l + e^-, \tag{2.12}$$

where l is the lepton flavor, is the dominant process for low neutrino energies up to the MeV range. Especially solar neutrino experiments, like SNO (see below), use the above reaction for the detection of neutrinos, where the recoil energy of the electron is measured as scintillation light.

– In the MeV up to 1 GeV energy range, neutrinos scatter predominantly with the whole nucleon in processes called **quasi-elastic scattering**. They can be described by the following interactions:

$$\text{CC:} \quad \begin{array}{l} \nu_l + X \longrightarrow l^- + Y, \\ \bar{\nu}_l + X \longrightarrow l^+ + Y, \end{array} \qquad \text{NC:} \quad \begin{array}{l} \nu_l + X \longrightarrow \nu_l + Y, \\ \bar{\nu}_l + X \longrightarrow \bar{\nu}_l + Y, \end{array} \tag{2.13}$$

where X and Y are hadronic (proton or neutron) states. One or more nucleons is usually removed from the core, which is why a change of hadronic state is also indicated in the NC case. The CC interaction is used especially in detectors aiming at the mid-energy range of atmospheric neutrinos, by means of the Cherenkov radiation emitted by the charged leptons. In addition to CC interactions, the NC interactions can as well be relevant to solar neutrino experiments, where the energy dissipated into the target material by the removed nucleon(s) can be measured.

– The prevailing process in the $\sim 1 - 10$ GeV range is **resonant Δ-meson production**, in which the inbound neutrino can excite a nucleon inside an atomic core into a Δ-meson state. The decay of the short lived meson resonance results in the emission of further hadrons (including nucleons and pions).

- **Deep inelastic scattering** can occur for neutrino energies of a few GeV, and quickly becomes the dominant process for energies $> 10\,\mathrm{GeV}$. The neutrino scatters with the constituent quarks, resulting in a hadronic cascade produced by nucleons being removed from the core. Deep-inelastic scattering processes can be described by the following equations for the charged and neutral current case:

$$\text{CC:} \quad \begin{array}{l} \nu_l + X \longrightarrow l^- + Z, \\ \bar{\nu}_l + X \longrightarrow l^+ + Z, \end{array} \qquad \text{NC:} \quad \begin{array}{l} \nu_l + X \longrightarrow \nu_l + Z, \\ \bar{\nu}_l + X \longrightarrow \bar{\nu}_l + Z, \end{array} \tag{2.14}$$

  where X denotes a hadronic state, and Z a hadronic cascade (shower). The schematic diagrams of the four possible deep-inelastic interactions, which are most important for high-energy neutrino astronomy with neutrino telescopes, are shown in Fig. 2.6.

The cross sections of the above-described processes as functions of the neutrino energy are shown in Fig. 2.7.

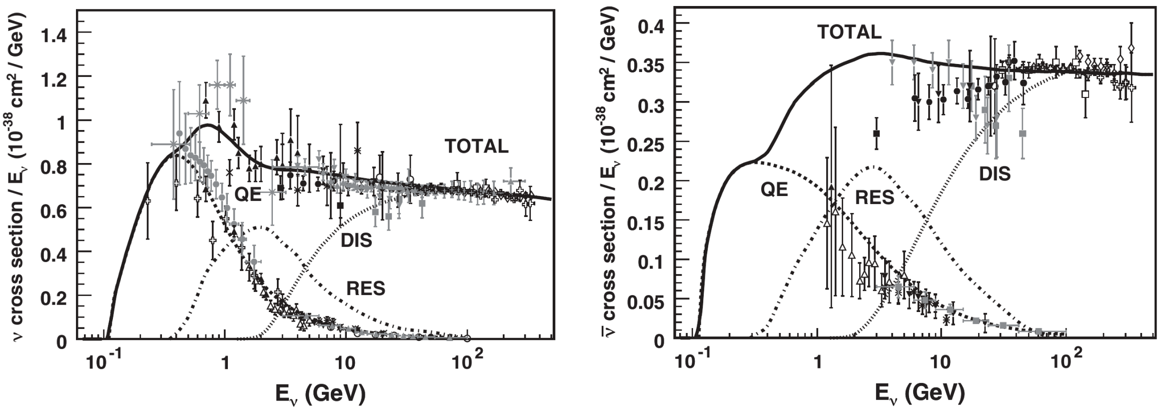

Figure 2.7: Neutrino (left) and antineutrino (right) interaction cross sections as functions of the neutrino energy. Shown are results from different experiments. The dotted lines describe quasi-elastic scattering, the dashed lines describe deep-inelastic scattering, and the dashed-dotted lines describe resonant meson production. The solid lines indicate the total cross sections. Plots taken from Ref. [34].

Examples of underground neutrino detectors

The SNO (Sudbury Neutrino Observatory) experiment [35] took data between 1999 and 2006. It was located in the Sudbury mine in Canada. It consisted of a plexiglass sphere with 12 m in diameter, filled with 1,000 tons of heavy water (D_2O). The sphere was surrounded by an outer volume of light water for shielding purposes. Thousands of inward-directed photomultiplier tubes (PMTs) mounted on a spherical support structure detected the radiation induced by neutrino interactions. A drawing of the detector is shown in Fig. 2.8, left.

Three different reactions could be used to detect neutrinos: The quasi-elastic CC and NC reactions of neutrinos with the deuterons, as well as elastic scattering with the electrons in the target material. This way, the experiment was sensitive to solar neutrinos of all flavors.

The construction principle of the Super-Kamiokande detector [36] is similar to that of SNO and other undergound neutrino experiments. It consists of a large cylindrical tank of roughly 40 m height and diameter, filled with 50,000 tons of highly purified light water. The tank

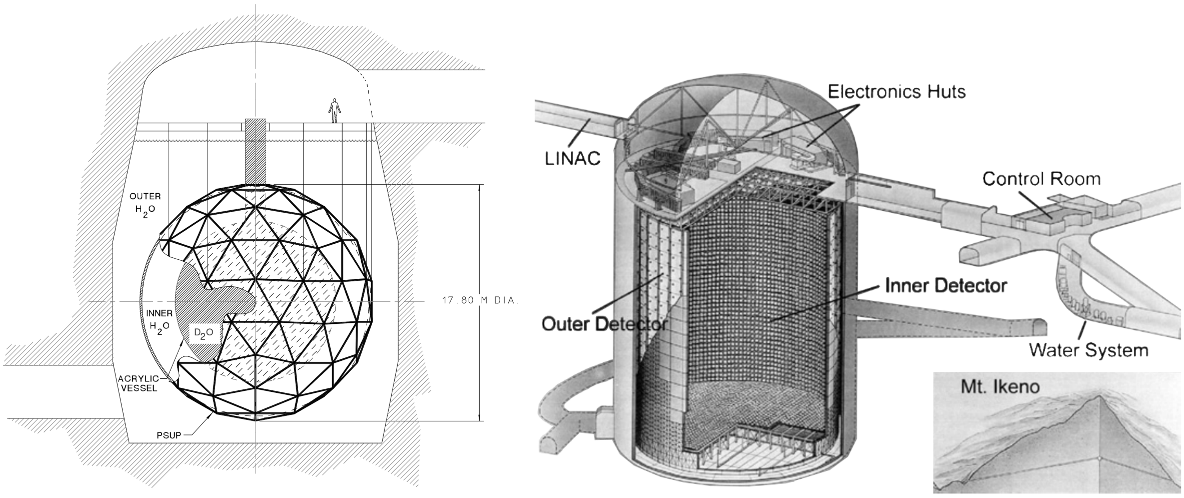

Figure 2.8: **Left:** The SNO experiment in the Sudbury mine in Canada. The spherical plexiglass tank holds 1,000 metric tons of heavy water, surrounded by a light water shielding volume. The inward-facing PMTs are mounted on the PSUP structure. Figure taken from Ref. [35], modified. **Right:** The Super-Kamiokande experiment beneath Mt. Ikenoyama in Japan. The detector chamber holds roughly 50,000 metric tons of ultra-pure water. The walls of the tank are covered in PMTs facing inwards (inner detector) and outwards (outer detector). The section labeled "LINAC" houses a low-energy electron linear accelerator for calibration purposes. Figure taken from Ref. [36], modified.

walls are covered with inward-facing and outward-facing PMTs. Atmospheric neutrinos are detected using quasi-elastic CC reactions, but the detector is also sensitive to elastic scattering of solar neutrinos. The outward facing PMTs are used as a veto detector, as well as to determine whether neutrino events are fully contained inside the tank or not, which affects the reconstruction of the neutrino energy.

The experiment is located in a re-purposed mine under Mt. Ikenoyama near the west coast of Japan. Roughly 1 km of solid rock shields the detector from radiation and cosmic rays, especially atmospheric muons. Fig. 2.8 (right hand side) shows a sketch of the detector.

2.3 Neutrino telescopes

The term "neutrino telescope" in this work refers to large-scale detectors that are somewhat similar to, but also different from the underground detectors introduced in the previous section, like Super-Kamiokande, SNO, KamLAND, or Daya Bay. The main differences are:

- The scientific goals. While underground detectors usually investigate neutrino properties like oscillation parameters or the composition of a particular neutrino flux by means of solar, reactor or atmospheric neutrinos, neutrino *telescopes* aim primarily at the detection of high-energy astrophysical neutrinos.

- The construction principle. Generally, the size of a neutrino experiment scales with the desired energy range. This has two main reasons: First, high-energy neutrino interactions are rare, and a big detector simply increases the chances of witnessing one. Secondly, the trace such an interaction leaves behind can spread out over an immense volume, and one wants to record as much of it as possible. While the investigation of lower energy neutrinos already requires the building of large tanks filled with many tons of detection medium, the energy ranges of neutrino telescopes require detector volumes beyond the artificially construable, relying on large natural reservoirs of target material. The medium is instrumented by placing optical sensors throughout the entire volume, while artificial underground detectors usually have their optical sensors placed at the perimeters of the tank.

In the following, the concept of detecting high-energy neutrinos is presented in more detail, alongside a short history of past and present-day neutrino telescopes.

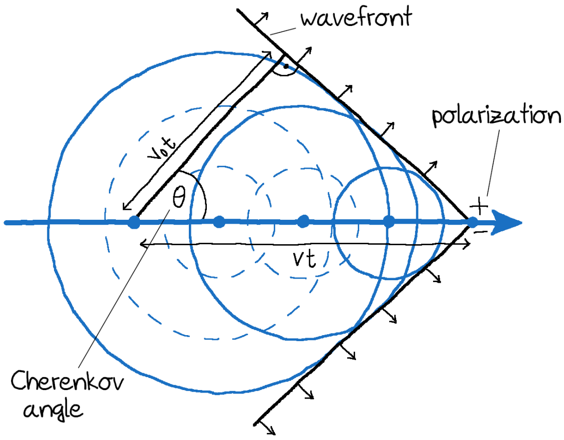

Figure 2.9: Production principle of Cherenkov radiation. A charged particle that moves along a trajectory (blue arrow) with velocity v polarizes the surrounding medium. The consequently emitted light travels with velocity $v_0 < v$, which results in constructive interference and the formation of a wavefront. The opening angle θ is characteristic for the medium.

2.3.1 Detection principle

Mainly due to their immense size, neutrino underground detectors and telescopes are stationary, wide-field (or all-sky) telescopes. The location of neutrino telescopes is chosen so that they provide a sufficient amount and optical quality of detector medium, as well as a suitable underground location that shields the detector from cosmic rays. The deep sea and the Antarctic plateau are the only locations that have been found to fulfill these requirements so far.

The reason for these exotic sites is that the detector medium needs to be transparent. When a neutrino undergoes a quasi- or deeply inelastic scattering process, light in (also) the visible frequency range is emitted which can be detected by optical sensors. This light is called *Cherenkov radiation*, and is explained in more detail below, following Refs. [37, 24].

The Cherenkov effect

Neutrino interactions can generate charged particles. Such a charged particle polarizes the surrounding (dielectric) material with its electric field, stretching the atoms out of their original shape. The relaxation of the atoms follows almost immediately, under the emission of electromagnetic radiation.

If the velocity v of the charged particle is lower than the phase velocity v_0 of light inside the medium, the polarization occurs symmetrically, and any (macroscopically measurable) radiation is swallowed by destructive interference. If, on the other hand,

$$v \geq v_0 = \frac{c}{n}, \tag{2.15}$$

with the speed of light c and the refractive index n of the medium, constructive interference leads to the formation of a wavefront and the emission of *Cherenkov radiation*. This radiation is generated in the shape of a cone along the trajectory of the charged particle, with an opening angle that follows the relation [37]

$$\cos\theta_C = \frac{v_0}{v} = \frac{1}{n\beta}, \tag{2.16}$$

with $\beta = v/c$, as can be calculated with basic geometry from Fig. 2.9. The *Cherenkov angle* θ_C is characteristic for the medium, and is approximately $1.4\,^\circ$ in air and $42\,^\circ$ in water/ice [24] for relativistic particles with $\beta \approx 1$.

At a hypothetical detector plane at distance d one would observe the image of a ring with radius

$$r = d\tan\theta_C. \tag{2.17}$$

The shape of the cone and ring can be used to identify the neutrino flavor: A muon as produced in a charged current muon neutrino interaction travels along a straight trajectory, depositing its energy gradually before decaying, and therefore producing a relatively sharp image of a ring in the detector plane. An electron, on the other hand, deposits its energy largely "on the spot" via many scattering processes, hence producing a blurred image [24]. High-energy neutrino telescopes usually can not resolve these rings, and muons and electrons are distinguished by their track- and spherical shaped signatures, as described in Sec. 2.3.3.

The spectrum of the Cherenkov radiation goes with $1/\lambda^2$, as shown with the relation [37]

$$\begin{aligned} \frac{d^2N}{d\lambda} &= \frac{2\pi z^2\alpha}{\lambda^2}\left(1 - \frac{1}{\beta^2 n^2(\lambda)}\right)L \\ &= \frac{2\pi z^2\alpha}{\lambda^2} L\sin^2\theta_C \end{aligned} \tag{2.18}$$

which can be derived from the Frank-Tamm formula [38]. The above equation describes the number N of emitted Cherenkov photons per wavelength λ over a distance L, with the particle's charge number z, and the fine-structure constant α. Cherenkov radiation is often associated with blue-ish color, which can be explained with the $1/\lambda^2$ proportionality. Furthermore, anomalous dispersion prevents the emission of Cherenkov radation in a medium for certain frequency regions. Typical (transparent) materials with Cherenkov emission feature such an anomalous dispersion band for $\lesssim 100\,\mathrm{nm}$, so that blue and UV frequencies in fact correspond to the region of maximum intensity. [37]

2.3.2 Brief history of large scale neutrino telescopes

Pioneer milestones on the field of neutrino telescopes were set by the DUMAND (Deep Underwater Muon and Neutrino Detector) project [39]. The original proposal for the project included a multi-cubic-kilometer array of thousands of optical modules in the deep Pacific Ocean off the coast of Hawaii, while later proposals down-scaled the experiment to much smaller arrays with a few hundred modules. Eventually, the project was abandoned completely. Even though never realized due to various difficulties, many technical and constructional concepts could be derived from the DUMAND plans for other telescopes to come.

The first of them to be ever realized was the Baikal Deep Underwater Neutrino Telescope

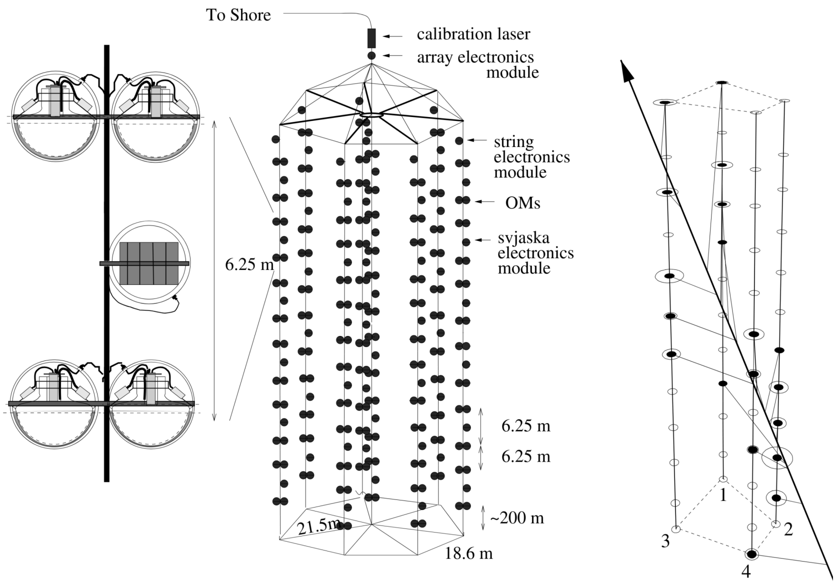

Figure 2.10: **Left:** The BDUNT experiment at the bottom of Lake Baikal, with a close-up of the optical and electronics modules. Constructed in 1990, the detector is still running today, with an upgrade under construction. **Right:** One of the first up-going muons measured with an early four-string configuration of the experiment. Figure taken from [4].

(BDUNT) [40], established in 1990, and still running today. The roughly 200 optical modules of the NT-200 array are located in a depth of 1.1 km at the bottom of Lake Baikal in Siberia, attached to several cables that are being held straight by buoys. An upgrade, called the Baikal Gigaton Volume Detector (Baikal-GVD), is currently under construction. Exemplary for all the neutrino telescopes described here, the BDUNT array is shown in Fig. 2.10.

The first attempt to use ice instead of water as a detector medium was realized with the AMANDA (Antarctic Muon And Neutrino Detector Array) experiment [41], near the Amundsen-Scott South Pole Station in Antarctica. It took data from 1996 until 2009. The final AMANDA detector configuration consisted of roughly 700 optical modules in a 200 m wide cylindrical detector volume, at a depth of $1.1 - 2.3$ km below the surface. When construction of the IceCube South Pole Neutrino Observatory began in 2004, the two experiments were operated in parallel for a five-year period, until IceCube eventually took over. The much larger IceCube was built around AMANDA, whose old strings are still inaccessibly frozen into the ice. More details about IceCube to follow in Sec. 2.3.3.

The ANTARES (Astronomy with a Neutrino Telescope and Abyss environmental RESearch) detector [42] was established between 2000 and 2008, and ran until early 2022. It was built at a depth of 2.5 km at the bottom of the Mediterranean sea off the coast of France. Similar to the BDUNT experiment, the twelve strings and the attached optical modules were being held up by buoys, where internal real-time position tracking systems compensated for the constant movements of the strings in the sea current. The project faced challenges as the first to be established in salt water (the difficult deep sea environment had been a main reason for the abandonment of the DUMAND project before), but was eventually able to take data for 16 years.

The KM3NeT experiment [43] can be viewed as the successor to ANTARES, with a similar concept at two different detector locations in the Mediterranean sea, off the coasts of France and Italy. The detector consists of a low-energy array named ORCA (Oscillation Research with Cosmics in the Abyss) with a footprint size of $\sim$ 200 m in diameter at the French site, and a high-energy array named ARCA (Astroparticle Research with Cosmics in the Abyss) with a footprint size of $\sim$ 1 km in diameter at the Italian site. Both arrays are taking data while still

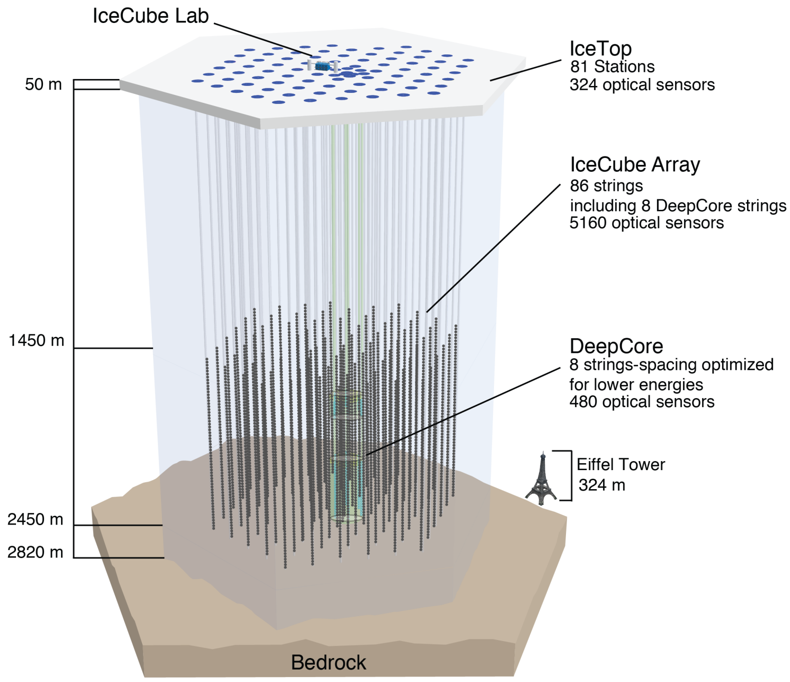

Figure 2.11: Scheme of the IceCube Neutrino Observatory at the South Pole, showing the In-Ice high-energy array (shaded-blue) and low-energy array DeepCore (shaded-green in the center), as well as the surface array IceTop (blue dots) around the IceCube Lab on top of the detector. [IceCube collaboration]

being under construction. The most outstanding new feature of the KM3NeT telescope is the multi-PMT design of the optical modules, in contrast to the single-PMT design of all other aforementioned experiments, allowing for a larger effective area and a per-module direction reconstruction.

2.3.3 The IceCube South Pole Neutrino Observatory

This work includes an analysis with nine years of data from the IceCube South Pole Neutrino Observatory (referred to as IceCube throughout this work). This section is dedicated to this fascinating machine. The detailed descriptions of its components and functionality are based on Ref. [44].

Detector layout

The IceCube experiment at the geographic South Pole is an experiment designed to detect neutrinos in the GeV to PeV energy range, and it is the biggest (and southernmost) telescope of its kind. The ice of the Antarctic plateau is used as a Cherenkov medium, and is instrumented with optical sensors in order to detect light from mostly deep inelastic neutrino scattering interactions.

In numbers: The detector's eyes and ears are 5,160 PMTs in digital optical modules (DOMs) deployed on 86 cables (strings), that reach down to a depth of about $2,450\,\mathrm{m}$. The total instrumented detector volume amounts to $1\,\mathrm{km}^3$, with a total surface area of $1\,\mathrm{km}^2$. If one would haul the whole detector onto a scale, it would read approximately $1,000,000,000$ metric tons. Fig. 2.11 gives an overview of the detector.

The reader might notice that the entire upper halves of the detector strings are not equipped with DOMs. This has several reasons: The un-instrumented layer can be used as a shield to reduce the intensity of the atmospheric muon flux that reaches the detection volume. Furthermore, the optical properties of the ice play an important role in this design choice,

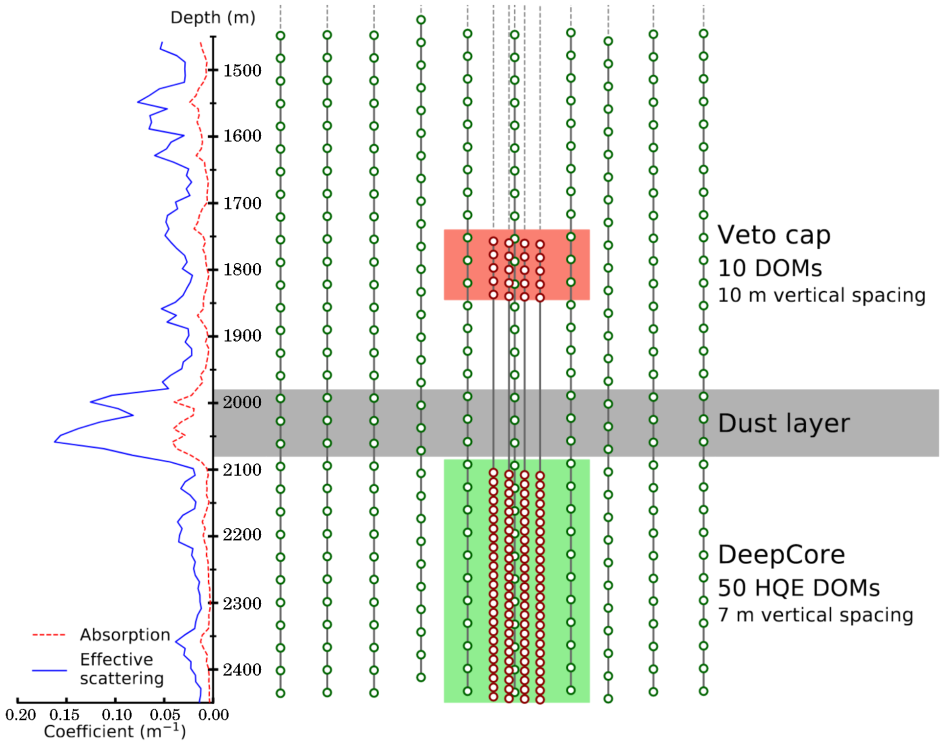

Figure 2.12: Schematic view from the side on the In-Ice and DeepCore sub-arrays. Green circles mark DOMs of the In-Ice array; red circles mark DeepCore DOMs. DeepCore is divided into the red and green shaded areas, that differ in terms of instrumentation density and DOM specification (see text). Also shown is the dust layer (gray area), and the absorption and scattering coefficients as functions of depths as blue and red curves on the left hand side. Figure taken from Ref. [46], modified.

since impurities mainly in the form of air bubbles lead to substantially increased scattering for shallower depths. The optical quality in general increases with depth [45], with the exception of the *dust layer* located between 2 – 2.1 km: Dust accumulated during a glacial period about 65,000 years ago associated with volcanic activity obscures this part of the detector, with increased absorption and heavily shortened scattering lengths. The absorption and effective scattering of the deep South Pole ice, including the dust layer, is shown as a function of depth in Fig. 2.12.

IceCube consists of three differently instrumented arrays:

– The **In-Ice array** [44] makes up the largest portion of the detector, with 78 out of the 86 strings. The strings are arranged in a hexagonal pattern with inter-string distances of $\sim 110 - 150$ m. The vertical distance between the optical modules is 17 m, with 60 DOMs per string. DOM- and string spacing are optimized for the detection of high-energy neutrinos. The instrumentation starts at a depth of roughly $1,450$ m and goes down almost to the Antarctic bedrock at $2,450$ m. The instrumentation of the In-Ice array is visualized in Fig. 2.12.

– The **DeepCore array** [47] is a set of eight strings located roughly in the center of the In-Ice array, with a higher DOM density and an average inter-string spacing of only 72 m. This denser instrumentation allows for the detection of neutrinos with energies down to 10 GeV. The DeepCore array has two sub-arrays: A smaller array in the depth of $\sim 1,750 - 1,850$ m with 10 DOMs per string and an inter-DOM spacing of 10 m, and a larger array starting at a depth of $\sim 2,100$ m down to the very bottom of the detector, with 50 DOMs per string and an inter-DOM spacing of only 7 m. The upper sub-array serves as a veto region against vertical down-going cosmic rays and is used for improving the reconstruction of low-energy horizontal neutrino events. The lower sub-array is located in a region of especially clear ice with good scattering and absorption properties. The space in between is not instrumented because of the dust layer. Selected DOMs in the lower DeepCore array feature PMTs with higher quantum efficiency (HQE), which results in an overall lower energy threshold. Instrumentation of the DeepCore is shown in Fig. 2.12.

– The **IceTop surface array** [48] is designed as a cosmic ray air shower detector. It consists of 81 stations organized in a grid that roughly coincides with the locations of the In-Ice and DeepCore strings. Each station consists of two tanks filled with ice, and each tank houses two DOMs that can detect Cherenkov light generated by cosmic ray air shower particles that strike the tanks. IceTop is most sensitive to particles from primary cosmic rays in the PeV energy range and above. The array is further used as a veto against atmospheric muons.

The data taken by the experiment is collected at the **IceCube Laboratory (ICL)** or counting house, shown in Fig. 2.13, which is the intersection of all 86 strings. The server room in the ICL houses the IT infrastructure, including the custom DOM readout servers (one per string), DOM power supplies, GPS clocks, processing and filtering machines, hot spares, UPSs, switches, fail-safe networking hardware and an *immense* amount of cabling. The IceCube data storage facility is located inside the nearby research outpost, from where the data is transferred north either by satellite on a daily basis, or on physical hard disks at the end of each South Pole season. (The data output amounts to about 1 TB per day, but the satellite bandwidth currently allows for only roughly 100 GB being sent via internet.)

Logistics

Physically, the concept of drilling into ice is simple: Hot water pumped at high pressure melts the ice away, and re-freezes after the scientific instruments are deployed. The logistics, however, are very complicated. Building a drill that reaches down to a depth of 2.5 km is a big endeavor, and requires elaborated engineering, especially at a place like Antarctica. At the geographic South Pole, only about three months of the year offer conditions in which transport and outside work are not too unpleasant; and even then, people and equipment tire easily at

Figure 2.13: The ICL, or counting house, under the Aurora Australis. The red glow of the building is the consequence of long exposure photography which magnifies the light of the red beacon that helps winterovers to find their way in the dark. Photo taken on August 17th, 2018.

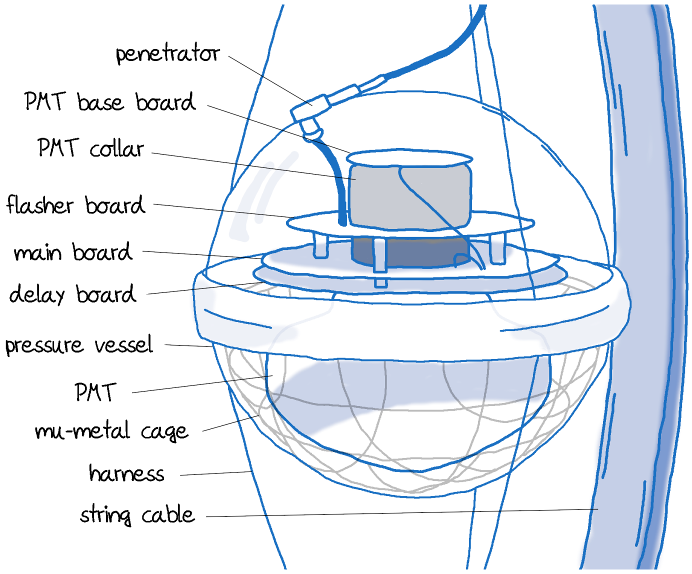

Figure 2.14: Schematic drawing of an IceCube digital optical module (DOM). See text for a description of the mechanical and electronic components.

almost 3 km of altitude, practically no humidity, and several tens of degrees centigrade below zero. It took seven years to build IceCube in these conditions.

The experiment is supported by the nearby Amundsen-Scott South Pole Station, a research outpost of the United States Antarctic Program (USAP), funded by the American National Science Foundation (NSF). The ICL is located about one kilometer away from the station. IceCube relies on the outpost infrastructure, including heating and electricity, office and lab space, housing, flight operation, emergency response and food supply. For eight to nine months of the year, the station is isolated, with only a skeleton crew of *winterovers* remaining on site.

IceCube continuously takes data since the year 2010, aiming at an uptime of 100 % (running 24 hours a day on 365 days a year). To ensure continuous and stable data taking, two IceCube winterovers are deployed each season to maintain the complex IT infrastructure, to conduct repairs and run calibration measurements.[5]

Digital Optical Modules (DOMs)

An IceCube DOM has three major components: A spherical glass vessel to withstand the high pressure in the ice, a PMT to detect Cherenkov radiation, and the control and readout electronics. A schematic layout of a DOM is shown in Fig. 2.14. The PMT takes up almost the entire "southern hemisphere", whereas the electronics are located in the upper part. All IceCube DOMs are facing downwards, meaning the PMTs inside the modules have their optically effective surface directed towards the center of the Earth. It was designed this way to optimize the detector for upward-going neutrino signatures, because the upward direction is supposedly free of atmospheric muon background.

The centerpiece of an IceCube DOM is the photomultiplier tube (PMT), which converts light into an electrical current. The PMT is roughly 25 cm in diameter and surrounded by a coarse wire mesh ("mu-metal cage") that reduces the negative effects of the Earth magnetic field on the PMT collection efficiency [44]. The functionality of a PMT is visualized in Fig. 2.15.

[5]For a short narrative about life and work of an IceCube winterover at the South Pole, see Apx. B.

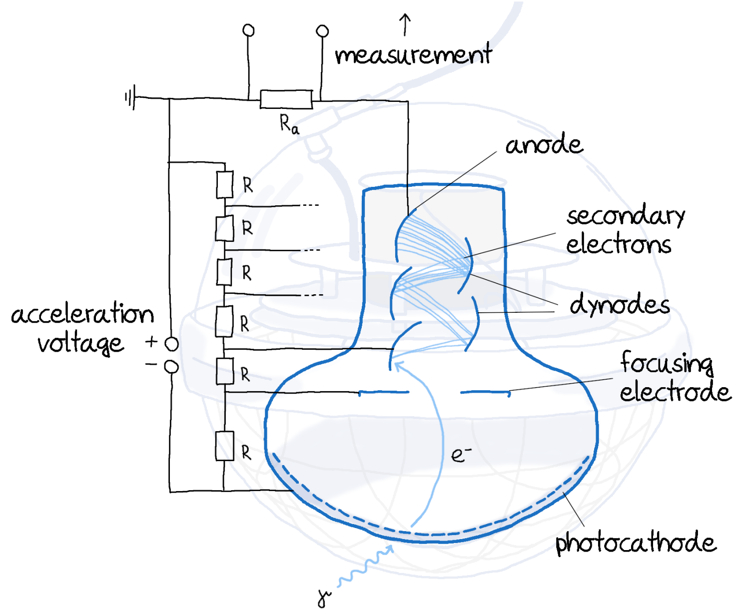

Figure 2.15: Schematic drawing of a PMT. A photon hitting the photocathode is converted into an electron. The applied high voltage potential accelerates the electron onto the first dynode, where the impact causes the emission of secondary electrons. The voltage divider circuit creates an electric field which accelerates the electrons from one dynode to the next, producing further electrons. The multiplied current can be measured at the anode.

The control and readout electronics consist of many individual parts, as shown in Fig. 2.14. The main board controls the entire DOM functionality, including data acquisition, digitization of the PMT signals, calibration controls, and communication to other DOMs and the ICL. A delay board is required for dynamic hit time windows. Calibration measurements are conducted by means of the flasher boards, outfitted with LEDs to test DOM response throughout the detector. The PMT itself obtains its power through the PMT base board and a high voltage control board (not shown in the drawing). [44]

Data acquisition

Data acquisition in IceCube is a complex chain of processes, which are described in great detail in Ref. [44]. Following the reference, this section is an overview of the most relevant steps.

The light information registered by a PMT is called a *hit*. A hit results in an amplified photo current, which is proportional to the intensity of the incident light, and is measured as a voltage waveform over time. If a waveform exceeds a certain intensity, the DOM is *launched*, meaning the waveform is recorded and digitized. The digitization process happens within the DOM by means of custom fast analog-to-digital converters (fADCs).

The detector was designed to collect signals generated by passing particles, i.e. external sources of radiation. But most DOM hits have internal causes. For instance, the PMT can randomly generate field electrons in the strong accelerating potential that can mimic a “real” signal. Furthermore, radioactive decays within the glass of the PMT or the DOM pressure vessel can be a source of DOM-internal light. These and other phenomena are summarized under the term *dark rate*.[6] (Further unwanted launches can technically be produced by the detector material surrounding the modules, though fortunately the ice sheet at the South Pole is alomst “optically dead” in this respect.[7])

[6] For more information on sources of PMT and DOM dark rates, and PMT characteristics in general, see Ref. [49].

[7] The KM3NeT detector in the Mediterranean Sea faces the irritating (but arguably quite funny) problem of light pollution from bio-luminescent jellyfish that live between the optical modules.

Dark rate launches are suppressed by the requirement of *hard local coincidence* (HLC), where at least one other DOM launch in the vicinity (direct or next-to-direct neighbors up and down the same string) and within time window of $\pm 1\,\mu$s is necessary for the waveforms to be considered non-noise. Furthermore, if a certain number of HLC events happen within a certain time window, they set off a *simple multiplicity trigger* (SMT). The SMT trigger conditions differ slightly for different physics categories, e.g. high-energy in-ice events contain 8 HLCs, while low-energy DeepCore events contain only 3. Whenever one or more SMTs are set off, all photon hits within a few microseconds before and after the first and last triggering waveforms are bundled up into a potential *physics event*. These physics events are the basis of most IceCube analyses, on which specific events are chosen in an *event selection*, optimized for the purpose of the respective study. The event selection process is further described in Chp. 5.

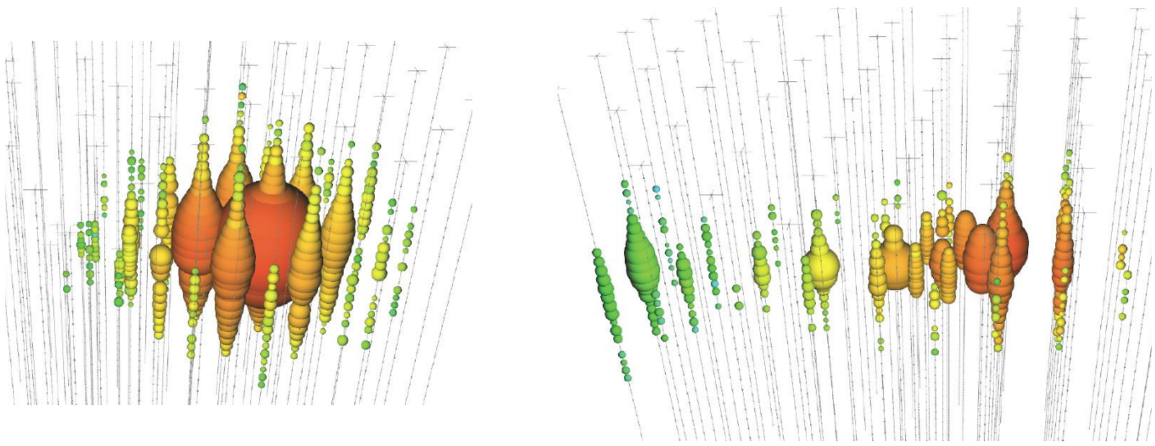

Figure 2.16: Particle signatures in the IceCube detector. The gray lines and dots represent the strings with the optical modules. A DOM that is displayed as a colored bubble has recorded light, where the size of the bubble corresponds to the light intensity and the color to the time stamp; red being earlier, blue being later in time. From top left to bottom right: Cascade signature, track signature, double bang signature. The displayed events are high-energy events, ranging from several hundred TeV to a few PeV. The upper two are real events (see Ref. [50]), the third one is simulated since individual tau neutrino events have not been observed so far. Images taken from Ref. [51], modified.

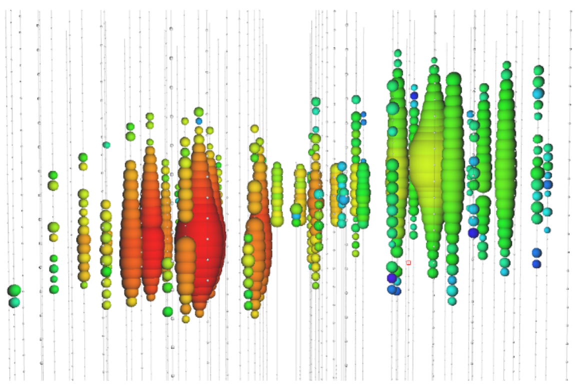

Particle signatures

Since the completion of the detector in 2010, many elaborated methods have been developed to distinguish particles and their properties by means of the different energy signatures they deposit in the instrumented ice. By the amount of Cherenkov light recorded by a specific DOM, its location in the detector, and the time stamp of the detection relative to those of the other DOMs, three different main particle signatures can be reconstructed: *Tracks*, *cascades*, and *double cascades*. Fig. 2.16 shows manifestations of the three signatures in the detector.

Track signatures are caused by CC interactions of muon neutrinos. The muons generated subsequently to the neutrino interaction travel with straight trajectories, depositing energy along their paths, compare Fig. 2.6 (c). Tracks set the best conditions for direction reconstruction, hence they are the key signatures for point-source analyses. The reconstruction of the neutrino energy is usually very difficult, because large parts of the tracks could lie beyond the instrumented volume.

Likewise from the CC interaction regime, there are the leptonic **cascade signatures**, caused by interactions of electron neutrinos, compare Fig. 2.6 (b). The electrons that are produced as the secondary particles have a much shorter scattering lengths than muons, therefore depositing their energy quickly and in a more spherical shape. Consequently, the direction reconstruction is usually very inaccurate, while the energy can be reconstructed well, especially in case of events that are fully contained in the detector volume.

A further cascade signature is the hadronic cascade. It is produced in *all* CC deep-inelastic scattering interactions shown in Fig. 2.6 (b)-(d), and is the only visible pattern for the NC reactions shown in (a).

Double cascade signatures (also double bang signatures) are the subsequent, correlated occurrences of two cascades. The cause is a CC tau neutrino interaction (compare Fig. 2.6, (d)), which upon impact generates a hadronic shower (first "bang"). The neutrino is converted into a tau lepton which travels a certain distance in the order of 100 m without depositing much energy itself. It then decays into an electron or a muon via the weak force, or into one or more pions via the strong force. The electron and pions result in electromagnetic/hadronic showers, creating the characteristic second "bang", while the muon produces a track as described above and therefore does not contribute to the double bang signature. So far, no individual tau neutrino event has been observed in IceCube.[8]

[8] A recently published article [52] presents two possible candidates for double bang signatures from astrophysical tau neutrinos, and another study [53] reports the observation of atmospheric tau neutrinos in a statistical analysis.

Chapter 3
Theories of dark and ordinary matter

In this chapter, theories of dark and ordinary matter are introduced, as a theoretical base for the studies of the Scotogenic Dark Matter Model discussed in Chp. 4. First, the renown theory of the Standard Model of particle physics is described in much detail in Sec. 3.1, including its particle content, the three fundamental forces, and the mathematical provisions that are required to formulate extensions; with an intrepid dive into group theory and symmetries. Note that specifically the more mathematical sections are written from an experimental physicist's point of view, and only scratch at the surface of group-, gauge-, and quantum field theory. Resources for further reading are provided at all points where lengthy explanations go beyond the scope of this work.

Theories of Dark Matter are introduced in Sec. 3.2. It is explained how the observational evidence that points to the definite existence of a mysterious, dark realm leads to many, substantially different theories about its nature. A very prominent one is that of weakly interacting massive particles (WIMPs), on which the focus lies in this study. So the last subsections are dedicated to WIMPs and the mechanisms to detect them with neutrino telescopes.

3.1 The Standard Model of particle physics

Dark Matter is a shady business. But it does not need to be completely obscure, abstract, and mysterious, for it can be described by heart warming math like almost everything else. In fact, until it is actually found, Dark Matter is little more than a mathematical extension of regular matter. This chapter serves the purpose to introduce this regular matter in terms of the *Standard Model of particle physics*, largely following the Refs. [54, 55, 56, 57].[1]

3.1.1 Elementary particles

The Standard Model of particle physics, visualized in Fig. 3.1, contains all the elementary building blocks of matter that are known today. It is a *quantum field theory*, but for now, the focus is on the much more graspable particle content.

It is divided into two major groups of particles: *Fermions* and *bosons*, which in turn divide into two sub-groups each. The two bosonic groups are *scalar bosons* which have a spin of zero, and the *vector bosons* (or gauge bosons) with spin one. Of the former kind one finds only one physical specimen in the Standard Model, the famous *Higgs* particle, that gives rise to the mass of three gauge bosons through its eponymous mechanism (which will be covered later in this chapter). These three massive gauge bosons, namely W^-, W^+ and Z^0, are the *force carriers* of

[1] The references will be mentioned separately throughout the text, obviously wherever direct quotes are used, but also where a quick pointer to further-reading literature might come in handy, e.g. for some definitions and the more complicated concepts.

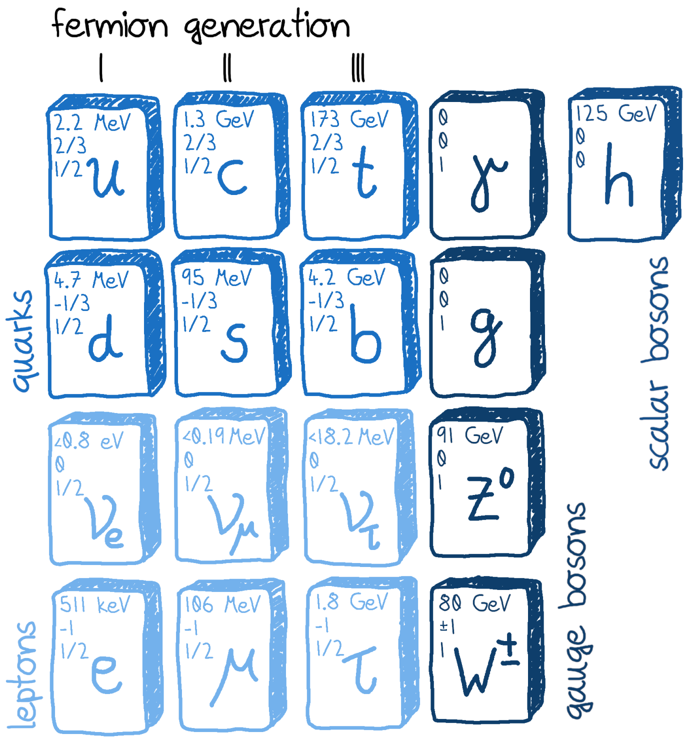

Figure 3.1: The building blocks of nature: The elementary particles of the Standard Model of particle physics, including the quarks (blue), the leptons (light blue), the vector bosons (dark blue) and Higgs boson (to the very right). The neutrino masses are zero in the current configuration of the Standard Model; the experimental upper limits are shown nonetheless for comparison. Values taken from Refs. [5, 58], approximated.

the *weak interaction*. They are accompanied by eight massless gluons as force carriers of the *strong interaction*, and the likewise massless photon of the *electromagnetic interaction*.

In the fermion sector, one finds six *quarks*, among them the up- and down quarks which are the constituents of neutrons and protons (themselves not elementary hence not part of the visualization in Fig. 3.1), and therefore of all visible matter. The other four appear in exotic particles that can, for instance, be created by colliding heavy ions at the *Large Hadron Collider* (LHC) [59] at CERN, but also in the "quark sea" of virtual quarks and gluons that surrounds the valence quarks within regular nucleons. Likewise in the fermion sector one finds the *leptons*, with the electron being the most famous as another crucial constituent of matter, and the muon and the tau as its so-to-say heavier sisters. All three have the same negative charge under the electromagnetic interaction. The remaining three particles are the electrically neutral counterparts of the charged leptons, namely the electron-, muon-, and tau neutrinos ν_e, ν_μ, and ν_τ. They are the co-stars in this work.

The picture that was just described presents the Standard Model in its nice and comprehensible vanilla edition. However, as mentioned earlier, it is actually a *quantum field theory* (QFT), and much more than the sum of its particles. In order to extend the model to accommodate Dark Matter, this, and a few more things, need to be understood.

What is a quantum field theory? The reader might be familiar with the concept of classical field theories, where a field represents a physical quantity as a function of spacetime. The quantity can be a scalar, like electric charge or temperature, a vector, like velocity or a force, or even a tensor or spinor; which makes the corresponding field a scalar field, vector field, tensor field, etc. An example for a classical field theory is electromagnetism. Although the term "classical field theory" is actually a bit misleading, in the sense that in general it covers both non-relativistic and relativistic classic fields, and "classic" merely refers to the fact the theory is not *quantized*.

When quantum mechanics is incorporated in a field theory by means of quantization[2], one talks about *quantum fields*: Their values in spacetime are no longer scalars, but operators acting on quantum mechanical states [55]. So from here on, one can think of particles as excitations of quantum fields. This makes a quantum field theory a combination of classical field theory, special relativity, and quantum mechanics. If further incorporating the concept of *gauge invariance*, one would end up with a *gauge quantum field theory*, enabling invariant transformations under local symmetries. The Standard Model is such a theory.

3.1.2 The Lorentz group

In a (gauge) quantum field theory such as the Standard Model, in general one has to assume that velocities in a system are or can be relativistic, meaning they reach significant fractions of the speed of light. Such a system can only be described accurately within the setting of the *Lorentz group*. With the Lorenz group comes a symmetry, the *Lorentz invariance*, which dictates that all laws of physics within the system remain the same when subjected to certain operations — the *Lorentz transformations*. This section is designed to help the experimental physicist reader understand the implications of Lorentz symmetry for the Standard Model, and how the Lorentz group ultimately determines the nature of its elementary particles.

To this avail, one needs to dive a little bit into group theory. But please note that the goal of the following sections is not to define important aspects of group theory in a complete or mathematically strictly accurate way, rather than provide descriptions and an easy-to-digest introduction. Some of the descriptions will actually contain mathematical definitions, some will contain explanations without any symbols, depending on the author's judgment on the necessity of math to understand the idea.[3]

Lie groups and algebras

The Lorentz group belongs to the *Lie groups*, which form a special category in the mathematical discipline of group theory. In fact, all groups that will be of interest in the following are Lie groups — *matrix Lie groups* to be even more exact — which is why our endeavor into group theory starts with them.

Description 1: Matrix Lie groups. A group is a combination of a set G and an operation $*$, written as $(G, *)$. The operation $*$ is usually referred to as "multiplication", and maps pairs of elements of G to an element of G, or in other words, $G * G \to G$. The following axioms are fulfilled:

- The associativity law, $(f * g) * h = f * (g * h)$, holds for all $f, g, h \in G$.
- There exists a *neutral* or *identity element* e with $g * e = e * g = g$.
- For each $g \in G$ there is an *inverse element* with $g * g^{-1} = g^{-1} * g = e$.

[2] This process is sometimes called *second quantization*, where *first quantization* would describe the transition from classical to quantum mechanics.

[3] At this point I highly recommend S. May's master thesis [55] for further reading. Chapter 3 therein contains a more complete and theoretical introduction to group theory, which served as a very important resource to this thesis.

A Lie group is a special group that, besides inheriting the above group properties, is also a smooth differentiable manifold, where a manifold is a topological space that locally resembles Euclidian space and as such can be studied using differential calculus. The manifold is of no further importance here for the understanding of matrix Lie groups, but it automatically implies that all Lie groups are *continuous*.

The set of $n \times n$ invertible matrices with real-valued entries, together with the matrix multiplication, form the $GL(n, \mathbb{R})$ or *general linear group*. A subset S of the $GL(n, \mathbb{R})$ can be *closed*, meaning:

– The result of a multiplication of two elements from S is also in S.

Then S is a subgroup of $GL(n, \mathbb{R})$. The subgroups of the $GL(n, \mathbb{R})$ are called *matrix Lie groups*. In this work, and in line with most literature, matrix Lie groups will be denoted with uppercase letters, an in parenthesis the dimension of the space the group's elements act on, e.g. "$U(1)$". [54, Secs. 5.3.3, 5.3.6.2]

In the following, "Lie group" will be used as a synonym for "matrix Lie group". While all the above might sound a little bit abstract at first, experimental physicists and Lie groups actually cross paths all the time, they are usually just not aware of each other. A famous example are rotations. From F. Halzen's book "Quarks and Leptons" [56]:

> *The set of rotations of a system form a group, each rotation being an element of the group. Two successive rotations R_1 followed by R_2 (written as the "product" R_2R_1) are equivalent to a single rotation (that is, to another group element). The set of rotation is closed under "multiplication". There is an identity element (no rotation), and every rotation has an inverse (rotate back again). The "product" is not necessarily commutative, $R_1R_2 \neq R_2R_1$, but the associative law $R_3(R_2R_1) = (R_3R_2)R_1$ always holds. The rotation group is a continuous group in that each rotation can be labeled by a set of continuously varying parameters (α_1,α_2,α_3). These can be regarded as the components of a vector $\boldsymbol{\alpha}$ directed along the axis of rotation with magnitude given by the angle rotation.*

As mentioned before, it is sufficient to consider matrix groups only, therefore the group operation will always the be matrix multiplication. However, even when limited to the world of matrices, rather unwieldy things can occur in Lie groups. Sometimes group elements are so all over the place (or rather all over spacetime) that it's hard to wrap one's head around. Fortunately, there exists something to help out: The *Lie algebra*. Even though Lie groups and Lie algebras share a name and are closely linked to one another, they are completely different things ("don't try to compare apples with horses!"). While a Lie group can be a strange shapeless blob of confusion, a Lie algebra is always a nice, simple, good-old vector space with the dimension of the Lie group's manifold[4].

Description 2: Lie algebras. A Lie algebra $\mathfrak{g}$ is a vector space together with a bilinear map, also known as the *Lie bracket*

$$[\cdot, \cdot] : \mathfrak{g} \times \mathfrak{g} \to \mathfrak{g}. \tag{3.1}$$

For the Lie bracket and for all $a, b, c \in \mathfrak{g}$, the following statements are true:

[4]It does not really make sense (or at least is not trivial) to speak of a "dimension of a Lie group", whereas a manifold (which in this case happen to have group properties) obviously has a dimension.

– $\mathfrak{g}$ is anticommutative, meaning $[a, b] = -[b, a]$.

– $[a, a] = 0$ holds.

– The *Jacobi identity* $[a, [b, c]] + [c, [a, b]] + [b, [c, a]] = 0$ holds.

The Lie algebra of a Lie group is the tangent vector space at the identity element of the Lie group. The elements of the Lie algebra are generators of the Lie group. Different Lie groups can (but not necessarily) have the same Lie algebra [54, p.358]. Lie algebras are here, and usually, denoted with lower-case blackletters, with parenthesis containing the dimension of the vector space that the corresponding Lie group's elements act on, e.g. $\mathfrak{su}(2)$. [54, Sec. 5.3.6.4]

One could say that the bracket is to the vector space what the multiplication operation is to the group's set. A Lie algebra is therefore defined by its commutation relations. Only matrix Lie groups are considered here, so the Lie bracket is always the matrix commutator. One commutation relation is required for each of the generators. But what exactly are these generators? A generator of a group is an element that, as one can guess, *generates* group elements:

Description 3: Generators. The elements of the Lie algebra generate the elements of the Lie group via the exponential function. The Lie algebra $\mathfrak{g}$ that belongs to a Lie group G is the set of matrices $\mathbf{X}$ so that

$$e^{t\mathbf{X}} \in G \tag{3.2}$$

holds for all real numbers t. The elements in the proximity of the identity element of given Lie group can be represented as $g(t) = e^{t\mathbf{X}}$ with $\mathbf{X} \in \mathfrak{g}$ and t near zero. The matrices

$$\frac{dg}{dt}g^{-1}, \quad g^{-1}\frac{dg}{dt} \tag{3.3}$$

are tangent matrices/elements to $g \in G$. For $t = 0$, these elements are $\mathbf{X}$ itself. That means $\mathfrak{g}$ is exactly the tangent vector space at the identity matrix. [54, Sec. 5.3.6.4]

All elements of the Lie algebra are generators of the respective Lie group. This is important because it is usually much more comfortable to work with algebras than with groups. The minimum required number of generators to generate the group corresponds to the dimension of the algebra (and therefore the manifold of the group). However, the Lie algebra actually does not "know" about the structure of the original group, rather than the structure of a *universal covering group*.

Description 4: Homomorphisms and isomorphisms of Lie groups and Lie algebras. The map $f : G \mapsto H$ is called a group homomorphism of the groups $(G, *)$ and $(H, \star)$, if for all elements $g_1, g_2 \in G$ the following is true:

$$f(g_1 * g_2) = f(g_1) \star f(g_2), \tag{3.4}$$

meaning that the image of the product is equal to the product of the images. An algebra homomorphism is defined similarly for the two algebras $\mathfrak{g}$ and $\mathfrak{h}$, with the map $\phi : \mathfrak{g} \mapsto \mathfrak{h}$, if for all $X, Y \in \mathfrak{g}$ the following holds:

$$\phi([X,Y]) = \left[\phi(X), \phi(Y)\right] \tag{3.5}$$

For groups, demanding a homomorphism is not particularly exciting, since one can always map on the neutral element. However, for vector spaces as in Lie algebras, it is a little less trivial because there (in general) is no neutral element.

If the homomorphism is *bijective*, meaning that every element from G (from $\mathfrak{g}$) is mapped to exactly one unique element of H (of $\mathfrak{h}$), f is called a *group (algebra) isomorphism*. Group and algebra isomorphisms are denoted by

$$G \cong H, \qquad \mathfrak{g} \cong \mathfrak{h}. \tag{3.6}$$

Groups or algebras that are isomorphic to each other share the same structure; their only difference is in the labeling/naming of their elements. [54, Sec. 5.3.3.3]

Description 5: Universal covers of Lie groups. Be G and H Lie groups with their corresponding Lie algebras $\mathfrak{g}$ and $\mathfrak{h}$. (H, f) is called the universal covering group to G, if

- the map $f : H \to G$ is a surjective group homomorphism,
- $\mathfrak{h} \cong \mathfrak{g}$, and
- H is *simply connected.*

[54, Sec. 5.3.3.3][60, Sec. 3.4.4]

For a topological structure, simple connectedness — very visually — means that all loops in the structure can be reduced to a single point, best explained with the famous example of the dog on a retractable leash: On the surface of a sphere, the dog can run any loop to any point and back to you, and you can retract the leash afterwards without moving yourself or the dog. On the surface of a torus, however, this is not always the case, e.g. when the dog runs through the hole or a full circle around it. The demand for simple connectedness only makes sense for groups with a topological structure like a manifold — such as Lie groups.

The property of simple connectedness automatically makes a Lie group a universal cover, at least to itself. As the name implies, there is no "higher level" of cover than the universal cover.

As an example for a universal cover, take the field[5] $\mathbb{R}$, which is the one-dimensional Euclidean space, and also a Lie group. It covers the circle Lie group $U(1)$, whose set consists of

[5]A ring is a set with two binary operations $(R, +, *)$, where $(R, +)$ is an abelian group (meaning the operation $+$ is commutative), and $(R, *)$ is a monoid, which is basically a group without an inverse elements (every group is a monoid, but not every monoid is a group!). The distributive laws hold:

$$\begin{aligned} a * (b + c) &= (a * b) + (a * c), \\ (b + c) * a &= (b * a) + (c * a). \end{aligned}$$

An example for a ring is $\mathbb{Z}$: For the operation of addition, you can find a neutral and inverse element, but for multiplication there is not always an inverse [54, p.363]. If $(R\backslash\{0\}, *)$ is an abelian group, then R is called a *field*. $\mathbb{R}$ and $\mathbb{C}$ are examples for fields. Not to be confused with the fermion and boson fields of the Standard Model.

complex unitary[6] 1×1 matrices, i.e. "the dots on the unit circle". $\mathbb{R}$'s elements can be thought of as an infinite number of dots together forming an infinite straight line. If modulated with 2π, $\mathbb{R}$ curls up like a spiral that, in top-down view, exactly "covers" the unit circle which is the $U(1)$. $\mathbb{R}$ is simply connected, so $\mathbb{R}$ is the universal cover of $U(1)$. In fact, it is an *infinite cover*, since every element in $U(1)$ corresponds to an infinite number of elements in $\mathbb{R}$, which is illustrated in Fig. 3.2.

There also exist *double covers*, meaning every element in the original group is covered by two elements from the covering group. Universal covers can, but not necessarily have to, be double or infinite covers.

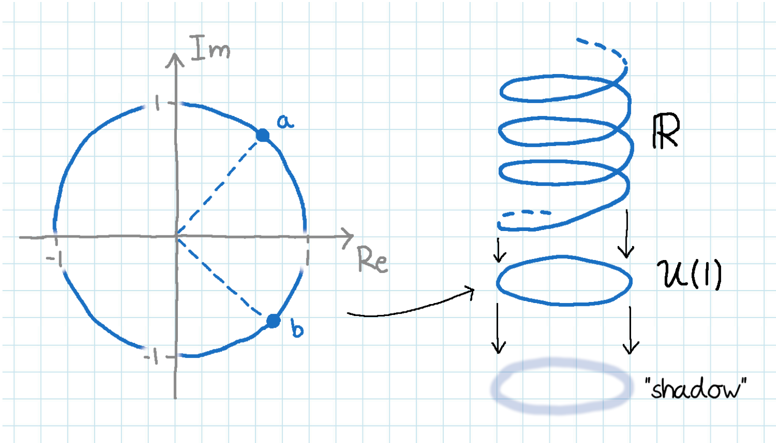

Figure 3.2: The (infinite number of) individual points on the circle form exactly the $U(1)$, together with the operation of complex multiplication. The $U(1)$ and its universal cover $\mathbb{R}$ (modulo 2π) could be imagined as casting the same "shadow".

Representations

Usually, in the experimental physics world, one does not come across groups and their algebras as they are, rather than encountering a *representation of a group or algebra*.

Description 6: Representations. A representation R of a matrix Lie group G is simply any group homomorphism

$$R(G) : g \mapsto R(g), \qquad g \in G. \tag{3.7}$$

The group that is "mapped into" is a matrix group that acts on a vector space or representation space V, which is always the case if only matrix Lie groups are considered (in contrast to Lie groups or groups in general). One could say that the group elements of G are embedded into operators that act on a vector space, or simply that the group is represented onto a vector space.

Accordingly, a Lie algebra representation is an algebra homomorphism, where the Lie bracket is the matrix commutator.

A representation is called *fundamental* or *defining* if it is the smallest, non-trivial representation of the group or algebra. [54, Sec. 5.3.4][57, Sec. 10.1.1]

One example of a *trivial representation* of group A is the mapping of every element in A to the identity matrix $\mathbf{1}$, i.e. the neutral element. It is not difficult to see that the condition for group

[6] Square matrices are matrices which have the same number of rows and columns. They can have the properties of *orthogonality* and *unitarity*. A matrix A is orthogonal if it is real-valued, invertible, and its inverse is equal to the transpose, $A^{-1} = A^T$. The matrix is called unitary in the complex case, $A^{-1} = (A^*)^T$ where A^* is the complex-conjugate of A. In $\mathbb{R}$, "orthogonal" and "unitary" are equivalent terms.

homomorphism, Eq. (3.4), holds in this case for $a_1, a_2, a_3 \in A$:

$$\begin{aligned} f(a_1 * a_2) &= f(a_1) \cdot f(a_2) \\ f(a_3) &= f(\mathbf{1}) \cdot f(\mathbf{1}) \\ \mathbf{1} &= \mathbf{1} \end{aligned} \tag{3.8}$$

(Remember that f is the mapping onto the neutral element; so it does not matter whether one multiplies something first and then maps it onto **1**, or if one maps the individual elements first and then multiplies the **1**s.) Examples for fundamental and other non-trivial representations will be given further down the road.

In a Lie algebra, the commutation relations dictated by the Lie bracket are representation independent. But: A Lie algebra representation is constructed by embedding the generators into matrices, so the generators look different for different algebra representations. When generating group elements from a (representation of a) Lie algebra, the result is always a representation of a (universal cover) of the Lie group.

Representations give physical meaning to Lie groups and Lie algebras. They serve as "manifestations" of the mathematical concept of a symmetry group in the physical world. As for the Standard Model, very roughly speaking, one could say that its fields are described each by a certain representation of the Lorentz group. The fields are part of the Standard Model Lagrangian, which must be invariant under the symmetries of the theory (the laws of physics must be the same in any frame of reference). So the representations (fields) that have to be found are all those that leave the Lagrangian Lorentz-invariant. Those representations are called *irreducible representations*.

Description 7: Reducible and irreducible representations. Be V the vector space with dimension n of a representation R of a Lie Group G. Then R is called reducible, if there exists a subspace W with dimension $m < n$ that is invariant under group operations. W is called invariant under G, if for any group element $g \in G$ and any vector $w \in W$ the linear transformation $R(g)$ maps w into W:

$$R(g)w \in W \qquad \forall g \in G, w \in W \tag{3.9}$$

If such a (non-trivial) subspace does not exist, R is called irreducible. *Trivial reductions* are the full vector space or the null space.

If R is reducible, meaning an invariant subspace exists, then it can be re-written by means of the sub-representations R_1 and R_2 with vector spaces V_1 and V_2 in the form

$$R(g) = \begin{pmatrix} R_1(g) & A(g) \\ 0 & R_2(g) \end{pmatrix} \qquad \forall g \in G, \tag{3.10}$$

such that V_1 is the invariant subspace. For the case that $A(g) = 0$, both V_1 and V_2 are invariant, R is called *fully reducible* and can be written as a direct sum of the representations R_1 and R_2. [54, Sec. 5.3.4.5][55, Sec. 3.1.1]

For example: Take the $U(1)$ as the multiplicative group of complex numbers of length 1. It acts on the $\mathbb{R}^3$ via the representation that maps $g \in U(1)$ to the rotation matrix that describes the rotation about the z-axis by the polar angle g. These rotations leave the z-axis and the x-y

plane invariant. Thus this representation could be decomposed into the trivial representation on the z-axis and the rotations of the x-y plane.

Description 8: Direct sum of representations. Two representations R_1 and R_2 of a group G with dimensions n_1 and n_2 can be combined to a new representation R_{1+2} with dimension $n_{1+2} = n_1 + n_2$ by "direct summation" of the representation matrices:

$$R_{1+2}(g) = R_1(g) \oplus R_2(g) = \begin{pmatrix} R_1(g) & 0 \\ 0 & R_2(g) \end{pmatrix}, \qquad g \in G. \tag{3.11}$$

The representation space $V_{n_{1+2}}$ is a direct sum of the invariant subspaces (see Desc. 7) V_1 and V_2,

$$V_{n_{1+2}} = V_1 \oplus V_2, \tag{3.12}$$

meaning that R_{1+2} is fully reducible, and also that $R_1(g)$ and $R_2(g)$ are irreducible.

[54, Sec. 5.3.4.3]

The circle group $U(1)$

The set of this group consists of complex-valued unitary 1×1 "matrices" with determinant 1, and its operation is the matrix multiplication (as is the case for all the groups considered here, so the definition of the operation can be omitted in the following). It has been introduced before as forming the "dots on the unit circle", see Fig. 3.2.

A complex number $a + ib$ can be represented by a 2×2 matrix:

$$a + ib \mapsto \begin{pmatrix} a & -b \\ b & a \end{pmatrix} \tag{3.13}$$

Therefore it is not surprising that the $U(1)$ is isomorphic to the $SO(2)$, the special orthogonal group in two dimensions. As the name implies, the matrices of the $SO(2)$ are real-valued orthogonal 2×2 matrices with determinant 1. It describes rotations about an angle on a circle with radius 1. Its manifold has the dimension 1, so does its Lie algebra $\mathfrak{so}(2)$. In the example given with Fig. 3.2, the reader has already learned that the universal cover of the $U(1)$ and $SO(2)$ is the one-dimensional Euclidean space $\mathbb{R}$. Hence exponentiating (see Desc. 3) the Lie algebra $\mathfrak{so}(2)$ generates the universal cover $\mathbb{R}$.[7]

[7] There are a few naming conventions that help categorizing different Lie groups (note that the following rules might not be true for all Lie groups in general, but they hold up pretty well for those which are relevant here):

- A group with two letters is a subgroup of the respective one-letter group, e.g. the $SO(3)$ is a subgroup of the $O(3)$.
- The number in parentheses is the dimension of the space the group elements are acting on. E.g. the $SO(3)$ elements act on the $\mathbb{R}^3$, and its elements are 3×3 matrices. Careful, since this is not to be mistaken for the dimension of the group (or rather the group's manifold). In the $SO(3)$ they happen to be the same, but in the $SO(2)$ for instance, the group dimension is 1.
- The second letter (or *the* letter if there's only one) describes properties of the group elements. In the case of the $O(3)$, it means "orthogonal" (see footnote 6) and their determinant has the absolute value of 1.
- The "S" stands for "special", which means that the determinant is +1. So the $SO(3)$ is a subgroub of the $O(3)$ with all the elements from the $O(3)$ whose determinant is +1.

The rotation group $SO(3)$

The special orthogonal group in three dimensions, or $SO(3)$, is the group of real-valued orthogonal 3×3 matrices with determinant 1. Its elements act on the $\mathbb{R}^3$, they describe rotations around an axis in three-dimensional space.

The elements of the algebra to the rotation group, the $\mathfrak{so}(3)$, are the components of the angular momentum operator $\vec{L}$, i.e. L_1, L_2, L_3, which generate infinitesimal rotations. The algebra is defined by the commutator

$$\left[L_i, L_j\right] = i\varepsilon_{ijk}L_k. \tag{3.14}$$

The spin group $SU(2)$

Exponentiating the aforementioned $\mathfrak{so}(3)$ generates the universal cover of the $SO(3)$, which is the $SU(2)$. The Lie algebras of the $SO(3)$ and the $SU(2)$ are isomorphic:

$$\mathfrak{so}(3) \cong \mathfrak{su}(2). \tag{3.15}$$

The $SU(2)$ is the special unitary group of degree 2, and its set consists of complex-valued unitary 2×2 matrices with determinant 1. Like the $\mathfrak{so}(3)$, the algebra $\mathfrak{su}(2)$ is defined by the commutator in Eq. (3.14). The Casimir[8] of this algebra is $\vec{L}^2$; it commutes with the generators,

$$\left[\vec{L}^2, L_i\right] = 0, \tag{3.16}$$

and has the well known eigenvalues $j(j+1)$, where "j labels the representation and is given the special name spin" [57, Sec. 25.1.1]. The js are half integers, and each of them characterizes an irreducible representation of the $\mathfrak{su}(2)$ with dimension $(2j+1)$.

In the fundamental representation, also called the *spin representation* of the $\mathfrak{su}(2)$, the generators are

$$L_i = \frac{1}{2}\sigma_i, \quad i = 1, 2, 3 \tag{3.17}$$

with the *Pauli matrices:*

$$\sigma_1 = \begin{pmatrix} 0 & 1 \\ 1 & 0 \end{pmatrix}, \quad \sigma_2 = \begin{pmatrix} 0 & -i \\ i & 0 \end{pmatrix}, \quad \sigma_3 = \begin{pmatrix} 1 & 0 \\ 0 & -1 \end{pmatrix}. \tag{3.18}$$

The spin group $SU(3)$

The special unitary group of degree 3 consists of complex-valued unitary 3×3 matrices with determinant 1. Its manifold has the dimension 8. The generators of the $\mathfrak{su}(3)$ in the fundamental representation can be written as

$$T_i = \frac{1}{2}\lambda_i, \quad i = 1, 2, ..., 8 \tag{3.19}$$

[8]In a Lie algebra, the *Casimir* or *Casimir operator* is an operator that commutates with all other operators.

where the λ_i are called the *Gell-Mann matrices*, the $SU(3)$ analog of the Pauli matrices [57, Sec. 25.1.1]:

$$\lambda_1 = \begin{pmatrix} 0 & 1 & \\ 1 & 0 & \\ & & 0 \end{pmatrix}, \quad \lambda_2 = \begin{pmatrix} 0 & -i & \\ i & 0 & \\ & & 0 \end{pmatrix}, \quad \lambda_3 = \begin{pmatrix} 1 & & \\ & -1 & \\ & & 0 \end{pmatrix},$$
$$\lambda_4 = \begin{pmatrix} 0 & & 1 \\ & 0 & \\ 1 & & 0 \end{pmatrix}, \quad \lambda_5 = \begin{pmatrix} 0 & & -i \\ & 0 & \\ i & & 0 \end{pmatrix}, \quad \lambda_6 = \begin{pmatrix} 0 & & \\ & 0 & 1 \\ & 1 & 0 \end{pmatrix}, \tag{3.20}$$
$$\lambda_7 = \begin{pmatrix} 0 & & \\ & 0 & -i \\ & i & 0 \end{pmatrix}, \quad \lambda_8 = \frac{1}{\sqrt{3}} \begin{pmatrix} 1 & & \\ & 1 & \\ & & -2 \end{pmatrix}.$$

The Lorentz group $O(1,3)$

All of what has been discussed in this chapter ultimately leads up to the Lorentz group — a group that can be used to describe fundamental particle physics phenomena, including the elementary particles of the Standard Model.

The Lorentz group $O(1,3)$ is the group of Lorentz transformations in Minkowski spacetime (in the least mathematical explanation, the 1 and 3 correspond to the spacetime coordinates; one for time and three for space), and basically a generalization of the rotation group that also incorporates boosts as additional transformations. Abstractly speaking, the set consists of the transformations, and the operation is the succession of these transformations. The set of the Lorentz group consists of the real-valued transformation matrices Λ.

The Lie algebra of the Lorentz group is called the Lorentz algebra $\mathfrak{so}(1,3)$, which is defined by the commutation relations [57, Sec. 10.1.1]

$$\begin{aligned} \left[J_i, J_j\right] &= i\varepsilon_{ijk}J_k, \\ \left[J_i, K_j\right] &= i\varepsilon_{ijk}K_k, \\ \left[K_i, K_j\right] &= -i\varepsilon_{ijk}J_k. \end{aligned} \tag{3.21}$$

The J_i and K_i are the generators of the Lorentz group. The first relation has been introduced already in Eq. (3.14): The J_i generate the group of 3D rotations as a subgroup of the Lorentz group.

The relations in Eq. (3.21) can be re-written as $L_i = \frac{1}{2}(J_i + iK_i)$ and $R_i = \frac{1}{2}(J_i - iK_i)$. With this basis transformation, one obtains [57, Sec. 10.1.2]

$$\begin{aligned} \left[L_i, L_j\right] &= i\varepsilon_{ijk}L_k, \\ \left[R_i, R_j\right] &= i\varepsilon_{ijk}R_k, \\ \left[L_i, R_j\right] &= 0. \end{aligned} \tag{3.22}$$

The above relations makes apparent one very important fact: The Lorentz group's Lie algebra has two (very familiar) sub-algebras that commute with each other. They are both algebras of the 3D rotation group, compare Eq. (3.14). Due to the isomorphism $\mathfrak{so}(3) \cong \mathfrak{su}(2)$, one can now say: The Lie algebra of the Lorentz group is a direct sum of two $\mathfrak{su}(2)$'s [57, Sec. 10.1.2]!

$$\mathfrak{so}(1,3) \quad \cong \quad \mathfrak{su}(2) \oplus \mathfrak{su}(2). \tag{3.23}$$

Why is this so important? By knowing Eq. (3.23), the task of finding all irreducible representations of the Lorentz group has become a lot easier. As has been mentioned above, the $(2j + 1)$-dimensional representations of the $\mathfrak{su}(2)$ are characterized by the half-integers j, so the irreducible representations of the Lorentz group are characterized by two independent half-integers (j_1, j_2), corresponding to two independent copies of the $SU(2)$. The task is now to iterate over all possible combinations of (j_1, j_2), to obtain the irreducible representations of the Lorentz group, and hence the nature of the fields in the Standard Model. The irreducible representations are:[9]

- **Lorentz scalars:** $(0, 0)$
  The trivial representation, consisting of two $SU(2)$ *singlet representations*. It has only one dimension and its elements describe scalar fields, which remain exactly the same when subjected to a Lorentz transformation. Scalar fields are usually denoted by symbols such as ϕ, h, η.

- **Weyl spinors:** $\left(\frac{1}{2}, 0\right)$ and $\left(0, \frac{1}{2}\right)$
  These two-dimensional representations use a singlet and a *doublet representation* of the $SU(2)$ each. The elements describe massless spin-1/2 particles, called Weyl fermions (left- and right-handed Weyl fermions for the $\left(\frac{1}{2}, 0\right)$, $\left(0, \frac{1}{2}\right)$ representations, respectively). There are no Weyl fermions in the Standard Model, because the Weyl theory lacks a proper description of antiparticles or mass. Weyl fermions are denoted with ψ_L, ψ_R.

- **Dirac spinors:** $\left(\frac{1}{2}, 0\right) \oplus \left(0, \frac{1}{2}\right)$
  A direct sum of the two Weyl spinor representations (which means it is reducible and technically does not belong in this list). Its elements consist of one left- and one right-handed Weyl spinor
  $$\psi_D = \begin{pmatrix} \psi_L \\ \psi_R \end{pmatrix}, \tag{3.24}$$
  forming four-dimensional objects called *Dirac spinors* or *bispinors*, that accurately describe massive fermion and antifermion fields (e.g. electron and positron) with two spin states each. ψ_L and ψ_R belong to separate irreducible representations, indicating that these two fermion components react differently to $SU(2)$ transformations.

- **Majorana spinors** also describe massive fermions. They are Dirac spinors with the additional constraint $\psi_M^c = \psi_M$, meaning that Majorana fermions are their own antiparticles and are invariant objects under the discrete group of charge conjugation.

- **Lorentz vectors:** $\left(\frac{1}{2}, \frac{1}{2}\right)$
  The four-dimensional irreducible representation, and the fundamental representation of the Lorentz group. Its elements are Lorentz vectors (four vectors), describing spin-1 fields, also called gauge fields or vector bosons. They are usually denoted with e.g. A_μ, where upper and lower indices describe contra- and covariant vectors according to the four-notation.[10]

The difference of the elements of each representation lies in their dimension and transformation properties, meaning that Lorentz transformations act differently on them. This is expressed by e.g. "the field ψ transforms like a Dirac spinor".

[9] For further reading, see again Ref. [55, Sec. 3.2].
[10] Below are some definitions of four-notation (and Feynman slash-notation) the reader might find useful.

By the way, demanding a Lagrangian to be symmetric under the Lorentz group is equivalent to demanding invariance towards spatial rotations, spatial translations and time translations. This leads to conservation of angular momentum, linear momentum and energy, respectively, which can be explained by means of *Noether's theorem*.

Description 9: Noether's theorem. "If a Lagrangian has a continuous symmetry then there exists a current associated with that symmetry that is conserved when the equations of motion are satisfied." [57, Sec. 3.3]

Such a *Noether current* results in a conserved physical quantity.

For a detailed explanation using the example of global invariance under $U(1)$ phase transformations, see [56, Sec. 14.2].

To summarize: In this past section, the most important aspects of group theory have been introduced, with definitions and descriptions that eventually led up to the *Lorentz group* and its representations. The fields of the Standard Model are characterized by the irreducible representations of the Lorentz group. These representations determine the spin of particles, and therefore appointing them bosonic or fermionic nature. In other words, the demand for a Lorentz-invariant Lagrangian, or *Lorentz symmetry*, leads to certain field properties, as well as the conserved quantities of energy, momentum, and angular momentum. The quantum field theory component of the Standard Model is thereby adequately described.

3.1.3 The Lagrangian

The representations of the Lorentz group clearly play an important role when it comes to the formulation of a theory such as the Standard Model, since they define properties the different fields can have. One now needs a way to combine the different fields within the theory, and describe their relation to one another. This is done by means of the *Lagrangian*.

While the reader should be familiar with the Lagrange formalism to some extend, they might not posses too much practice when it comes to quantum field theory Lagrangians. As a quick reminder, the following statements are true for a (valid) Lagrangian:

- It summarizes the dynamics of a system in units of energy. Classically with $\mathcal{L} = T - V$, where T and V are the kinetic and potential energy. In QFT it is more applicable to talk about *kinetic terms* and *interaction terms*.
- It contains all information about the theory, including all constraints and forces.

four-vector, contravariant:	$x^\mu = (ct, \mathbf{r})$	time derivative:	$\partial_0 = \frac{\partial}{\partial t}$
four-vector, covariant:	$x_\mu = (ct, -\mathbf{r})$	d'Alembert operator:	$\Box = -\partial_\mu \partial^\mu$
transformation:	$x_\mu = g_{\mu\nu} x^\nu$		$= -\frac{1}{c^2}\frac{\partial^2}{\partial t^2} + \Delta$
scalar product:	$x \cdot y = g_{\mu\nu} x^\mu x^\nu$	Feynman slash vector:	$\not{A} = \gamma^\mu A_\mu$
energy momentum rel.:	$(p^\mu) = \left(\frac{E}{c}, \vec{p}\right)$	squared energy-mom. vector:	$p_\mu p^\mu = m^2 c^2$
partial deriv., contravariant:	$\partial_\mu = \frac{\partial}{\partial x^\mu}$	partial deriv., covariant:	$\partial^\mu = \frac{\partial}{\partial x_\mu}$
	$(\partial_\mu) = \left(\frac{1}{c}\frac{\partial}{\partial t}, \nabla\right)$		$(\partial^\mu) = \left(\frac{1}{c}\frac{\partial}{\partial t}, -\nabla\right)$
field strength tensor	$F_{\mu\nu} = \partial_\mu A_\nu - \partial_\nu A_\mu$		

– It is Lorentz-invariant.

– It describes the equations of motion by means of the *Euler-Lagrange equations*.

The full Lagrangian of the Standard Model is very complex, and it is not necessary to show it here (and would easily fill a few pages depending on the degree of detail). Instead, a few examples of simpler Lagrangians will be shown in order to (re-)familiarize the reader with the different terms. As mentioned in the list above, these terms can mostly be categorized into *kinetic terms* and *interaction terms* (following Ref. [57, Sec. 3.1]):

Kinetic terms always contain exactly two fields, they are *bilinear*. They describe a free theory, so basically they are saying "there exists this particle", hence there has to be a kinetic term for each particle in the system. In addition to being bilinear, they contain at least one time derivative, which makes them *dynamic*. Examples for some possible fields[11] are:

$$\overset{\text{real scalar}}{\left(\partial_\mu\phi\right)^2}, \qquad \overset{\text{complex scalar}}{\left(\partial_\mu\phi\right)\left(\partial^\mu\phi^*\right)}, \qquad \overset{\text{bispinor}}{\bar{\psi}\gamma^\mu\partial_\mu\psi}, \qquad \overset{\text{vector}}{\frac{1}{4}F_{\mu\nu}F^{\mu\nu}}. \tag{3.25}$$

Everything else falls in the category of interaction terms. Although, there is the special case of mass terms, which technically belong to the free theory and hence the kinetic energy, but are often viewed as interaction terms (for unfamiliar notations please refer to footnote 10).

Mass terms are also bilinear in fields, but do not contain derivatives. Fields that are not represented by a mass term in the Lagrangian are massless. Mass terms, especially for vector fields, are sometimes not invariant under the theory's symmetries, and such fields need to obtain their masses through the famous Higgs mechanism, which is explained in Sec. 3.1.5. Examples for mass terms are:

$$\overset{\text{real scalar}}{\frac{1}{2}m^2\phi^2}, \qquad \overset{\text{complex scalar}}{m^2\phi\phi^*}, \qquad \overset{\text{bispinor}}{m\bar{\psi}\psi}, \qquad \overset{\text{vector}}{m^2A_\mu A^\mu}. \tag{3.26}$$

Interaction terms are all other terms containing three or more fields. They can describe a field's self-interaction, they can be sources of fields, or couple fields to one another. Examples are:

$$\overset{\text{real scalar self-interaction}}{\lambda\phi^3}, \qquad \overset{\text{Yukawa cpl. of Dirac spinor and real scalar}}{y\bar{\psi}\psi\phi}, \qquad \overset{\text{cpl. of vector to Dirac spinor}}{e\bar{\psi}\gamma^\mu A_\mu\psi}. \tag{3.27}$$

To summarize: Even though the Standard Model Lagrangian in its full glory cannot be discussed here, many examples of terms that appear in the Standard Model Lagrangian in similar form have been introduced and explained. The Lagrangian, as the container of all fields and physics that are part of a system, has been identified as one of the important building blocks of a particle physics theory.[12]

[11] The reader might wonder about the usage of real and complex scalar fields. The physical meaning of a complex scalar $\phi = \phi_1 + i\phi_2$, which basically has to be viewed as two separate fields, is a charged spin-0 particle/antiparticle pair, whereas a real scalar does not possess the necessary degree of freedom to be charged (and therefore an antiparticle does not exist). While the Higgs field is an example for a complex scalar field, there is no known representative of a real scalar field in nature.

[12] The Lagrangian is immensely handy when defining a theoretical model, but it can be derived from the field content and symmetries, and is therefore not *actually* a building block of a new theory, rather than a consequence

3.1.4 Gauge symmetries

There is more to the Standard Model than determining the spins of the fields' particles by finding the corresponding irreducible Lorentz group representations, because it is not just a quantum field theory, but also a *gauge theory*, and therefore further defined by its *gauge symmetries*. Much like with Lorentz symmetry and the Lorentz Lie group, gauge symmetries describe transformations belonging to certain gauge Lie groups that leave the Lagrangian of the system invariant, i.e. unchanged. However, the Lorentz symmetry is a *global symmetry*, while gauge symmetries are *local symmetries*.

Description 10: Global and local symmetries. Transformations under a global symmetry, such as Lorentz symmetry in the case of the Standard Model, affect a system in equal ways at every point in space x. A local symmetry, on the other hand, may affect a system differently, depending on x, but still leave the system as a whole unchanged. Therefore, a local symmetry is a much stronger imposition on a system than a global symmetry. Every local symmetry is also a global symmetry, but not the other way around.

For instance, the reader may imagine a system, say, a magical pouch full of perfect marbles, uniformly colored and impeccably spherical. The pouch is transparent, and the marbles can be remotely manipulated by some magical force. There exists a global rotation symmetry to this pouch: Every single marble in the pouch may be rotated about a certain angle; a process that leaves the system visibly unchanged, and one will not be able to tell that it ever happened. But the pouch has another global symmetry which is that of translation: Moving the pouch around the room carefully will also leave it and its system of marbles unchanged.

Now the pouch also possesses a *local* rotation symmetry. The action of rotation would be applied to each marble in the system, but with slightly different angles, which also clearly leaves the system as a whole unchanged. Translation, however, is *not necessarily* a local symmetry of the pouch system: Moving the marbles around individually will most likely result in a differently shaped pouch with marbles in different places.

Local symmetries are much stronger impositions on a system than global symmetries, but they also bring forth new interactions, which, in the case of the Standard Model, are quite literally fundamental. While the demand for global symmetry, like the Lorentz symmetry, "merely" results in field properties, one could say that the demand for local symmetry results in new *forces* that can act on the system.

The reader has already casually encountered the components of the Standard Model's gauge Lie group in the last section: The $SU(3) \times SU(2) \times U(1)$, corresponding to group of quantum chromodynamics (QCD), the group of the weak interaction, and the group of quantum electrodynamics (QED); it is a direct product of the familiar Lie groups $SU(3)$, $SU(2)$ and $U(1)$.

Description 11: Direct product of groups. For two groups $(G, *)$ and $(H, \star)$ one can construct the direct product $(G \times H, \circ)$ so that

$$\left(g_1, h_1\right) \circ \left(g_2, h_2\right) = \left(g_1 * g_2, h_1 \star h_2\right) \tag{3.28}$$

of the physics. It can be incredibly hard to derive correctly though, especially without a background in theoretical physics.

with $g_{1,2} \in G$, $h_{1,2} \in H$. The sets of $(G \times H, \circ)$ is the Cartesian product of the original sets:

$$G \times H = \left\{ (g, h) \,|\, g \in G, h \in H \right\}. \tag{3.29}$$

The identity element of $(G \times H, \circ)$ is denoted by (e, e), and the inverse element to (g, h) is denoted by (g^{-1}, h^{-1}). [54, Sec. 5.3.3.2]

Gauging a theory

When a local symmetry is imposed on a theory, one says that the theory is being *gauged*. This process is illustrated using the $U(1)$ as the simplest applicable example, following Ref. [56, Secs.14.2,14.3].

It starts out with the Dirac Lagrangian

$$\mathcal{L} = i\bar{\psi}\gamma^{\mu}\partial_{\mu}\psi - m\bar{\psi}\psi, \tag{3.30}$$

i.e. the theory that describes fermions[13], where ψ and $\bar{\psi}$ are Dirac spinors that each describe the spin-up and spin-down state of a particle ψ or antiparticle $\bar{\psi}$. $\mathcal{L}$ is invariant under the global symmetry $U(1)$ of phase transformations. With a real, constant phase α, the fields in $\mathcal{L}$ transform like

$$\begin{aligned} \psi(x) &\rightarrow e^{i\alpha}\psi(x), \\ \bar{\psi}(x) &\rightarrow e^{i\alpha}\bar{\psi}(x), \\ \partial_{\mu}\psi(x) &\rightarrow e^{i\alpha}\partial_{\mu}\psi(x). \end{aligned} \tag{3.31}$$

However, for *local* phase transformations, i.e. when $\alpha(x)$, this does not work anymore for the last equation; the derivative introduces a term $\partial_{\mu}\alpha(x)$ that breaks invariance:

$$\partial_{\mu}\psi(x) \rightarrow e^{i\alpha(x)}\partial_{\mu}\psi(x) + ie^{i\alpha(x)}\psi(x)\partial_{\mu}\alpha(x). \tag{3.32}$$

To keep the Lagrangian invariant, the derivative is therefore replaced by a *covariant derivative*,

$$\partial_{\mu} \rightarrow D_{\mu} \equiv \partial_{\mu} + iqA_{\mu}, \tag{3.33}$$

where q is a *coupling constant* or charge, and A is the *gauge field*. One can see that the covariant derivative determines the strength with which fields are going to be coupled to A. The gauge field transforms as

$$A_{\mu} \rightarrow A_{\mu} - \frac{1}{q}\partial_{\mu}\alpha. \tag{3.34}$$

[13] It can be shown that Eq. (3.30) is the Dirac Lagrangian by means of the Euler-Lagrange equation:

$$\begin{aligned} \frac{\partial\mathcal{L}}{\partial\bar{\psi}} - \partial_{\mu}\left(\frac{\partial\mathcal{L}}{\partial\left(\partial_{\mu}\bar{\psi}\right)}\right) &= 0 \\ i\gamma^{\mu}\partial_{\mu}\psi - m\psi - \frac{\partial}{\partial x^{\mu}}(0) &= 0 \\ \left(i\gamma^{\mu}\partial_{\mu} - m\right)\psi &= 0 \end{aligned}$$

One arrives at the Dirac equation for ψ in the last step.

To appoint dynamics to the new field, it needs an invariant kinetic term in the Lagrangian in form of the squared field strength tensor $F_{\mu\nu} = \partial_\mu A_\nu - \partial_\nu A_\mu$, so that the final, gauge invariant Lagrangian of QED becomes:

$$\begin{aligned}\mathcal{L} &= i\bar{\psi}\gamma^\mu D_\mu\psi - m\bar{\psi}\psi - \frac{1}{4}F_{\mu\nu}F^{\mu\nu} \\ &= \underbrace{\bar{\psi}\left(i\gamma^\mu\partial_\mu - m\right)\psi}_{\text{kinetic energy, mass of }\psi} + \underbrace{q\bar{\psi}\gamma^\mu A_\mu\psi}_{\text{interaction}} - \underbrace{\frac{1}{4}F_{\mu\nu}F^{\mu\nu}}_{\text{kinetic energy of }A_\mu}\end{aligned} \tag{3.35}$$

The second term couples the original fields to A. Note that a mass term of the form $\frac{1}{2}m^2 A_\mu A^\mu$ is not gauge invariant and can therefore not be part of the Lagrangian, which means that the gauge particle that arises from A, the photon, is necessarily massless.

Since q is a constant in the above Lagrangian, only one particular charge is allowed. For different fermions to have different charges, one is required to add a charge operator Q which so far has been omitted. When lastly re-defining q to be the elementary charge e, Eqs. (3.31) and (3.35) change according to

$$\begin{aligned}\psi(x) &\to e^{i\alpha(x)Q}\psi(x), \\ \mathcal{L} &= \bar{\psi}\left(i\gamma^\mu\partial_\mu - m\right)\psi + e\bar{\psi}\gamma^\mu Q\psi A_\mu - \frac{1}{4}F_{\mu\nu}F^{\mu\nu},\end{aligned} \tag{3.36}$$

where the charge could take values of $Q = -1$ for the electron, or $Q = \frac{2}{3}$ for the up-quark, for instance.

This example of gauging by means of a $U(1)$ is relatively simple because the $U(1)$ is *abelian*, meaning that the group generators commute. For the $SU(2)$ and $SU(3)$, this is not the case. Non-abelian gauge theories, also referred to as *Yang-Mills theories* [57, Chp. 25], are more complicated. First of all, one uses the same method of introducing covariant derivatives, but when adding dynamics to the system by means of the field strengths, not all terms are purely kinetic, but can be cubic and quartic in terms of the field strength tensors. These terms are *self-interaction terms*, and are an inevitable result of gauging non-abelian theories. They imply that the new fields are charged themselves.

Gauge fields give rise to vector bosons, which are also called *gauge particles* or *force carriers*, in number equal to the number of generators of the respective Lie algebras. In the case of the $SU(3)$, the Lie algebra has eight generators, so eight new gauge fields need to be introduced: The gluon fields G_α, which give rise to eight gluons and themselves carry color charge. The $SU(2)$ has three generators, and one arrives at the three fields W_1, W_2 and W_3. Deducing the force carriers from those fields is not that trivial, though, and will be the subject of the next sections.

To summarize: The Standard Model of particle physics is described by local symmetries under the gauge group $SU(3) \times SU(2) \times U(1)$. Local symmetries introduce conserved quantum numbers. In addition, the symmetries introduce gauge fields which are associated with the three fundamental interactions; in total eight gluon fields for the $SU(3)$, three weak fields for the $SU(2)$, and the photon field for the $U(1)$. Gauge fields give rise to force carriers.

3.1.5 The Higgs mechanism

Despite being non-abelian, gauging the $SU(3)$ is a relatively simple processes, and even more so the $U(1)$. The reason is that their gauge fields are adequately described by a Langragian that does not allow a gauge mass term — the gluons and the photon are massless. The vector bosons of the weak interaction are, however, *pretty* massive. How, without breaking the gauge invariance of the theory?[14]

The answer is to add the mass terms "accidentally"; a process that is explained in the following, based on Ref. [56, Chp.14]. Imagine a complex scalar field $\phi = (\phi_1 + i\phi_2)/\sqrt{2}$ which is described by this Lagrangian:

$$\mathcal{L} = \underbrace{(\partial_\mu \phi)^* (\partial^\mu \phi)}_{\text{kinetic energy}} - \underbrace{\mu^2 \phi^* \phi}_{\text{mass term}} - \underbrace{\lambda (\phi^* \phi)^2}_{\text{self-interaction}} \tag{3.37}$$

So the potential includes a mass term that is quadratic in ϕ with mass parameter μ, and a quartic self-interaction term with coupling λ. This Lagrangian is invariant under a global $U(1)$ symmetry. Assuming $\lambda > 0$, there are two possible configurations of this potential, one for $\mu^2 > 0$ and one for $\mu^2 < 0$, which are shown in Fig. 3.3. The first configuration (left) is the "normal" potential of a complex scalar field with the lowest energy state being the vacuum at $\phi = 0$. A little ball at the bottom of this potential would have no reason at all to move about, since the ground state is already the most stable one. The Lagrangian of the ball-system is quite obviously invariant under rotations.

The second configuration (right), however, has minima, an infinite number of them to be exact; resembling the bottom part of a wine bottle. The Lagrangian of a ball sitting at $\phi = 0$ would still be rotation-invariant, but the point is now unstable: A ball residing there would roll down the slope at the slightest perturbation. Once the ball "chooses" its new arbitrary ground state v, the rotation invariance is lifted — so transferring the system into the ground

[14] The devastating effects of "just adding a couple of mass terms" to the $SU(2)$ Lagrangian might not be obvious to the reader. They shall not be elaborated here, let it just be said that it would eventually lead to unsolvable divergences. Divergences occur e.g. in loop diagrams, when there is an infinite number of possible energy-momentum combinations of virtual particles that has to be integrated over. Some of these make the Lagrangian "unrenormalizable", basically stripping the theory of its predictive powers. This is quite well explained in Ref. [56, Sec.14.5].

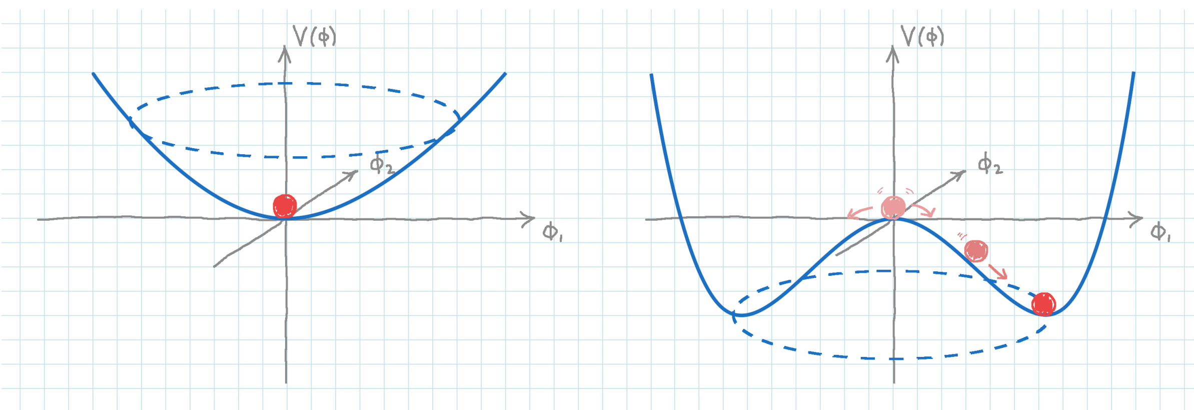

Figure 3.3: **Left:** The familiar potential $\mu^2\phi^*\phi + \lambda(\phi^*\phi)^2$ of a complex scalar field, with $\mu^2, \lambda > 0$. The red ball resides stably in the vacuum position $\phi = 0$. **Right:** The same potential with $\mu^2 < 0, \lambda > 0$, the "wine bottle potential", with an infinite number of minima at the bottom.

state breaks the symmetry (although in a sense, there is still a rotation symmetry present in terms of the choice of ground state; all points on the circle that is formed by the very bottom of the wine bottle are equally likely to hold the ball). This is called *spontaneous symmetry breaking* or *Higgs mechanism*.

But choosing $\mu^2 < 0$ seems to leave the mass term in (3.37) with the wrong sign. One can show, however, that transferring the field to one of the minima, e.g. $(\phi_1 = v, \phi_2 = 0)$ with $v^2 = -\mu^2/\lambda$, and performing perturbative calculations, i.e. replacing the field with fluctuations η, ξ (two fluctuations are necessary because there are two degrees of freedom in this system) around this new vacuum by substituting

$$\phi = \sqrt{\frac{1}{2}}\left(v + \eta(x) + i\xi(x)\right) \tag{3.38}$$

in the Lagrangian, in fact results in the correct sign of the mass term:

$$\mathcal{L}' = \frac{1}{2}\left(\partial_\mu \xi\right)^2 + \frac{1}{2}\left(\partial_\mu \eta\right)^2 + \underbrace{\mu^2\eta^2}_{\text{mass of }\eta} + \text{const.} + \text{h.o. terms in } \eta, \xi \tag{3.39}$$

So the choice of $\mu^2 < 0$ is justified, and a massive scalar field η was successfully created whilst keeping the global $U(1)$ symmetry of the Lagrangian intact. As the reader correctly saw above, the system has another degree of freedom ξ in the ground state, which is the "movement about the circle" at the bottom of the bottle. Because the potential in this direction is absolutely flat, ξ must be massless — a so-called *Goldstone boson*.

While this is all very interesting, it may seem that nothing really exciting has been achieved so far. If a massive scalar field is all we wanted, it could have been achieved with the left configuration in Fig. 3.3 without having to deal with a Goldstone boson. But the goal is to obtain not any massive scalar field, but a *massive gauge field*.

According to what was done previously, a gauge field is obtained by demanding *local* gauge invariance. After formulating the covariant derivative, the new gauge invariant Lagrangian is

$$\mathcal{L} = \underbrace{\left(\partial^\mu + ieA^\mu\right)\phi^*\left(\partial_\mu - ieA_\mu\right)\phi}_{\text{kinetic energy and interactions}} - \underbrace{\mu^2\phi^*\phi}_{\text{mass}} - \underbrace{\lambda\left(\phi^*\phi\right)^2}_{\text{self-interaction}} - \underbrace{\frac{1}{4}\left(F_{\mu\nu}F^{\mu\nu}\right)}_{\text{kinetic energy of }A_\mu} . \tag{3.40}$$

Again $\mu^2 < 0$ is assumed, and ϕ is moved to the ground state v in the same procedure as above. One obtains

$$\mathcal{L}' = \frac{1}{2}\left(\partial_\mu \xi\right)^2 + \frac{1}{2}\left(\partial_\mu \eta\right)^2 + \mu^2\eta^2 + \underbrace{\frac{1}{2}e^2v^2A_\mu A^\mu}_{\text{mass of }A} - evA_\mu\partial^\mu\xi - \frac{1}{4}\left(F_{\mu\nu}F^{\mu\nu}\right) + \text{interaction terms.} \tag{3.41}$$

with the desired mass term for the gauge field A! Note that the massless ξ can be shown to vanish from the Lagrangian, and instead becomes the longitudinal mode[15] to A.

Since a massive photon is not what was sought after, rather than massive weak bosons, one can repeat the procedure for a local $SU(2)$ symmetry and end up with three massive W_1,

[15]Once A obtains mass it obtains a new degree of freedom, which is, so to say, compensated by taking away ξ's degree of freedom. In literature it is sometimes said that a field "obtains mass by eating up the Goldstone boson".

W_2, W_3 and the massive scalar η, which from now on is called h — the Higgs boson. It was experimentally confirmed in 2012 [61], for which F. Englert and P. W. Higgs were awarded the Nobel Prize in Physics one year later.

3.1.6 Electroweak unification and symmetry breaking

Now that it is clear how gauge bosons obtain mass in general without destroying the system's symmetry, it is left to explain how to obtain the familiar massive W^+, W^-, and Z^0 bosons of the weak interaction, instead of the W_1, W_2, W_3. The answer is (the resolving of) *electroweak unification*; following Refs. [56, Chp. 15][57, Sec. 29.1].

For high energies, the electromagnetic and weak interactions actually are a single *electroweak interaction*, a gauge group denoted by $SU(2) \times U(1)_{\mathrm{Y}}$. This unification is dissolved for lower, nowadays (compared to early-universe) energies below the unification threshold, a process which is called *electroweak symmetry breaking*, denoted by

$$SU(2) \times U(1)_{\mathrm{Y}} \to U(1)_{\mathrm{EM}}. \tag{3.42}$$

The above equation means that when the symmetry of $SU(2) \times U(1)_{\mathrm{Y}}$ is broken (hidden) by the Higgs mechanism, the system is left with only the $U(1)_{\mathrm{EM}}$ as a (visible) symmetry. The two $U(1)$s in Eq. (3.42) are *not* the same! The $U(1)_{\mathrm{Y}}$ is a symmetry of hypercharge Y, whereas the $U(1)_{\mathrm{EM}}$ is a symmetry of electromagnetic charge. The two groups will be distinguished like that in the following whenever there is room for confusion. The quantum numbers of the left hand side symmetry are the weak isospin T and, as mentioned before, the hypercharge Y.

The reader has seen in the last section why it is not enough to break the symmetry of $SU(2)$ — one obtains the wrong massive weak bosons. The symmetry of the product $SU(2) \times U(1)_{\mathrm{Y}}$ has to break instead, which forces the generators of the two groups to commute with each other, and the resulting fields to mix (mixing of the W and B fields means that their physical states are actually linear combinations of the original fields):[16]

$$W^{\pm} = \frac{1}{\sqrt{2}} \left(W_1 \pm i W_2 \right), \tag{3.43}$$

$$\begin{pmatrix} \gamma \\ Z^0 \end{pmatrix} = \begin{pmatrix} \cos\theta_{\mathrm{W}} & \sin\theta_{\mathrm{W}} \\ -\sin\theta_{\mathrm{W}} & \cos\theta_{\mathrm{W}} \end{pmatrix} \begin{pmatrix} B \\ W_3 \end{pmatrix}, \tag{3.44}$$

where the mixing angle θ_{W} is called the *Weinberg angle*. The W_1 and W_2 fields mix into the massive $W^{\pm}$, and the W_3 and B fields mix into the massive Z^0 and the massless photon γ. The photon remains massless because it turns into the gauge boson of the unbroken $U(1)_{\mathrm{EM}}$.

Unification, in a stricter sense, means that two forces share a single, unified coupling constant. But the electroweak theory has two coupling constants: g which arises from gauging the $SU(2)$, and g' from gauging the $U(1)_{\mathrm{Y}}$; so technically, the unification is not "complete". But the two couplings are connected by

$$e = g \sin\theta_{\mathrm{W}} = g' \cos\theta_{\mathrm{W}}, \tag{3.45}$$

where e is the elementary charge. The connection of the two groups further manifests in the

[16]Using the symbol B instead of A (as in the earlier example) is to indicate that they arise from the gauging of two different $U(1)$s.

quantum numbers T and Y, which are not conserved individually. But a specific combination of them is, which happens to be the electric charge

$$Q = T_3 + Y_{\mathrm{W}}, \tag{3.46}$$

the conserved quantum number of the unbroken $U(1)_{\mathrm{EM}}$!

If the reader is now confused whether the two groups are unified or not: They are *in a sense but not really*. One could argue that "electroweak mixing" would describe the situation better than "unification". This mixing of the two groups shows in the couplings, and also in the force carriers[17].

3.1.7 Fermions

Fermions in general are described by Dirac spinors[18], meaning they transform under the $\left(\frac{1}{2},0\right) \oplus \left(0,\frac{1}{2}\right)$ representation of the Lorentz group. Generations aside, there are four of these Dirac spinors in the Standard Model: The up and down quarks u and d, and, for the lepton side, the electron and electron neutrino e and ν. Now from a gauge group point of view, it is important to remember that the Dirac spinor is a two-component object formed by a left- and right-handed Weyl spinor, recalling Eq. (3.24).

What is the deal with *handedness*? First of all, it defines under which of the two two-dimensional irreducible representation of the Lorentz group, $\left(\frac{1}{2},0\right)$ or $\left(0,\frac{1}{2}\right)$, a spinor transforms under. Another word for this is *chirality*.

Description 12: Chirality. As a property of spinors, it only makes sense to talk about chirality in the context of fermions. It describes an asymmetry of Lorentz representations (A,B) with $A \neq B$, meaning that objects from (A,B) transform differently than objects from (B,A).

Chirality is a Lorentz-invariant quantum number, but is not a constant of motion.

[57, Sec 11.1]

Another concept that often pops up alongside chirality is *helicity*. The two are somewhat related, but also very different.

Description 13: Helicity. A concept that describes the projection of the spin to the direction of motion of a particle. There are only two helicity states: Aligned and anti-aligned spin and direction.

Helicity is a constant of motion, but not generally Lorentz-invariant, except for massless particles: Massless particles travel with the speed of light. Their direction of motion can never be inverted by an observer faster than the particle itself, because such an observer does not exist. For slower, massive particles, a fast-enough observer could Lorentz-boost herself into a reference frame from which the direction of motion appears to be inverted, effectively changing the helicity. [57, Sec 11.1]

[17]The expression that was used in the beginning of this chapter, "$SU(3)\times SU(2)\times U(1)$ is the gauge symmetry of the Standard Model", certainly has some unified ring to it. This is a bit misleading, so far there is no coupling that would include the $SU(3)$ as well. The Standard Model is *not* a unified theory! Although there exist different *Grand Unification Theories* (GUTs) that would merge the $SU(3)$ with the $SU(2) \times U(1)_{\mathrm{Y}}$, such as the $SU(5)$, a scientific consensus is yet to be found and experimentally confirmed.

[18]Weyl and Majorana fermions can be treated as special, somewhat simpler cases of Dirac fermions.

For massless fermions, helicity and chirality take the same values, but they are not the same! The main difference between chirality and helictiy is that the first is an inherent property of a particle, and the other is not (hence one is a Lorentz-invariant property and the other is not). Chiral right-handed and chiral left-handed particles are really two different particles, whereas helicity merely describes the spin alignment; spin and direction of motion can be flipped and changed. In contrast, a particle with a certain chiral handedness will *always* have this handedness. Another difference is that there exists a certain "symmetry" to helicity: If a particle has aligned helicity, the same particle with anti-aligned helicity is just as imaginable. For chirality, this is not necessarily the case — the best example are neutrinos (at least until they find right-handed ones)!

Now, the weak interaction is a *chiral theory*, meaning it discriminates between left- and right-handed particles. To be exact, the charged $W^{\pm}$ bosons only couple to left-handed fermions (and right-handed antifermions) and do not "talk" to right-handed ones *at all*. Each (massive) fermion is described by a spinor composed of a left- and right-handed component, the former transforming as an $SU(2)$ doublet, the latter as an $SU(2)$ singlet (ergo, not at all). So, while the components are similar (i.e. conjugates) regarding their Lorentz representations, they are completely different things regarding their $SU(2)$ representations!

To circle back to the four fermion fields, one can now write their components as the corresponding doublets and singlets by "ganging up" the left-handed ones: [57, Sec. 29.3]

$$Q_L = \begin{pmatrix} u_L \\ d_L \end{pmatrix}, \qquad L_L = \begin{pmatrix} \nu_L \\ e_L \end{pmatrix}, \qquad u_R, \qquad d_R, \qquad e_R, \qquad (\nu_R)\,. \tag{3.47}$$

The right handed neutrino has not been confirmed experimentally, so it is written in parenthesis. Another term for "$SU(2)$ doublet" is "weak isospin doublet", which makes apparent that the components of Q_L and L_L are appointed weak isospins $-1/2$ and $1/2$, while the right-handed components come away empty-handed.

The question of the "physical particles" remains. What do people mean when they talk about the "electron" for instance, in a more casual way? The physical electron is actually a quantum mix of the left- and right-handed electron, basically inheriting the properties of both. How is this possible? In order for fields to mix, the following conditions need to be fulfilled:

– The fields must be massive, and

– they must be equal in quantum numbers.

So the mixing of e_L and e_R *should* be forbidden, because they have distinguished weak isospin and therefore the mixing should break gauge symmetry. But as one recalls correctly from the last sections, that same gauge symmetry has been broken by the same process that appoints mass to the fields, the Higgs mechanism, and, roughly speaking, one can not violate a symmetry that is already broken. So mass is the key to the physical electron![19]

By the way, $U(1)_Y$ is not a chiral symmetry, and appoints hypercharge to the left- and right-handed fermions. As has been explained above, hypercharge and weak isospin add up to form the electric charge, Eq. (3.46), after electroweak symmetry breaking.

[19] Breaking the unwritten law to never quote a website by itself: Ref. [62] proved very helpful for understanding the concept of chirality.

Generations

Recalling Fig. 3.1 from the very beginning of this section, it is evident that there are not only two quark- and two lepton fields, but six and six. For each of the quark and lepton categories, the additional four fields group up into two and two, forming copies of the original fields, so that there are a total of three fields that behave like the u, and likewise for the d, e and ν. The three copies are called *generations* or sometimes *families*, and the quantum numbers in one generation are the same as in the other two. Consequently, for the quark sector there are the generation pairs of up and down (u, d), charm and strange (c, s), and top and bottom (t, b). For the lepton sector, they are the electron neutrino and electron (ν_e, e), the muon neutrino and muon (ν_μ, μ), and the tau neutrino and tau (ν_τ, τ).

The only (quite substantial) difference between the generations are the masses of the fields, with the exception of the neutrinos which remain massless in the theoretical description of the Standard Model. It is not clear why there are exactly three generations of quarks and leptons, and why the mass differences are what they are.

3.1.8 Field content of the Standard Model

As a conclusion to this section, the field content of the Standard Model is presented in tabular form, summarizing the information from the last sections in a nice overview: See Tab. 3.1. The field content shown here is unbroken and unmixed, and through electroweak symmetry breaking gives rise to the elementary particles shown in Fig. 3.1 in the very beginning of this section. So we've come full $U(1)$!

Section 3.1 summary

In this past section, the elementary particles of the Standard Model have been introduced, and it has been successively explained how the field content of the theory gives rise to those particles. The reader has learned that spin is a property determined by the representations of the Lorentz group, and that charge and multiplett character are determined by the representations of the gauge groups. These local symmetries required to describe nature give rise to the gauge fields and the fundamental forces that are known as the strong, weak and electromagnetic interactions, where the last two are united for high energies in the electroweak interaction. An additional scalar field, known as the Higgs field, spontaneously breaks the electroweak symmetry and appoints mass to the weak bosons in the process. The Higgs field further interacts with all other fields that possess weak hypercharge, and therefore gives rise to the masses of the fermions.

Table 3.1: Charges of the Standard Model fields. Listed are the number of generations i.e. "copies" of each field, the spin and the related representation of the Lorentz group, as well as the gauge group representations that each field transforms under. Empty cells mean that the field is not charged (transforms as a singlet under the corresponding gauge group). The right-handed neutrino is grayed out because there is no experimental evidence for its existence. Based on [57, Chp. 29.3] (table design inspired by [55]).

Name	Generations	Spin	Lorentz rep.	$SU(3)$	$SU(2)$	$U(1)_Y$
Gauge fields:						
G	—	1	$(1/2, 1/2)$	8		
W	—	1	$(1/2, 1/2)$		3	
B	—	1	$(1/2, 1/2)$			
Scalar field:						
H	1	0	$(0, 0)$		2	$1/2$
Fermion fields:						
Q_L	3	$1/2$	$(1/2, 0)$	3	2	$1/6$
L_L	3	$1/2$	$(1/2, 0)$		2	$-1/2$
u_R	3	$1/2$	$(0, 1/2)$	3		$2/3$
d_R	3	$1/2$	$(0, 1/2)$	3		$-1/3$
ν_R	3	$1/2$	$(0, 1/2)$			
e_R	3	$1/2$	$(0, 1/2)$			-1

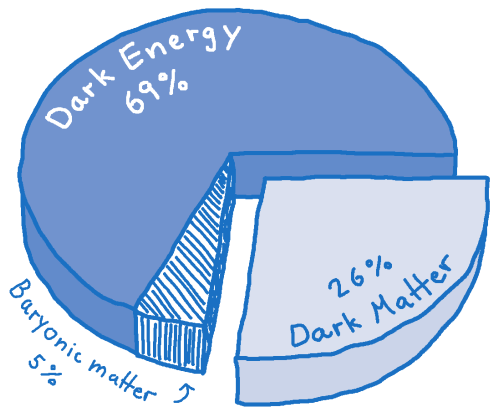

Figure 3.4: Pie chart of the universe. The relevant fractions in descending order are Dark Energy with 69 %, Dark Matter with 26 %, and baryonic matter with 5 %. A negligible fraction consists of non-baryonic "ordinary" matter, e.g. photons and neutrinos (not shown). Values taken from Ref. [63].

3.2 Dark Matter

The Standard Model of particle physics is a very accurate description of nature; its predictions being confirmed by experimental data many times. It is not a perfect model, though. As mentioned in the last section, it is not a unified theory with regard to the strong and electroweak interactions, and even less so with regard to gravity, which actually isn't part of the model at all. Furthermore, it predicts the neutrinos to be massless, which they are clearly not (recall Sec. 2.2.2). And, under the load of overwhelming observational evidence, it also fails to account for most this universe.

The present scientific consensus states that our universe has three major constituents. With $\sim 69\,\%$, the major constituent is *Dark Energy*, the second largest is *Dark Matter* with $\sim 26\,\%$, and only a tiny fraction of $\sim 5\,\%$ consists of baryonic matter. [63]

The matter that accounts for most of the visible mass — like stars, planets, humans, dust — is baryonic in nature, meaning it consists of strongly interacting quarks in a bound state surrounded by electrons; atoms for short. Atoms are part of the "ordinary" matter described in the last section. Further baryonic matter is found in objects that do not shine, for instance non-burning stellar objects, black holes, or cold interstellar gas clouds. The fraction and distribution of this "dark" baryonic matter is not yet understood completely, and therefore considered Dark Matter even though baryonic in nature. Free leptons, i.e. neutrinos and electrons, and technically also their unstable heavier generations, are not baryonic, and make up their own presumably insignificant mass fraction, too small to be depicted in the pie chart.

Then there is non-baryonic Dark Matter. As the name implies, it is non-luminous, and its nature is yet unknown. Including this work, there exist many theories about what Dark Matter might be, which will be covered later in this section. The one certainty is its existence, for which there is plentiful evidence.[20]

An even more mysterious concept is that of Dark Energy. As part of the widely accepted ΛCDM model (also called Standard Model of Cosmology, see e.g. Refs. [24, 66]), the unknown form of energy counteracts gravity throughout the entire universe, causing an accelerated expansion, as indicated by observations of distant supernovae [67, 68]. In contrast to the distributions of dark and ordinary matter in the universe, which are extremely lumpy, the

[20] At this point it is in order to mention Modified Newtonian Dynamics (MOND) [64] as a completely alternative approach to explain the structures of the universe observed today. As the name implies, it proposes modifications of Newton's laws of gravity. The predictions of MOND models, however, face several unresolved challenges, as described in Ref. [65, Sec. 1.7] and references therein.

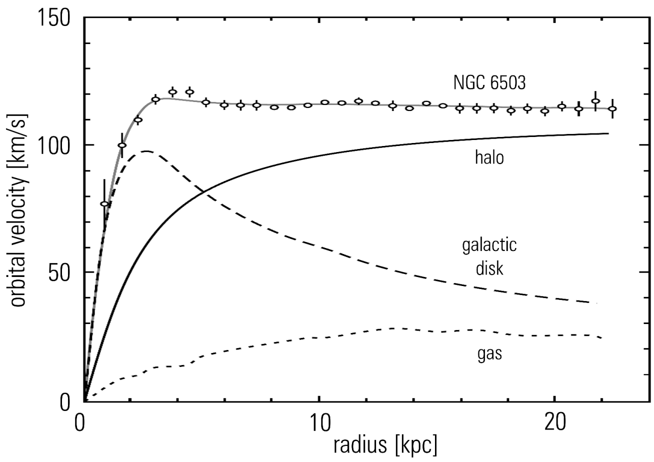

Figure 3.5: Measurement of the orbital velocities of stars in the galaxy NGC 6503. Also shown are the theoretical expectations of the disc alone, the dissipated gas, and a Dark Matter halo. Graph taken from Ref. [24], modified.

distribution of Dark Energy is supposedly uniform as a sort of vacuum energy, which explains its large abundance despite the extremely low density. [24]

Leaving the Dark Energy be, *this* work is a contribution to the continuing effort to unravel the mystery of the nature of non-baryonic Dark Matter, and to thereby help understanding the very substance of existence.

3.2.1 Observational evidence

The argument for Dark Matter had already been made in the 1930's by Swiss Astronomer F. Zwicky, stating that galaxies and clusters of galaxies, specifically the Coma Cluster, would require a large amount of invisible matter to explain certain gravitational behavior like internal rotations [69]. Evidence for the existence of Dark Matter, and for its density being larger than that of baryonic matter, are since then found all over cosmological observations. The most important of these observations are listed in the following.

Large scale structures

The universe is not homogeneous. When viewed on large scales, matter tends to cluster together, forming conglomerations of galaxies, which again form super-clusters and galaxy walls. On the largest scales, these clusters form so-called filaments, with massive voids in between. This "lumpiness" of the universe originates back to tiny quantum fluctuations in the energy distribution of the very, very young universe. These fluctuations should have been smoothed over by inflation. However, the structures that are visible today suggest substantial gravitational influence that can not possibly have been generated by visible matter only. [24]

Rotational curves of galaxies

Kepler's laws of motion dictate that the orbital velocity of objects orbiting a center of mass is proportional to the square root of the radius, $v \sim \sqrt{r}$. Measurements of the orbital velocities of stars in spiral galaxies have shown a very different, almost constant behavior, see Fig. 3.5, which could be explained by large amounts of invisible matter in a spherical halo surrounding the observed galaxies; see e.g. Ref. [70].

Interstellar gas clouds

When being gravitationally accelerated, interstellar gas clouds emit X-ray bremsstrahlung from which the temperature and mass density profile can be calculated. This allows for the calculation of the total mass density profile of the galaxy that these gas clouds sit in. In cases like the Bullet Galaxy Cluster, the center of mass determined from X-ray observations does not coincide with the center of mass of the visible, baryonic matter. [65]

Cosmic Microwave Background (CMB)

The CMB are photons thermally decoupled from the rest of the universe, meaning the rate of interaction which kept the photons in thermal equilibrium could not keep up with expansion, leaving them "adrift" in space (a process also known as *freeze-out*). This happened roughly 380,000 years [24] after the Big Bang. Earlier, when the universe was very young, the counter-play of gravitation and radiation caused by small density fluctuations in the hot plasma bath led to *acoustic oscillations* (matter waves). The oscillation patterns got imprinted into the CMB upon decoupling, and therefore measurements of the temperature anisotropies in the CMB today allow for conclusions about the geometry of the universe. Following Refs. [24, 65, 66], the geometry is directly linked to the *density parameter*

$$\Omega = \frac{\rho}{\rho_{\text{crit}}} \tag{3.48}$$

with the total mass density ρ and the critical mass density (critical energy density) [65]

$$\begin{aligned} \rho_{\text{crit}} &= \frac{3H_0^2}{8\pi G} \approx 10^{-29}\,\frac{\text{g}}{\text{cm}^3}, \\ \rho_{\text{crit}} c^2 &\approx 1\,\frac{\text{keV}}{\text{cm}^3}, \end{aligned} \tag{3.49}$$

which is the density that leads to a flat universe (and expansion would eventually come to halt); with the Hubble constant[21] H_0 and the gravitational constant G.[22] The density parameter can be expressed as the sum of several density parameters,

$$\Omega = \Omega_{\text{rel}} + \Omega_{\text{b}} + \Omega_{\text{DM}} + \Omega_{\Lambda}, \tag{3.50}$$

with the density parameter Ω_{rel} for light and relativistic particles such as neutrinos, Ω_{b} for baryonic matter, Ω_{DM} for (cold) Dark Matter, and Ω_{Λ} for Dark Energy. Due to the relation of the geometry and the density parameter, the terms of Eq. (3.50) can be inferred from measurements of the acoustic oscillations. The latest and most accurate CMB anisotropy measurements were taken by the PLANCK satellite [63].

[21]Following the symbol assignment in [66] with H for the Hubble parameter (Hubble expansion rate), H_0 for the present day value of H, and h for the reduced Hubble constant $h = H_0/100$. The value of H_0 has been measured many times in the recent years, with results between 67 and 77 $\frac{\text{km}}{\text{s Mpc}}$. The 2018 PLANCK mission determined $H_0 \simeq 67.4\,\frac{\text{km}}{\text{s Mpc}}$ [63].

[22]$G = 6.6742 \cdot 10^{-11}\,\frac{\text{m}^3}{\text{kg s}^2}$ [24]

Weak gravitational lensing

Following Ref. [65], a gravitational lens is a distant heavy cosmological object, e.g. a galaxy or galaxy cluster, in line of sight to a second, very bright object even further away, whose light is bend and distorted by the gravitational pull. If this effect is strong, multiple images or a so-called *Einstein ring* of the hidden object is produced, more or less concentric around the lens depending on the relative alignment. Weak gravitational lenses produce only distortions of the images that are difficult to detect in single cases, and are usually investigated in statistical analyses including many such lensing effects. The distortions depend on the total mass of the lens, which can then be reconstructed. Such observations revealed total masses much larger than the portion of visible matter in the lensing objects.

3.2.2 Candidates

The theories about the nature of Dark Matter are plenty and colorful. Some of them are able to account for all of Dark Matter, others offer an explanation only for parts of the predicted density, and therefore need be in some combination with other models. In the following, some of the most important candidates are listed (in alphabetical order), based on Refs. [24, 65], which are viable in light of the observational evidences (some more than others), and subjects of present day research.

In general one distinguishes *hot* and *cold Dark Matter* candidates. The terms refer to the temperature T_f of the remnant particles upon freeze-out, where hot particles are relativistic to the time of decoupling and $T_\mathrm{f} \gg m_\mathrm{DM}$, and vice-versa for cold particles (more on this in Sec. 3.2.3). The only hot Dark Matter candidate discussed here are the Standard Model neutrinos.

Axions

Axions are hypothetical light, weakly coupled elementary particles. Following Refs. [24, 65], they are postulated to solve the *strong CP problem* of QCD, the non-observation of CP violation to be exact, and are the result of an additional, spontaneously broken symmetry of the QCD Langrangian. The axion mass could lie somewhere in the range of μeV up to meV, and axions of certain masses can still viably account for all of the cold Dark Matter. However, no experimental evidence whatsoever has been found in their support. Possible attack points of detection include the decay of axions into two photons, or the photon-axion conversion in electromagnetic fields ("shine-through-the-wall" experiments).

Dark baryonic matter

The galactic halo does not contain objects of unknown nature entirely; baryonic matter is known to linger there in form of dark stellar objects. Measurements of our own galaxy suggest that their combined mass is not sufficient to explain rotational curves of galaxies or large scale structures, but they could account for some several percent of matter in the halo.

Following Refs. [24, 65], the term "dark stellar object", also known as MACHO (Massive Astrophysical Compact Halo Object), covers brown dwarfs, which are Jupiter-like gas balls with masses insufficient to ignite hydrogen burning; as well as neutron stars and black holes. The latter two are the results of Supernovae explosions. Extrapolating from the number of explosions observed throughout human history, it is unlikely that many such objects exist in the halo. Brown dwarfs, however, are assumed to be quite abundant. They can be detected by means of *microlensing*, an even weaker form of weak gravitational lensing that does not produce distinct distortions rather than increase the luminosity of a background object for a certain amount of time, depending on the dwarf's mass and alignment with the object. Nearby galaxies like the Magellanic Clouds or Andromeda are suitable background objects because they elevate beyond the galactic disk. For instance, the MACHO collaboration has observed about 15 [71] such microlensing events with the Large Magellanic Cloud.

Primordial black holes (PBHs)

In the last paragraph, black holes have been dismissed somewhat prematurely. Following Ref. [65], a special kind of so-far hypothetical *primordial black holes* (PBHs) is generated in the early universe by small density fluctuations, and hence does not require a dying star to be formed. Early universe here meaning the radiation-dominated era, hence PBHs are not considered (purely) baryonic. Their masses may range from µg to several thousand times the mass of the Sun, however certain mass ranges are constrained, e.g. by Hawking Radiation or microlensing. Even though viable mass ranges remain, PBHs are not considered to plausibly account for Dark Matter by themselves.

Standard Model neutrinos

Because of their abundance and unknown mass, the Standard Model neutrinos have long been considered good candidates for Dark Matter. But in light of recent experimental limits on the neutrino masses [72], the argument for their candidacy substantially lost in weight as well. Their combined mass can not possibly explain all of Dark Matter; furthermore, the large structures of the universe are unthinkable to have formed on the basis of hot relics alone. [24, 65]

Sterile neutrinos (and the seesaw mechanism)

Recalling Sec. 3.1.7, right handed neutrinos would be a very well motivated option for the SM neutrinos to obtain mass via the Higgs mechanism. The simplest generic extension of the Standard Model to achieve this introduces a fermion singlet (in *all* SM gauge group representations) with a variable number of generations as as the only new field. The singlet nature prohibits all gauge interactions for these fermions, hence the name *sterile neutrinos*.

Based on the explanations in Ref. [65], the introduction of the sterile neutrinos leads to a Majorana mass term in the Lagrangian. The Majorana mass matrix can be chosen to be diagonal, of the (simplified) form

$$M = \begin{pmatrix} 0 & y_N \langle H \rangle \\ y_N \langle H \rangle & M_N \end{pmatrix}. \tag{3.51}$$

with the Higgs VeV $\langle H \rangle$ and the new Yukawa coupling y_N, which enables an interaction of the new fermions with the Higgs and SM lepton fields, see Fig. 3.6. The mass eigenstates of the above matrix are

$$\lambda_\pm = \frac{M_N \pm \sqrt{M_N^2 + 4 \left(y_N \langle H \rangle \right)^2}}{2} \tag{3.52}$$

As long as $M \gg y_N \langle H \rangle$, the eigenvalues will be $\lambda_+ \approx M_N$ and $\lambda_- \approx -\left(y_N \langle H \rangle \right)^2 / M_N$. Hence, as long as the sterile neutrinos are *very* heavy, the light neutrinos can obtain the small mass eigenstates m_i that are in line with experimental evidence (*without* demanding extremely small Yukawa couplings, instead enabling a $y_N \langle H \rangle$ that fits the electroweak scale). The more M_N goes up, the more the m_i go down — like on a seesaw.

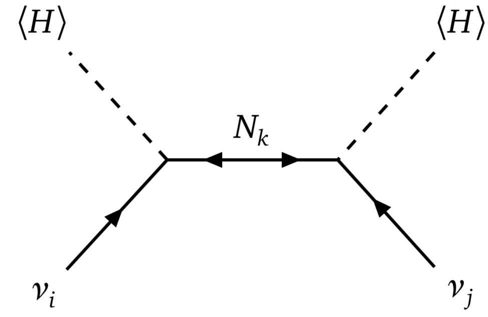

Figure 3.6: Neutrino mass generation with the type I seesaw mechanism, with the Higgs VEV $\langle H \rangle$, the SM neutrinos ν and the right handed Majorana neutrinos N.

The main and most obvious motivation for the Seesaw Model are the SM neutrino masses. But it is part of this list because it also comes with a Dark Matter candidate: At least three sterile neutrinos are required to explain the minimum of two observed SM neutrino masses, the lightest of which could, in principle, be Dark Matter. There are, however, a number of conditions: The mass of the Dark Matter candidate is constrained by the smallness of the SM neutrino masses, but at the same time a light N has to live long enough to be in line with observational evidence (in the Scotogenic Model this problem is solved by an additional symmetry that prevents the lightest new particle from decaying, but no such symmetry exists here), which dictates a mass in the keV range [65, 73].

What is explained above is also known as the type I seesaw mechanism. There are type II and type III seesaw mechanisms that offer two additional options for SM neutrino masses without loop corrections. They shall not be elaborated here, but more information can be found, for instance, in Ref. [55].

Weakly interacting massive particles (WIMPs)

WIMPs currently belong to the clear favorites of Dark Matter searches. As the name implies, they are massive and interact weakly; other than that there exists a generous flexibility when it comes to WIMP theories: From minimal, one-field extensions of the Standard Model to complex supersymmetric models, and everything in between. A wide range of masses is thinkable, the DM particle could be scalar or fermionic, there could be more than one species, and so on.

In Supersymmetry (following Ref. [24]), the elementary particles are ganged up in supermultiplets, where each SM lepton gets a quark partner and vice versa, called *squarks* and *sleptons*. The force carrier regime is extended in a similar way by the *gauginos*. Even though this makes for quite a rich field content, supersymmetric models are often considered favorable WIMP theories for their "symmetric aesthetics". The lightest of the supersymmetric particles would be stabilized by a new, conserved quantum number called *R-Parity,* and hence be the remnant Dark Matter particle to look for in experiments. The Large Hadron Collider (LHC) [59] at CERN has long been thought to be the machine that would finally produce and detect supersymmetric Dark Matter. These hopes have not been fulfilled until today, which is why Supersymmetry has since lost much of its former attraction.

Other approaches have been shifted into focus which aim not quite as high as Supersymmetry, which basically tries to solve all the problems of the universe at once. Among these approaches are *minimal models* that propose simple extensions to the Standard Model by adding only a few new fields, in a more bottom-up approach. The model studied in this work is such a minimal model.

Depending on the particular WIMP model, there are three general ways to probe them experimentally, as visualized in Fig. 3.8. One either generates them in particle colliders by e.g. proton-proton collisions and tries to detect the deficit in energy, as was attempted for Supersymmetry. Another technique dubbed *direct detection* is to let Dark Matter collide with regular matter and measure the recoil energy. And last but not least, one can look out for signals produced by decay or annihilation of Dark Matter in distant objects where they might be more abundant, without ever having to be in direct contact with it. This is called *indirect detection* and the basis for the analysis in this work. The three WIMP detection methods are explained in more detail in Sec. 3.8.

3.2.3 WIMP relic density

In general, the Dark Matter particle of a WIMP model is a remnant. The lightest neutral particle χ of the given model is stable, and all other dark sector particles have long disappeared from the world stage by decay. So χ has frozen out of thermal equilibrium as a cold relic. This means, on the one hand, that the available energy is not sufficient anymore for the annihilation diagram to go the other way and for χ to be produced; and on the other hand, that the number of remnant χ can only go in one direction — down, by means of annihilation. With the universal expansion, however, it gets more and more unlikely for a Dark Matter particle and its antiparticle to find each other and annihilate, so the number evolution is effectively halted. The (current) abundance or mass density of χ is called the *relic density* [24, 66]

$$\Omega h^2 = \frac{\rho_\chi}{\rho_{\text{crit}}} h^2, \tag{3.53}$$

using Eqs. (3.48) - (3.50). This is an important quantity, because it is well constrained by measurements of the CMB, recalling Sec. 3.2.1.

Freeze-out

In this paragraph, the process of WIMP freeze-out is described in more detail, based on Refs. [65, 74]. Other theories about the production of the relic density in the early universe exist, which shall not be elaborated here (see instead Ref. [65]).

When using the term "early universe" in a WIMP context, one usually means the time when Dark Matter was still in thermal equilibrium with the rest of the universe. Production and annihilation was kept in balance by collisions of particles and antiparticles,

$$\chi\bar{\chi} \leftrightarrow \text{SM}\,\overline{\text{SM}}. \tag{3.54}$$

The early-universe WIMP annihilation rate is given by

$$\Gamma = \langle \sigma v \rangle \, n_{\text{eq}} \tag{3.55}$$

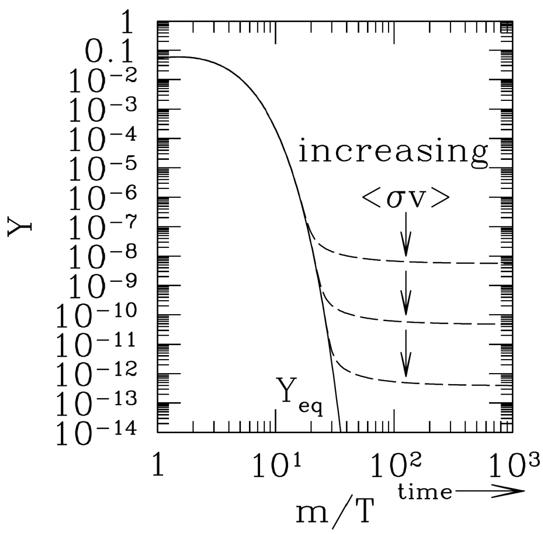

Figure 3.7: Freeze-out of thermal relics. The evolution of the co-moving number density Y over time (with decreasing temperature) is shown for three different thermally averaged annihilation cross sections. $Y_{\rm eq}$ corresponds to the number density for $x = 1$. Graph taken from Ref. [74].

with the equilibrium number density $n_{\rm eq}$. The expression $\langle\sigma v\rangle$ denotes the annihilation cross section times the relative velocity of the WIMPs, averaged over the WIMP thermal distribution, also called the *thermally-averaged annihilation cross section* ("times velocity" often omitted in literature). When Γ drops below the Hubble expansion rate H (meaning "the mean free path for WIMP-producing collisions became longer than the Hubble radius" [74]), χ is no longer in chemical equilibrium[23] — it has frozen out.

WIMPs are cold Dark Matter candidates, which, as briefly mentioned earlier, means that freeze-out happened in the cold regime with $T_{\rm f} \ll m_\chi$, so that

$$x \equiv \frac{m_\chi}{T_{\rm f}} \gg 1, \tag{3.56}$$

for cold Dark Matter, with the freeze-out temperature $T_{\rm f}$ and the Dark Matter mass m_χ. A development over x can be viewed as a development over time since $t \propto 1/T$. Using the entropy density s, one can now define the yield or *co-moving number density*[24]

$$Y = \frac{n}{s} = \frac{\rho_\chi}{m_\chi s}, \tag{3.57}$$

which relates to the relic density and $\langle\sigma v\rangle$ through [65, 74]

$$\Omega_\chi h^2 = \frac{m_\chi s Y}{\rho_{\rm crit}} h^2 = \frac{m_\chi \Gamma}{\langle\sigma v\rangle\, \rho_{\rm crit}} h^2. \tag{3.58}$$

The evolution of Y over x is shown in Fig. 3.7 for different $\langle\sigma v\rangle$, and demonstrates the nearly constant co-moving number density after freeze-out.

---

[23]Kinetic equilibrium ceases later, because particles can draw kinetic energy from the thermal bath to sustain production mechanisms for a while after chemical decoupling. [65]

[24]Co-moving coordinates: The coordinates of a stationary object in space stay the same within an expanding universe.

Co-annihilation

Based on Ref. [65], if one or more heavier dark particles have masses sufficiently similar to m_χ, the freeze-out process can be affected by co-annihilation, which can have significant impact on the relic density. Co-annihilating species change the effective annihilation cross section $\langle \sigma v \rangle$. The most intuitive assumption would be that an additional annihilation partner will result in a faster decrease of number density and hence a less abundant relic density; however that need not necessarily be the case. If the co-annihilation is less efficient than the self-annihilation, one can observe a dampening effect and a larger relic density. The Scotogenic Model, which is discussed extensively in the next chapter, is a candidate for such "parasitic" co-annihilation.[25]

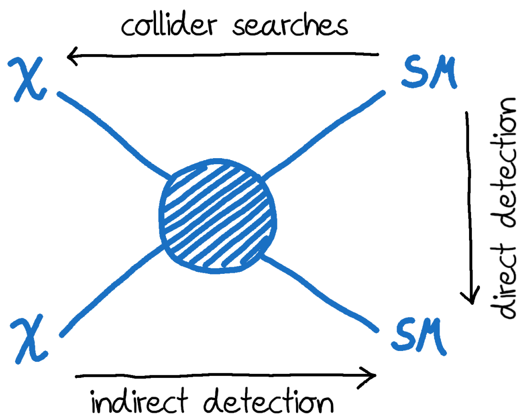

Figure 3.8: The three ways to search for WIMPs. This "Feynman diagram" visualizes approaches to detect DM particles (labelled with χ) from interaction with SM particles. Depending on the direction of reading, it describes the production of DM by colliding SM particles in collider searches (right to left), the scattering of DM with SM particles used for direct detection (top to bottom), and the annihilation of DM into SM particles used in indirect detection (left to right). The details of the middle part are model dependent.

3.2.4 Three recipes for WIMP detection

As mentioned earlier, the three "recipes" for WIMP detection can be summarized with the pseudo-Feynman diagram shown in Fig. 3.8. Depending on the reading direction, the diagram shows a different detection mechanism. This work focuses on the indirect detection of WIMPs (left to right in diagram) with the IceCube experiment. The results will be evaluated by means of comparison with other experiments, not only those which also use the indirect detection method. In this section, all three detection methods are introduced, with examples of past and present experiments.

Collider searches

Reading from right to left in the diagram, one obtains the recipe for collider searches, which are described in this section based on Refs. [65, 75]. In collider searches, Standard Model particles are being collided with high force to produce potential Dark Matter particles. Since those particles, should they have been successfully produced, leave no direct trace in the detector (somewhat similar to neutrinos), one tries to single out their potential creation through missing energy in the remaining particle tracks. This can be quite challenging, since especially in high-energy collisions, a huge number of particles are generated that need to be accounted for.

In order to interpret all the different energy signatures produced in a collision, one first needs some idea of what is being looked for. In general, there are two methods for making predictions: The *top-down* approaches, which try to explain the universe, more or less, all at

[25] The terms "parasitic" and "symbiotic" co-annihilation are adapted from Ref. [65].

once, and which require a rich particle content in the dark sector. An example is Supersymmetry, which was briefly described in Sec. 3.2.2. There are many supersymmetric models, and the procedure, in a nutshell, is this: Given a certain model with a certain number of parameters, one can simulate WIMP production events and define cuts; the same cuts applied to the background gives a signal-to-noise ratio as a basis to determine limits on the WIMP mass. The advantage here is the completeness of the model, and the simulations that can be built on this basis.

Then there are the *bottom-up* approaches, which can make do with a somewhat scantier Dark Matter particle content. Under the assumption that a DM-SM interaction happens in a different energy ballpark compared to the mass of mediating particle (i.e. the mediator is very heavy), *effective field theories* can be employed; approximations which allow for some ignorance concerning energy scales other than that of the interaction itself. (The Fig. 3.8 actually depicts a somewhat crude effective theory in which the interaction, including its mediator, is a "black box", and one only needs to care about the "end products" of the interaction.) If, on the other hand, the collider does reach energies with which the creation of such a mediator becomes possible, the effective theory does not suffice — and regarding the energies of present-day collider experiments, effective theories are therefore often unsuitable.

Simplified models offer a compromise between complete and effective theories, going a little bit beyond the DM candidate itself, e.g. making assumptions about the mediator or some simple field content extension. (The Scotogenic Model is such a simplified model, although the term *minimal model* will be used in the rest of this work instead.) Simplified models are designed to profit from the advantages of both a certain complexity that allows for some prediction of collider signatures, as well as a sufficient simplicity that prevents a search from being too narrow.

The **LHC** (Large Hadron Collider) [59] at CERN (Conseil Européen pour la recherche Nucléaire) in Switzerland is probably the best known example of a particle collider. With a circumference of 27 km, it is the largest of its kind. It is home to several nuclear research experiments, including ATLAS, ALICE, and CMS [76, 77, 78]. As the name implies, the LHC is a hadron collider, mostly producing proton-proton and heavy-ion-proton collisions.

The **LEP** (Large Electron-Positron Collider) experiment was the predecessor of the LHC at CERN, disassembled in the year 2000 so that the tunnel could be recycled for the LHC. As the name implies, it collided leptons instead of hadrons, and housed the ALEPH, DELPHI, OPAL and L3 detectors [79, 80, 81, 82].

Both the LHC and the LEP produced limits and constraints which are very important for this work, including the mass of the Higgs boson, and limits on the mass of dark charged and neutral scalars. These constraints are described in more detail in Sec. 4.3.

Direct detection

If read from top to bottom, the diagram shows the recipe for direct detection searches. The idea is that WIMPs can interact with Standard Model particles via elastic or inelastic scattering. Remnants of this scattering process, like recoil energy that is being released as photons, can be collected in e.g. scintillation detectors. One of the biggest challenges of direct detection searches is the background (mainly from radioactivity) which has to be suppressed very efficiently in order to single out the arguably very rare WIMP interaction events.

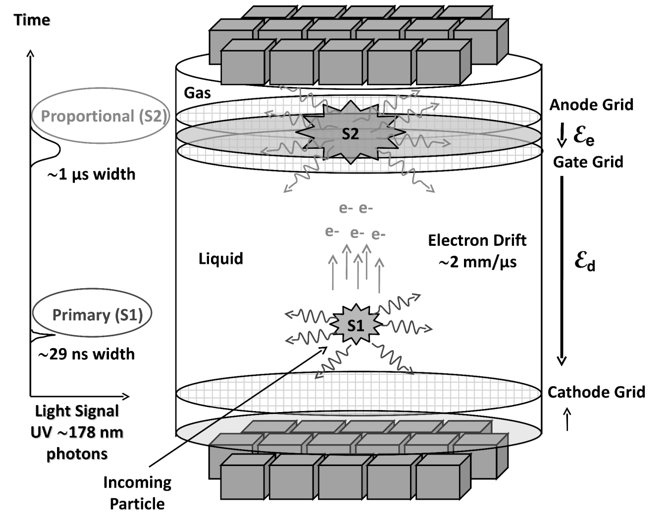

Figure 3.9: A dual-phase TPC as used in the XENON experiments. An incoming particle produces scintillation light in the liquid phase (S1). The electrons generated through ionization drift upwards in an electric field. They are accelerated further when entering the gaseous phase, exciting the atoms which produces a second optical signal (S2). Timing, location, and intensity of the two signals allow for the distinction of nuclear and electronic recoil interactions. Figure taken from Ref. [83].

The **XENON Dark Matter Project** [83, 84] relies on elastic DM-SM particle interactions. The centerpiece of the detector is a dual-phase time projection chamber (TPC). Top and bottom of the chamber are equipped with photomultiplier tubes. The target material is ${}^{54}_{131}$Xe, from which the experiment got its name. The inside of the chamber is filled with liquid xenon in the lower, and gaseous xenon in the upper phase. A (WIMP) elastic scattering event in the liquid phase leads to excitation and ionization of the xenon atoms. The scintillation light resulting from excitation is immediately detected as a first signal (S1), while the ionization-produced electrons “drift” upwards towards the gaseous phase in an electric field. Escaping the liquid phase, they are accelerated which excites the gaseous xenon, which produces a second scintillation flash (S2). The timing, location, and ratio of the two signals is used to identify the type of interaction: Electronic recoils are considered background from gamma- or beta particle interaction, while nuclear recoils could be the result of a scattering WIMP. Fig. 3.9 shows a sketch of the dual-phase TPC.

The choice of the noble gas xenon isotope has several advantages: For once, it is efficient to collect background photons from radioactive decays in the detector’s surroundings due to its high atomic charge, creating a relatively “quiet” zone in the center of the chamber (fiducial volume). Because of its high atomic number, it is also especially suitable for spin-independent WIMP-nucleon scattering which is proportional to A^2 (more on this in Sec. 3.2.6).

Located in the underground in the INFN Laboratori Nazionali del Gran Sasso, Italy, the experiment is quite efficiently shielded against cosmic rays. The main background arises from radioactive decays in the surrounding rock.

Starting with the prototype XENON10 in 2006, the experiment has since been upgraded several times, with XENON100, XENON1T, and the currently running detector, XENONnT (the figures behind “XENON” thereby stand roughly for the order of magnitude of liquid xenon mass employed in the respective version of the experiment; 10 kg, 100 kg, 1 t and “several” tons). [83]

A neighbor to the XENON Dark Matter Project is the **DAMA** observatory [85], located as well in the Laboratori Nazionali del Gran Sasso. In its latest DAMA/LIBRA (Large sodium Iodide Bulk for RAre processes) configuration, the direct detection experiment aims to find seasonal variations in the flux of Dark Matter particles in the galactic halo. The model independent seasonal variations arise due to the relative velocity of the Earth / the detector towards the WIMPs. Since the Sun moves as part of the galactic spiral arm, there is a time of the year when the Earth moves along "with" the Sun through space, and a time when it moves exactly against it, in which case the relative velocity to halo WIMPs is at its smallest point.

The target volume of the experiment consists of 25 sodium-iodide crystal scintillators with a total mass of roughly 250 kg, connected to photomultiplier tubes. The crystals are heavily shielded by several layers of different material, including the Gran Sasso rock itself, and housed in an isolated atmosphere. Scintillation light generated by WIMP-crystal scattering interactions are collected over the course of several years to search for the seasonal signal modulation.

The DAMA collaboration has claimed to have measured the seasonal variation [86, 87] and therefore to have directly detected Dark Matter for the first time. The results are disputed for the lack of full disclosure of analysis methods by DAMA, and because the results could not be reproduced so far, despite many attempts, for instance by the ANAIS and COSINE-100 [88, 89] collaborations.

The **PICO project** is another direct detection experiment located at SNOLAB in Canada, formed by a merger of the PICASSO (Project In CAnada to Search for Supersymmetric Objects) and COUPP (Chicagoland Observatory for Underground Particle Physics) collaborations [90, 91]. The experiment consists of a superheated bubble chamber filled with C_3F_8 as target material. The principle of bubble chambers relies on a fluid that is kept at a temperature just below the fluid's boiling point. A sudden reduction of pressure induced by a piston connected to the chamber puts the system into a superheated state. Particles entering the target liquid then produce a track of vaporized bubbles along their trajectory.

Temperature control for the PICO chamber is achieved by a water tank surrounding the stainless-steel pressure vessel. Several cameras point at the target fluid through glass windows in the walls of the chamber to photograph bubbles from particle interactions. Additionally, the vessel is equipped with piezoelectric acoustic sensors that can detect acoustic emissions of such events.

Similar to XENON, the project aims at detecting signals of nuclear recoils produced by scattering Dark Matter particles. The background from electronic recoil events is substantially smaller than in XENON, since the sensitivity to such interactions can be actively controlled by temperature and pressure inside the chamber.

Several iterations of the PICO project, each an improvement in target volume and measurement technique, have been taking data in the past; currently, PICO-40L is commissioned at SNOLAB, and an even larger PICO-500 is in the planning phase.

Indirect detection

Last but not least, from left to right in Fig. 3.8, the mechanism of indirect detection is shown. In a nutshell: WIMPs annihilate[26] into Standard Model particles, which can be detected directly or by means of their further decay products, e.g. photons or neutrinos. Since WIMP annihilation cannot be artificially enforced, one needs to wait for it to happen naturally. Regions of high Dark Matter density are hence of special interest. The center of the Milky Way is such a region,

[26]WIMPs could also decay instead of annihilate to produce a flux of Standard Model particles for indirect detection. This option is not further considered in this study, but investigated e.g. in Ref. [92].

or large celestial objects like the Sun in which WIMPs can accumulate due to the object's gravitational pull. Unfortunately, the particle detectors required to detect a Standard Model particle flux from such annihilation are still Earth bound (so far), and hence that flux needs to be sufficiently strong. So, an obvious advantage of indirect detection is that the physical presence of Dark Matter in the detector is not required, but on the flip side, the indirect messengers might have to hit quite the road.

Indirect detection of Dark Matter by means of neutrinos with IceCube is covered extensively in this work. The KM3NeT, ANTARES and AMANDA experiments, whose measurement principles were already introduced in Chp. 2, are more examples for potential indirect detection experiments using neutrinos. Therefore in the following, the focus lies instead on indirect detection using photons.

Gamma-ray photons can be used as messengers of WIMP annihilation. Projects operating in this realm are, for instance, the **H.E.S.S.** (High Energy Stereoscopic System) [93, 94] and **MAGIC** (Major Atmospheric Gamma Imaging Cherenkov Telescopes) [95, 96] telescopes, located in Namibia and the Canary Island of La Palma, respectively. When gamma rays produced in WIMP annihilation strike Earth's atmosphere, they produce a shower of secondary particles, the charged ones among them generating Cherenkov light. So instead of ice or water, H.E.S.S. and MAGIC use air as a Cherenkov medium. Observations are therefore limited to the night sky; with time, place and weather conditions that are dark enough for the Cherenkov light flashes to stand out. The instruments used for this purpose are large mirror telescopes usually arranged in array formation; five in the case of H.E.S.S, and two in the case of MAGIC.

Since gamma-rays are very efficiently blocked by the atmosphere, observations in the lower energy regime need to be conducted from space. One such instrument is the **FERMI** satellite. The low orbit satellite houses the LAT (Large Area Telescope) [97, 96], a track-chamber system combined with a crystal calorimeter and an array of photomultiplier tubes to detect individual gamma rays.

The case relevant for this study — the indirect detection by means of neutrinos from WIMP annihilation in the Sun — is described in detail in the next section.

3.2.5 Indirect detection of solar WIMPs

Indirect detection experiments share a common prerequisite, and that is an object as a source, that, for some reason or the other, accommodates a higher density of Dark Matter than "empty" space. Popular choices are the center of the Milky Way and the Sun, but also Earth and Jupiter. The idea with the latter three objects is that their mere movement through the Dark Matter halo necessarily has them "collide" with dark particles, which occasionally scatter with nuclei inside these objects. The Dark Matter particles loose energy in the process, until they can no longer escape the gravitational potential of that object, eventually sinking into its core, where they accumulate. This accumulation leads to a higher density of Dark Matter in the core, compared to the rest of the halo. It's easy to see that in such a region of abundance, a Dark Matter particle and its antiparticle are more likely to meet and annihilate, hence a boost

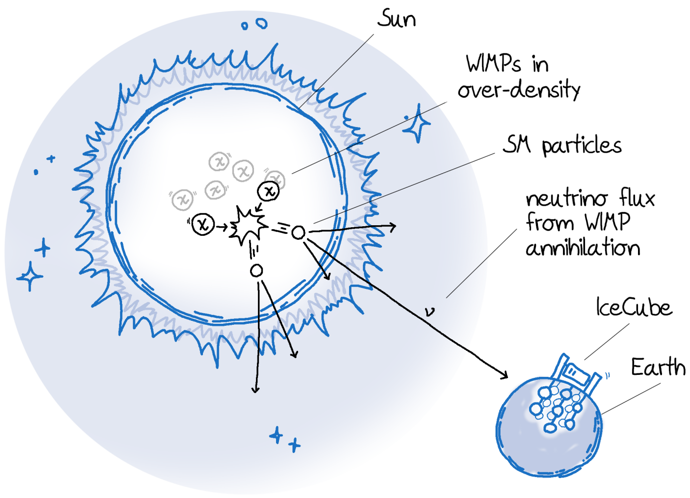

Figure 3.10: Neutrinos generated by WIMP annihilation in the Sun. WIMPS from the galactic halo scatter with nuclei in the Sun, forming an over-density in the core, where they annihilate into SM particles that further decay into neutrinos. Some of them may be detected at a certain neutrino telescope on Earth.

of annihilation signals from these sources is expected. An attempt to sketch this principle is made with Fig. 3.10.

The concept with the center of the Milky Way is slightly different; the higher Dark Matter density does not so much arise from scattering and accumulation, but is simply the integrated density along the line of sight. Assuming a spherical halo with a certain density profile, the direction of the galaxy's center provides the largest possible slice of the Dark-Matter-halo-cake.

In this work the focus lies on the Sun as the region of local Dark Matter over-density, which is described in more detail in the following, based on Refs. [65, 98].

Models that predict signals from annihilating WIMPs inside the Sun generally make two assumptions about WIMPs: First, in order to ensure accumulation inside the celestial body, WIMP scattering off of nuclei needs to be an allowed process, hence some interaction with the quark sector. And second, channels in which the WIMPs self-annihilate into Standard Model particles have to exist.

When both of these conditions are given — independent of the specific WIMP model — one has a continuous interplay of capture and self-annihilation of Dark Matter inside the core of the Sun. Or, to put it more scientifically, the number evolution of Dark Matter particles inside the effective volume is described by the differential equation [65]

$$\dot{N} = C_\chi - A_{\chi\chi}N^2 - EN \tag{3.59}$$

where C_χ is the **capture rate**, $A_{\chi\chi}$ is the depletion rate and E the evaporation rate. The latter can be neglected for the relevant WIMP masses in this work (more than a few GeV [65]). The relation defining the **annihilation rate** [65]

$$\Gamma_{\chi\chi} = \frac{1}{2}A_{\chi\chi}N^2 \tag{3.60}$$

lets one express the differential Eq. (3.59) by means of the two (for this study) most important quantities:

$$\dot{N} = C_\chi - 2\Gamma_{\chi\chi} \tag{3.61}$$

The capture rate is governed by the WIMP-nucleon scattering cross section which is highly model-dependent, and many different scenarios are possible. Depending on the framework, WIMPs can scatter off protons or neutrons, either elastically or inelastically or both, in a spin-dependent or spin-independent manner, all of which can affect the capture characteristics of a model. The total WIMP-nucleon scattering cross section is therefore hard-coded by the field content and the Lagrangian of a specific Dark Matter model. Hence measuring signals from WIMP annihilation in the Sun enables direct probing of this quantity (in contrast to studies regarding WIMP annihilation signals from the center of the Milky Way, for instance, which are merely sensitive to the annihilation cross section), which makes such studies comparable to direct detection methods.

The annihilation rate is, of course, directly affected by the annihilation cross section $\sigma_{\chi\chi}$ and the capture rate, and can be expressed by these quantities in the following way [65]:

$$\Gamma_{\chi\chi} = \frac{C_\chi}{2} \tanh^2\left(\sqrt{C_\chi \frac{\langle\sigma_{\chi\chi}\rangle}{V_{\text{eff}}} t}\right), \tag{3.62}$$

where V_{eff} is the effective volume of Dark Matter over-density, $\langle\sigma_{\chi\chi}\rangle$ is the velocity-averaged annihilation cross section, and t is the age of the Sun.

The equation simplifies immensely if the expression inside the parentheses becomes much larger than 1:

$$\tanh^2\left(\sqrt{C_\chi \frac{\langle\sigma_{\chi\chi}\rangle}{V_{\text{eff}}} t}\right) \longrightarrow 1 \ \text{ for } \ \sqrt{\frac{C_\chi \langle\sigma_{\chi\chi}\rangle}{V_{\text{eff}}} t} \gg 1 \tag{3.63}$$

This means that capture and annihilation reach **equilibrium**. This will happen eventually, always, if one waits long enough.[27] The more interesting models are generally those where equilibrium has already been established. (For the studies conducted in this work, the reader will see that some scenarios have reached equilibrium and others have not, where none of the scenarios belonging to the latter kind give rise to a neutrino flux in reach of IceCube). In capture-annihilation equilibrium one then has

$$\Gamma_{\chi\chi} = \frac{C_\chi}{2}, \tag{3.64}$$

so that the right-hand side of Eq. (3.61) vanishes, meaning no further number evolution of Dark Matter particles in the volume of local over-density in the Sun.

Now is a good time to address the question what those WIMPs are annihilating *into*. In general there are two possibilities from a neutrino telescope point-of-view: Annihilation directly into neutrinos, or annihilation into other Standard Model particles — most of which have neutrinos as their decay products. The first option would produce a neutrino line-signal roughly at the mass of the annihilating WIMPs, the latter would produce a continuous spectrum with a cut-off at the WIMP mass. Either way, there most likely will be a flux of neutrinos. A line spectrum would of course be convenient because it is easier to identify. In the framework of the Dark Matter model in this work however, direct annihilation into neutrinos is strongly suppressed, as explained in the next chapter.

The **neutrino flux** at Earth from WIMP annihilation in the Sun, differential in neutrino

[27]For further studies on capture-annihilation equilibrium in the Scotogenic Model see [99].

energy, is given by [98]

$$\frac{d\phi}{dE} = \frac{1}{4\pi d_{\odot}} \Gamma_{\chi\chi} \sum_{f} Br_{f\bar{f}} \frac{dN_f}{dE}, \tag{3.65}$$

with the distance $d_{\odot}$ of Sun an Earth, the branching fraction $Br_{f\bar{f}}$ of annihilation into the particle state $f\bar{f}$, and the corresponding differential neutrino spectrum $\frac{N_f}{dE_\nu}$. The sum over all final states f ensures that all possible annihilation channels are included.

The **expected number of signal events** can be calculated for different indirect detection experiments by multiplying the flux from Eq. (3.65) with the respective detector's effective area [98]:

$$\frac{dN}{dE_\nu} = t_e \left(\frac{d\phi_\nu}{dE} A_\nu(E) + \frac{d\phi_{\bar{\nu}}}{dE} A_{\bar{\nu}}(E) \right), \tag{3.66}$$

where $A_{\nu(\bar{\nu})}(E)$ are the energy-dependent neutrino (antineutrino) effective areas.

3.2.6 WIMP-nucleon scattering processes

As established over the last sections, scattering of Dark Matter particles with Standard Model particles is very important for indirect detection mechanisms. Thereby it is important to understand the details of such scattering processes. Low-mass Dark Matter particles, for instance, tend to scatter off the electrons in a target material. WIMPs in the GeV mass regime, as they are relevant for this study, scatter mostly with atomic nuclei.

The details of a DM-nucleus scattering process depend on the couplings. WIMPs can either couple to the nucleus via *nucleon number A*, meaning the number of protons and neutrons in (or simply the mass of) the nucleus. The DM-nucleus scattering cross section $\sigma_{\chi K}$ in this case scales linear with the DM-nucleon[28] scattering cross section $\sigma_{\chi N}$, and quadratic with A [100]. In case the WIMPs couple via the nucleon spin instead, the cross section is significantly smaller, since spins add up incoherently within the atomic nucleus (the spins "cancel each other out"). The first case is called **spin-independent** (SI), the latter **spin-dependent** (SD) scattering [65]:

$$\sigma_{\chi K,\mathrm{SI}} \sim \sigma_{\chi N} A^2, \qquad \sigma_{\chi K,\mathrm{SD}} \sim \sigma_{\chi N}. \tag{3.67}$$

The A^2 dependence in the spin-independent case greatly enhances the scattering rate for heavy target materials. This is the reason that many direct detection experiments, like XENON [83, 84], are much more sensitive to the spin-independent scattering cross section.

If the relevant scattering energies are high enough to probe the nucleus' structure, one has to take the constituent nucleons into account. The exact cross sections are then calculated after a three-step recipe, starting from the smallest constituents and ending with the atomic core (based on Refs. [65, 101, 100]):

1. Determine the WIMP-quark interactions, and formulate the non-relativistic limit (at small squared momentum transfer $\mathbf{q}^2$) of the relevant Lagrangian; meaning an effective interaction-level theory. This step reveals whether the total scattering cross section is spin-independent, spin-dependent, or the sum of both components. In the experimental physicist's nutshell: If axial parts of the Lagrangian survive the transition to the non-relativistic limit, one obtains a spin-dependent cross section component; if vector (or

[28] To avoid a mix-up: The term *nucleus* (plural nuclei) describes the core of an atom, while the term *nucleon* (plural nucleons) refers to one of its constituents, i.e. a proton or a neutron.

scalar) parts survive, one obtains spin-independent components.

2. Find the contributions of the quarks to the nucleon's mass and spin. This means to "sandwich" the quark operators found above into nucleon states, hence requires the calculation of the matrix elements like $\langle N|\bar{q}q|N\rangle$ (N being a neutron or proton), for all relevant quarks as parts of the total scattering amplitude.

3. The nucleus-level step can actually be divided into two separate steps:

   (a) Take into account the distribution of the nucleons in the atomic core for zero momentum transfer, $\mathbf{q} = 0$. This calculation is coherent, but differs for spin-dependent and spin-independent interactions. For the former, it is equivalent to taking the average spins of all protons $\langle S_p \rangle$ and neutrons $\langle S_n \rangle$; while for the latter it is sufficient to simply "count" the nucleons since, as mentioned earlier, spin-independent interactions couple to nucleus mass A.

   (b) Calculate the loss of coherence at non-zero momentum transfer, $\mathbf{q} > 0$. This is expressed by a *nuclear form factor F* that depends on the chosen nuclear model.

The total differential cross section is in general defined as [100]

$$\frac{d\sigma}{d\,|\mathbf{q}|^2} = \frac{\sigma_0}{4\mu^2 v^2} F^2\left(|\mathbf{q}|\right) \tag{3.68}$$

with the cross section at zero momentum transfer σ_0, the reduced mass $\mu = m_N m_\chi / \left(m_N + m_\chi\right)$ and the WIMP-target relative speed v. The quantity σ_0 carries all information obtained in steps 1 through 3 a), while the form factor F is the result of step 3 b). The total cross section is the integral of Eq. (3.68) over all momentum transfers.

Chapter 4
The Scotogenic Model

As the reader learned in the previous chapter, our solar system moves through space, "collecting" WIMPs like a giant fishing net, and the WIMPs can then accumulate in large bodies like the Sun. They eventually annihilate into Standard Model particles that further decay into neutrinos. As the largest neutrino telescope in the world, the IceCube Observatory is predestined to search for these neutrinos from WIMP annihilation inside the Sun.

The description of Dark Matter accumulation and annihilation processes requires the formulation of an underlying theoretical model, upon which predictions for observable neutrino fluxes can be made. Many approaches to such models exist. The model this work focuses on is called the *Scotogenic Model*. The catchy name "scotogenic" (a combination of the greek words σκοτος, "darkness" and γενης, "offspring, kind" that roughly translates to "made from the darkness") describes a simple but effective extension to the Standard Model, first proposed by E. Ma in Ref. [102]. It belongs to the class of *radiative seesaw minimal Dark Matter models*. The term "radiative seesaw" refers to the neutrino mass generation in a seesaw-similar manner by Higgs interactions including heavy right-handed neutrinos, although not on tree level but by means of loop corrections. Different radiative models are discussed for instance in [103, 104]. The Scotogenic Model stands out among other radiative models through its particularly simple field content that still offers wildly interesting phenomenology, like a natural Dark Matter candidate as well as the aforementioned neutrino mass generation.

This chapter is organized as follows: Model characteristics, including the field content and possible Dark Matter particles, are explained in Sec. 4.1. The process of WIMP capture and annihilation inside the Sun is discussed in Sec. 4.2. Constraints of theoretical and experimental nature are listed in Sec. 4.3. Observables of exemplary scotogenic scenarios are shown and discussed in Sec. 4.4. In Sec. 4.5, the concept of parameter scans and the computational methods are introduced. The following subsections contain descriptions and results of: A first parameter scan conducted in order to make predictions about the model potential in terms of expected event rate in the IceCube detector; a second scan with the attempt to better exploit the viable parameter space of the model using enforced scalar-fermion co-annihilation; a third parameter scan, based on the concept of inelastic scattering, and a fourth and final scan combining inelastic scattering with co-annihilation. Sec. 4.6 gives a summary and discussion of the findings.

The work presented in this chapter is the result of close collaboration with Thede de Boer and Sybrand Zeinstra. Our work has been previously published in two articles and one proceedings contribution, see Refs. [105, 106, 107]. The portions of the work that are predominantly my contribution to this joined effort are indicated specifically throughout this chapter.

4.1 Model characteristics

4.1.1 Lagrangian and field content

The Scotogenic Model [102] extends the Standard Model by two new fields: One Majorana fermion singlet N_i with three generations, and one scalar doublet η with the components $\left(\eta^+, \eta^0\right)$. Both new fields are singlets under the $SU(3)$, as is the case for all new fields in the class of radiative seesaw models. The field content is summarized in Tab. 4.1.

Besides the new fields, a discrete global symmetry is added. Under this $\mathbb{Z}_2$ symmetry, all dark sector fields are charged "odd" (receive the quantum number of −1), while all Standard Model particles are charged "even" (+1); which in literature is sometimes described as "R-Parity being conserved". It prohibits uneven numbers of new particles in interaction vertices, with the effect that new particles can not decay into Standard Model particles (they can, however, annihilate, since two is an even number). This is a very important feature, because this automatically ensures the stability of the lightest new particle. This lightest new particle is the natural Dark Matter candidate of the Scotogenic Model — provided that it is electrically neutral.

The new symmetry has an additional impact on the scotogenic phenomenology: Neutrino mass generation via a Higgs mechanism in a type I seesaw fashion is not possible. This is where the model becomes *radiative*. A closer look at this will be taken in Sec. 4.1.2.

The Lagrangian of the Scotogenic Model, including the new kinetic terms, reads [102]

$$
\begin{aligned}
\mathcal{L}_{\mathrm{Sc}} \quad \supset \quad & \left(D_\mu \eta\right)\left(D^\mu \eta^\dagger\right) + \bar{N} \gamma_\mu \partial^\mu N && \text{kinetic terms} \\
& - \frac{m_{N_i}}{2} \bar{N}_i N_i && \text{Majorana mass} \\
& + y_{i\alpha} \left(\eta^\dagger L_\alpha\right) N_i + \text{h.c.} && \text{Yukawa term} \\
& \left.\begin{aligned}
& - m_\phi^2 \phi^\dagger \phi - m_\eta^2 \eta^\dagger \eta - \frac{\lambda_1}{2}\left(\phi^\dagger \phi\right)^2 - \frac{\lambda_2}{2}\left(\eta^\dagger \eta\right)^2 \\
& - \lambda_3 \left(\phi^\dagger \phi\right)\left(\eta^\dagger \eta\right) - \lambda_4 \left(\phi^\dagger \eta\right)\left(\eta^\dagger \phi\right) \\
& - \frac{\lambda_5}{2}\left[\left(\phi^\dagger \eta\right)^2 + \left(\eta^\dagger \phi\right)^2\right]
\end{aligned}\right\} && \text{scalar potential}
\end{aligned}
\tag{4.1}
$$

where m_{N_i} is the Majorana mass matrix of the new fermion, and m_η is the mass parameter of the scalar. The L_α is the left-handed Standard Model lepton doublet with $\alpha = 1, 2, 3$ generations, $y_{i\alpha}$ is a new Yukawa coupling matrix where $i = 1, 2, 3$ are the generations of N. The Standard Model Higgs field is denoted by ϕ, and the λ_{1-5} are the new scalar couplings.

After electroweak symmetry breaking (ESWB), the scalar sector gives rise to the Higgs boson h and four new physical particles, so that the total new particle content of the Scotogenic Model reads

$$
\underbrace{N_1, N_2, N_3,}_{\text{fermionic}} \quad \underbrace{\eta^\pm, \eta^{0\mathrm{R}}, \eta^{0\mathrm{I}},}_{\text{scalar}}
\tag{4.2}
$$

with the charged scalars $\eta^\pm$, and the neutral scalars $\eta^{0\mathrm{R}}$ and $\eta^{0\mathrm{I}}$ (the real and imaginary parts of the neutral doublet component $\eta^0 = \left(\eta^{0\mathrm{R}} + i\eta^{0\mathrm{I}}\right)/\sqrt{2}$). Due to their singlet nature, the N_i do not mix among each other, and the mass eigenstates remain exactly $N_{1,2,3}$. The masses of the

Table 4.1: Field content of the Scotogenic Dark Matter Model. Listed are the number of generations i.e. "copies" of each field, the spin and the related representation of the Lorentz group, as well as the gauge group representations that each field transforms under. Empty cells mean that the field is not charged/transforms as a singlet under the corresponding gauge group. The last column contains the charge under the additional new global symmetry under which the new fields are odd (−1) and all SM fields are even (+1). [102, 55]

Field	Generations	Spin	Lorentz rep.	$SU(3)$	$SU(2)$	$U(1)$	$\mathbb{Z}_2$
SM fields (Tab. 3.1)							1
η	1	0	$(0,0)$		2	1	−1
N	3	1/2	$(1/2, 0)$				−1

physical scalar bosons are given by [102]

$$\begin{aligned} m^2_{\eta^\pm} &= m^2_\eta + \frac{1}{2}\lambda_3 \langle\phi^0\rangle^2, \\ m^2_{\eta^{0\mathrm{R}}} &= m^2_\eta + \frac{1}{2}\left(\lambda_3 + \lambda_4 + \lambda_5\right)\langle\phi^0\rangle^2, \\ m^2_{\eta^{0\mathrm{I}}} &= m^2_\eta + \frac{1}{2}\left(\lambda_3 + \lambda_4 - \lambda_5\right)\langle\phi^0\rangle^2, \end{aligned} \tag{4.3}$$

where $\langle\phi^0\rangle = 246.22\,\mathrm{GeV}/\sqrt{2}$ is the vacuum expectation value (VEV) of the Higgs field [5]. As can be seen in the above equation, the $\eta^{0\mathrm{R}}$ and $\eta^{0\mathrm{I}}$ obtain different masses through their coupling $\lambda_3 + \lambda_4 \pm \lambda_5$. This particular feature proofs to be very important to this study, as will be argued later.

4.1.2 Neutrino masses

As already mentioned shortly in the previous section, neutrino mass generation is not possible at tree level due to the global $\mathbb{Z}_2$ symmetry that prohibits an odd number of new particles in an interaction vertex. The solution is that neutrino masses are generated in a loop, which is the name-giving process for the class of radiative seesaw models. In the Scotogenic Model, this loop is of topology *T3-B*, after the classification in Ref. [103]. The corresponding diagram is shown in Fig. 4.1.

The new fermion field N, which takes the role of the right-handed neutrinos, can not couple to the Standard Model Higgs field ϕ directly, instead a detour with the "new Higgs field"[1] η, which acts as a mediator, is required. The reason that we can still speak of a seesaw mechanism, is that the eponymous seesaw concept still holds true: The left-handed neutrinos obtain small masses determined by the heavy right-handed neutrinos and small coupling strengths. (A brief introduction to the type I seesaw mechanism is given in Sec. 3.2.2.)

The couplings responsible for this effect are λ_5 and the Yukawa matrix $y_{i\alpha}$. The Standard Model neutrino masses are connected to the masses of the dark sector particles by the relation

$$(m_\nu)_{\alpha\beta} = \left(y^T \Lambda y\right)_{\alpha\beta}, \tag{4.4}$$

[1]The new scalar field does not actually have "Higgs character", since it does not obtain a vacuum expectation value. This is another effect of the new $\mathbb{Z}_2$ symmetry. For this purpose the symmetry would have to be spontaneously broken (see Sec. 3.1.5), which it is not.

where Λ is a diagonal mass matrix with the eigenvalues [102]

$$\Lambda_i = \frac{m_{N_i}}{32\pi^2}\left[\frac{m^2_{\eta^{0R}}}{m^2_{\eta^{0R}} - m^2_{N_i}} \log\left(\frac{m^2_{\eta^{0R}}}{m^2_{N_i}}\right) - (\mathrm{R} \leftrightarrow \mathrm{I})\right]. \tag{4.5}$$

The expression (R $\leftrightarrow$ I) here means that this term is the same as the other one inside the square brackets, but with interchanged η^{0R} and η^{0I}. Here, λ_5 comes into play: Recalling Eq. (4.3), one sees that the mass difference of η^{0R} and η^{0I} is determined by λ_5. Hence Eq. (4.5) vanishes if and only if $\lambda_5 = 0$. In other words: A mass splitting of the two neutral scalar particles inevitably leads to non-zero neutrino masses. Hence the value of λ_5 is naturally small.

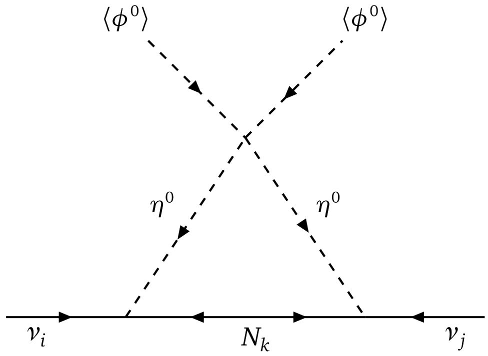

Figure 4.1: Process of the one-loop generation of neutrino masses in the Scotogenic Model, with the SM neutrinos ν, the SM Higgs VEV $\langle\phi^0\rangle$, and N and η^0 as dark sector fermions and scalar, respectively.

4.1.3 Dark Matter candidate

The lightest neutral particle of the Scotogenic Model is stable due to conservation of R-parity. Out of the seven physical particles presented above, each of the electrically neutral η^{0R}, η^{0I} and N_i is a possible Dark Matter candidate; whichever of them happens to be the lightest. That means the Scotogenic Model provides both possibilities of fermion and scalar Dark Matter.

The problem with fermion Dark Matter in the Scotogenic Model: Due to their singlet nature, the N_i have no direct couplings to the Higgs. Furthermore, the N_i are completely uncharged under the Standard Model gauge groups, and as one can see in the Lagrangian Eq. (4.1), no interaction with the gauge fields is present. However, as the reader will see in a bit, scattering with nuclei inside the Sun requires the interaction with either the h or the Z^0. Hence for fermion Dark Matter, no scattering with nuclei would be possible (and subsequently no neutrino fluxes that are measurable with IceCube).

That leaves the two neutral scalars η^{0R} and η^{0I}. Both cases, one in which η^{0R} is the DM candidate and η^{0I} its heavier state, and vise versa, are possible. As can be seen in Eq. (4.3), this depends solely on the sign of λ_5, the choice of which has no impact on the phenomenology of the model.

For scalar Dark Matter, things look a little more rosy than for fermion Dark Matter. Scalar Dark Matter *does* scatter with nuclei and can accumulate in the Sun. Therefore we choose the Scotogenic Model in a scalar Dark Matter configuration for this work.

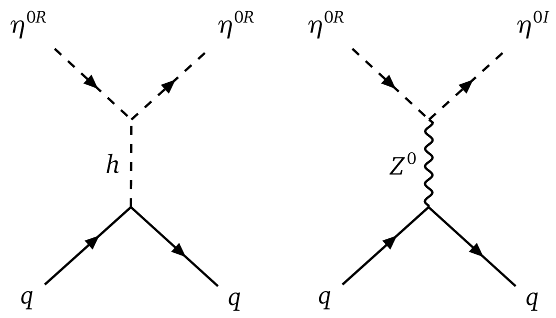

Figure 4.2: Feynman diagrams of scalar DM-nucleon scattering processes in the Scotogenic Model, in the elastic (left) and inelastic cases (right). Both diagrams contribute to the spin-independent scattering cross section. The $\eta^{0\mathrm{R}}$ takes the deputy role as the DM candidate and $\eta^{0\mathrm{I}}$ as the heavier state, however switched roles of $\eta^{0\mathrm{R}}$ and $\eta^{0\mathrm{I}}$ are just as possible.

4.2 Capture and annihilation

4.2.1 Dark Matter – nucleon scattering

When WIMPs undergo scattering processes with nuclei inside the Sun, they may at some point have lost so much energy that they no longer can escape from the Sun's gravity well. They are then captured, and slowly sink further and further towards the core. How many WIMPs are being captured per time unit is measured by the capture rate. The nature of the WIMP-nucleon scattering impacts the capture rate directly.

Scalar Dark Matter can scatter with nuclei via the two interactions shown in Fig. 4.2. The more intuitive one is the elastic spin-independent scattering with the Higgs mediator in the left diagram. However, there is another, Z^0-mediated inelastic spin-independent option, shown in the right diagram. Inelastic in this case simply means that the particle state changes in the interaction, from the Dark Matter candidate into the heavier state ("up-scattering"), while in the elastic case, the in- and out-going particles are the same. This inelastic scattering phenomenology has not been investigated before in the framework of the Scotogenic Model with regard to indirect detection rates, and is the central point of study in this work.

The mass splitting between the Dark Matter candidate and its heavier state,

$$\delta = \left| m_{\eta^{0R(I)}} - m_{\eta^{0I(R)}} \right| , \tag{4.6}$$

is the key feature which enables inelastic scattering in the Scotogenic Model. It is governed by the model parameter λ_5 (from here on also called *mass splitting parameter*), compare Eq. (4.3). As mentioned above, inelastic scattering is kinematically constrained, and only possible for mass splittings that fulfill [108]

$$\delta < \frac{\mu v^2}{2} = \frac{v^2}{2} \frac{m_{\mathrm{DM}} m_N}{(m_{\mathrm{DM}} + m_N)}, \tag{4.7}$$

(in other words, the kinetic energy in the center of mass frame must bridge the inelastic "gap") where μ is the DM-nucleon reduced mass, and v being the relative velocity. With Eq. (4.3) and the fact that λ_5 is naturally small (as argued in Sec. 4.1.2), the mass splitting can be approximated by

$$\delta \approx \frac{\lambda_5 \langle \phi^0 \rangle^2}{m_{\mathrm{DM}}} \tag{4.8}$$

via Taylor expansion. Details of the elastic and inelastic scattering processes are presented in the following.

Elastic scattering

For the formulation of the elastic scattering process we follow mainly Refs. [100, 109]. As can be seen in Fig. 4.2 a), elastic scattering is h-mediated. The relevant Lagrangian of DM-quark interaction is [109]

$$\mathcal{L}_{\text{el}} = -\frac{1}{2} g_{\eta^{0\text{R}}\eta^{0\text{R}}h} \left(\eta^{0\text{R}}\right)^2 h - g_{\bar{q}qh} \bar{q} q h, \tag{4.9}$$

with $\eta^{0\text{R}}$ being the Dark Matter candidate ($\eta^{0\text{R}}$ and $\eta^{0\text{I}}$ can be switched out for one another as Dark Matter candidates). Following the recipe for cross section calculations in Sec. 3.2.6, Eq. (4.9) is transitioned to the non-relativistic limit by integrating out the mediator h in a first step. The effective Lagrangian and the effective coupling read [100, 109]

$$\mathcal{L}_{\text{eff}} = \frac{1}{2} a_q 2 m_{\eta^{0\text{R}}} \left(\eta^{0\text{R}}\right)^2 \bar{q} q, \tag{4.10}$$

$$a_q \equiv \frac{g_{\eta^{0\text{R,I}}\eta^{0\text{R,I}}h}\, g_{\bar{q}qh}}{2 m_{\eta^{0\text{R,I}}} m_h^2}. \tag{4.11}$$

The couplings $g_{\eta^{0\text{R,I}}\eta^{0\text{R,I}}h} = (\lambda_3 + \lambda_4 \pm \lambda_5) \langle \phi^0 \rangle \sqrt{2}$ and $g_{\bar{q}qh} = y_q/\sqrt{2}$ are fixed by the high-energy Lagrangian. The $y_q = m_q/\langle \phi^0 \rangle$ is the Standard Model quark Yukawa coupling that is calculated using the model building tool SARAH (see Sec. 4.5.1).

As a second step, the quark contributions to the elastic scattering amplitude

$$\mathcal{M} = 2 m_{\eta^{0\text{R}}} m_N \sum_q a_q \left\langle N | \bar{q} q | N \right\rangle \tag{4.12}$$

off a nucleon N are calculated, with the proton or neutron mass m_N. For light ($q = u, d, s$) and heavy quarks ($Q = c, b, t$) with masses m_q and m_Q, the matrix elements read [100, 109]

$$\begin{aligned} m_q \left\langle N | \bar{q} q | N \right\rangle &= m_N f_q^{(N)}, \\ m_Q \left\langle N | \bar{Q} Q | N \right\rangle &= \frac{2}{27} m_N \left[1 - \sum_{q=u,d,s} f_q^{(N)} \right]. \end{aligned} \tag{4.13}$$

The $f_q^{(N)}$ are the scalar quark form factors for which the default values in micrOMEGAs are used [110, Tab. 2]. This leads to the proton (neutron) effective coupling

$$\frac{f_{p(n)}}{m_{p(n)}} = \sum_q f_q^{p(n)} \frac{a_q}{m_q} + \frac{2}{27} \left[1 - \sum_q f_q^{p(n)} \right] \sum_Q \frac{a_Q}{m_Q}. \tag{4.14}$$

For the final step in the calculation, one formulates the cross section at zero momentum transfer ($\mathbf{q} = 0$). Because this is a spin-independent interaction that couples to the mass of the nucleus A, one obtains [100, 109]

$$\sigma_0 = \frac{\mu^2}{\pi} \left[Z f_p + (A - Z) f_n \right]^2 \tag{4.15}$$

with the number of protons Z, the number of neutrons $A - Z$, and the reduced mass μ. For the $\mathbf{q} > 0$ transition one evaluates Eq. (3.68) by choosing a nuclear form factor. Here, we use the Gaussian form factor [100], implying a Gaussian density profile of the nucleus:

$$F^2(Q) = \exp\left(-Q/Q_0\right), \tag{4.16}$$

with the energy transfer $Q = |\mathbf{q}|^2/(2m_A)$. The energy transfer (recoil energy) ranges from $Q_{\mathrm{min}} = 0$ to $Q_{\mathrm{max}} = 4\mu^2 v^2/(2m_A)$, with $Q_0 = 3/\left(m_A R^2\right)$ and the radius of the nucleus

$$R = \left[0.91\left(\frac{m_A}{\mathrm{GeV}}\right)^{\frac{1}{3}} + 0.3\right] \times 10^{-13}\,\mathrm{cm}. \tag{4.17}$$

Choosing a Gaussian form factor speeds up the numerical scans significantly, because it allows for an analytical calculation of the scattering cross section.

Inelastic scattering

The same three-step recipe from Sec. 3.2.6 is applied for inelastic scattering, again following mainly Refs. [100, 109]. First, the relevant Lagrangian is identified. As shown in Fig. 4.2, inelastic scattering is Z^0-mediated [109]:

$$\mathcal{L}_{\mathrm{inel.}} = g_{\eta^{0\mathrm{R}}\eta^{0\mathrm{I}}Z^0}\left(\eta^{0\mathrm{R}}\partial^\mu\eta^{0\mathrm{I}} - \partial^\mu\eta^{0\mathrm{R}}\eta^{0\mathrm{I}}\right)Z^0_\mu + g_{\bar{q}qZ^0}\bar{q}\gamma^\mu q Z^0_\mu. \tag{4.18}$$

No elastic scattering is present for this interaction. In the non-relativistic limit, the axial part of $\bar{q}qZ^0$ disappears, hence the remaining vector interaction is spin-independent. The $SU(2)_L \times U(1)_Y$ gauge couplings g and g', their ratio $\tan\theta_W = s_W/c_W = g'/g$, as well as the quark weak isospin $I_q = \pm 1/2$ and the fractional charge $e_{u,d} = (2/3, -1/3)$ fix the two couplings $g_{\eta^{0\mathrm{R}}\eta^{0\mathrm{I}}Z^0} = ig/(2c_W)$ and $g_{\bar{q}qZ^0} = g\left(I_q - 2e_q s_W^2\right)/(2c_W)$. They are obtained using the tool SARAH [111]. The effective Lagrangian and effective coupling read [109]

$$\mathcal{L}_{\mathrm{eff}} = -b_q\left(\eta^{0\mathrm{R}}\partial_\mu\eta^{0\mathrm{I}} - \partial_\mu\eta^{0\mathrm{R}}\eta^{0\mathrm{I}}\right)\bar{q}\gamma^\mu q, \tag{4.19}$$

$$b_q \equiv \frac{g_{\eta^{0\mathrm{R}}\eta^{0\mathrm{I}}Z^0}\,g_{\bar{q}qZ^0}}{m_Z^2}. \tag{4.20}$$

The second step of the calculation is again the formulation of the scattering amplitude by determining the quark contribution matrix elements (where the scalar-four momenta add up to $p_\mu^{\eta^{0\mathrm{R}}} + p_\mu^{\eta^{0\mathrm{I}}} \approx 2m_{\eta^{0\mathrm{R,I}}}\delta^0_\mu$):

$$\mathcal{M} = 4m_{\eta^{0\mathrm{R}}}m_N\sum_q b_q\delta^0_\mu\left\langle N|\bar{q}\gamma^\mu q|N\right\rangle. \tag{4.21}$$

Only valence quarks (u, d) contribute to vector interactions, and they add up coherently [100]. So the matrix elements read

$$2m_N\left\langle N|\bar{q}\gamma^\mu q|N\right\rangle = n_q\bar{u}_N\gamma^\mu u_N \approx n_q 2m_N\delta^\mu_0, \tag{4.22}$$

and the proton and neutron couplings considering all relevant quark contributions simply are

$$b_p = 2b_u + b_d, \qquad b_n = b_u + 2b_d. \tag{4.23}$$

Table 4.2: Overview of the different WIMP-nucleon scattering cross sections present in the Scotogenic Model.

	mediator	$\sigma_p(SI)$	$\sigma_n(SI)$	$\sigma_p(SD)$	$\sigma_n(SD)$
elastic scattering	h	✓	✓, $\sim \sigma_p(SI)$	—	—
inelastic scattering	Z^0	✓	✓	—	—

In contrast to the scalar interaction in the elastic case, the vector interaction for inelastic scattering introduces a significant difference for proton and neutron scattering amplitudes.

The third step is again the transition to the whole nucleus. Like in the elastic case, the interaction is spin-independent, so it is sufficient to consider the masses within the nucleus. The zero momentum cross section therefore is [109]

$$\sigma_0 = \frac{\mu^2}{\pi}\left[Zb_p + (A-Z)\,b_n\right]^2, \tag{4.24}$$

very similar in form to the elastic zero momentum cross section. We use again the Gaussian form factor for the transition to $\mathbf{q} > 0$ with Eq. (3.68). The inelasticity enters through the integration boundaries [112, 113, 114]

$$\begin{aligned} Q_{\min} &= \frac{1}{2} m_{\eta^{0\mathrm{R,I}}} v^2 \left(1 - \frac{\mu^2}{m_A^2}\left(1 + \frac{m_A}{m_{\eta^{0\mathrm{R,I}}}}\sqrt{1 - \frac{2\delta}{\mu v^2}}\right)^2\right) - \delta, \\ Q_{\max} &= \frac{1}{2} m_{\eta^{0\mathrm{R,I}}} v^2 \left(1 - \frac{\mu^2}{m_A^2}\left(1 - \frac{m_A}{m_{\eta^{0\mathrm{R,I}}}}\sqrt{1 - \frac{2\delta}{\mu v^2}}\right)^2\right) - \delta, \end{aligned} \tag{4.25}$$

δ being the scalar mass splitting.

The Z^0 boson mediation of the inelastic process leads to much larger cross sections than in the elastic h-mediated case. The reason is that Z^0 boson mediation is governed by Standard Model gauge couplings, which are significantly larger than the new couplings that take part in the h-mediation; and, since the gauge couplings are known and fixed, the inelastic cross sections will take more or less constant values of $\sim 1.7 \cdot 10^{-4}$ pb for all scotogenic scenarios in which inelastic scattering exists. The different WIMP-nucleon scattering cross sections present in the Scotogenic Model are summarized in Tab. 4.2.

4.2.2 Capture rate

Following Refs. [112, 113, 114, 115], the cross sections enter the Dark Matter capture rate through Ω_v^-. This is the rate with which Dark Matter particles scatter off nuclei to below the escape velocity $v(r)$ of the Sun at shell radius r, and it is defined by:

$$\Omega_v^- = \frac{2 m_A n_A \sigma_0 w}{4\mu^2 v^2} \int\limits_{Q'_{\min}}^{Q'_{\max}} dQ F^2(Q), \tag{4.26}$$

with the total scattering rate $n_A \sigma_A^0 w$, where n_A is the number density of nucleus A inside the Sun, and

$$w = \sqrt{u^2 + v(r)^2} \tag{4.27}$$

describes the Dark Matter particle velocity after it has entered the gravitational potential of the Sun, while u is the particle velocity at infinite distance. The escape velocity scattering rate enters the Dark Matter capture rate per unit shell volume in the following way:

$$\frac{dC}{dV} = \int_0^\infty du \frac{f(u)}{u} w \Omega_v^-(w), \tag{4.28}$$

with $f(u)$ being the Dark Matter velocity distribution outside the gravitational potential of the Sun, which we assume to follow the Maxwell-Boltzmann distribution.

The condition for a DM particle to be captured is an energy transfer of

$$Q_{\text{cap}} > \frac{1}{2} m_{\eta^{0\text{R,I}}} \left(w^2 - v(r)^2\right) - \delta, \tag{4.29}$$

so that the effective lower boundary is $Q'_{\text{min}} = \max\left(Q_{\text{cap}}, Q_{\text{min}}\right)$. For inelastic scattering, the boundaries are given in Eq. (4.25) (where v is to be replaced with w); the limit $\delta \to 0$ reverts to elastic scattering.

The model independent particle number evolution by capture and annihilation in celestial bodies is described in Sec. 3.2.5.

4.2.3 Annihilation channels

WIMP annihilation in the Sun mostly happens into heavy quarks and bosons. Because the Higgs coupling is proportional to the mass of the particle, annihilation into leptons and light quarks is suppressed. The annihilation diagrams can be obtained using SARAH [111, 116]; the most relevant channels are shown in Fig. 4.3.

Resonant annihilation is a possibility if $m_\chi/2$ is close to the mass of a possible annihilation final state, as will be seen in Sec. 4.5.2. However, resonances do not play a role for the scenarios of interest which are investigate in the IceCube data analysis, due to significantly larger Dark Matter masses.

4.3 Constraints

The parameter space of the model is constrained by a variety of limits. These limits are either considered directly as boundaries within the numerical implementation of the model, or used for our results to be tested against. When not described otherwise, all our presented results comply with the constraints listed in this section.

Limits on the relic density

A major constraint on the parameter space of the Scotogenic Model is given by the precise Planck satellite measurement of the Dark Matter relic density [63],

$$\Omega h^2 = 0.120 \pm 0.001, \tag{4.30}$$

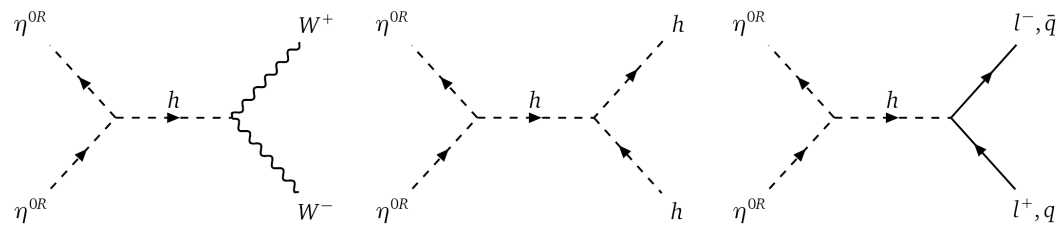

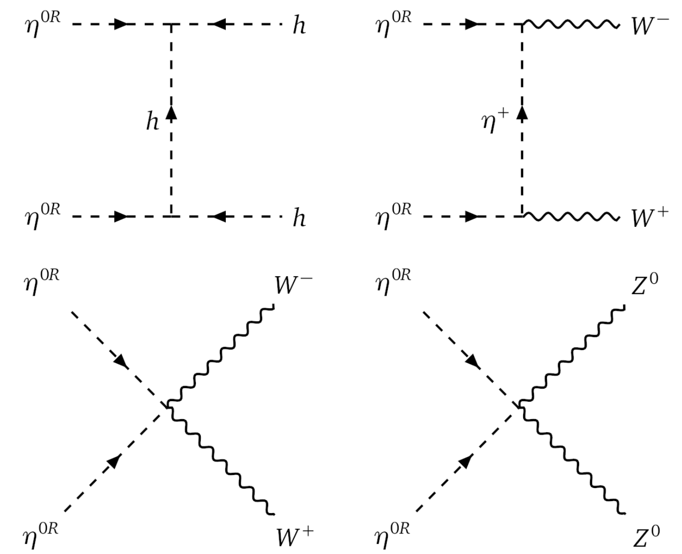

Figure 4.3: S-channel (top), T-channel (middle) and quartic (bottom) Feynman diagrams of some relevant WIMP annihilation in the Sun in the framework of the Scotogenic Model, for the scalar DM candidate η^{0R} (which can be interchanged with η^{0I} as DM candidate). The diagrams were obtained using SARAH [111, 116]. The top right diagram describing annihilation into (light) quarks and leptons is suppressed by the proportionality of the Higgs coupling to the particle mass.

where Ω is the Dark Matter density parameter (see Sec. 3.2.1) and h is the reduced Hubble constant. Each scotogenic scenario investigated in this thesis is required to comply with this limit in order to be categorized as potentially viable; however we allow a range of $\Omega h^2 = 0.12 \pm 0.02$ to compensate for numerical uncertainties.

More than one particle species can be involved in the early-universe production of the relic density. These co-annihilation processes have to be taken into account, and can have a large impact on the relic density, as the reader will see later in this chapter. The mechanisms behind co-annihilation are described in Sec. 3.2.3.

Technically, several (unrelated) sources of cold Dark Matter could exist and contribute to the relic density. In this work, we assume that scotogenic Dark Matter is the only contributor, and therefore do not allow values below the margin around the Planck relic density given above.

Limits on SM neutrino parameters

The new Yukawa matrix $y_{i\alpha}$ can be constrained by the limits on the neutrino mixing parameters presented in Ref. [117] with the Casas-Ibarra parametrization [118]. For that purpose, we use that the neutrino mass matrix of Eq. (4.4) is diagonalized by the PMNS matrix U_{PMNS} in the following way:

$$U^T_{\text{PMNS}} m_\nu U_{\text{PMNS}} = \hat{m} \equiv \text{diag}\,(m_1, m_2, m_3)\,. \tag{4.31}$$

Solving Eq. (4.4) for y then gives

$$y = \sqrt{\Lambda}^{-1} R \sqrt{\hat{m}_\nu} U^\dagger_{\text{PMNS}}. \tag{4.32}$$

The Λ is known by the mass parameters of the Scotogenic Model, see Eq. (4.5). The PMNS matrix is "fixed" by the SM neutrino mixing angles (the angles are chosen randomly within their respective 3σ range). The diagonal neutrino mass matrix $\hat{m}$ is obtained by choosing a random small number for m_1, and calculating $m_{2,3}$ from the 3σ ranges of the squared mass differences given in Ref. [117], for normal hierarchy. That leaves an orthogonal matrix R which depends on three arbitrary rotation angles $\theta_i \in [0, 2\pi]$.

In the numerical implementation, the new Yukawa matrix is calculated with the Casas-Ibarra prametrization described here, which is why all studied scotogenic scenarios are automatically viable in terms of the limits on Standard Model neutrino parameters.

Limits on lepton flavor violating processes

Lepton flavor violation (LFV) does occur naturally in the Scotogenic Model and other radiative seesaw models, so limits on LFV processes have to be taken into account. They affect mostly fermion Dark Matter [119], but we consider them here as well to be conservative. The most important ones are the limits for the branching ratios of the processes $\mu \to e + \gamma$ and $\mu \to 3e$, as well as the conversion ratio of $\mu - e, \mathrm{Ti}$:

$$\begin{aligned} \mathrm{BR}\left(\mu \to e + \gamma\right) &< 4.2 \cdot 10^{-13}, \\ \mathrm{BR}\left(\mu \to 3e\right) &< 1.0 \cdot 10^{-12}, \\ \mathrm{CR}\left(\mu - e, \mathrm{Ti}\right) &< 4.3 \cdot 10^{-12}, \end{aligned} \tag{4.33}$$

which were published by the MEG collaboration in [120], and the SINDRUM and SINDRUM II collaborations in [121] and [122], respectively.

Cross sections limits

There exist several experimental limits on the spin-independent elastic WIMP-proton scattering cross section $\sigma_p(SI)$. In the following sections we will compare our results to indirect-detection limits from ANTARES [123], previous IceCube studies [124] and Super-Kamiokande [125], as well as direct-detection limits from XENON-1T [126].

Other cross section constraints that we use for comparison in this work include the limits on the Dark Matter self-annihilation cross section from combined ANTARES and IceCube searches [127] and Super-Kamiokande [128]. We further compare to the annihilation cross section expectation for the thermal relic scenario [129]; a benchmark value that can be derived from the observed relic density for cold (i.e. thermally produced) WIMP Dark Matter.

The so-called neutrino floor describes a parameter space in which coherent scattering with neutrinos becomes a very important background to direct detection experiments. Larger and larger target volumes make the detectors sensitive to cross sections in which a WIMP signal can not easily be distinguished from a neutrino event anymore. The neutrino floor consists of several different fluxes, including solar, diffuse supernova, and atmospheric neutrinos. We show the neutrino floor presented in Ref. [130], for the sake of comparison. Note that indirect detection is not affected in the same way as direct detection by this particular background.

Limits on dark sector particle masses

The masses of new charged scalars are bound by the limit [131]

$$m_{\eta^\pm}^{\mathrm{LEP}} > 98.5\,\mathrm{GeV}, \tag{4.34}$$

measured by the OPAL collaboration at the Large Electron-Positron Collider (LEP) experiment at CERN. Recalling equations (4.3), there is indeed a charged particle among the scalar states. In a viable scotogenic Dark Matter scenario, the charged scalar is necessarily (at least slightly) heavier than the neutral ones, which is why the LEP limit is a lower bound to the neutral scalars as well.

An even stronger constraint can be derived from LEP measurements of the invisible decay width of the Z^0 boson [132], the results of which lead to an effective exclusion of Dark Matter candidate masses lighter than half the mass of the Z^0 boson [133, 134]:

$$m_{\mathrm{DM}}^{\mathrm{LEP}} > \frac{m_{Z^0}}{2} \approx 45.5\,\mathrm{GeV}. \tag{4.35}$$

Limits on inelastic Dark Matter

In the aftermath of the controversial DAMA/LIBRA findings [86, 87, 135], other direct detection experiments targeted inelastic Dark Matter specifically. We use the limits derived from these experiments to compare with our results. They include: The limit on the scalar mass splitting by XENON100 after the first 100.9 days of data taking [136] which excludes mass splittings up to 140 keV; the XENON100 run II (224.6 days) results [137] which can be translated into a limit on the mass splitting as well, as explained in more detail in Ref. [138, Chp. 6]. This excludes mass splittings up to 250 keV in the mass region beyond 300 GeV. Furthermore, the PandaX-II results for fixed Dark Matter masses of 1 and 10 TeV [139] are quoted, which translate into a slightly weaker limit than the XENON100 run II results.

Coupling constraints

The LHC measurement of the SM Higgs boson mass $m_h = 125\,\mathrm{GeV}$ [140] and the relation

$$m_h^2 = 2\lambda_1 \langle \phi^0 \rangle^2 = -2m_\phi^2 \tag{4.36}$$

constrain the coupling parameter λ_1 to the fixed value of $\lambda_1 = 0.26$.

The scalar couplings are further bound by vacuum stability [141] to follow the relations

$$\begin{aligned} \lambda_{1,2} &> 0, \\ \lambda_3 &> -\sqrt{\lambda_1 \lambda_2}, \\ \lambda_3 + \lambda_4 - |\lambda_5| &> -\sqrt{\lambda_1 \lambda_2}, \end{aligned} \tag{4.37}$$

and perturbativity imposes[2]

$$|\lambda_{1,2,3,4,5}| < 4\pi, \qquad \lambda_5 < \mathcal{O}\left(10^{-3}\right). \tag{4.38}$$

[2]Violation of perturbativity: If a coupling becomes so large that higher order terms in an interacting Lagrangian can no longer be ignored; making QFT calculations impossible.

Due to the way of implementation in the numerical analysis software, the constraints in Eqs. (4.36) through (4.37) are automatically fulfilled in all scotogenic scenarios studied here.

4.4 Benchmark scenarios

In this section, observables of two exemplary scenarios of the Scotogenic Model are shown. The parameter points of these "benchmark scenarios", that are named 0849 and 9777 after the approximate masses of their Dark Matter candidates, are given in Tab. 4.3, and selected observables are shown in Tab. 4.4

The two scenarios are viable with regard to all constraints described in Sec. 4.3, and are both "inelastic scnearios", meaning an inelastic scattering cross section is present due to a sufficiently small mass splitting. We show the respective elastic and inelastic neutrino and antineutrino fluxes as seen on Earth as a function of the neutrino energy in Fig. 4.4.

The shape of the elastic and inelastic fluxes are very similar; however the inelastic fluxes are several orders of magnitude stronger than the elastic fluxes in both cases. This can be explained by the substantially different elastic and inelastic capture rates, which are also listed in Tab. 4.4. The continuous shape of the curves and the sharp cut-off at the Dark Matter mass is explained with the fact that there is no Dark Matter annihilation directly into neutrinos, rather than annihilation into Standard Model particle pairs. In both cases, W^+W^- is the dominant channel (the shown fluxes include the contributions from all channels). The neutrino yield gets exponentially weaker for very high energies, which explains the missing-statistics-fluctuations at the end of the spectrum for scenario 9777.

Recalling Eq. (3.66), the expected number of signal events in the IceCube detector can be calculated on the basis of the shown fluxes by convolution with the effective area, which we adapt from a previous publication as explained in Sec. 4.5.1. For our two benchmark scenarios, we expect an elastic and inelastic combined number of signal events of roughly 23,422 (for 0849) and 20 (for 9777) per year.

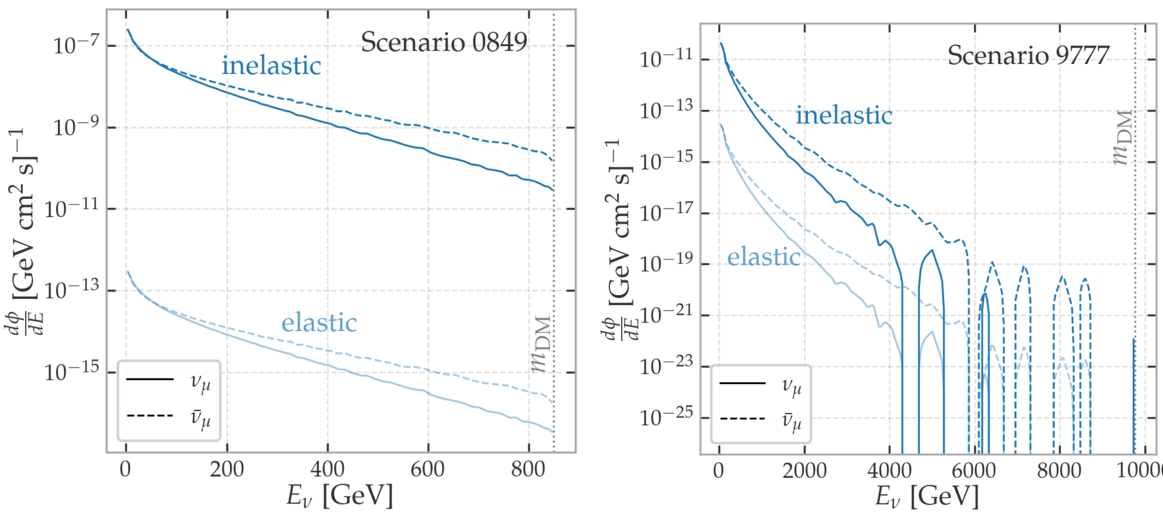

Figure 4.4: The muon neutrino and antineutrino fluxes at Earth as a function of neutrino energy, for the benchmark scenarios 0849 (left) and 9777 (right) of the Scotogenic Model. The light blue curves show the fluxes arising from elastic scattering in the Sun, the dark blue curves show those from inelastic scattering.

parameter	scneario 0849	scenario 9777
λ_1	0.26	0.26
λ_2	0.50	0.50
λ_3	0.44	12.50
λ_4	-0.30	-3.88
λ_5	$-8.97 \cdot 10^{-6}$	$-1.55 \cdot 10^{-4}$
m_η^2	$7.18 \cdot 10^5\,\mathrm{GeV}^2$	$9.53 \cdot 10^7\,\mathrm{GeV}^2$
m_{N_1}	2092.81 GeV	9795.37 GeV
m_{N_2}	8378.58 GeV	9877.79 GeV
m_{N_3}	8757.52 GeV	9982.46 GeV
$Y_\mathbb{R} \times 10^{-3}$	$\begin{pmatrix} -1.51 & -1.29 & 2.93 \\ 1.18 & -0.56 & -0.64 \\ 0.61 & 4.53 & 4.62 \end{pmatrix}$	$\begin{pmatrix} 0.02 & 3.36 & 3.82 \\ 0.88 & 1.74 & -0.66 \\ -1.42 & -2.41 & -1.11 \end{pmatrix}$
$Y_\mathbb{I} \times 10^{-4}$	$\begin{pmatrix} 1.82 & -1.46 & -1.67 \\ -1.12 & 1.13 & 1.29 \\ 9.15 & 0.28 & 0.32 \end{pmatrix}$	$\begin{pmatrix} 1.39 & -0.15 & -0.13 \\ 0.28 & 0.16 & 0.13 \\ -0.76 & -0.22 & -0.19 \end{pmatrix}$

Table 4.3: Input model parameters of the scotogenic benchmark scenarios 0849 and 9777. Shown are the coupling parameters λ_{1-5}, the mass parameters of the new fermions $m_{N_{1-3}}$, the squared mass parameter m_η^2 of the new scalar, and the real and imaginary parts of the new Yukawa matrix, $Y_\mathbb{R}$ and $Y_\mathbb{I}$.

observable	symbol	0849	9777
relic density	Ωh^2	0.1209	0.1079
DM candidate	χ	η_R	η_I
DM mass	m_χ	849.45 GeV	9777.35 GeV
capture rate (elastic)	C_el	$5.11 \cdot 10^{17}\,\frac{1}{\mathrm{s}}$	$1.23 \cdot 10^{17}\,\frac{1}{\mathrm{s}}$
capture rate (inelastic)	C_inel	$9.10 \cdot 10^{23}\,\frac{1}{\mathrm{s}}$	$4.58 \cdot 10^{20}\,\frac{1}{\mathrm{s}}$
main annih. channels	W^+W^-	70.6 %	64.1 %
	Z^0Z^0	21.1 %	15.3 %
	$W^+W^-\gamma$	6.0 %	5.6 %
	hh	2.2 %	15.1 %

Table 4.4: Selected observables of the scotogenic benchmark scenarios 0849 and 9777.

4.5 Parameter scans

4.5.1 Numerical analysis implementation

In order to systematically analyse the parameter space of the Scotogenic Model, we employ a numerical analysis tool chain consisting of different software packages which subsequently perform the necessary computational steps, from the formulation of the Lagrangian all the way to the calculation of the number of neutrino signal events to be expected in IceCube. An overview flowchart of the tool chain is shown in Fig. 4.5, and will be explained in more detail below.

In this study, we build on the work of S. May who presented a tool chain in Ref. [55]. We extended and modified the chain to encompass the Scotogenic Model and especially inelastic Dark Matter, and developed an automation environment that facilitates very effective scans of model parameter spaces with minimal required human intervention, and allows for effective modular integration of new models. The upper part of Fig. 4.5 thereby corresponds mainly to S. May's work (down to the "SLHA spectrum file" box); the lower part to our work, including the automation wrapper which roughly translates to the dashed box labeled "parameter scan".

In the following, the different software packages and tools are listed, together with a brief explanation of their purpose within the tool chain.

MINIMAL-LAGRANGIANS [55] formulates the Lagrangian of minimal Dark Matter models from a given field content. It provides SARAH-compatible files containing the Lagrangian, field content, gauge groups, symmetries, mixing, particles, and all parameters that fully define the model.

SARAH (version 4.14.0) [111, 116] is a WOLFRAM-MATHEMATICA package for model building and implementation. Among other things, it can formulate additional terms of the Lagrangian, calculate the vertices, loop corrections, vacuum expectation values and coupling constants. It also checks the model for inconsistencies or missing definitions. The output is a fully implemented model code package which serves as the base for all further numerical calculations.

SPheno (version 4.0.3) [142, 143, 144] uses the SARAH-generated code to calculate the mass spectrum for a specific set of model parameters. It can as well provide mass matrices, decay rate and branching fractions. The results are saved in micrOMEGAs-compatible format.

CalcHEP [145] is used to calculate the scattering amplitudes and cross sections based on the SPheno spectrum file. We use it for the calculation of the inelastic WIMP-nucleon scattering cross sections specifically. (We use the version that comes with micrOMEGAs, see below.)

DarkSUSY (version 6.2.6) [146, 147, 148] is used to calculate the inelastic Dark Matter capture rate based on the cross sections provided by CalcHEP.

micrOMEGAs (version 5.0.8) [149, 110] is the tool to compute the Dark Matter observables like the relic density, particle fluxes from annihilation processes, and even expected signal events in specific detectors, based on the definitions provided by SARAH, the spectrum file provided by SPheno, and the inelastic scattering cross sections and capture rate provided by CalcHEP and DarkSUSY.

A detailed description of the some of the individual tool chain steps, including what files need to be modified at which point, is given in Ref. [55]. The flowchart in Fig. 4.5 shows the file progression throughout our modified version of the tool chain, for a single scenario (i.e. set of model parameters) of a specific model. The upper box shows the tool chain sequence for model implementation up to the output files of SARAH. This sequence defines the model completely and has to be run only once for a specific model. The resulting code can be used to explore the parameter space and calculate observables for different scenarios, which is described by the tool chain sequence in the lower box. It has to be run once for each scenario.

Parameter scan automation

My (the author's) contribution to this project encompassed specifically the automation and modularization of the modified tool chain, which is described in detail in this paragraph.

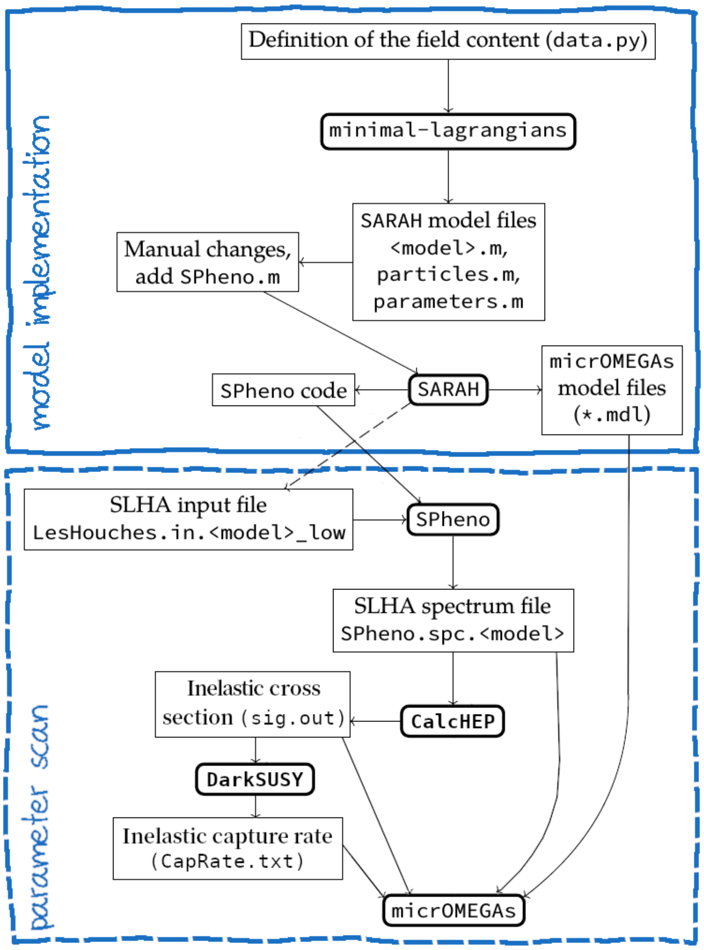

Figure 4.5: Elements of and file progression within the numerical analysis toolchain. The software packages that are part of the toolchain are shown as fields with rounded corners, while files that are passed on between them are represented by fields with sharp corners. The toolchain sequence within the upper, dashed box describes the complete implementation of the model and has to be run only once, while the sequence in the lower, dotted box is input-parameter dependent and modified for each scenario in the parameter scan. Flowchart adapted from Ref. [55, Fig. 6.1], modified.

In order to efficiently perform systematic scans of the parameter space of the Scotogenic Model, I developed a Python environment to automate the lower part of the tool chain. The program takes as input a settings file, in which the boundaries of the parameter space (see the "Parameter ranges" paragraph below), as well as a desired number of parameter points is specified, along with logistics information, like the paths to additional, optional routines that can be defined by the user (for instance, the Casas-Ibarra parametrization is implemented as such an additional routine). For each point, the model input parameters are chosen randomly or according to user-defined rules, within the given bounds.

Subsequently, the input parameters are automatically passed on to the different steps in the tool chain, along with all information that is computed along the way and required by the next program in line: The input parameters determined from the settings file are written to the SPheno input file (to the left of the "SPheno" field in Fig. 4.5). After running SPheno, the mass spectrum serves as input to CalcHEP and micrOMEGAs. Since the employed micrOMEGAs version can not handle inelastic WIMP-nucleon scattering (see the "Implementation of inelastic scattering" paragraph below), we use CalcHEP and DarkSUSY to compute the inelastic scattering cross sections and the inelastic capture rate inside the Sun, respectively, which is implemented to be passed on to micrOMEGAs. A number of temporary files gets created during the process; these files are distributed among the programs automatically.

Should either one of the tool chain steps fail, the script prompts a warning and continues with the next parameter iteration. The user can define custom rules as well that check the success of each step.

The result of each iteration is a Python dictionary with all input parameters and observables, so that the scenarios can be compared in terms of different pre- and post-annihilation aspects. The dictionary is then either written to file directly, or checked for viability and then written or discarded based on a user-defined rule; for instance, the user might decide to only keep parameter points with the correct relic density.

The resulting file in Json format is filled with parameter points iteratively, meaning the scan can be aborted any time without loosing the data that has been already computed.

All user-specific code is supposed to be implemented in the settings file by design, so that no alterations to the original code are necessary. This simplifies the usage of the modified tool chain substantially. In theory, this also allows for a relatively simple implementation of new models. So far, the script has been successfully tested with the Scotogenic Model and the Model T1-3-B which has been studied in Refs. [150, 138].

Furthermore, the tool comes with an installation script that automates the otherwise quite tedious setup of the tool chain environment, provided that the user has downloaded and installed all prerequisites and provides the corresponding software paths. An "initial-run" script checks the correct interplay of the tool chain programs, and serves as a flag line for manual setup, if necessary.

Implementation of inelastic scattering

Inelastic scattering of Dark Matter with nuclei in the Scotogenic Model is an edge case, and a sufficient implementation fitting to our purposes is not present in micrOMEGAs, which we use to calculate the elastic scattering case. As can be seen in Fig. 4.5, we therefore take a "detour" using our own modified CalcHEP routine to compute the inelastic cross sections, and especially a modified DarkSUSY program for the inelastic capture rate, namely `dssenu_capsunnum` and associated routines, that can perform the calculations described in Sections 4.2.1 and 4.2.2. The values are then fed back into micrOMEGAs. For a detailed explanation of the numerical calculation of the capture rate, and why especially heavy elements are relevant for inelastic capture, please refer to Ref. [150, Chp. 8].

Calculation of neutrino fluxes

We use the `neutrinoFlux` [149, 110] routine in micrOMEGAs to compute the neutrino fluxes near the surface of the Earth. The routine takes into account the neutrino spectra from all annihilation channels. It therefore depends on the annihilation branching fractions as well as the WIMP capture rate of the respective scenario. These quantities are calculated internally based on the files provided by the previous steps in the tool chain. In case of inelastic scattering, the inelastic capture rate is provided by CalcHEP and DarkSUSY in form of the dedicated file `CapRate.txt`. We modified the `neutrinoFlux` function to take into account this additional file.

Once capture and annihilation have been set by the respective scenario, the neutrino fluxes are then calculated by the `neutrinoFlux` routine based on tables, taking into account the oscillation effects inside the Sun and between the Sun and Earth, as well as solar matter effects on particles prior to their decay into neutrinos. MicrOMEGAs offers different sets of tables; in this work we choose the WimpSim [151] tables.

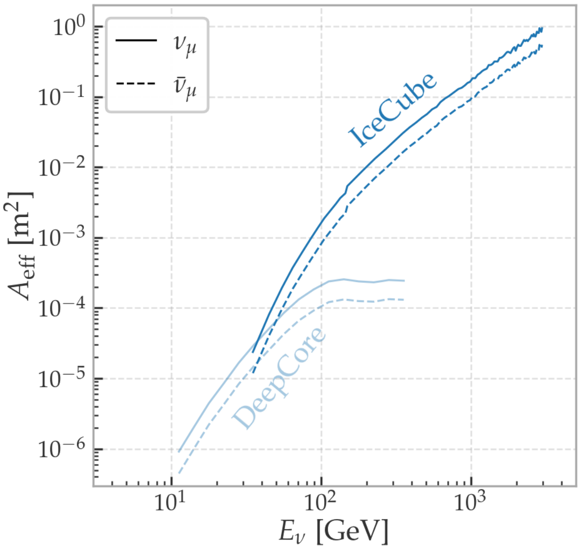

Figure 4.6: The effective areas of DeepCore (light) and IceCube (dark) used in this work to predict the number of signal events. The combined $\nu + \bar{\nu}$ data was taken from Ref. [124], the individual effective areas (solid and dashed lines) were calculated with Eq. (4.39).

Implementation of IceCube event rates

This paragraphs describes another aspect of our joined work that is my (the author's) contribution.

Since we are especially interested in the number of signal events that each scenario might produce in the IceCube detector, a method is needed to predict this number. micrOMEGAs provides a function to do this, in which the neutrino flux is multiplied by the detector's effective area according to Eq. (3.66); although for the quite old detector configuration IC22 (consisting of only 22 strings) that dates back to the construction phase. In order to obtain more modern predictions, I implemented a newer IC86 effective area [124] into micrOMEGAs, by creating a modified version of the original function that employs the new effective area. Ref. [124] provides a combined $\nu_\mu + \bar{\nu}_\mu$ effective area only, so the individual effective areas for ν_μ and $\bar{\nu}_\mu$ were calculated with

$$A_{\nu(\bar{\nu})} = \frac{A_{\rm combined}}{1 + \frac{\sigma_{\bar{\nu}(\nu)}}{\sigma_{\nu(\bar{\nu})}}}, \tag{4.39}$$

by taking into account the different deep inelastic scattering cross sections σ_ν and $\sigma_{\bar{\nu}}$ for neutrinos and antineutrinos, which were taken from Ref. [152]. The resulting effective areas are shown in Fig. 4.6. (The values are extrapolated for neutrino energies outside of the provided range.)

Parameter ranges

The free parameters of this study and the ranges they are sampled from in the numerical scans are listed in Tab. 4.5. The sampling ranges for the scalar couplings $\lambda_{2,3,4,5}$ are bound by perturbativity to fulfill $|\lambda| < 4\pi$. Vacuum stability constraints might limit the individual ranges further in some cases, as explained in Sec. 4.3. Since the parameter λ_2 is responsible only for self-interactions of η which are irrelevant to this work, its value can be fixed (without loss of generality). The sampling range for the mass splitting parameter λ_5 is chosen according to the natural smallness of the coupling, following Ref. [153], and is well below the perturbativity-imposed bound of $\lambda_5 < \mathcal{O}\left(10^{-3}\right)$.

The mass parameters of the new fields, m_η and m_N, are varied in the range of $10^2 - 10^4$ GeV, where the lower bound is oriented towards the LEP limit on charged scalars [131].

The new Yukawa matrix $y_{i\alpha}$ that couples the Standard Model leptons to the new fields is sampled indirectly via the Casas-Ibarra parametrization [118]. As described in Sec. 4.3, the parametrization depends on the smallest neutrino mass parameter m_1, the rotation angles θ_i, and a CP-violating phase δ_{CP}, so we provide instead the sampling ranges of these quantities. The upper bound of m_1 is thereby motivated by the KATRIN upper limit on the effective mass of the (anti)electron neutrino $m_{\nu_e} < 1.1\,\mathrm{eV}$ [154, 58].[3] We set δ_{CP} to zero because CP-phenomenology is not studied in this work. The angles θ_i are unconstrained in the Casas-Ibarra parametrization.

Table 4.5: Free parameters of the Scotogenic Model, and the sampling ranges used in the numerical scans. The ranges are given as comma-separated lower and upper bounds.

parameter	m_η [GeV]	m_{N_i} [GeV]	λ_2	λ_3, λ_4	$\lvert\lambda_5\rvert$	m_1 [eV]	θ_i	δ_{CP}
sampling range	$10^2, 10^4$	$10^2, 10^4$	0.5	$-4\pi, 4\pi$	$10^{-12}, 10^{-8}$	$4\times10^{-3}, 1.1$	$0, 2\pi$	0

4.5.2 Scans I and II: Trial runs with elastic Dark Matter

The first parameter scans have been conducted with exclusion of inelastic scattering; for testing the numerical analysis tool chain on the one hand; on the other because the implementation of inelastic scattering into the framework of the Scotogenic Model was not completed at the time. The results of these "premature" parameter scans proved instructive for the further development of the scan routines, and provide a good first overview of the scotogenic parameter space.

The very first run serves the purpose of "staking out" the parameter space. The values of the free parameters are chosen at random, only bound by the sampling ranges given in the last section, and the restrictions imposed by Eqs. (4.36) and (4.37).

The results of this first scan are shown in the left panel of Fig. 4.7, presented in the relic density vs. number of expected signal events plane, and colored according to the respective elastic spin-independent DM-proton scattering cross sections. Roughly 387,000 parameter points are shown in the plot. The presented scenarios are not yet subjected to experimental constraints, but do comply with all automatically fulfilled limits (Higgs boson mass, Standard Model neutrino parameters, etc.). The reader may notice a very distinct vertical column of points located just shy of one signal event per year. This cluster of points contains scenarios with Dark Matter masses near the masses of the Higgs and Z^0 bosons, which leads to annihilation resonances and therefore significantly reduced relic densities. This phenomenon, along with other interesting features of the scotogenic parameter space, is further described in Ref. [99].

We notice that the spin-independent DM-proton scattering cross section appears to correlate well with the number of expected signal events, increasing from left to right. This can be explained by larger cross sections leading to larger capture rates, which again result in increased Dark Matter annihilation that leads to a stronger flux of neutrinos.

Furthermore, it is apparent that only a small portion of scenarios fall within the (conservative) margin around the Dark Matter density measured by Planck. All scenarios outside of the indicated area are therefore non-viable, even before considering further experimental

[3]The latest KATRIN upper limit is $m_{\nu_e} < 0.8\,\mathrm{eV}$ [58], which was not available at the time of the scan.

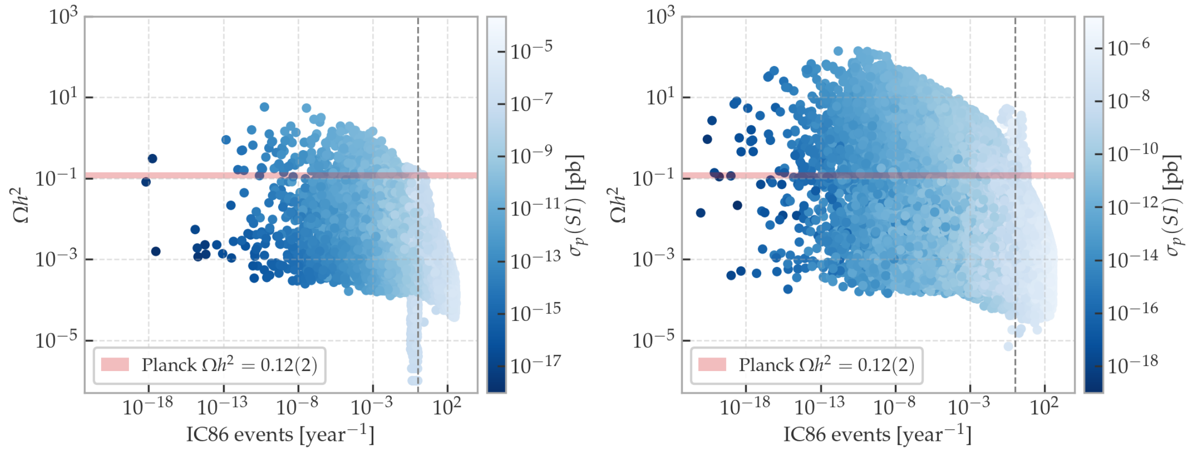

Figure 4.7: Results of the parameter scans I and II, shown in the plane of the relic density vs. the expected signal events per year in IceCube, with the elastic spin-independent DM-proton scattering cross section on the third axis. A margin around the relic density measured by PLANCK [63] is indicated by the red band. To guide the eye, the dashed gray line indicates one IceCube signal event per year. **Left:** Results of scan I with the free parameters listed in Tab. 4.3. **Right:** Results of scan II with enforced scalar-fermion co-annihilations, with the same free parameters, and the additional constraint of M_{N_i}=m_{DM} + 0.1 GeV, with $N_1 = N_2 = N_3$.

constraints. In addition, most scenarios are located to the left of the dashed vertical line, meaning they yield less than one signal event per year which we consider a (very optimistic) lower detection threshold for IceCube. Hence the number of scenarios that are viable *and* promising in terms of event rates is *very* small. A parameter scan that produces a sufficiently large number (~1, 000) of viable and promising scenarios would be computationally very expensive; disregarding that most, if not all, the scenarios would be concentrated inside a tiny portion of the whole parameter space. Based on these facts we conclude that this implementation of the Scotogenic Model is not well suited for an indirect detection analysis with IceCube data, and would at least need some fine-tuning to shift the parameter space to more interesting regions.

Fermion-Scalar co-annihilations

In order to explore the possibility of a more promising shape of the parameter space, we implemented enforced fermion-scalar co-annihilations. A co-annihilation describes the early-universe process of Dark Matter particles not only annihilating with themselves, but also with other slightly mass-degenerate new particles (see Sec. 3.2.3), in our case with the fermions N_i. For the Scotogenic Model, a boost in relic density due to co-annihilation is in fact possible, as described in Refs. [65, 155].

The Dark Matter candidate in our study is scalar, so the co-annihilation partners can be any or all of the three fermions. Since co-annihilation effects are most prominent for small mass differences between the Dark Matter particle and the fermions, we enforce $M_{N_i} = m_{\mathrm{DM}} + 0.1$ GeV, with m_{DM} being the mass of the Dark Matter candidate. The effect becomes even stronger for more possible co-annihilation partners, so we also set $N_1 = N_2 = N_3$. The other parameters are varied freely within the same bounds as for the first scan.

The results of the co-annihilation scan are shown in the right panel of Fig. 4.7, again in the plane relic density vs. number of expected signal events, and colored according to the elastic spin-independent DM-proton scattering cross section. The plot consists of roughly $349,000$ scenarios. When compared to the left panel, it is evident that the enforced co-annihilation does in fact alter the parameter space, and results in the desired boost of the relic density. However, the viable and promising region (within the relic density band and to the right of the dashed line) is only enlarged by a small factor.

Enforcing co-annihilation is considered fine-tuning and a high price to pay[4] for a rather marginal increase of promising parameter space. A more appealing solution is presented in the following.

4.5.3 Scans III and IV: Inelastic Dark Matter

Inelastic scattering of Dark Matter particles with nucleons inside the Sun can boost the capture rate substantially. This results in a greatly enhanced neutrino flux from WIMP annihilation, without having to mess with early-universe annihilation processes, as was done by enforcing co-annihilation in scan II. The theory behind inelastic scattering and capture in the Sun is described in Sec. 4.2, and the implementation of inelastic scattering cross sections and capture rates into the tool chain is described in Sec. 4.5.1.

We find that inelastic Dark Matter opens a large parameter space for indirect detection; nonetheless, for the sake of curiosity, we also investigate the combination of inelastic Dark Matter *plus* enforced fermion-scalar co-annihilation. Both studies (scan III without, and scan IV with enforced co-annihilation), are discussed in the following.

Exploration of the parameter space

To demonstrate the substantial differences in the parameter space that were achieved by introducing inelastic Dark Matter, we show an exploration plot in the left panel of Fig. 4.8, that represents the parameter space in the same plane as Fig. 4.7. On the third axis, the spin-independent DM-proton scattering cross section is drawn, this time as a combination of elastic and inelastic cross sections for all scenarios in which inelastic scattering is present, and as elastic cross section only for those scenarios in which inelastic scattering is absent. The difference between these two groups of scenarios can be clearly identified by the color scale and the expected event rate: Purely elastic scenarios are drawn in darker shades and towards smaller event rates; the inelastic scenarios with their much larger and more or less constant inelastic cross section component are drawn in lighter shades and yield more events. Shown are approximately 15,000 scenarios.

Again the correct PLANCK relic density and one expected signal event per year are indicated in the plot. We find that the parameter space looks much more promising in terms of expected IceCube events; now significantly more scenarios that fulfill the relic density constraint are located to the right of the one-event line.

The right panel of Fig. 4.8 shows the results of the parameter scan with enforced fermion-scalar co-annihilation. Like before, this means we set an additional constraint on the mass of the dark fermions: $M_{N_i}{=}m_{\mathrm{DM}} + 0.1\,\mathrm{GeV}$, with $N_1 = N_2 = N_3$. Again we observe a boost in relic

[4]Physicists, too, are bound by the philosophical principle of *Occam's razor*, which basically states that a simple theory is preferred over a theory of higher complexity, when both theories describe the same phenomenon. So a fine-tuned model in which certain parameters have to be squeezed and cranked to comply with nature is a less appealing solution to the Dark Matter problem than a simple model in which the correct observables are achieved more "naturally".

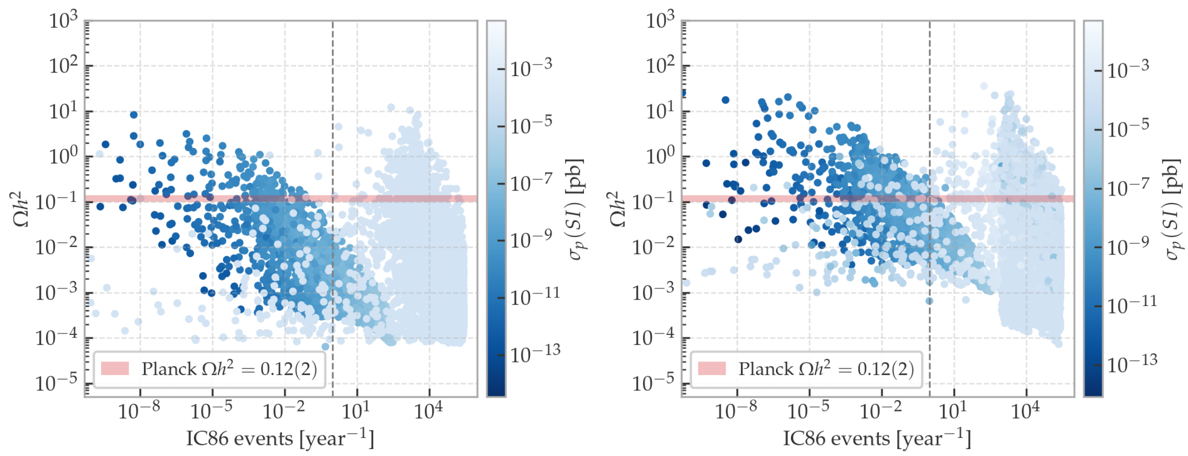

Figure 4.8: Results of the parameter scans III and IV, shown in the IC86 events per year vs. relic density plane, with the elastic spin-independent DM-proton scattering cross section on the third axis. The darker parameter points represent the scenarios in which no inelastic scattering is present; the lighter ones posses an inelastic scattering cross section and therefore yield more events as a result from both elastic *and* inelastic scattering processes in the Sun. The correct relic density [63] is indicated by the red band, the dashed gray line indicates one IceCube signal event per year. **Left:** Results of scan III, with free parameters as listed in Tab. 4.3. **Right:** Results of scan IV with enforced scalar-fermion co-annihilation, with the same free parameters, and the additional constraint of $M_{N_i}=m_{\mathrm{DM}} + 0.1\,\mathrm{GeV}$, with $N_1 = N_2 = N_3$.

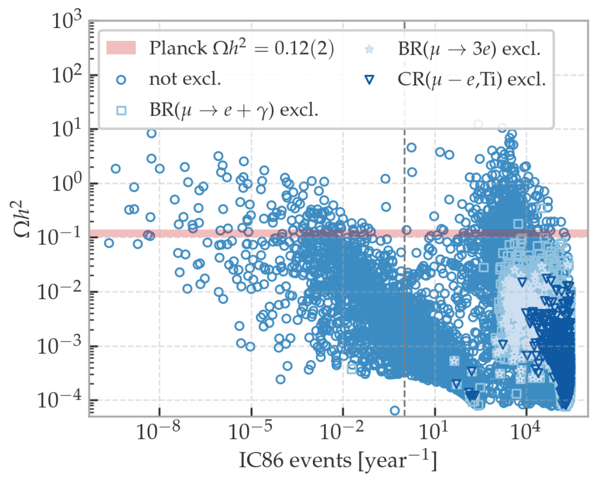

Figure 4.9: Results of the parameter scan III, shown in the IC86 events per year vs. relic density plane. The scenarios are colored/ shaped according to constraints from branching and conversion ratios of lepton flavor violating processes listed in Sec. 4.3, namely exclusion for the process BR$\left(\mu \to e + \gamma\right)$ (squares), BR$\left(\mu \to 3e\right)$ (stars), and CR$\left(\mu — e, \mathrm{Ti}\right)$ (triangles). The scenarios marked with circles are not excluded for LFV processes. The correct relic density [63] is indicated by the red band, the dashed gray line indicates one IceCube signal event per year.

density, which is more pronounced for the purely elastic scenarios. Both scans consisted of roughly 15,000 scenarios, substantially less than in the previous scans I and II, which explains the absence of the distinct resonance features, compared to Fig. 4.7.

In the next step, we investigate to what extend the parameter space is constrained by limits on lepton flavor violating (LFV) processes, which are described in Sec. 4.3. The data points obtained in scan III are used for this purpose, and the results are plotted in Fig. 4.9. Again, we show the scenarios in the IceCube events vs. relic density plane; the colors and marker shapes indicate exclusion due to the different LFV limits. Scenarios that remain viable in this context are shown as well. The regions of the parameter space that are affected the most by LFV constraints seem to concentrate mainly on scenarios with high event rate, in the lower right corner of the plot. However, this corner region is of low importance to this work, since the scenarios located there are already excluded by the PLANCK relic density constraint. Only

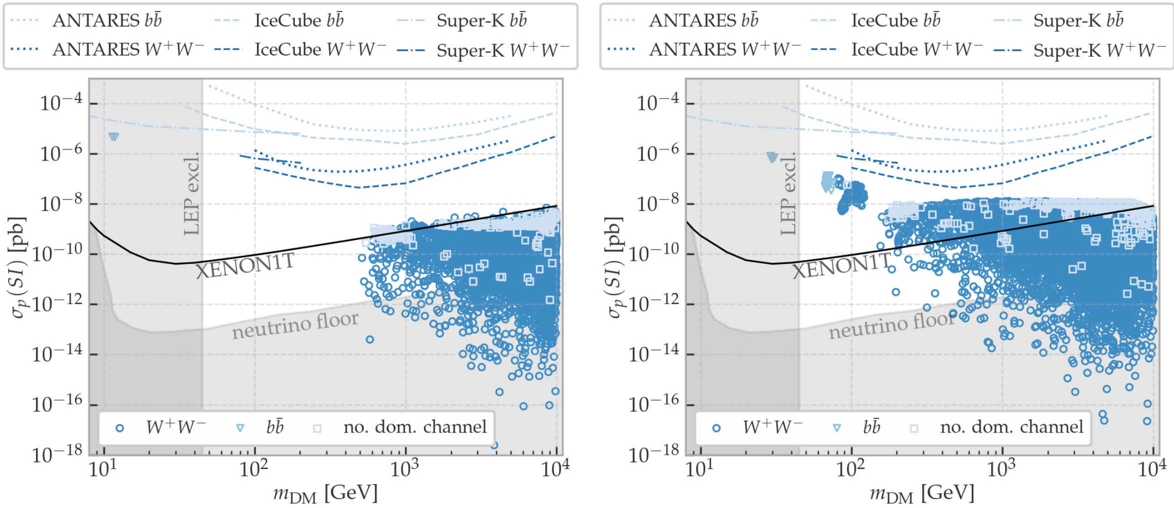

Figure 4.10: Results of the parameter scans III and IV, in the plane of the elastic spin-independent DM-proton scattering cross section vs. the Dark Matter mass. The scenarios are colored/ shaped according to their dominant annihilation channel. All shown scenarios are viable in terms of relic density and limits from LFV processes. The following additional limits are shown: The LEP limit from the invisible Z^0 boson decay, the limits on the elastic scattering cross section by ANTARES, IceCube, Super-Kamiokande, and XENON1T, as well as the neutrino floor (for references see text and Sec. 4.3). **Left:** Results of scan III with the free parameters as listed in Tab. 4.3. **Right:** Results of scan IV with enforced scalar-fermion co-annihilation, with the same free parameters, and the additional constraint of M_{N_i}=m_{DM} + 0.1 GeV, with $N_1 = N_2 = N_3$.

very few LFV-constrained scenarios appear within the gray shaded band which marks the region close to the correct relic density. We therefore conclude that the LFV limits do not have a significant impact on our study.

Limits on the elastic scattering cross section

Now that an overview of the parameter space including inelastic scattering is given, more constraints are applied to filter out non-viable scenarios: All scenarios studied beyond this point comply with the relic density constraint and the limits on lepton flavor violating processes, in addition to the constraints that are applied automatically by the parameter scan algorithm (see Sec. 4.3).

We compare our results to the latest limits on the elastic spin-independent DM-proton scattering cross section by means of Fig. 4.10, left panel. The scenarios are shown in the Dark Matter mass vs. elastic cross section plane, marked according to their respective main annihilation channel. Scenarios that are marked “no dom. channel” do not possess a single annihilation channel with a branching ratio $\geq 50\,\%$. Only two different dominant annihilation channels are observed: For very small masses, the dominant channel is $b\bar{b}$, while for masses beyond the W-boson threshold of $\sim 80\,$GeV, the WIMPs annihilate mainly into W^+W^-. Furthermore, we observe that the correct relic density generally prevents viable scenarios with a Dark Matter mass between $\sim 20\,$GeV and $\sim 500\,$GeV; while scenarios below $\sim 45.5\,$GeV are excluded by the limit derived from the LEP measurement on the invisible Z^0 boson decay.

From the current experimental limits on the elastic spin-independent DM-proton scattering cross section, the one measured by XENON1T is the strongest, drawn as a black line in the plot. We quote as well the much weaker indirect detection limits by ANTARES, IceCube, and

Super-Kamiokande, for the channels $b\bar{b}$ and W^+W^-, for the sake of completeness (for references see Sec. 4.3). From these limits, only the XENON1T limit constraints our parameter space by a small portion.

It is worth noting that a large part of our scenarios, especially for Dark Matter masses larger than 1 TeV, do in fact feature elastic cross sections small enough to reach down into the neutrino floor, a part of the general WIMP parameter space which direct detection measurements can only probe with great difficulty due the background of neutrinos.

The results of the scan with enforced fermion-scalar co-annihilation are shown in the right panel of Fig. 4.10. We observe that co-annihilation opens lower-mass regions of the parameter space to viable scenarios in terms of relic density: Scan IV reveals viable scenarios in the $\sim 50 - 500\,\mathrm{GeV}$ Dark Matter mass region, while in scan III the viable region started only at $\sim 500\,\mathrm{GeV}$. However, many of these additional scenarios lie above the XENON1T upper limit, and are therefore excluded.

Limits on the scalar mass splitting

Recalling Sec. 4.2.1, we expect inelastic scattering to be possible only below a certain threshold of the mass splitting δ between the Dark Matter candidate and its heavier state, η^{0R} and η^{0I}. We investigate this threshold in the following.

In the left panel of Fig. 4.11, we show the results of scan III, in the plane of the mass splitting δ vs. the capture rate C_χ. Because all scenarios come with an elastic capture rate, the scenarios that support inelastic scattering are represented in the plot twice. The scenarios are further marked according to their viability or exclusion due to different experimental constraints. While the progression of the elastic capture rate remains unaffected by δ, the inelastic capture rate decreases first slowly, then very steeply with increasing δ, and drops off to zero at approximately 600 keV. This observation holds for scan IV with enforced co-annihilation, shown in the right panel. After subtraction of all XENON1T-excluded scenarios, the remaining distribution of scenarios does not differ much at all in this plane, when compared to the scan results in the left panel. Furthermore, the limit on the mass splitting derived from the XENON100 run II results are shown, which exclude all scenarios below a mass splitting of $\sim 250\,\mathrm{keV}$.

From the plots, the mass splitting value at which inelastic scattering becomes kinematically available appears to be $\delta \simeq 600\,\mathrm{keV}$. To be a bit more precise, the minimum mass splitting among the purely elastic scenarios ($\delta^<_{\text{inel.}}$), and the maximum mass splitting among the inelastic ones ($\delta^>_{\text{el.}}$), are extracted from the parameter points, and are determined to

$$\delta^<_{\text{inel.}} = 595.05\,\mathrm{keV}, \qquad \delta^>_{\text{el.}} = 627.64\,\mathrm{keV}. \tag{4.40}$$

The relatively large gap between the two values shows that the inelasticitiy does not depend on the mass splitting alone. However, it can be a good estimator for the inelastic scattering potential of a specific scenario. For now, $\delta^<_{\text{inel.}} = 595.05\,\mathrm{keV}$ is called the "threshold mass splitting for inelastic scattering", below which all investigated scenarios are inelastic.

In a next step, we consider only those scenarios that feature inelastic scattering, and a closer look shall be taken at the remaining limits on inelastic Dark Matter. For this purpose, the scalar mass splitting is plotted vs. the Dark Matter mass in the left panel of Fig. 4.12, indicating as well the number of expected signal events in IceCube. In addition to our results, we show the following limits: The LEP limit on the dark neutral scalar mass, the XENON100

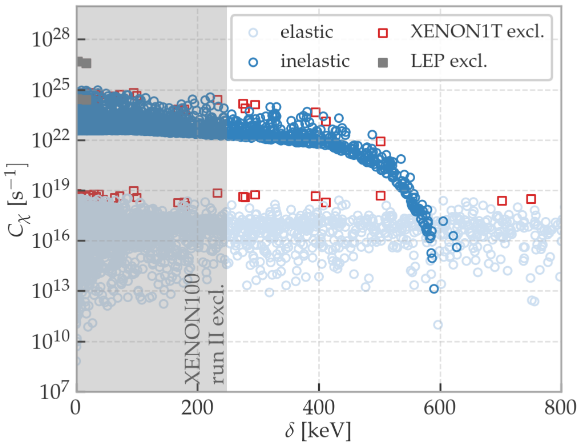

Figure 4.11: Results of the parameter scans III and IV, in the plane of the capture rate vs. the mass splitting between the two dark neutral scalars. Note that the elastic and inelastic contributions to the capture rate are plotted separately, so scenarios with both an elastic and inelastic capture rate are represented in the plot twice. Red and gray squares denote scenarios that are excluded by XENON1T/ LEP, respectively. The gray shaded area indicates mass splittings excluded by the XENON100 run II limit (for references see text and Sec. 4.3). **Left:** Results of scan III with the free parameters listed in Tab. 4.3. **Right:** Results of scan IV with enforced scalar-fermion co-annihilation, with the same free parameters, and the additional constraint of M_{N_i}=m_{DM} + 0.1 GeV, with $N_1 = N_2 = N_3$.

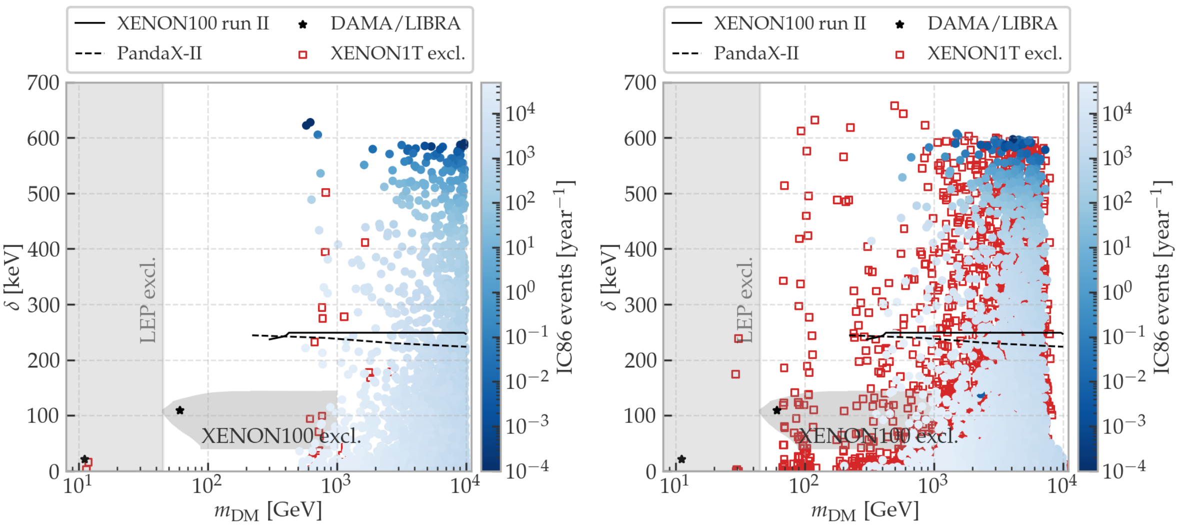

Figure 4.12: Results of the parameter scans III and IV, in the plane of the neutral skalar mass splitting and DM candidate mass, for all inelastic scenarios. Colors indicate the expected IceCube event rate. XENON1T-excluded scenarios are drawn as red squares. The following additional limits are shown: The LEP limit from the invisible Z^0 boson decay (gray band), the limits on the mass splitting by XENON100 (gray area), XENON100 run II (solid black line), PandaX-II (dashed black line) and the two DAMA/LIBRA best fits (black stars); for references refer to Sec. 4.3. **Left:** Results of scan III with the free parameters listed in Tab. 4.3. **Right:** Results of scan IV with enforced scalar-fermion co-annihilation, with the same free parameters, and the additional constraint of M_{N_i}=m_{DM} + 0.1 GeV, with $N_1 = N_2 = N_3$.

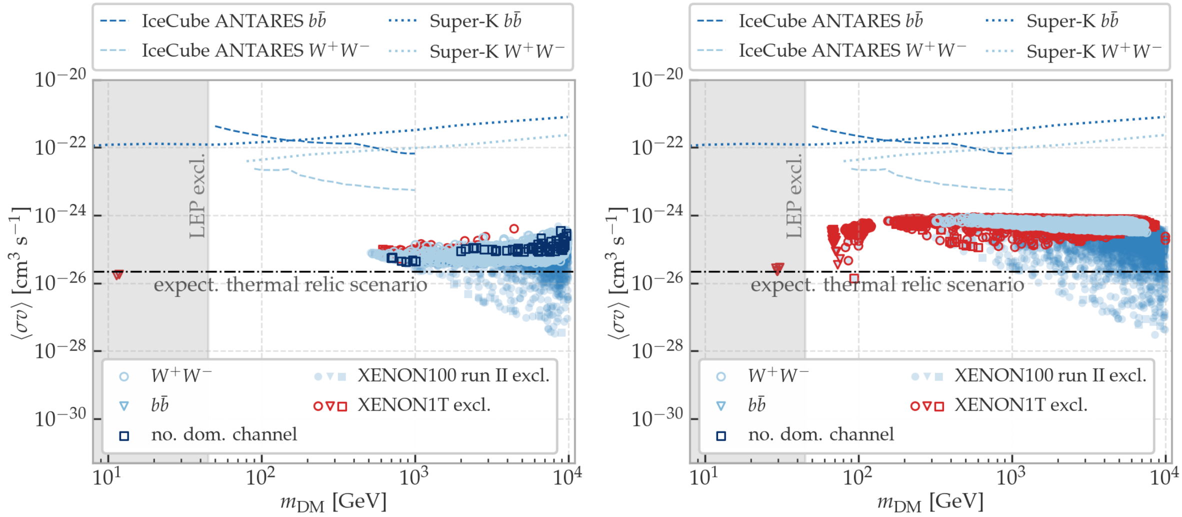

Figure 4.13: Results of the parameter scans III and IV. Shown is the thermally averaged self-annihilation cross section vs. the DM candidate mass. The shapes and colors indicate the respective dominant annihilation channel, where grayed-out scenarios are excluded by the XENON100 run II limit on δ, and red-bordered scenarios are excluded by the XENON1T limit on $\sigma_p(SI)$. The following additional limits are shown: The LEP limit from the invisible Z^0 boson decay (gray band), the channel-dependent limits on the annihilation cross section for the $b\bar{b}$ (dark lines) and W^+W^- (light lines) channels from a combined ANTARES-IceCube search (dashed) and Super-Kamiokande (dotted), and the expectation for the thermal relic scenario (dashed-dotted black line). For references refer to Sec. 4.3. **Left:** Results of scan III with the free parameters listed in Tab. 4.3. **Right:** Results of scan IV with enforced scalar-fermion co-annihilation, with the same free parameters, and the additional constraint of M_{N_i}=m_{DM} + 0.1 GeV, with $N_1 = N_2 = N_3$.

limit on the mass splitting, the XENON100 run II limit, and the PandaX-II limit on the mass splitting, as well as the DAMA/LIBRA low-mass and high mass best fits. The scenarios that have been determined excluded by XENON1T in the previous steps are marked accordingly. (For references see Sec. 4.3.)

As expected, the IceCube signal events decrease with increasing δ, since the event rate directly correlates with the inelastic scattering cross section which is stronger for smaller mass splittings. However, the largest event rates from the scenarios with the smallest mass splitting are excluded by the XENON100 run II and PandaX-II limits for Dark Matter masses larger than $\sim$ 300 GeV. The XENON100 exclusion area contains the high-mass point of the DAMA/LIBRA results; the low-mass point is excluded by LEP.

Considering enforced co-annihilation in scan IV in the right panel, we observe that the results do not differ significantly from the scan III results. Again, many scenarios "gained" from co-annihilation are excluded by XENON1T; and no distinct surplus of viable scenarios is visible compared to the left panel.

Limits on Dark Matter annihilation in the Galactic center

Besides the DM-nucleon scattering cross sections discussed in a previous paragraph, indirect detection experiments can probe the cross section for DM-DM self-annihilation in the Galactic center. Such studies require the assumption of a certain Dark Matter halo profile describing the distribution of WIMPs in the Galactic halo, for instance the Navarro-Frenk-White (NFW) [156] profile.

In this work, the thermally-averaged annihilation cross section is calculated in MICROMEGAs with the `calcSpectrum` routine. In Fig. 4.13, the thermally averaged annihilation cross section $\langle \sigma v \rangle$ is plotted vs. the Dark Matter mass for the scenarios from parameter scans III and IV (without and with enforced co-annihilation). The scenarios are colored according to the respective dominant annihilation channel, where again a point is marked having "no dominant channel" if no single annihilation branching is stronger than 50 %.

As before, the few low mass scenarios that survived the relic density constraint are excluded by LEP. The results are further compared to the channel-dependent limits set by a combined ANTARES and ICECUBE search, and the weaker limits from SUPER-KAMIOKANDE (for references refer to Sec. 4.3). Both studies assume the NFW galactic halo density profile. All non-excluded scenarios lie below the quoted limits, for both scans without (left panel) and with (right panel) enforced co-annihilation.

Furthermore, the scenarios that are excluded by the previously introduced XENON100 and XENON1T limits are marked specifically. Especially XENON100 excludes scenarios with lower rates (smaller annihilation cross section), while the surviving scenarios are concentrated towards larger rates. Intuitively one would assume that direct detection experiments would exclude the *larger* rates first. This can be explained by the fact that, contrary to the Sun, the Dark Matter density in the Galactic center is determined by the halo profile, and not by the scattering cross section that XENON is sensitive to.

Shown as well is the $\langle \sigma v \rangle$ expectation value for the thermal relic scenario of generic WIMPs [129]. While the scenarios obtained in scan III very roughly agree with it, many in the co-annihilation scan IV lie well above. These larger values of $\langle \sigma v \rangle$ are required to yield the correct relic density, because co-annihilation increases the relic density in the Scotogenic Model. Note that the thermal relic expectation value is a benchmark orientation value for generic WIMPs, and not considered restrictive towards our scenarios, in contrast to the much more important constraint of the correct relic density.

Expected event rates in IC86

After we have studied the parameter space of the Scotogenic Model in a variety of different aspects over the last sections, and compared our scenarios to recent experimental findings in terms of different observables, in this last step we want to take a closer look at the expected signal events in ICECUBE. Fig. 4.14 shows the scotogenic scenarios from the parameter scans III and IV including inelastic Dark Matter in the total (elastic plus inelastic) signal events per year vs. Dark Matter mass plane. The different colors and shapes indicate whether a scenario features inelastic scattering or not, and whether it is excluded by experimental limits. As in the previous figures, the right and left panels show the results from scans III and IV (without and with enforced co-annihilation), respectively.

Disregarding the scenarios that are already excluded; we observe two groups of scenarios in both panels, one consisting of purely elastic scattering scenarios, and one consisting of scenarios with an inelastic component. The "elastic scenarios" are located in the lower half in both plots, below the line that indicates one ICECUBE event per year. This value was chosen as a conservative detection threshold; any scenario that yields less than one signal event per year is not considered in reach of ICECUBE sensitivity. We can conclude that none of the purely elastic scenarios are in reach of an ICECUBE analysis. The inelastic scenarios, however, spread over a region of several orders of magnitude of promising event rates. While scenarios with a

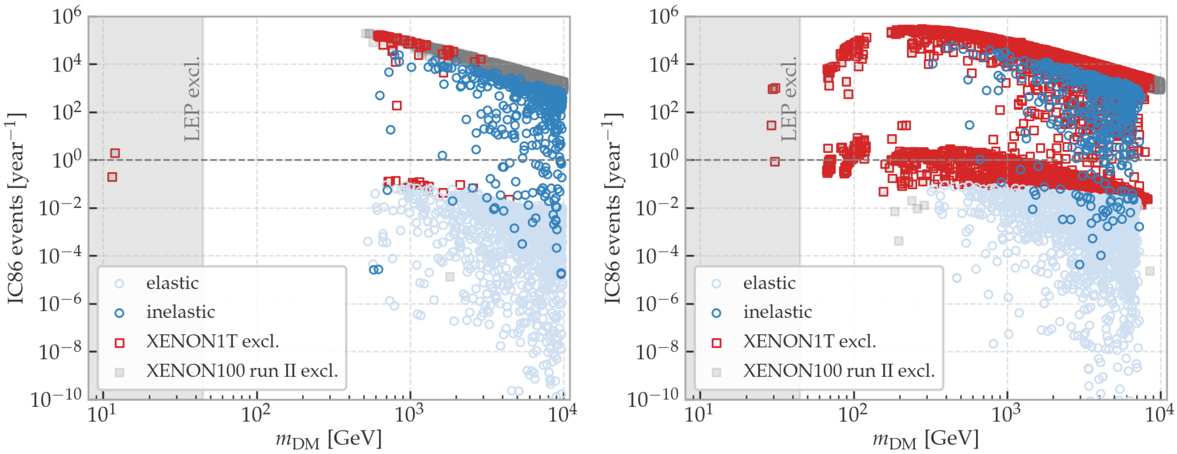

Figure 4.14: Results of the parameter scans III and IV, shown in the plane of the expected IceCube event rate vs. the Dark Matter mass. The colors and shapes indicate whether the scenarios feature an inelastic scattering component (dark circles) or not (light circles), and whether they are excluded by XENON100 run II (gray squares) or XENON1T (red squares). Furthermore, the LEP limit from the invisible Z^0 boson decay is shown as a gray band (for references refer to Sec. 4.3). **Left:** Results of scan III with the free parameters listed in Tab. 4.3. **Right:** Results of scan IV with enforced scalar-fermion co-annihilation, with the same free parameters, and the additional constraint of M_{N_i}=$m_{\rm DM}$ + 0.1 GeV, with $N_1 = N_2 = N_3$.

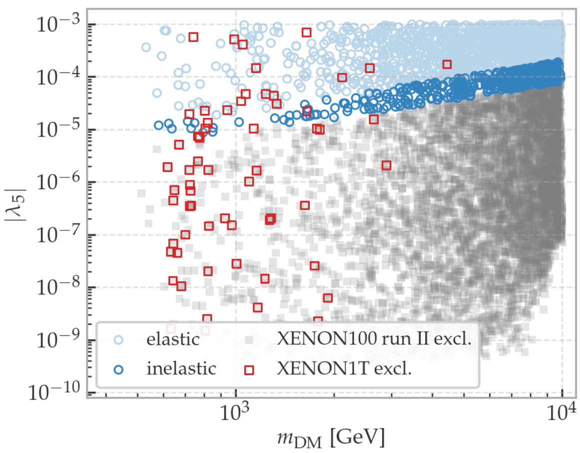

Figure 4.15: Results of the parameter scan III, shown in the λ_5 vs. Dark Matter mass plane. The colors indicate whether the scenarios feature an inelastic scattering component (dark circles) or not (light circles), and whether they are excluded by XENON100 run II (gray squares) or XENON1T (red squares); for references refer to Sec. 4.3.

very large number of signal events are not exactly promising candidates either (such a signal would most likely have been observed already), there are many scenarios in a realistic range of $\sim 1 - 1,000$ events per year. Note that these event rates have been calculated with effective areas from a previous analysis [124], and are likely to change by a small factor once we apply the effective areas from this study.

The results from the co-annihilation scan do not differ substantially from those of the random scan, if not taking into account the already excluded scenarios. In fact we observe that the parameter space that is gained by enforcing co-annihilation is almost completely restricted by XENON100 and XENON1T.

Since we aim to constrain the scotogenic parameter space in terms of λ_5, we plot the scenarios again in the plane of the model parameter λ_5 vs. the Dark Matter mass in Fig. 4.15, again in terms of elasticity and exclusion by means of direct detection. We see that a large portion of the λ_5 parameter space is already restricted by XENON100 run II data, which concerns exclusively scenarios with smaller λ_5 and therefore "stronger" inelasticity. XENON1T excludes a few more scenarios which are scattered all over the λ_5 range, but are located more towards smaller Dark Matter masses (note that in Fig. 4.15 we adjusted the mass scale to better fit the visible scenario space). The scenarios that are not marked excluded are viable with respect to all constraints presented in Sec. 4.3.

In the data analysis in Chp. 5, the scenarios that "survived" the viability scrutiny of the previous sections are investigated, i.e. all not-excluded scenarios shown in Fig. 4.15; a total of $1,723$ viable scenarios, 437 inelastic and $1,286$ purely elastic. As concluded earlier, a larger viable parameter space is not achieved by enforcing co-annihilation, so the focus is on the scenarios from scan III in which co-annihilation is not enforced.

4.6 Summary

The Scotogenic Model extends the Standard Model by a new Majorana fermion singlet with three generations, and a new scalar doublet, in addition to a new global $\mathbb{Z}_2$ symmetry under which all new fields are charged odd. This new field configuration gives rise to five new electrically neutral particles — three fermions and two scalars — the lightest of which is a natural Dark Matter candidate. Fermionic Dark Matter does not accumulate in the Sun, which is why we focus on scalar Dark Matter in this work. The small mass splitting between the two scalars enables the Dark Matter candidate to up-scatter inelastically into its heavier state with the nuclei inside the Sun. We find that inelastic scattering can boost the capture rate and therefore the expected neutrino flux from Dark Matter annihilation inside the Sun substantially.

Several parameter scans were conducted to probe the parameter space of the Scotogenic Model. We find that the "regular" Scotogenic Model does not offer a parameter space that is particularly open to indirect detection methods. Enforced early-universe co-annihilation between the new fermions and new scalars shifts the parameter space slightly in favor of indirect detection, at the prize of fine-tuning. In contrast to that, the implementation of inelastic Dark Matter opens large parts of the parameter space to neutrino telescopes, by boosting the expected event rates by several orders of magnitude. A combination of inelastic Dark Matter and co-annihilation strengthens the effect even more, but the parameter space regions that are gained in this way are found to be excluded by direct detection results.

Focusing on the results from the parameter scan including inelastic Dark Matter without enforced co-annihilation, we find that the mass splitting threshold below which all investigated scenarios feature inelastic scattering is $\delta^{<}_{\text{inel.}} = 595.05\,\text{keV}$. We identify $1,723$ scenarios — 437 inelastic and $1,286$ purely elastic scattering scenarios — that remain viable after comparison with a variety of experimental constraints; these scenarios will be the subjects of the IceCube data analysis in Chp. 5. In the scope of the analysis, the IceCube data will be probed for the fluxes predicted in this chapter, with the goal of constraining the parameter space further in terms of the mass splitting parameter λ_5.

Chapter 5
Analysis with nine years of IceCube data

In the data analysis, the scenarios of the Scotogenic Model found in the previous chapter are subjected to a comparison with experimental data, taken by the IceCube experiment in nine years from 2011 until 2020.

This chapter is organized as follows: In Sec. 5.1, the general concepts of (IceCube) data analyses are introduced. In Sec. 5.2 the theoretical sources of background events are identified, before the technical specifications about the data samples are described in Sec. 5.3. The effective area of this analysis is presented in Sec. 5.4. The statistical methods of the analysis are explained in Sec. 5.5. The sensitivities (results of the blind analysis) are presented in Sec. 5.6; followed by the upper limits in Sec. 5.7 and a quantification of the systematic uncertainties in Sec. 5.8. The final results are presented and discussed in Sec. 5.9.

5.1 Analysis introduction

In the following, underlying concepts and terms commonly used in IceCube data analyses are explained. This introduction should provide the reader with all the necessary tools to understand the methods used in this study.

Event selection

The reader has learned about the IceCube data acquisition process in Sec. 2.3.3, where the explanations ended with the so-called physics events. In this section it is described how these physics events enter an analysis, following Ref. [44].

The physics events that trigger the detector are sorted by means of an online processing and filtering (PnF) system running on hardware inside the ICL. It is the lowest filter level in the IceCube event selection chain. It sorts events into rough categories like cascades, tracks, DeepCore events, etc. These filters are based on relatively simple algorithms like SMT trigger conditions (recall Sec. 2.3.3) or very basic reconstruction quantities that can be efficiently applied to large amounts of raw data. The events that pass the PnF system as physics events make up about 10 % of the data, and are sent North over satellite on a daily basis, while the other 90 % are stored on disk and shipped out at the end of South Pole season.[1]

[1]Hits that fall through the trigger-and-PnF grid still bear potential for some studies. For instance, very low-energy neutrinos (in the MeV region), as they would be generated by supernovae explosions, would leave a signature in the detector that the system would identify as a mere rise in the noise level. So in general, all raw data is considered potentially interesting for (future) analyses, and is archived on disk.

Even after the initial filtering, IceCube puts out an immense, unpractical amount of physics events. So depending on the requirements, an analyser has to pick out those events that are most relevant to her particular study. This process is called *event selection*, which usually refers to all successive filtering after the PnF level. This higher level event selection happens offline and is specific to the different working groups[2] or even single analyses. Each selection level applies different algorithms to reduce the event content further and to improve the sample purity, where the filter complexity usually increases with decreasing event rate.

In case of this analysis, the interesting events are neutrino signals from WIMP annihilation inside the Sun. Based on Chp. 4, one has an idea of what the flux might look like in terms of energy spectrum, and know that it must originate in the Sun — but whether it actually exists, one can *not* know. One might be able to find similar events in the pool of data, but they could be *anything*, not only because reconstruction is difficult and imperfect, but also because the background is overwhelming. *Background* means all events that resemble those that are looked for, but are of different origin; versus the *signal*, which describes only those (hypothetical) events from WIMP annihilation in the Sun. Studies like this are often compared to the figurative search of the "needle in a haystack".

Many IceCube analyses which aim at finding neutrinos from a specific source, be it within or beyond the Standard Model, face this challenge.[3] The recipe is similar for all (point-source) studies: Select an energetically relevant haystack of events, and apply a statistical method that is able to identify a potential excess of events in regard of the directional information. The margins of the haystack are chosen as small as the reconstruction uncertainty permits. For instance: Is the direction reconstruction reasonably accurate, one could select events close to the point of interest and discard all others. Often, the initial sample will contain almost exclusively background; it is the analyser's job to apply appropriate techniques to identify any potential signal.

What is considered background in a point-source study might be signal to a so-called "diffuse analysis". With this type of study one can investigate oscillation of atmospheric neutrinos, seasonal variations in the atmospheric muon flux, or other quantities that are tied to a specific kind of particle, but not a particular point of origin.

The event selection is an important and usually very complex part of the analysis, and not rarely improved over the course of several years in order to increase yield and purity. That is why often several analyses are based on the effort of a single event selection. Most selections are modular, meaning they select certain events in several subsequent levels, and different analyses can intersect at any level that is closest to the particular requirements and take it from there.

The term *purity* refers to the quality of the selection. This does not describe the signal to background ratio — which is different for every analysis — rather than the ratio of events that are selected on purpose, and events that end up in the sample "by accident" (for instance, a selection of atmospheric neutrino events would consider atmospheric muon events as impurities). Of course the purity can be increased by harder cuts — at the expense of yield. Balancing these two quantities is a major challenge of the event selection.

---

[2] The working groups within the IceCube collaboration and their primary fields of research are listed here in alphabetical order: Beyond Standard Model (Dark Matter, magnetic monopoles, sterile neutrinos), Cosmic Rays (cosmic ray muon analyses, distribution and chemical composition of cosmic rays), Diffuse/ Atmospheric (atmospheric neutrinos and diffuse fluxes of cosmic neutrinos), Neutrino Sources (high-energy neutrinos of astrophysical origin), Oscillations (neutrino oscillation physics), Supernova (low-energy neutrinos from supernovae).

[3] For examples of other Dark Matter point-source searches, see Refs. [157, 158, 159, 160].

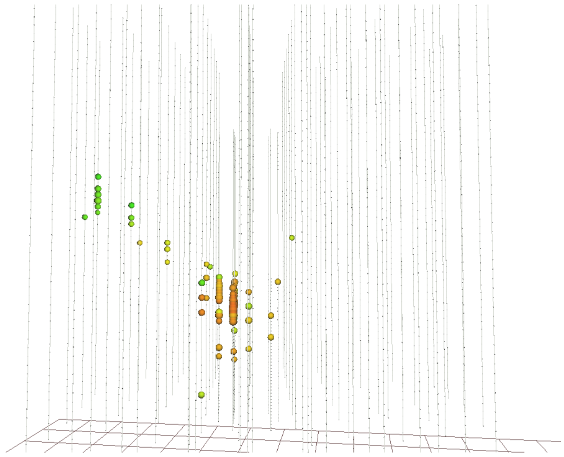

Figure 5.1: Visualization of a track signature in the IceCube detector. The shown event is a muon neutrino event from the combined event selection used in this study, with a reconstructed energy of $\sim 400\,\mathrm{GeV}$.

Event reconstruction

Once an event is identified as a physics event, it has to be *reconstructed*, meaning one tries to estimate direction and energy, and even quantities like particle type of the presumed original particle, from the amount, spacial distribution and timing of the collected hits. First reconstruction is actually done by PnF [44] itself, but it is usually quite basic due to the sheer amount of data the system has to crunch. More sophisticated reconstruction is working group specific and part of the complex and computationally expensive event selection process. Also, as it should be stressed in particular: Reconstruction is never perfect. But modern techniques like machine learning algorithms and general improvement of simulations result in increasingly accurate reconstruction. As a rule of thumb: The more light detected, the easier and more accurate the reconstruction. (Accuracy can be determined by reconstructing simulated events of which the true quantities are known.)

All events are unique, but can be categorized into groups (recall Fig. 2.16). The most interesting category for this analysis is that of track-like events. Tracks are the signatures of muon neutrinos, and they usually enable the most precise direction reconstruction, by which they can be traced back to their potential source. In the case of this analysis, the source of the neutrinos would be the Sun — although the neutrinos of interest would not produce signatures quite as impressive as the one in Fig. 2.16, due to their significantly lower energy. An example of a track signature much more representative to this study is shown in Fig. 5.1. The shown event has a reconstructed energy of roughly 400 GeV, and is one of the more "presentable" ones, since the shape of the track is clearly visible.

The IceCube coordinate system

Directional information of neutrino events is obviously of immense importance to this study, since the events of interest come from a certain point in the sky — the Sun. The information is provided as a pair of angles, *azimuth* and *zenith*, which define the reconstructed point (or true point for simulation events) in the sky from which the event originated. But coordinates at the poles of the Earth can arguably be very confusing, and on top of that, IceCube uses a non-standard convention. All events in the chosen data samples come with directional information, conveniently converted into that special coordinate system, so one does not need to worry much about it. Nonetheless, a short excursion on the quite interesting peculiarities of polar coordinates is given in Appendix A.

Unblinding

The standard procedure in IceCube (and scientific research in general) dictates a "blind" analysis. It means that the analyser is not granted full access to the event selection before the analysis methods have been thoroughly tested and reviewed, in order to avoid unintentional bias towards the outcome of the study.

Blindness can be realized in different ways: Either the analyser is given a small fraction of the data (e.g. 10 %), which is called the "burn sample". It is sufficient to build and test methods and techniques, but does not hold enough events to nudge the investigation towards any sort of statistically significant result. Another option is to use the full data sample, which is modified in a way that eradicates all traces of potential signal, e.g. by assigning new, random directions to the events. This method is called "scrambling" and is a popular choice for point-source like analyses, and is employed in this study as well. A third option is to work with entirely artificial simulation data, which offers certain flexibility but comes with a whole new set of challenges of its own.

Unblinding means to gain access to the full/ real event selection. The analysis in question undergoes thorough scrutiny by two experienced collaboration members appointed by different working groups, and unblinding is eventually only granted upon approval of the entire collaboration, after a certain review procedure and the presentation of a detailed unblinding proposal.

Simulation

Event simulation means the creation of artificial particles, which interact with artificial ice in an artificial IceCube detector — all virtually in a computer, of course. Simulations help to improve the understanding of physical processes, for instance the interaction of neutrinos in the ice or the atmosphere, as well as detector properties, by comparison with real data. Simulated events are usually generated by means of Monte Carlo (MC) random sampling, and then propagated through space/ atmosphere/ ice, interacting with other particles according to equations and probabilities that represent state-of-the-art knowledge of the underlying physics. Depending on the number of events, the complexity of the interactions and the length of propagation, these simulations can take weeks of processing to complete.

The most obvious advantage of such artificial data is that the true values of all quantities are known. Reconstructed values made by some algorithm can therefore be compared to the true values, and be used to improve the algorithm until it performs well enough to be applied with some confidence to real data, for which "true values" in that sense do not exist. A crucial prerequisite to this approach is, of course, that simulated and real data are sufficiently alike. This is called *data-MC agreement*.

The event selections used in this study come with corresponding simulation sets, which is an invaluable advantage, because they can provide precise images of what the hypothetical neutrinos from WIMP annihilation in the Sun would look like in the particular sample, if they existed. This can be achieved by weighting the artificial events.

Weights

When originally generated, simulation events have a detector interaction rate of 100 %, because it would be a waste of computational efforts to create a particle, propagate it and have it interacting in all kinds of ways, to then let it pass the detector unnoticed. Such a high hit rate is of course not physical. Therefore, every simulation event gets assigned a *weight*, which takes into account the actual physical event rate that is to be expected from a particular flux. By changing the weights, a single simulation set can resemble multiple fluxes, according to the needs of the analyser.

The weight is defined as

$$\omega = \frac{d\phi}{dE}\frac{O}{N}, \tag{5.1}$$

where ϕ is a flux, E is the neutrino energy, N is the total number of events in a simulation, and O is a quantity called *one-weight*. It is the factor by which the simulation set, in combination with the chosen flux, obtains physical meaning. It is defined as

$$O = \frac{P_{\text{int.}}}{E^{-\gamma}} \int_{E_{\text{min}}}^{E\text{max}} E^{-\gamma} dE \cdot A \cdot \Omega, \tag{5.2}$$

with units $\left[\text{GeV}\,\text{cm}^2\,\text{sr}\right]$, and takes into account the interaction probability P_{int}, the spectral index γ, the minimum and maximum generation energies $E_{\text{min/max}}$ of the simulation set, the generation area A and the generation solid angle Ω. Every single event created with IceCube simulation software is delivered with a one-weight, for the practical reason that re-weighting does not require knowledge about how the set was generated.

The weight ω is equivalent to an event rate and comes in units $\left[\text{s}^{-1}\right]$ (since a flux has units $\left[\text{GeV}\,\text{cm}^2\,\text{sr}\,\text{s}\right]^{-1}$). When integrating the weights over E and and multiplying by some lifetime, one obtains the absolute number of events in the sample.

In this study, the simulation sets are weighted with the flux of neutrinos from WIMP annihilation in the Sun that is predicted by our studies of the Scotogenic Model, in order to construct probability density functions of the signal.

Effective area

A concept that is not trivial but also not overwhelmingly well explained in literature is that of the effective area. One might find definitions suggesting that the effective area is a property of the detector, or a property of the neutrino flux, while actually it is both:

The effective area is a property of a detector in regard of a specific neutrino flux. It is a function of energy and zenith angle, and describes the equivalent area that the detector would have assuming that it was 100 % sensitive to the neutrinos in the given flux, while holding the total event rate constant.

For neutrino telescopes, the "effective detector" is typically about a few cm^2 up to m^2 wide, depending on the energy. A detector can have different effective areas depending on the "use case". A small effective area in a certain energy region could either mean that the detector as a machine is not suited (e.g. because of size or instrumentation density), or that not many events survive the event selection in that energy band, or both. In other words, the effective area has to always be viewed in light of the specific analysis.

A question that comes to mind is why the effective area is, in fact, an area, and not a volume. That again is particular to the analysis: For searches that focus on track-like events, like this study, one can assume infinite tracks starting outside the instrumented volume. The

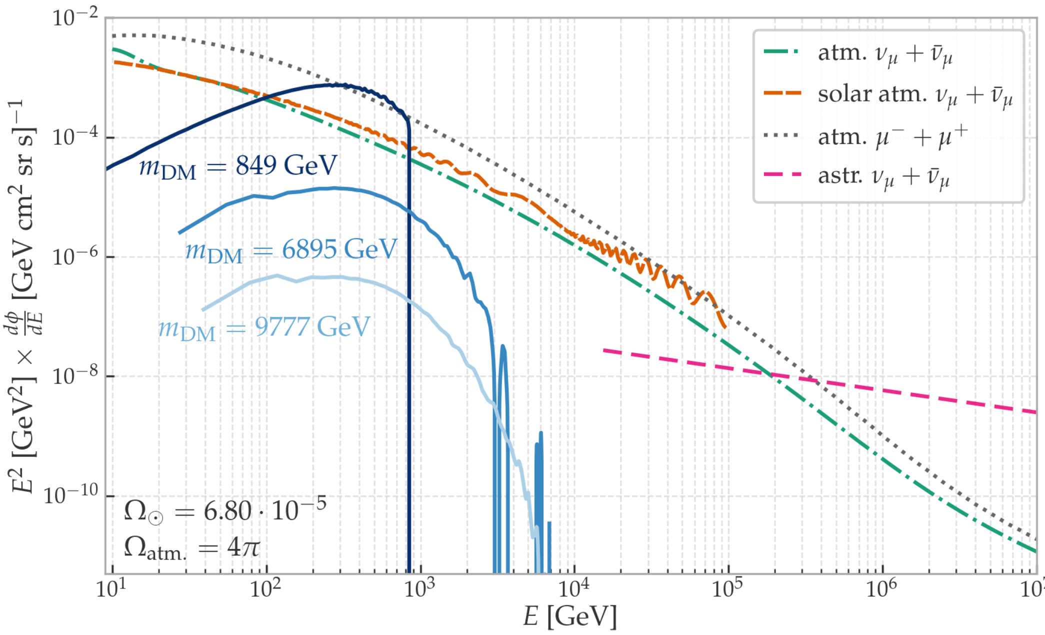

Figure 5.2: The signal and background fluxes of this analysis. The solid blue curves show examples of possible neutrino signals from WIMP annihilation in the Sun for different WIMP masses. The green dashed-dotted and brown dashed curves are the background fluxes of atmospheric and solar atmospheric neutrinos, respectively. While they appear to be of roughly the same magnitude, the atmospheric flux is omni-directional, whereas the solar atmospheric flux is suppressed by the solid angle of the Sun, $\Omega_\odot$. The gray dotted curve shows the background of atmospheric muons. The pink dashed curve is the background of astrophysical neutrinos. All fluxes are averaged over zenith and represent combined particle and antiparticle fluxes of muon flavor. The curves are multiplied with E^2 to bring out steeper regions in the spectrum.

point of interaction is not important here, one just needs the track to hit the detector *at all*. So the relevant quantity is an area. For analyses of cascade events, on the other hand, one has to consider an effective volume, since those signals are (ideally) contained within the detector.

5.2 Background

In this analysis, the (in principle) relevant backgrounds are: Atmospheric muons, atmospheric neutrinos, solar atmospheric neutrinos, and astrophysical neutrinos. An overview plot of the background and exemplary signal fluxes is shown in Fig. 5.2. Since the neutrino energy can not exceed the total half energy involved in a WIMP annihilation, one observes a sharp cut-off at the WIMP mass for the signal fluxes, whereas the background fluxes are based on much broader spectra with no such limitations. The individual background fluxes are listed in the following, and their relevance to this study is discussed.

Atmospheric muons

Atmospheric muons are part of the secondary flux that arises from the cosmic ray bombardment of the atmosphere, recall Sec. 2.2.1. Even though muons are their own interesting field of research, they are considered an impurity to studies that focus on neutrinos, including this one. Depending on the energy, atmospheric muons can penetrate the crust of the Earth down to several kilometers below the IceCube detector (which lowest DOMs are located roughly 2.5 km beneath the surface). So despite the muon-shielding effect of the ice layer above the detector, the vast majority of particles that interact in the instrumented volume coming "from above" are muons — the event rate is about 3 kHz. No atmospheric muon can travel as far as to enter the detector from below, so a very efficient method to suppress them is by discarding events with down-going direction. The event selections used in this study use the same approach, reducing the muon impurity to a negligible fraction of the background. (A great deal of collaboration effort is dedicated to less "wasteful" methods of muon suppression, for instance using IceTop as a veto mechanism to distinguish track signatures that start within the in-ice array from tracks that start above it. These alternative methods become important e.g. for studies that search for point-sources in the Southern hemisphere.) For a characterization of the atmospheric muon flux with IceCube, see Ref. [161].

Atmospheric neutrinos

They are the main background and main ingredient of the event selections used in this analysis. They, too, are a part of the secondary cosmic ray flux and about as abundant as atmospheric muons, but trigger the detector with a frequency only remotely comparable, with a ratio of about $1 : 10^6$. But unlike atmospheric muons, they can enter the detector from all sides. By means of a statistical analysis, especially by considering the directional information of the events, an excess of events from the Sun could be singled out from the atmospheric neutrino background.

Solar atmospheric neutrinos

These events form a somewhat tricky impurity to the data sample. They are not distinguishable from signal events on an event by event basis, just like the Earth atmospheric neutrinos. However, unlike for the latter, a statistical analysis using the directional information of the events is impeded by the fact that this flux, like the signal, comes from the direction of the Sun. So if an excess of events from the Sun was measured, a way of distinguishing solar atmospheric events from signal events would still have to be found. The two fluxes differ in terms of energy spectrum, and also the solar atmospheric neutrino flux would be the same for all investigated scenarios, while the signal neutrino flux would not. This information could be incorporated by means of an additional background probability and estimator in the likelihood function (for the statistical methods see Sec. 5.5). For analyses aiming at discoveries, some way of accounting for the solar atmospheric flux would be required; for exclusion analyses aiming at upper limits, the solar atmospheric flux could also be taken as one component of a combined background without treating it specially, which comes at the price of weaker sensitivities and more conservative upper limits. In this study, the latter approach is taken.

Astrophysical neutrinos

The astrophysical neutrino flux has the hardest spectrum of all fluxes shown in Fig. 5.2. IceCube was optimized for these high-energy neutrinos, but to this search astrophysical neutrino events are considered an impurity. They can not be distinguished from high-energy atmospheric neutrinos on an event by event basis. However, the astrophysical flux is extremely low, and

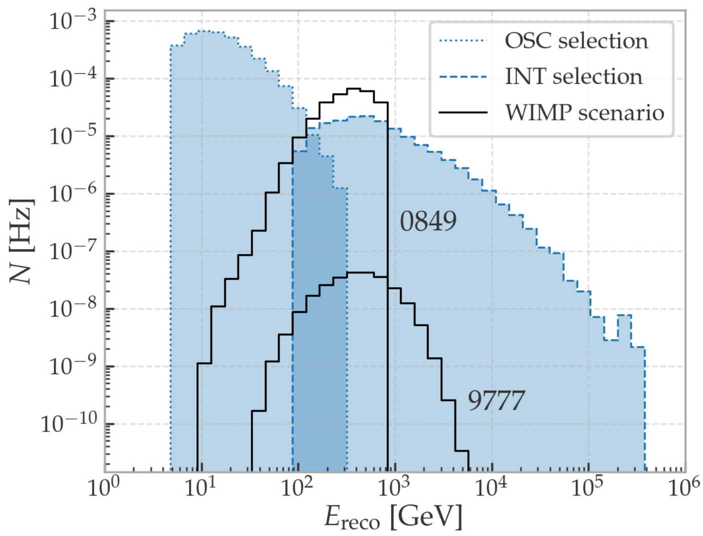

Figure 5.3: Event rate of the two event selections (blue histograms) at final filter levels and after applying all additional cuts; and the expected signal event rates for the benchmark scenarios 0849 and 9777 (black solid histograms). The effective area used to compute the signal event rate is taken from [124].

does not share an energy range with the expected flux from WIMP annihilation. This impurity is therefore not considered problematic.

For details about sources, production mechanisms, and further properties of the listed fluxes, please refer to Chp. 2.

5.3 Data sets

The analysis is performed with nine years of IceCube data, taken between 2011 and 2020. Two different existing data sets are combined to cover the entire relevant energy range: The OscNext sample for the low-energy region of up to $\sim 300\,\mathrm{GeV}$, and the Improved Northern Tracks sample for the high-energy region of $\sim (100 - 10,000)$ GeV. This section presents a description of the two sets, and explains the respective event selections.[4] Note that the event selections used in this study are entirely the work of others; any possible modifications to the resulting samples made by the author are indicated as such in the following subsections.

In Fig. 5.3, the sample coverage of this analysis is presented, to show that the chosen event selections provide events of relevant energies.

Concerning the "combination" of the two data sets: In the statistical analysis, the selections are treated separately, meaning events from the low- and high-energy selections are analysed with probability density functions based on the respective sets, and no combined probabilities are applied. For the statistical methods, refer to Sec. 5.5.

[4]Readers with access to the IceCube internal data storage find a much more detailed documentation of the event selections at the following locations:

`https://wiki.icecube.wisc.edu/index.php/OscNext.`
`https://user-web.icecube.wisc.edu/~tglauch/PS_Analysis/_build/html/index.html`
`https://diffuse-sample-doc.readthedocs.io/en/latest/`

Data set versions, file locations and analysis code can furthermore be accessed via the author's analysis wiki:

`https://wiki.icecube.wisc.edu/index.php/Solar_inelastic_WIMPs_analysis`

5.3.1 Low-energy event selection

The OscNext event selection is used at final filter *Level 7*, the so-called "high stats sample", covering nine years of data (2011 — 2020) in the DeepCore detector configuration. This selection aims at low-energy events, to study atmospheric neutrino oscillations among other things (hence the name). At final filter level, the set is dominated by all-flavor atmospheric neutrino events from the Northern sky, with a zenith cut-off at $\theta \approx 73\,°$, and a negligible flux of atmospheric muons.

Reconstruction of low-energy events can be quite challenging, especially the reconstruction of event direction. Elaborated reconstruction techniques and filter methods are employed to reach the best possible reconstruction quality; and with it the best possible sample purity at maximum neutrino event rate. In the following, an attempt is made to describe the different filter levels and methods briefly. Since filtering and reconstruction in this case is an effort of the Oscillation working group, the reader is pointed to their publications in Refs. [46, 162] for more information.

Level 2: Selects all events that pass the *DeepCore filter*, meaning events with at least three hard local coincidences inside the DeepCore region. The filter features a veto algorithm that aims to identify hits that might be causally related to muon events, depending on time and location, therefore discards first atmospheric muons from the sample.

Level 3: Removes regions of data-MC disagreement that arise from certain events that have no simulation counterparts in the OscNext MC data sets. The total event rate after level 3 is below 1 Hz.

Level 4: The data-MC agreement at this stage is sufficient for machine learning algorithms, which are applied to further separate noise and muon events from atmospheric neutrino events.

Level 5: All "obvious" muon events are successfully rejected at this stage. Level 5 aims at identifying less obvious muon events, e.g. those that escape the DeepCore veto region through so-called corridors, arising from the geometrical grid structure of the detector.

Level 6: The last two filter levels 6 and 7 are unique to the OscNext high stats sample. At this stage, elaborated reconstruction algorithms are applied to the remaining events, which evaluate the quality of some reconstructed quantities and cut or pass events on the basis of this evaluation.

Level 7: Rejects further muons on the basis of the improved event reconstruction quality after level 6. Estimates neutrino flavor by distinguishing track- and cascade-like events.

The expected event rates from different interactions present after the final filter are summarized in Tab. 5.1. Only few additional modifications to the high stats sample are made in the scope of this work to account for the specific requirements of this analysis. These modifications are:

- All events that initially passed the *Muon filter*, which is a level 1 filter, are retroactively rejected, in order to avoid overlap (double-counting of events) with the high-energy event sample. Roughly 2/3 of the original sample remain after this step.
- Certain alterations to the structure of the sample, such as file type and field names, which do not alter the event content.

Both the experimental data set and the corresponding MC simulation set of the OscNext selection are essential prerequisites to this analysis. A residual data-MC disagreement between the two sets can not be ruled out due to a limited — though constantly improving — understanding of neutrino properties, atmospheric interactions, and particle propagation. The agreement has recently been improved by introducing a new bulk ice model into the simulation which incorporates bi-refringence (BRF) properties of the ice. These new BRF sets are used in this study to estimate signal probabilities. For this purpose, the simulation events are weighted with the fluxes obtained in the Scotogenic Model studies.

The background is based on the assumption that very few signal events (if any) are present in the sample, and that the atmospheric neutrino flux is distributed homogeneously in azimuth across the sky, so that the experimental sample delivers an almost perfect background straight out of the box. Systematic background uncertainties are automatically ruled out when using real data as background, which is a huge advantage over using simulation data.

	rate [mHz]	N [9.3 yrs]	% of sample
ν_e CC	0.165	48234 ± 75	23.0
ν_μ CC	0.436	127725 ± 129	61.0
ν_τ CC	0.033	9678 ± 21	4.6
ν_α NC	0.076	22245 ± 51	10.6
μ_{atm}	0.005	1463 ± 87	0.7
noise	0.005	~ 0	< 0.03
total	0.715	209346 ± 182	100

Table 5.1: Expected event rates from different interactions in the OscNext high stats events selection, after final filter level. [IceCube collaboration, Oscillation working group]

5.3.2 High-energy event selection

The Improved Northern Tracks event selection is a high-purity sample of up-going muon neutrino events, as the name implies. The current selection covers nine years of data (2011 — 2019) in the IC86 detector configuration (using all 86 deployed strings). With a zenith cut of $\theta \approx 85\,°$, this selection is slightly more restrictive than the OscNext selection concerning up-going events.

The event selection is split into the levels described below. Filtering and reconstruction is the work of the Diffuse working group; for more details and information on the selection process, the reader is pointed to their publications in Refs. [163, 164, 165].

Level 2: Selects all events that pass the *Muon filter*, which aims at identifying track signatures, hence events that have muon neutrino origin.

Level 3: Selects up-going events from the muon branch. Applies corrections concerning split events (events that consist of two separate, not causally connected events), and algorithms to improve reconstruction quality.

Level 4: Applies machine learning algorithms to further improve reconstruction quality and reject unwanted events.

Level INT: The previous levels describe the selection of the Northern Tracks sample. The Improved Northern Tracks sample is based on this selection, but improves the reconstruction (hence the name). The main improvements are new machine learning estimators, namely the GNN (graph neural network) energy estimator and the BDT (boosted decision tree) angular error estimator.

The final level contains atmospheric muon neutrino events with an event rate of $2 \cdot 10^{-5}$ Hz and a sample purity of $> 99\,\%$, with negligible muon and electron neutrino contamination. The following minor modifications have been applied to the sample in the scope of this work to accommodate the requirements of the analysis:

- Due to the good angular reconstruction, the event content can be limited to events with an angular distance from the Sun $\Psi \leq 10\,^{\circ}$ in the final, unblinded sample.
- The true particle type information (i.e. neutrino flavor) of an event's primary particle is not saved as part of the original MC sample. The set has been modified to include this important field (because the events are weighted for muon and antimuon neutrinos separately).
- Similar to the OscNext sample, alterations to the structure of the sample are applied without any impact on the event content.

Much like for the low-energy sample, both the simulation and experimental data is important for this work. The simulation events are weighted with the theoretical fluxes to obtain a set of signal events, while the experimental set is used as background, based on the assumption that only very few (if any) actual signal events are contained.

5.4 Effective area

The reader might recall that in Sec. 4.5 an effective area of a previous IceCube work [124] was used to make predictions about the number of signal events to expect in the detector from the different scenarios of the Scotogenic Model. In Fig. 5.4, those "old" effective areas are shown, together with the new effective areas obtained in the scope of this analysis; for both the low- and high energy event selections, individually for muon neutrinos and antineutrinos. The effective areas are calculated from simulation signal events, because the simulation sets contain the required information about the true quantities of zenith direction θ_{true} and neutrino energy E_{true}. The plot shows the effective areas averaged over zenith.

It can be seen in the graph that the analysis conducted in this work performs better than the old analysis for lower energies up to ≈ 30 GeV, equally well between ≈ 300 GeV and 1 TeV, and better from there upwards (by extrapolating the old effective area for higher energies). In the mid-energy range from $30 - 300$ GeV however, a "gap" is observed where the new effective area is substantially worse than the previous one. This can be explained by the fact that the chosen event selections are not optimized for this energy region. A currently on-going IceCube solar WIMPs analysis aims at closing this gap by including yet another event selection.

5.5 Statistical methods

The analysis conducted in the scope of this work is based on data sets prepared by others. The statistical methods used in the analysis are also not new, of course, and are described for instance in Refs. [166, 167]; they have proven efficient for IceCube analyses in the past (e.g.

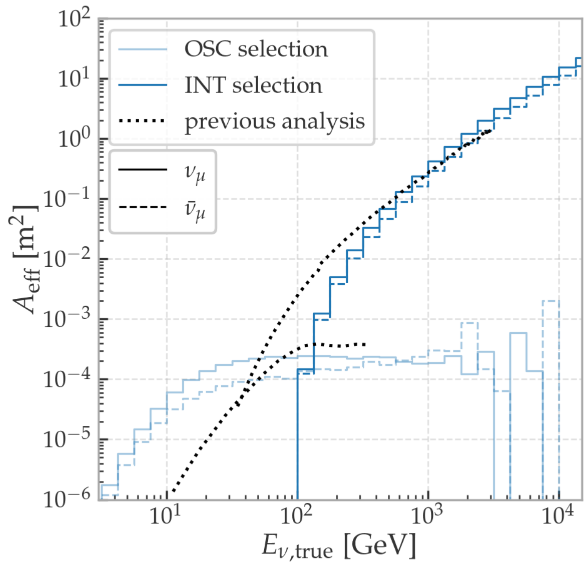

Figure 5.4: The muon neutrino (solid lines) and antineutrino (dashed lines) effective areas of this analysis, for the low-energy (light) and the high-energy (dark) selections, as a function of the true neutrino energy, averaged over zenith. Shown is furthermore the combined neutrino and antineutrino effective area of a previous analysis [124], which has been used in Chp. 4 to predict the number of IceCube signal events.

[157, 158, 159, 160] and many more). The application of the statistical methods to the data in the particular setup of this study, however, is my (the author's) effort, and encompasses the development of an entirely new software framework. This framework is described in more detail in Sec. 5.5.6.

But first, a description of the statistical potential and limitations of this analysis is given, followed by an overview of the employed statistical methods.

The true nature of the WIMPs that have accumulated in the Sun — *if* there are any — is hidden in the neutrino signals, given that the current detector configuration is sensitive enough. The signals themselves are hidden within an overwhelming amount of background (remember the "needle in a haystack" analogy). One can not know which WIMP scenario is the "correct" one, but one can systematically scrutinize the haystack for all the different "needles", one at a time. There are 1,723 scotogenic scenarios that withstand the many viability tests implemented into the parameter scan, and all of those could theoretically embody the correct description of Dark Matter.

One way of telling which of the scenarios fits the data best is to conduct a parameter estimation (parameters here meaning the free parameters of the Scotogenic Model; m_η^2, λ_5, etc.). This proves difficult in the case of this work, for two reasons: First of all, the parameter space, or at least some regions of it, are most likely not continuous. Secondly, the parameters are highly correlated, meaning it is difficult to only change one parameter at a time. The only parameter that can really be estimated is not a model parameter, but the number of signal events mingled in the data (which will be looked at in more detail below). The scenarios, i.e. parameter points, that were obtained during the numerical scan, do not represent a likelihood distribution, meaning that one cannot infer certain better or worse ranges of values for individual parameters from them. This would only be possible if the parameter points were sampled *from* a likelihood distribution. In other words, the way this study is set up does not allow for a parameter estimation.

What can be done, however, is to test the degree of consistency of each scenario with the hypothesis that there *are* WIMP signals hidden in the data, versus that there are not. Those two hypotheses are defined as follows:

Hypothesis (HS): The data sample consists of events originating from background, as well as events produced in the Sun by the annihilation of WIMPs defined by scenario $\vec{\chi}$, with a certain number of signal events n_s.

Null-hypothesis (H0): The data sample consists of background events only ($n_s = 0$).

The $\vec{\chi}$ hereby represents the collection of the scenario parameters. To subject a scenario to an *hypothesis test* [166], one first needs to define the *likelihood function*, which is done in the next section.

5.5.1 Likelihood function

Suppose there are a number of events N in the final sample, and each event i can be associated with a set of observables $\vec{y}_i$. From these observables one can formulate probability distributions, or *probability density functions* (PDFs), which are different for signal and background: $S_{\vec{\chi}}(\vec{y})$ and $B(\vec{y})$, where $\vec{\chi}$ embodies the model parameters that define a specific Dark Matter scenario. The events in the sample can then be drawn from the combined PDF, which depends on the number of signal events n_s in the sample:

$$P\left(\vec{y}_i|n_s\right) = \frac{n_s}{N} S_{\vec{\chi}}(\vec{y}_i) + \left(1 - \frac{n_s}{N}\right) B(\vec{y}_i). \tag{5.3}$$

From this, one can formulate the *likelihood function* [166] which is defined as the product of the PDFs of all individual (independent) events:

$$L\left(\left\{\vec{y}_i\right\}|n_s\right) = \prod_{i=1}^{N} P\left(\vec{y}_i|n_s\right) = \prod_{i=1}^{N} \left\{\frac{n_s}{N} S_{\vec{\chi}}(\vec{y}_i) + \left(1 - \frac{n_s}{N}\right) B(\vec{y}_i)\right\}. \tag{5.4}$$

It is a measure for the agreement of the data set with the parameters n_s and $\vec{\chi}$. For the null-hypothesis, this simplifies to

$$L_0\left(\left\{\vec{y}_i\right\}|n_s = 0\right) = \prod_{i=1}^{N} B(\vec{y}_i). \tag{5.5}$$

L is a function of n_s explicitly, but only implicitly of $\vec{\chi}$. That is why, recalling from above, n_s is the only parameter that can be estimated. This is done by maximizing L: **The value for n_s that maximizes L is the best estimator μ_s for the signal strength in the data sample.**

Maximizing the likelihood function can be difficult, though, due to multiplication of very small numbers. Therefore it makes sense to use the *log-likelihood function* instead, to circumvent the necessity of multiplication in favor of a sum:

$$\ln L\left(\left\{\vec{y}_i\right\}|n_s\right) = \sum_{i=1}^{N} \ln \left\{\frac{n_s}{N} S_{\vec{\chi}}(\vec{y}_i) + \left(1 - \frac{n_s}{N}\right) B(\vec{y}_i)\right\}. \tag{5.6}$$

Later in the analysis, the log-likelihood *ratio* will be used to define a *test statistics*; but before this is explained in Sec. 5.5.3, a closer look is taken at $S_{\vec{\chi}}$ and B.

5.5.2 Probability density functions

The two relevant observables that were so far denoted with $\vec{y}_i$ are the angular distance from the Sun Ψ, and neutrino energy E. "Angular distance from the Sun" means the space angle between the center of the Sun and the reconstructed origin direction of the neutrino, which is defined with the law of cosines as [54, Chp. 3]:

$$\Psi = \arccos\left\{\sin(\theta)\sin(\theta_\odot)\cos\left(\phi - \phi_\odot\right) + \cos(\theta)\cos(\theta_\odot)\right\}, \tag{5.7}$$

with ϕ being the azimuth coordinate, and θ being the zenith coordinate of the direction the neutrino is coming from, and $\phi_\odot$, $\theta_\odot$ being the azimuth and zenith coordinates of the center of the Sun, as measured in the IceCube coordinate system at the time of the event.

Background PDF

The background PDF $B(\Psi, E)$ is obtained relatively straight forward. Since there is justified reason to believe that the vast majority of the recorded events are background events, with at most a handful of signals among them, experimental data sample can be treated as pure background. The last traces of possible signals are obliterated by scrambling the events in ϕ. This means that each event is assigned a new, random azimuth coordinate between 0 and 2π, and thereby randomizing Ψ, which is safe to do because the background events are uniform in azimuth when averaged over time (not in zenith, however, which is why the zenith coordinate remains untouched). At the same time, scrambling ensures that the analysis is performed blind. The events can then be binned in terms of Ψ and E (or $\log_{10} E$ to be precise), and weighted so that the sum of all bins is one, to obtain a probability density in form of a 2D-histogram.

Signal PDF

The signal PDF $S_{\vec{\chi}}(\Psi, E)$ is a little more complicated to construct, because unlike the background, there is no sample of real data for this purpose. Instead, artificial events from simulation data sets are used, which are weighted with the flux[5] predicted by the specific scenario. Notably, this means that $S_{\vec{\chi}}$ needs to be constructed for every scenario individually, while B is computed only once. After the flux weights are applied, the signal PDF can be obtained in the same way as the background PDF, by binning the (now artificial) data set in Ψ and E.

The simulation sets that are used for this purpose are diffuse sets, meaning they contain neutrino events from all directions, uniformly in azimuth, much like the real data. Since the true observables of simulated events are known, the sets can be filtered for those events that originated in the Sun. Only very few fulfill this requirement; not enough to build a meaningful PDF. So the set is *over-sampled* several times: A random new time stamp is chosen for each event, sampled uniformly over one year, along with the location of the center of the Sun given in $\phi_\odot$ and $\theta_\odot$, and the distance between Sun and Earth $d_\odot$ (which is subject to seasonal

[5]The flux weight is applied by multiplying it with the one-weight of each event. The one-weight comes in units of $\left[\text{GeV cm}^2\ \text{sr}\right]$; however, the flux predicted by micrOMEGAs is a point-source flux with units $1/\left[\text{GeV cm}^2\ \text{s}\right]$ and thereby not differential in steradian. To fix this steradian unit problem, one must either divide the flux by the solar solid angle, $\sim 6.80 \cdot 10^{-5}$ sr, or take only those simulated events from the sample that *actually* originate from within the sun's disk, effectively eradicating the steradian.

variations), corresponding to the new time stamp.[6] The true space angle Ψ_{true} is calculated from the true neutrino direction and the previously determined $\phi_\odot$, $\theta_\odot$, after which the sets are again filtered for the events that originated in the Sun. This process is repeated until sufficient statistics is reached. Technically, only events from the *core* of the Sun are relevant, but we allow for a slightly larger angle corresponding to the solid angle of the Sun's disk,

$$\gamma = \arctan\left(\frac{r_\odot}{d_\odot}\right), \tag{5.8}$$

$r_\odot = 6.9 \cdot 10^5$ km in radius, because the uncertainty of the angular resolution of the event selections is much larger than the radial difference, while the wider radius speeds up the over-sampling process significantly.

The resulting 2D-histogram representations of the signal and background PDFs can be smoothed using *kernel density estimation* (KDE). Both the 2D-histograms and the final PDFs produced by means of KDE are shown in Fig. 5.5. The process of creating KDE-PDFs is explained in the following.

Kernel density estimation

Kernel density estimation (KDE) [168, 169] describes a method to create a smooth probability distribution from a data set in a non-parametric way. This is done by defining a kernel for each point in the data set and summing up all kernels; the resulting curve (or surface in 2D) is the PDF. In this analysis, 2D Gaussian kernels are used, with two different standard-deviations b ("bandwidths"), one for each dimension. At each point i of the sample with the coordinates $\left(\Psi_i, \log E_i\right)$ one can define such a kernel

$$K\left(\Psi, \log E\right) = \frac{1}{\sqrt{(2\pi)^d}} \frac{w_i}{b_\Psi b_E} \exp\left[-\frac{1}{2}\left(\frac{(\Psi - \Psi_i)^2}{b_\Psi^2} + \frac{\left(\log E - \log E_i\right)^2}{b_E^2}\right)\right], \tag{5.9}$$

with $d = 2$ dimensions and the weight w_i. The PDF is then

$$G\left(\Psi, \log E\right) = \sum_{i=0}^{n} K_i. \tag{5.10}$$

A good choice of bandwidths is very important, since it has a critical impact on the KDE. Several methods were tried in this work to determine good bandwidths; none of which produced KDEs that represented the data reasonably well[7]. It was found that the bandwidths calculated with the Silverman Rule-of-Thumb [170] yielded the most reasonable results, which were iterativeley improved until the final bandwidths were chosen to those listed in Tab. 5.2. They are used for the background and all signal KDEs. When kernels for all points in a data set have been defined, the sum over all kernels results in a surface that can be evaluated at all positions

[6]One might wonder why the events are scrambled in time rather than direction. The Sun's movement across the sky as seen from South Pole is nearly uniform in azimuth, but not in zenith — there are zenith bands the Sun spends a lot of time in throughout the year, and bands it does not touch at all (e.g. $\theta \gtrsim 23^\circ$ in the South Pole horizontal coordinate system). Randomizing the event times within a full year is equivalent of "moving" the Sun across the sky, without having to account for zenith weights.

[7]The goodness of the KDE was determined by conducting signal recovery tests, a procedure described in Sec. 5.5.4.

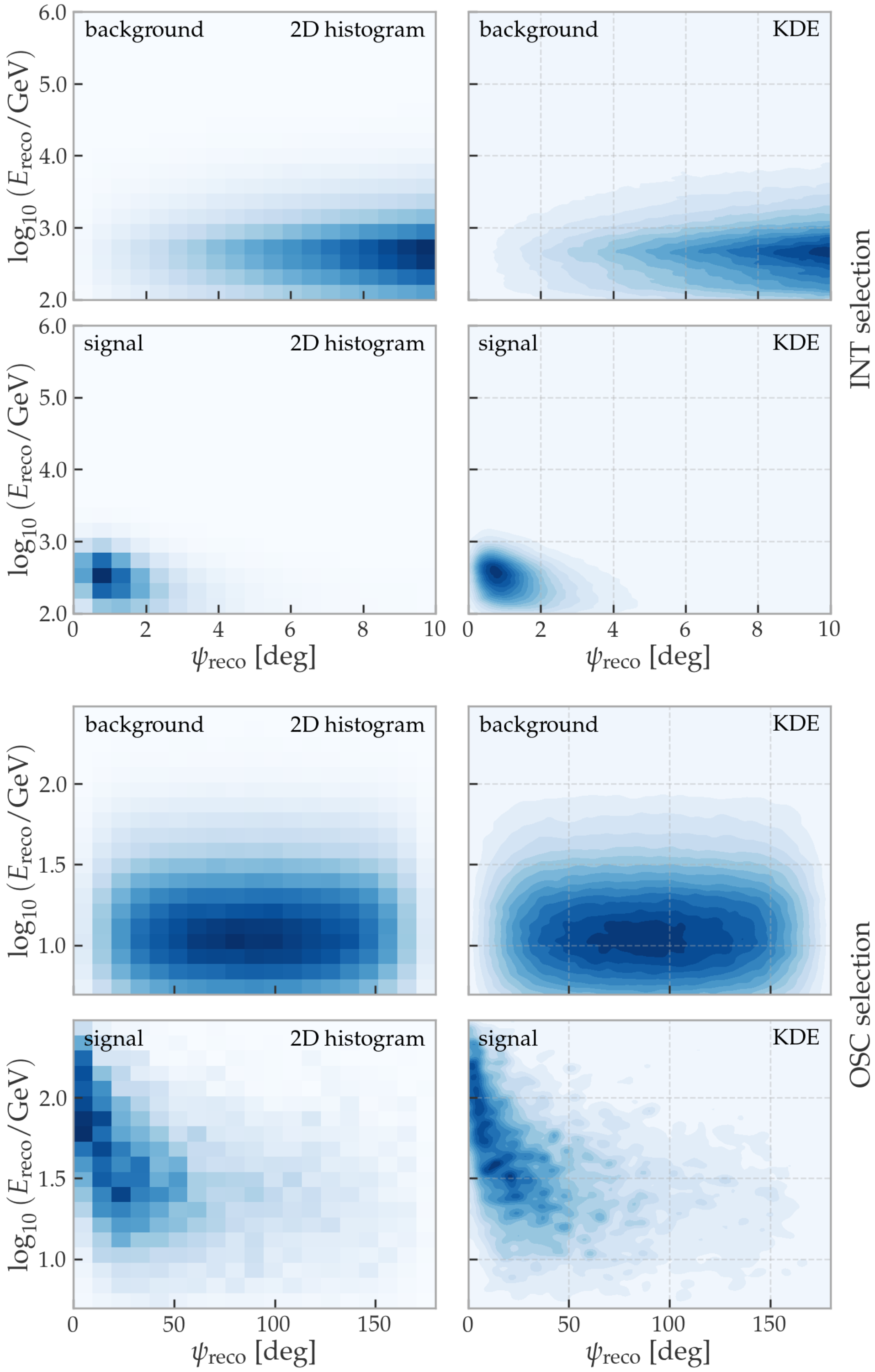

Figure 5.5: The PDFs for the high-energy INT selection (top) and the low-energy OSC selection (bottom). The respective top panels show the background PDFs, the bottom panels the signal PDFs (exemplary for the benchmark scenario 0849), in reconstructed quantities Ψ and $\log_{10} E$. The left hand panels show the normalized 2D-histograms (with event intensities increasing from light to dark), the right hand panels show the kernel density estimations (KDEs) which are used for the statistical analysis.

Table 5.2: Gaussian kernel bandwidths in Ψ and $\log E$ dimensions for both data sets used in this analysis.

data set	b_Ψ	$b_{\log E}$
Improved Northern Tracks	0.0020	0.020
OscNext	0.0420	0.020

in the $\Psi - \log E$ plane. This surface is the preferable choice as PDF over the 2D histogram, because of its non-parametric nature, but also because it is non-zero throughout the whole plane,[8] which is crucial especially for the background PDFs (the mathematical necessity of which is apparent in Eq. (5.12)). The KDE-PDFs for background and signal for both data sets, and their corresponding 2D histograms for comparison, are shown in Fig. 5.5. At close inspection, one might notice the absence of white space in the KDE surfaces, indicating once again that all values are non-zero.

The choice of bandwidths is not the only difficulty when it comes to calculation of KDEs. In the case of this analysis, the data sets are bound, meaning data points are concentrated at the edges of the defined space; for instance the INT background PDF has boundaries at $\Psi = 10\,^\circ$ and $\log E = 2.0$ as can be seen in the plots. The problem is that parts of the Gaussian kernels will flow out of bounds for data points at the very edges, which on the one hand results in data being under-estimated near the boundaries, and on the other hand results in the integral over the whole PDF to be slightly smaller than 1. These issues can be fixed by applying boundary-correction measures, e.g. using truncated Gaussian kernels, or mirroring the kernels at the boundaries. The latter option was used here. The Figs. 5.6 and 5.7 illustrate the difference between KDEs with different boundary treatments, in one and two dimensions.

Since a suitable software to calculate KDEs that handles both 2D data sets with different bandwidths *and* boundary effects was not available at the time, I developed a Python class tailored to the requirements of this study, as part of the analysis software framework. It offers KDE calculation in one and two dimensions, allowing up to four boundaries to the data sets in two dimensions, and lets the user choose between two boundary correction methods: Truncated kernels and boundary reflection. The Silverman Rule-of-Thumb is implemented as the default bandwidth determination method, with the option of setting the bandwidths manually. Because the evaluation of the KDE surface on large data sets can be computationally very expensive, an optional speed-up factor reduces the number of contributing kernels to any specific surface position. (Theoretically, all kernels have non-zero contributions at all positions, but one can assume that the contribution of kernels that are far away from the point to be evaluated is negligible; e.g. for distances of $> 5b$.) The project is publicly available, see Ref. [171].

When taking a closer look at the PDFs in Fig. 5.5, the reader may notice a few peculiarities; for instance, one might expect the high- and low-energy selection PDFs to be quite similar (except in energy range), which they most apparently are not. The main reasons are:

– The high-energy selection has a very good angular resolution, meaning the reconstructed directions of the events can in general be assumed to lie near the true directions. The directions of low-energy events, on the other hand, are harder to reconstruct. This becomes evident when comparing the signal PDFs: The high-energy signal PDF is a rather small, smooth event concentration towards the direction of the Sun ($\Psi = 0\,^\circ$),

[8] This of course only holds true in theory; positions far from a potential concentration of data points will sometimes evaluate to numerical zeros.

while the low-energy signal PDF is "smeared out" to cover almost the entire defined angular range with values significantly larger than zero.

– The low-energy background PDF is symmetric in Ψ around $90\,°$ as is expected (because of the azimuth-uniform distribution of the atmospheric neutrino flux and the locations of the Sun in the sky), while that of the high-energy selection is not. The simple explanation is again the good energy resolution of the INT sample: Even though the signal PDF is, by means of the Gaussian kernels, non-zero throughout the entire sky, it is so well "contained" in one corner of the plane that virtually no signal events are present beyond a few degrees away from the Sun. Therefore it was possible to cut the whole sample at $\Psi = 10\,°$, speeding up calculations significantly.

From the PDF plots, the reader might also have noticed that an energy overlap exists between the two selections. This overlap is approximately 200 GeV wide, compare Fig. 5.3. A corresponding event overlap is prevented by a filter applied to the OSC selection, recalling Sec. 5.3.

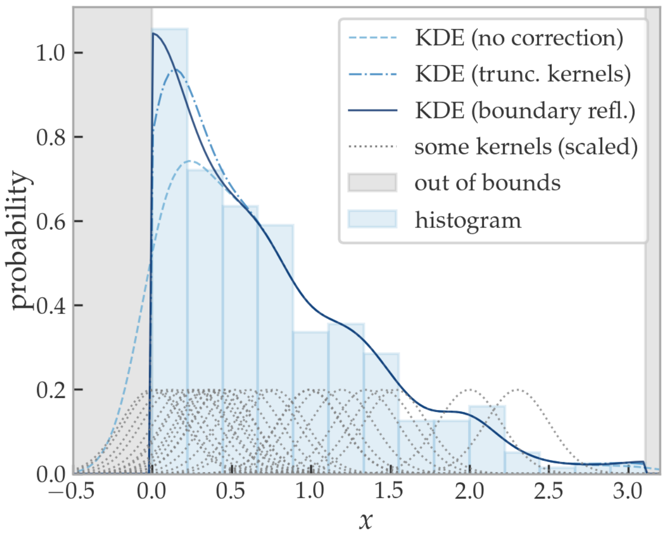

Figure 5.6: Demonstration of boundary correction on a KDE in the 1D case. The blue bars represent a histogram of some sample data that is not defined outside of the white area. A regular KDE without any boundary correction is shown as the dashed blue line, with some of the corresponding Gaussian kernels drawn in dotted gray. The dashed-dotted orange and solid black lines show KDEs with the boundary correction methods of truncated kernels and boundary reflection, respectively.

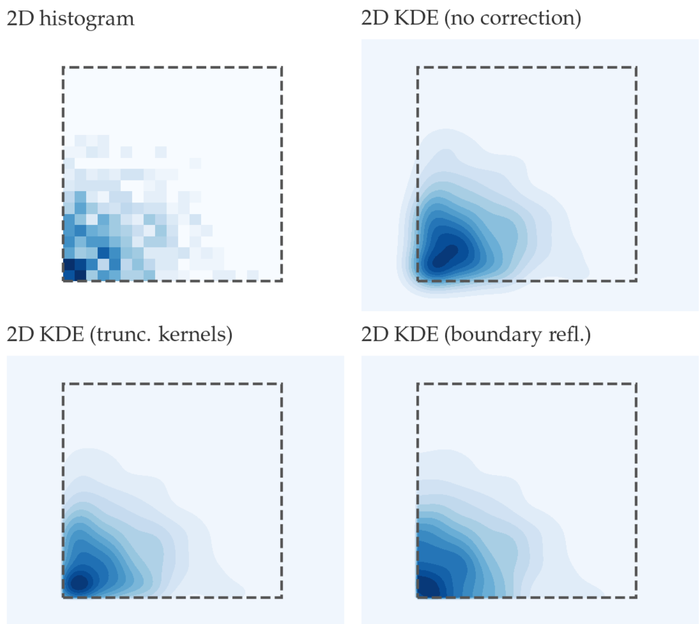

Figure 5.7: Demonstration of boundary correction effects on a 2D KDE. The top left panel shows a 2D histogram of some sample data which is confined by (i.e. not defined outside of) the dashed rectangle. Top right shows a regular KDE applied to the data, without any boundary correction. The lower left and right panels show the boundary correction methods of truncated kernels and boundary reflection, respectively.

5.5.3 Test statistics

If, for a certain data sample, one subtracted the log-likelihood of the null hypothesis from the log-likelihood of the hypothesis, theoretically one should obtain a measure of preference: The larger the result, the more preferable the hypothesis, and vice versa. One can formulate a *log-likelihood ratio*:

$$\ln L - \ln L_0 \quad = \quad \ln\left(\frac{L}{L_0}\right). \tag{5.11}$$

After the *Neyman-Pearson Lemma* [172], a hypothesis test [166] using a likelihood ratio function has the strongest statistical power (correctly rejecting H0) while having the lowest probability of a false-positive (rejecting H0 even though it is true).

Maximizing Eq. (5.11) over n_s would deliver not only the best estimator μ_s for the signal strengths in the data sample, but also the corresponding measure of preference, Λ. For the log-likelihood function in Eqs. (5.6) used in this analysis, the function reads

$$\Lambda = 2\sum_{i=1}^{N} \ln\left(\frac{\mu_s}{N}\frac{S(e_i)}{B(e_i)} + \left(1 - \frac{\mu_S}{N}\right)\right), \tag{5.12}$$

which is called the *test statistics*.[9] For a single data set, however, a certain value Λ does not say much at all — how can one know if, for instance, $\Lambda = 4$ is considered large? How can one decide which value is large enough to disfavor the null hypothesis? The answer lies in the name of the equation itself: Test *statistics*. A large amount of data sets is required, and the corresponding thorough distribution of Λ, to be able to judge the statistical significance of either one Λ.

Test samples

For this purpose, one creates a *test sample* from the one "true" data set. This is done by scrambling the events in azimuth (a procedure that is described in more detail in Sec. 5.5.2). One obtains a sample with the same energy spectrum but completely different Sun-event distances Ψ, therefore effectively "new" events; a procedure that can be repeated any number of times to reach the desired number of samples and statistics. From here on until the very last step in the analysis, it is worked exclusively with such test samples — never with the original data set — to keep the analysis blind and bias-free.

Boundaries of μ_s

Intuitively, the boundaries of μ_s would be 0 and the number of events in the sample, N. However, since $\mu_s = 0$ means that the sample is in perfect agreement with the background-only hypothesis, under-fluctuations are physically viable, meaning negative values are *not* prohibited. Nonetheless, for negative μ_s the respective value for Λ is artificially set to zero in this analysis. Because: The test statistics measures how consistent a theory is with the null hypothesis, H0, and the signal hypothesis, HS. Values of e.g. $\mu_s = 20$ and $\mu_s = -20$ would

[9] The factor of 2 ensures that the distribution of Λ, should the hull-hypothesis be true, is a χ^2-distribution (with one degree of freedom, for we have only one fit parameter).

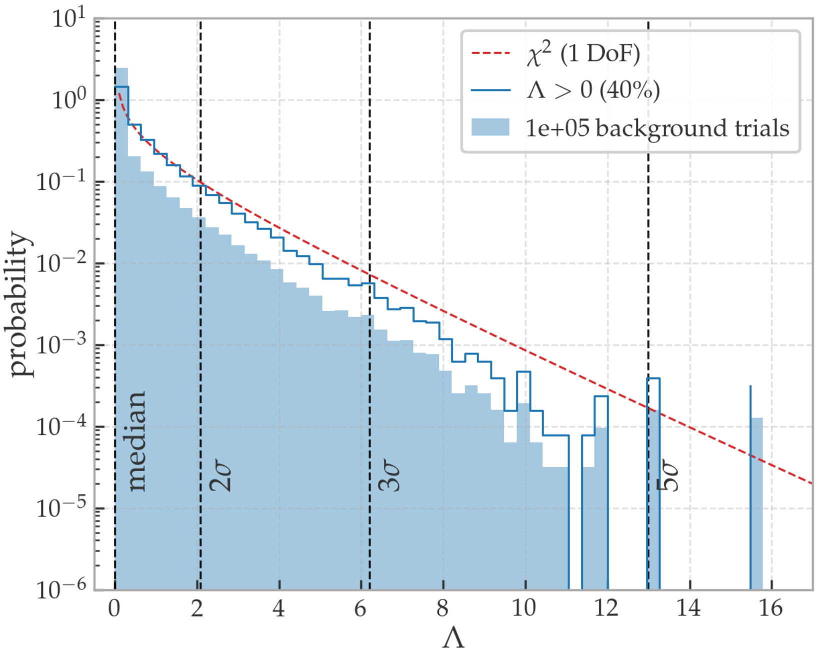

Figure 5.8: Background test statistics of the benchmark scenario 0849. Shown is the histogram of the Λ values of all 10^5 test samples (filled histogram, normalized); the histogram of only those samples that yielded $\Lambda > 0$ (hollow histogram, normalized); the χ^2 distribution with one degree of freedom (dashed red line), as well as the median, 2σ, 3σ and 5σ thresholds (dashed vertical lines).

result in very similar values for Λ, even though 20 is somewhat consistent with HS, while −20 is arguably much more consistent with H0.

Because the estimation comes never close to the upper bound $\mu_s = N$, over- and under-fluctuations need not be considered for that case.

Test statistics distribution

The TS distribution for 100,000 test samples is shown in Fig. 5.8, for the example scenario 0849. The portion of tests that yielded a Λ different from zero is 40 % in this case, and varies between 40 % and 45 % in different scenarios. The distribution of $\Lambda > 0$ tests is shown as the blue line, and roughly follows a χ^2-distribution with one degree of freedom (red dashed line), indicating that the background is modeled reasonably well.[10] The graph shows further the median value,

$$\tilde{\Lambda}_0 \equiv \text{Median (second quartile) of the background test statistics,} \tag{5.13}$$

as well as the values corresponding to 2σ, 3σ and 5σ of the cumulative distribution, indicating that 50 %, ∼ 95.45 %, ∼ 99.73 %, and ∼ 99.99 % of all values are located to the right of the respective line. While the 2σ, 3σ and 5σ thresholds are useful tools in discovery analyses, only the median is of importance in this non-discovery analysis, therefore the number of test samples can be safely limited to 1, 000 in order to reduce computing time.

5.5.4 Signal recovery tests

A good measure to find potential bias in the analysis method is a signal recovery test. The recipe to conduct such a test is this:

[10] It means that the distribution of μ_s resemble a normal distribution with an expectation value corresponding to the true value (zero in this case).

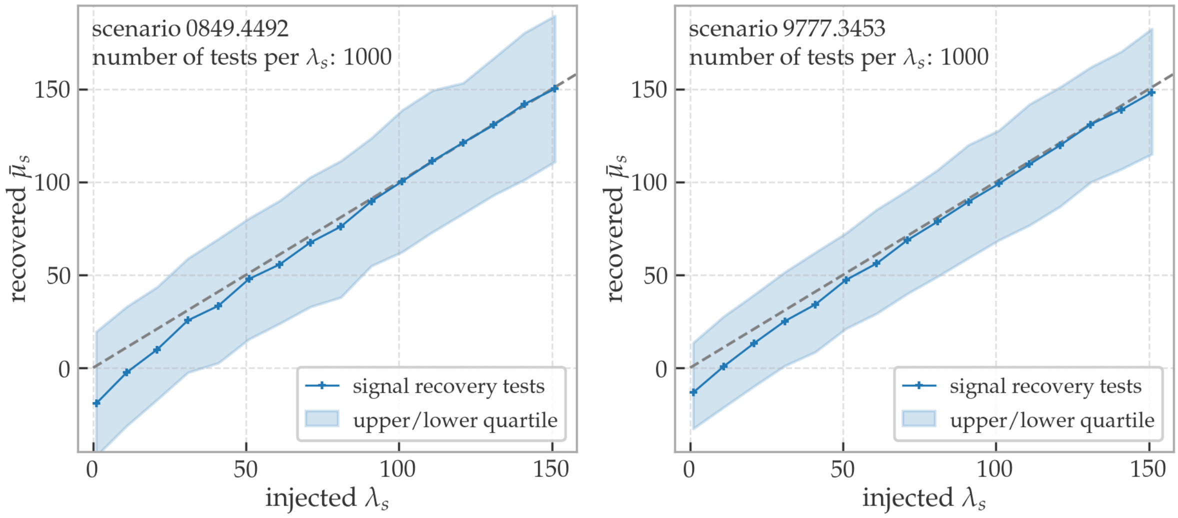

Figure 5.9: Signal recovery test for the benchmark scenarios 0849 (left) and 9777 (right). Shown are the reconstructed average best signal strength estimates $\bar{\mu}_s$ versus λ_s (the actual number n_s of injected events is drawn from a Poisson distribution with λ_s as expectation value) for 10^3 test samples per data point, as markers connected by a solid line. The shaded areas indicate the region of upper and lower quartiles. The dashed line indicates the purely theoretical line of "perfect signal recovery".

1. Create a large amount of test samples, e.g. $k = 1,000$.
2. Inject signals from a Poisson distribution with expectation value λ_s (where λ_s is the same for all test samples, but the number n_s of actually injected signals will vary from sample to sample). The background must be reduced by the same number of injected signal events, where the events to be dropped are picked at random.
3. Maximize the test statistics to determine μ_s for each sample. Take the average $\bar{\mu}_s$ over all samples.
4. Repeat steps 1.-3. for several different λ_s.

For a perfect signal recovery, $\bar{\mu}_s = \lambda_s$ would hold, but a perfect recovery is of course not expected. The results of the tests for benchmark scenarios 0849 and 9777 are shown in Fig. 5.9, with $k = 1,000$ test samples for each λ_s. The average $\bar{\mu}_s$ is shown with its upper and lower quartiles. A slight under-bias can be seen for small numbers of injected signals, which is not considered critical.

5.5.5 Confidence level, sensitivities, and model rejection

The result of the maximum likelihood method ("maximum log-likelihood ratio method" to be exact) described earlier is the best estimator μ_s of the signal strength in the data sample. One now must define a confidence level (CL) to give statistical meaning to μ_s. For this analysis, CL = 90 % is chosen, which is a common confidence level in relevant literature.

Because this is not a discovery analysis, the results of this study will be *upper limits* at the chosen confidence level. Since unblinding approval is required to work the original data set, one calculates the *sensitivity* first, which has a very similar definition but is obtainable with test samples only.

Sensitivity: A large number of test samples are injected with an increasing number of Poisson-distributed signal events (randomly sampled from the signal PDF, and with dropping the respective number of randomly picked background events), until the maximum likelihood method returns $\Lambda > \tilde{\Lambda}_0$ for 90 % of the test samples, where $\tilde{\Lambda}_0$ is the median of the background test statistics (recall Eq. (5.13)). The corresponding average signal strength that has to be injected is the sensitivity $\bar{\mu}_{90}$ at the 90 % confidence level, also called the *average median upper limit*.

Upper limit: The upper limit at 90 % confidence level is the signal strength μ_{90} that has to be injected so that the maximum likelihood method returns $\Lambda > \Lambda_0$ for 90 % of the test samples, where Λ_0 is the best fit test statistic value for the original (unblinded) data set with no injected signal.

In the following paragraphs, the terms "sensitivity" and "sensitivity at 90 % confidence level" will be used as equivalents, same for "upper limit" and "upper limit at 90 % confidence level". (Note that per the above definitions, the sensitivity and upper limit do not take into account the predicted flux strengths; they are incorporated in the definition of the model rejection factor, see below.)

The sensitivities are calculated prior to the upper limits as pre-unblinding results. Practically, the method of injecting $\lambda_s = 1, 2, 3, ...$ until $\Lambda > \tilde{\Lambda}_0$ is fulfilled for 90 % of the test samples is computationally too expensive. Instead, tests are performed for $\lambda_s \in \{0, 10, 20, 30, 40, 55, 65, 85, 90\}$, then the ratio

$$R = \frac{k_{\Lambda > \tilde{\Lambda}_0}}{k} \tag{5.14}$$

is calculated with the number of tests $k = 1,000$ for all λ_s, and a fit function is applied to the resulting pairs of λ_s and R. The fit function is a simple saturation function of the form

$$R(\mu) = 1 - (1 - b) \exp\left(-\frac{\mu}{a}\right) \tag{5.15}$$

with the free parameters a and b. The value of μ for which $R(\mu) = 0.9$ is the desired $\bar{\mu}_{90}$. A demonstration of the fit performance for the two benchmark scenarios is shown in Fig. 5.10. For the benchmark scenarios, and also for other scenarios that are not shown, the fit seems to under-perform slightly for larger numbers of injected signals, starting at around $\lambda_s = 70$. This results in a slightly conservative $\bar{\mu}_{90}$, which is accepted since a better saturation model could not be found.

Once unblinding approval is obtained, it is in practice quite simple to determine the upper limits based on the sensitivity calculations. For each λ_s one simply needs to calculate a new ratio, substituting $k_{\Lambda > \tilde{\Lambda}_0}$ with $k_{\Lambda > \Lambda_0}$ in Eq. (5.14), and re-perform the saturation fit. The resulting signal strength is the upper limit μ_{90}.

As a next step, the knowledge about the theoretical fluxes that are predicted in the 1,723 scenarios need to be incorporated. The rejection of a particular flux in the background-only case has to be quantified; the *model rejection factor* serves this purpose:

Model rejection factor: The MRF[11] [173] is defined as

$$\mathrm{MRF} = \frac{\mu_{90}}{\mu_{\mathrm{th}}}, \tag{5.16}$$

[11] We use the term that is in line with relevant literature, even though "scenario rejection factor" would be more appropriate in this case.

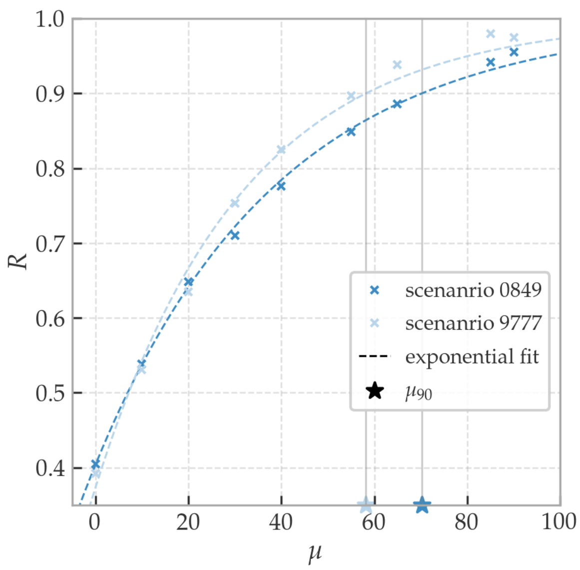

Figure 5.10: Saturation of R with increasing number of injected signals λ_s (Poisson expectation value), for the two benchmark scenarios 0849 (dark) and 9777 (light). The crosses mark the performed tests, the dashed line is the saturation function fitted to these points. We used 1000 test samples per data point.

where μ_{th} is the signal strength predicted for the scenario under investigation, and μ_{90} is the upper limit.

So the MRF is a measure for the rejection of a particular signal strength given a corresponding upper limit. According to the definition, MRF ≤ 1 means exclusion of the particular scenario with at least 90 % probability. Because the scenarios are highly correlated, the upper limits are expected to be fairly similar, so the deciding factor on the MRF is the expected signal strength; where a small MRF indicates a strong signal flux, a large MRF consequently indicates a weak signal flux with respect to the detector sensitivity.

About the non-discovery nature of this analysis

The (previous versions of the) event selections employed in this study have been scrutinized for generic WIMP signals from the direction of the Sun before (e.g. in Refs. [157, 124], as well as in a currently ongoing study), without finding a signal excess from the direction of the Sun. Such generic WIMP searches cover neutrino energy spectra that are similar to those obtained and tested in this study. Therefore, a discovery of a signal is very unlikely for this analysis.

Furthermore, a potential discovery requires the calculation of a P-value, "*[...] the probability for getting a value of the test statistic at least as extreme as that observed solely by chance, provided the null hypothesis is true*" [167], for each scenario. But P-values are only meaningful in combination with a *trial factor*, that takes into account the number of attempts made at the discovery — naively, this would amount to 1,723 such attempts, i.e. the number of tested scotogenic scenarios. Since these scenarios are highly correlated, the (naive) trial factor would introduce an extreme, unjustified reduction of sensitivity. The determination of a trial factor that accounts for *correlated* attempts correctly, on the other hand, can be very complex, and goes beyond the scope of this work.

So instead, this study focuses on the *rejection* of particular fluxes by means of the MRF defined in the last paragraph, and aims at the exclusion of the corresponding Dark Matter scenarios. The upper limits that are necessary to calculate the MRFs are valid without a trial factor (however they still require an unblinded data set).

5.5.6 Implementation of the analysis framework

This particular analysis differs from other IceCube studies mainly in the aspect of the investigated Dark Matter scenarios. It is more common to study generic WIMPs, in which the only variable parameters are the mass of the Dark Matter particle and the dominant annihilation channel. The resulting neutrino flux from WIMP annihilation in the Sun (or other bodies) is model-independent, and allows the formulation of an upper limit on the spin-dependent WIMP-nucleon cross section (since the spin-independent cross section is heavily constrained by direct detection experiments).

In this study, a particular Dark Matter model — the Scotogenic Model — is probed instead, meaning that the resulting flux very much depends on the model parameters, which are numerous and highly correlated. In contrast to generic WIMP searches, the annihilation channels and the Dark Matter mass are precisely known for a specific set of model parameters. Generic cross section upper limits can *not* be obtained with this study, but it allows for the potential exclusion of specific WIMP production processes in the Sun, i.e. scotogenic parameter combinations. This is what is done in this work, for a total of $1,723$ scenarios.

A main challenge to the analysis software framework is the efficient implementation of such a large number of scenarios. As mentioned earlier, many steps in the analysis have to be conducted for each individual scenario separately, which requires careful and inventive implementation to stay within the margins of the available computing resources.

The `solarinelastic` package

The Python analysis framework that I developed in the scope of this thesis is named `solarinelastic`. It is based on two classes: The `Model` class and the `Selection` class. All scotogenic scenarios are instances of the `Model` class, and the two event selections used in this study are instances of the `Selection` class. The most important attributes of a `Selection` instance are:

- The total number of events in the selection, along with the total exposure time, event rate per day, etc.,
- the boundaries of the $\Psi - \log E$ space and the bandwidth for the calculation of the KDEs,
- the (locations of the) nominal and systematic data sets,
- the effective area.

Each `Model` instance has the following (most important) attributes:

- The two selections `INT` and `OSC`, along with the respective background PDFs,
- the signal PDFs (which are scenario- and `Selection` specific),
- a dictionary containing all relevant model parameters and observables associated to the scenario,
- the predicted neutrino and antineutrino fluxes.

A scenario is initialized with the parameter- and observables dictionary and the neutrino fluxes. The first step is then the calculation of the signal KDEs with the dedicated method `CreatePDF` in the `Model` class, which relies on the `KDE2B` package described in Sec. 5.5.2 (also developed in the scope of this thesis). It creates the KDE-kernels for the respective data sets based on the provided boundaries and bandwidths, which takes a few seconds at most. The computing-intensive part is the evaluation of the KDEs on a fine grid (160×160 points). The grid is calculated only once for each scenario, and can later be interpolated whenever the PDF is needed in the analysis, which saves an immense amount of computing time compared to evaluating the KDE "on the fly". (The background PDFs are created in the same way, but they are constant for all scenarios and therefore require negligible resources.) The fine-grid evaluated PDFs are saved as NUMPY instances.

Once the signal PDFs are created, statistical analyses can be conducted. The statistical methods described in the last sections are implemented as a collection of functions in the `frequentist` script belonging to the `solarinelastic` package. Due to the large number of conducted tests, the calculation of the background test statistics and sensitivities requires approximately $2+18$ hours in the ICECUBE computing infrastructure for each scenario, amounting to a total of 34, 460 hours for the nominal data set alone (times nine if counting the systematic data sets as well). Fortunately, the process can be parallelized, e.g. run for all scenarios at the same time. In order to not clog up the available computing slots for other users, the scenarios are grouped into batches of twelve, so that only 143 slots were occupied at a time. The processes are in general not memory intensive (in contrast to the oversampling of the data sets, but oversampling has to be done only once for each set). The files containing the test statistics and sensitivity calculations are stored as NUMPY instances as well. Storage-wise, after completion of all calculations, a single scenario amounts to approximately 11 MB.

The fit of the saturation function to the sensitivity test points and the calculation of the MRFs are computationally inexpensive and can be conducted on local machines.

Likelihood ratio maximization

Maximizing the likelihood ratio in Eq. (5.12) delivers the best estimator μ_s for the signal strength. Software-wise, it is a lot easier to implement a minimization than a maximization, which is why Eq. (5.12) is multiplied with a factor of -1 before and after the fit process. The function is minimized for a single parameter (the best fit value μ_s for the signal strength), so the "minimizer" — the numerical implementation of the minimization process — is relatively straight forward. Nonetheless, numerical minimization has a number of caveats and is to be handled with care. Most minimizers have trouble to distinguish local and global minimums, or derail completely when given bad start values as a first guess. In this analysis, the `scipy.optimize.minimize` package is used, which proved to be quite robust; it found the global minimum in all test runs when given the injected number of signal events (zero in this case) as a start value for the optimization. As an additional safety net, a lower bound for the possible values of μ_s is implemented in the analysis software framework, in order to prevent the minimizer from running into false global minimums. These may arise when it tries values that causes the expression in the parenthesis to become ≤ 0, for which Λ is not defined, and which could cause numerical mayhem. This lower bound is determined by coarsely scanning over a certain range of possible μ_s "by hand" to see where Eq. (5.12) starts to return NaN's,[12] (which happens far away from the actual minimum), and cutting the range accordingly. Since the estimation of μ_s is technically a minimization, but *physically* a maximization, it will be called the latter throughout this work.

[12] "Not a Number".

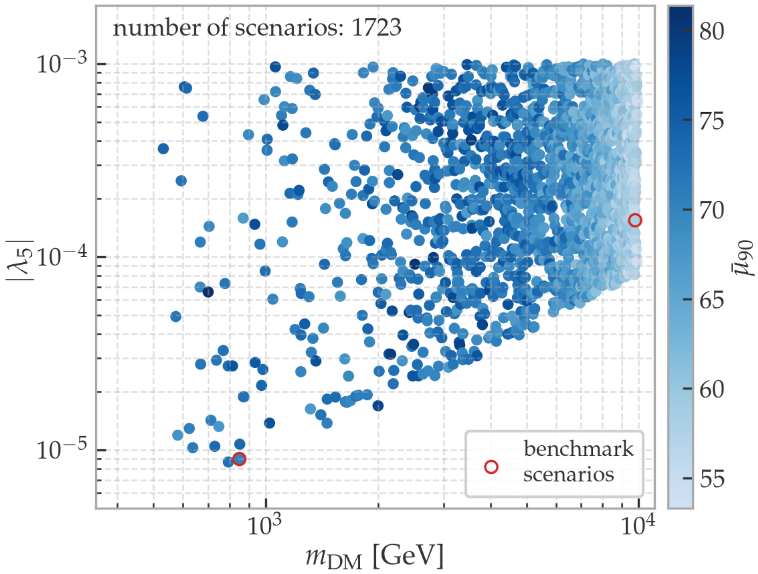

Figure 5.11: The viable scenarios of the Scotogenic Model, in the $|\lambda_5|$ vs. m_{DM} plane. The colors indicate the sensitivity $\bar{\mu}_{90}$. The red circles mark the benchmark scenarios 0849 and 9777.

5.6 Sensitivities

In Chp. 4, 1,723 viable scenarios of the Scotogenic Model have been identified that are now tested with the IceCube data. Each scenario is analysed individually, meaning signal PDFs, background test statistics and sensitivities are calculated for all 1,723 scenarios separately. (Signal recovery tests are only performed in a few randomly picked cases for test and verification purposes.) The sensitivities are calculated according to the methods described in the previous section.

The sensitivities of all scenarios are shown in Fig. 5.11 in the plane of the DM mass m_{DM} and the absolute value of the mass splitting parameter, $|\lambda_5|$. The plot shows the same plane as Fig. 4.15 of the last chapter, but is scaled in $|\lambda_5|$ to better fit the range of non-excluded scenarios. Only those scenarios not marked "excluded" in Fig. 4.15 are shown here. The two benchmark scenarios 0849 and 9777 that have been used as examples throughout this chapter are marked specifically.

As can be seen in the plot, the sensitivities fluctuate between scenarios, from approximately 53 to 81. As a reminder, this means that on average, between 53 and 81 events sampled from the signal PDF had to be injected into the background sample so that a test statistic value of $\Lambda > \tilde{\Lambda}_0 = 0$ was returned in 90 % of the tests. A smaller value of $\bar{\mu}_{90}$ therefore represents a better sensitivity than a larger value. The sensitivity takes into account the probability distribution of the scenario-specific flux by means of the signal PDF (but not the flux intensity). So it is interpreted as a measure of the detector response towards a specific flux *energy* spectrum specifically, because averaged over time, the position of the Sun in the sky is uniform in azimuth, as is the IceCube detector response due to its nearly symmetric layout.

Besides the small fluctuations between adjacent scenarios, a clear trend of better sensitivities towards higher WIMP masses is observed. The 10 % of scenarios with the best sensitivities ($\bar{\mu}_{90} < 59$) are all located in the mass region above $m_{\mathrm{DM}} = 8.1 \times 10^3$ GeV. Given the explanation above, from the trend one can conclude an overall superior reconstruction quality of neutrino events with higher energy; since the neutrino energy is limited by the mass of the DM candidate, larger WIMP masses allow for more well-reconstructed events. Furthermore, larger

WIMP masses result in a slightly smaller overlap of signal and background PDFs in energy dimension. This makes a correct distinction between signal and background events easier, resulting in smaller fluctuations of the signal strengths recovered by the analysis method in the individual tests that enter the calculation of $\bar{\mu}_{90}$. The effective area for this analysis shown in Fig. 5.4 reflects these observations as well. It is concluded that the IceCube detector is in general more sensitive to scotogenic scenarios with larger WIMP masses.

Verification tests prior to unblinding

As explained in Sec. 5.1, the analysis methods have to be tested and verified in order to gain unblinding approval, i.e. access to the real, unscrambled data set. In order to check for inconsistencies in the entirely new analysis framework developed in the scope of this work, a so-called *far-sample test* is conducted, following a procedure of a currently on-going IceCube study. This test, tailored to the requirements of this analysis, consists of the following steps:

1. The combined event selection is unblinded, meaning the unscambled neutrino directions are unveiled. The data set is split 50 : 50 into the events closer to the Sun, and the events further away from the Sun.[13] The latter is called the far-sample, which is used as the verification sample. The other half is put aside for now.

2. The best estimator of the signal strength μ_{far}, and the corresponding test statistics value Λ_{far}, is determined for the far-sample in all 1,723 scenarios.

3. A dedicated far sample background test statistics distribution is created for each scenario in order to calculate P-values. These are not to be confused with P-values of the actual unblinded sample, which are not calculated in this study (recall Sec. 5.5.5).

4. If very small values are found, or the spread of values is very large (which it should not be because the scenarios are highly correlated), the unblinding process is stopped, and the analysis methods are investigated further. Otherwise, unblinding is approved, and the upper limits can be calculated.

The far-sample P-values can be determined by means of the number of test samples k in the background test statistics distribution for which $\Lambda > \Lambda_{\text{far}}$, where Λ_{far} is the test statistics value for the unblinded far-sample:

$$P_{\text{far}} = 1 - \frac{k_{\Lambda > \Lambda_{\text{far}}}}{k}. \tag{5.17}$$

A histogram of the P_{far}-values of all 1,723 scenarios is shown in Fig. 5.5.5. As can be seen in the plot, no large spread of values, and no value below 0.59 is observed. Therefore it is concluded that the analysis method functions correctly in regard of a sample from which all signal was removed. The analysis can now move on to the full unblinded data sample.

[13]The threshold angles for the INT and OSC events that are included in the far-sample were originally based on the MC set angular resolutions, for which the standard deviation of the angular difference between true and reconstructed angle can be determined. Events that are $\Psi > 2\sigma$ away from the Sun would then be included in the far-sample. For the INT selection, the threshold angle is $\Psi_{2\sigma} = 2.7°$, and for the OSC selection it is $\Psi_{2\sigma} = 86°$. The far-sample would then contain roughly 50 % of the OSC selection, but over 90 % of the INT selection. So it was decided to just cut the samples in halves event-wise, since for the OSC selection this roughly corresponds to 2σ anyway, and for the INT selection one avoids including almost the whole sample in the verification test.

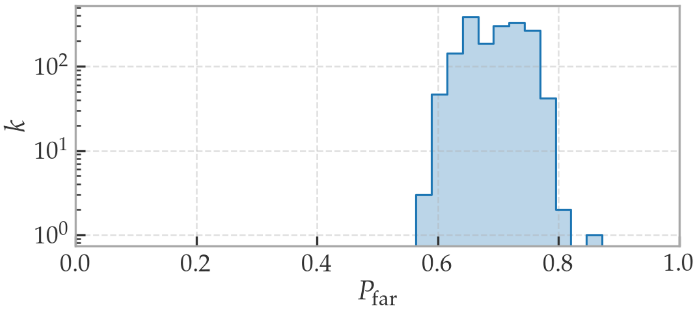

Figure 5.12: Histogram of the far-sample P_{far}-values.

5.7 Upper limits

The pre-unblinding results of the last section are now replaced by results based on the unblinded data sample. The upper limits for all 1,723 scenarios are calculated according to the description given in Sec. 5.5.5. The results are shown in Fig. 5.13, in the same plane as in Fig. 5.11.

In general, the conclusion can be made that the upper limits are very close to the sensitivities presented in Fig. 5.11; in fact, no visible changes in color between the two plots can be noticed, and the same trend of better upper limits towards larger WIMP masses is observed.

Since the differences between upper limits and sensitivities are apparently marginal, the deviations $1 - (\bar{\mu}_{90}/\mu_{90})$ are presented as well in Fig. 5.14. It becomes apparent that deviations do exist, and mainly for scenarios with smaller WIMP masses. Quantitatively, 17.3 % or an absolute number of 254 scenarios reveal a slightly worse (larger) upper limit compared to the pre-unblinding sensitivity. The deviation for those scenarios is 1.5 % on average, and the maximum deviation is 6.5 %, and corresponds to the scenario with the smallest WIMP mass $m_{\text{DM}} = 531.26\,\text{GeV}$. A gross decline from sensitivity towards upper limit would point to the presence of a signal in the unblinded sample, however such a deviation is not observed.

Especially in the mass regions $\gtrsim 4 \times 10^3\,\text{GeV}$, most of the scenarios have equal or almost equal upper limits and sensitivities. For the majority of the scenarios with $\mu_{90} = \bar{\mu}_{90}$, a slight under-fluctuation of signal strength is observed in the unblinded sample. Under-fluctuations are not considered strictly unphysical in this analysis, meaning negative values for the best estimator of the signal strength μ_{Λ_0} of the unblinded data sample are permitted. As explained in 5.5.3, the test statistics is implemented to return $\Lambda = 0$ for negative signal strengths best estimators. Since the median background test statistics is $\tilde{\Lambda}_0 = 0$ in all tested scenarios, and the unblinded background test statistics is necessarily $\Lambda_0 \geq 0$, the value of the sensitivity is automatically the best possible upper limit,[14] and one observes $\mu_{90} = \bar{\mu}_{90}$ for all scenarios in which under-fluctuations ($\mu_{\Lambda_0} < 0$) occur.

[14]Technically, an improvement from sensitivity to upper limit is in line with the statistical method, if the median of background test statistics, $\tilde{\Lambda}_0$, takes non-zero values, meaning the maximum likelihood method returns signal in more than half the background-only trials (which can indicate that the data is not described well by the PDFs). This is not the case for any of the investigated scenarios. Since the unblinded background test statistics Λ_0 can only take values of ≥ 0, the sensitivity therefore describes the best possible upper limit. Other analysis techniques permit improvements of the upper limits due to under-fluctuations in the unblinded sample more easily, however such improvements are statistically questionable.

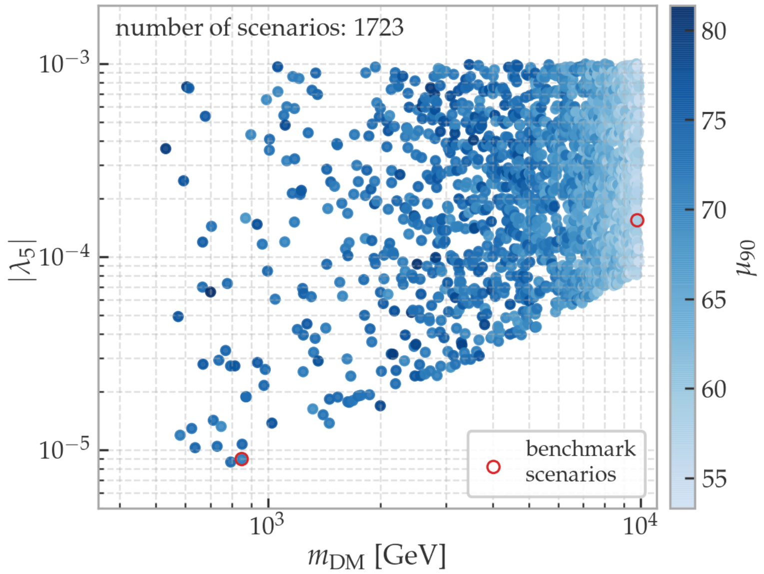

Figure 5.13: The viable scenarios of the Scotogenic Model, in the λ_5 vs. m_{DM} plane. The colors indicate the upper limit μ_{90}. The red circles mark the benchmark scenarios 0849 and 9777.

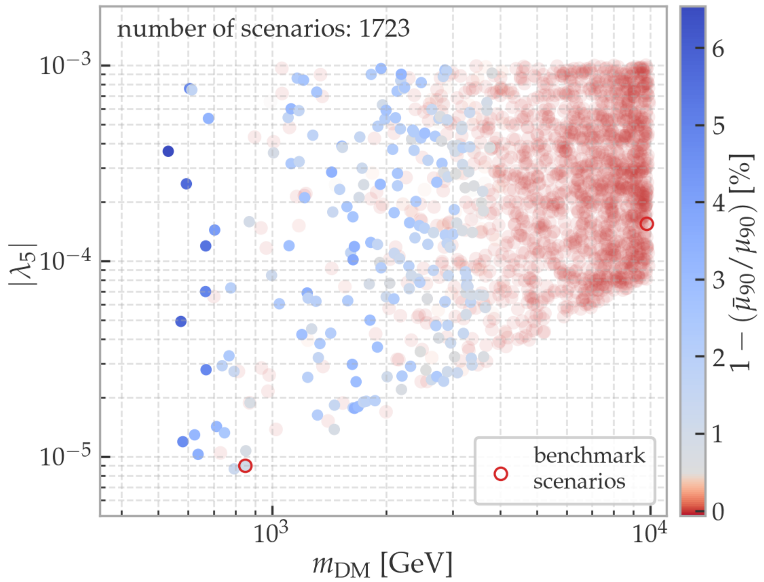

Figure 5.14: The viable scenarios of the Scotogenic Model, in the λ_5 vs. m_{DM} plane. The colors of the filled points indicate the percentage deviation between sensitivity and upper limit. Scenarios with only very small deviations are drawn with a transparency to better emphasize the points with larger deviations. The red circles mark the benchmark scenarios 0849 and 9777.

5.8 Systematic uncertainties

The background in this analysis consists of real data scrambled in azimuth, and is thereby free of (significant) systematic uncertainties. The MC-simulated signal, however, contains several intrinsic systematic uncertainties. Following previous studies, these uncertainties can be divided into two classes, **class I** uncertainties on cross sections and particle propagation and oscillation properties, and **class II** uncertainties that regard detector response. The treatment of the two classes is described in more detail below.

Class I systematic uncertainties

Particle interaction and propagation properties are sources of systematic uncertainties in the signal simulation process. These properties are listed below, with the corresponding percentage impact on the model rejection factor:

– The neutrino-nucleon cross section (3.5 %),

– the neutrino oscillation parameters (6.0 %),

– the propagation of muons in the ice (< 1 %).

These values have been determined by previous IceCube studies [124, 157]. They are subdominant in this analysis compared to the class II uncertainties. Summed up in quadrature, the total class I systematic uncertainty is 7.0 %.

Class II systematic uncertainties

Systematic uncertainties of class II arise from the imperfect characterization of the detector and the surrounding ice. The corresponding properties can be investigated and modeled as close to reality as possible, and have "nominal" values that represent the current best knowledge; but they can not be known completely. The main sources of class II systematic uncertainties are explained in the following.

— The DOM optical efficiency

The DOM optical efficiency [44] means the probability of a photon being "recorded" when hitting the module, i.e. converted into an electrical signal. In an event simulation, an increased DOM efficiency leads to an increased rate of low-energy events and to a more efficient background rejection due to better event reconstruction, while a decreased DOM efficiency consequently has the opposite effects. The DOM efficiency parameter is currently assumed to possibly vary from the nominal value within ±10 %.

— The optical properties of the bulk ice

Scattering and absorption of light in the ice depend mainly on the depth [45, 174]. The almost pristine ice in the deep layer of the South Pole ice cap instrumented by IceCube has excellent optical qualities (with exception of the dust layer; recall Sec. 2.3.3). However, scattering and absorption are approximated by an ice model which is imperfect. Both properties are assumed to vary from the nominal value within ±5 %.

— The optical properties of the hole ice

The hole ice refers to the ice that formed in the 50 cm wide drilling holes in the hours after deploying the strings. The re-freezing process trapped air in the center of the hole, called the "bubble column" [175]. The result is increased scattering in the ice surrounding the modules, affecting primarily photons with vertical trajectories. The size of the bubble column and the deviation from the nominal scattering length, among other parameters, are uncertain, and different models concerning these values exist. The hole ice model used in this study is parameterized by two values encompassing all of the uncertainties, $p0$ and $p1$ (which are unitless and have no physical interpretation). A variation of ±0.1 around the nominal value of $p0$ (while keeping $p1$ constant) is assumed to cover a variety of established ice models.

To quantify the impact of the above listed uncertainties on the analysis, alternative simulation sets that come with the Improved Northern Tracks and OscNext event selections are used,

Table 5.3: Class II systematic sets with modified detector response values. For DOM efficiency, bulk ice absorption (BI abs.) and scattering (BI sct.), 100 % corresponds to the nominal value. The nominal values for the hole ice (HI) parameters $p0$ and $p1$ differ for the two selections ($p0 = 0.102$, $p1 = -0.049$ for the OSC selection and $p0 = 0$, $p1 = 0$ for the INT selection). Each systematic set has variations in positive and negative direction, so the values are given in pairs of +/−.

syst. set	**DOM eff. [%]**	**BI abs. [%]**	**BI sct. [%]**	**HI $p0$ (OSC)**	**HI $p0$ (INT)**
nominal	100	100	100	0.102	0
DOM eff.	90/110	100	100	0.102	0
BI abs	100	95/105	100	0.102	0
BI sct	100	100	95/105	0.102	0
HI $p0$	100	100	100	−0.2/0.3	−1/+1

created by the respective working groups specifically for this purpose. Those sets contain artificial events that were "recorded" using a detector with modified values for the properties listed above. Each property is varied in both directions around the nominal (best model) value, so there is a “positive” and “negative” set, and eight systematic sets in total. The modified values are listed in Tab. 5.3.

The percentage impact of one specific systematic set is calculated as follows:

1. A sample of signal events is created by oversampling the data set a large number of times (to obtain ~ 1 Mio events from the Sun per sample).
2. For each scenario, the events in the sample are weighted with the theoretically predicted flux. The signal strength $\mu_{\text{th,syst}}$ is obtained by summing up all event weights and multiplying with the lifetime.
3. For each scenario, the “systematic” signal PDF is constructed from the sample. The sensitivity $\bar{\mu}_{90,\text{syst}}$ is obtained by running the analysis chain as was done for the nominal set, except that now the signals are injected by sampling from the systematic signal PDF. The MRF is calculated with (recalling Eq. (5.16))

$$\text{MRF}_{\text{syst}} = \frac{\bar{\mu}_{90,\text{syst}}}{\mu_{\text{th,syst}}}. \tag{5.18}$$

4. The percentage impact of the systematic uncertainty, per direction of variation, is

$$s_{\text{MRF}} = \frac{\text{MRF}_{\text{nom}}}{\text{MRF}_{\text{syst}}} - 1, \tag{5.19}$$

averaged over all scenarios. Further calculated are the scenario-averaged impacts on the predicted signal strength and sensitivity with:

$$s_{\mu_{\text{th}}} = \frac{\mu_{\text{th,syst}}}{\mu_{\text{th,nom}}} - 1, \qquad s_{\bar{\mu}_{90}} = \frac{\bar{\mu}_{90,\text{nom}}}{\bar{\mu}_{90,\text{syst}}} - 1 \tag{5.20}$$

(The ratios in Eqs. (5.19) and (5.20) are defined such that a positive value means an improvement of the quantity in the systematic set compared towards the nominal one,

Table 5.4: Impact of the class I and class II systematic uncertainties. In the last column the percentage impacts on the MRF are shown, averaged over all 1,723 scenarios. The scenario-averaged individual impacts on the predicted theoretical signal strength μ_{th} and the sensitivity $\bar{\mu}_{90}$ are shown in the middle columns. The total systematic uncertainty is calculated by adding the class I and class II values in quadrature (using the more conservative of the two values in each field, printed in bold).

syst. uncertainty	**impact on** μ_{th} [%]	**impact on** $\bar{\mu}_{90}$ [%]	**impact on MRF** [%]
class I total			7.0
DOM efficiency	−14.8/+13.2	−14.4/+5.4	**−27.0**/+19.3
Bulk ice sct.	−3.0/+3.1	−16.7/−17.0	**−19.1**/−14.4
Bulk ice abs.	−3.6/+3.5	−16.9/−9.0	**−19.9**/−5.8
Hole ice $p0$	−1.7/+0.8	−18.3/−17.1	**−19.7**/−16.4
class II total			43.3
total			**43.9**

and consequently a negative value means a decline. E.g. $s_{\text{MRF}} < 0$ means the average MRF of the systematic set is larger/worse than the nominal MRF.)

The total percentage impact of the systematic uncertainties are the class I and class II values added in quadrature, where for the class II systematic uncertainties only the larger, more conservative value from the respective pair of variations is considered, meaning only the variation which affects the result most enters the total systematic uncertainty. The results of the systematic uncertainty investigations are shown in Tab. 5.4.

To gain further insight into the effects of the systematic uncertainties, the impacts on the theoretical signal strength μ_{th} and the sensitivity $\bar{\mu}_{90}$ for the class II properties are listed as well. For instance, the reader might wonder why asymmetric uncertainty impacts on the MRF are obtained for the two directional sets of one specific property, even though the variations around the nominal value are symmetric. The reason is a combination of several factors that have to be taken into account:

– The theoretical signal strength is calculated by summing over the weights of the events in the specific simulation set. For the systematic sets, the theoretically expected signal strengths are expected to be roughly symmetric around the nominally expected signal strength, going up with positive variations and down with negative variations. This expectation can be confirmed by the second column in Tab. 5.4.

– The quality of event reconstruction increases (declines) with positive (negative) variations of the detector properties, making it easier (harder) to distinguish signal from background. The effects on the sensitivity are not necessarily symmetric.

– The signals that are injected to determine the sensitivity of the systematic sets are injected from the systematic signal PDFs. These PDFs differ from the nominal signal PDFs with which the signals are recovered, therefore deviations from the nominal PDF necessarily introduce a decline in signal recovery quality. Hence the effect on the sensitivity is always negative, and can outweigh possible positive effects on event reconstruction quality.

The last item over-compensates positive effects in most cases, as can be seen in the table. The only systematic set for which a positive net effect is observed is the +10 % DOM efficiency set.

Since the final results of this analysis are MRFs calculated using upper limits, they have to be worsened by the total percentage impact of the systematic uncertainty of 43.9 % to be as conservative as possible. The results presented in the following section take into account the total systematic uncertainty, if not otherwise noted.

5.9 Results and discussion

After presenting the upper limits in Sec. 5.7, it is now time to consider the predicted fluxes of the scotogenic scenarios. As a reminder, a flux can be translated into a signal strength μ_{th} by means of multiplication with an effective area and a detector exposure time, or practically by summing up all events in the combined simulated nine-year event selection that has been weighted with the predicted flux.

Mass splitting constraints

The signal strengths μ_{th} of the scotogenic scenarios allow the formulation of a constraint on the mass splitting δ and the mass splitting parameter λ_5. For this purpose, the $1,723$ viable scenarios are plotted in Fig. 5.15 in the plane of the combined (elastic plus inelastic) capture rate C_χ and the mass splitting δ between the two neutral scalars, colored according to the signal strengths. The parameter plane is chosen to show again the relationship between mass splitting and capture rate that the reader might recall from Fig. 4.11, as well as emphasize the relationship of both quantities to the signal strength. Shown as a dashed black line is the mass splitting threshold for inelastic scattering $\delta^<_{\text{inel.}} = 595.05\,\text{keV}$ that was determined in the last chapter, Eq. (4.40). One can see that the capture rate is unaffected by the mass splitting above the threshold, and that the overall signal strength is very low. Below the threshold, however, the signal strength increases rapidly with larger capture rate and smaller mass splittings. This confirms what has been concluded in Chp. 4 already; that smaller mass splittings in general lead to larger inelastic scattering cross sections/capture rates, which results in stronger neutrino fluxes.

A new mass splitting threshold can now be formulated by means of the signal strength. With the MRF defined in Eq. (5.16), one can now determine a mass splitting $\delta^<_{\text{excl.}}$ below which all scenarios are excluded with 90 % probability; in other words, the minimum mass splitting out of all non-excluded scenarios. After calculating the MRFs for all scenarios, the threshold mass splitting for scenario exclusion amounts to

$$\delta^<_{\text{excl.}} = 416.82\,\text{keV}, \tag{5.21}$$

including the total systematic uncertainties. The newly determined threshold is drawn as a red line in the plot. (Without accounting for systematic uncertainties, the threshold is 437.25 keV. For orientation it is shown in the plot as well with a thin dotted red line). All scenarios to the left of the line are excluded by the analysis with 90 % probability (there are excluded scenarios to the right of the line, but no not-excluded scenarios to the left of it).

The mass splitting threshold $\delta^<_{\text{excl.}}$ can be translated into a mass-dependent threshold of

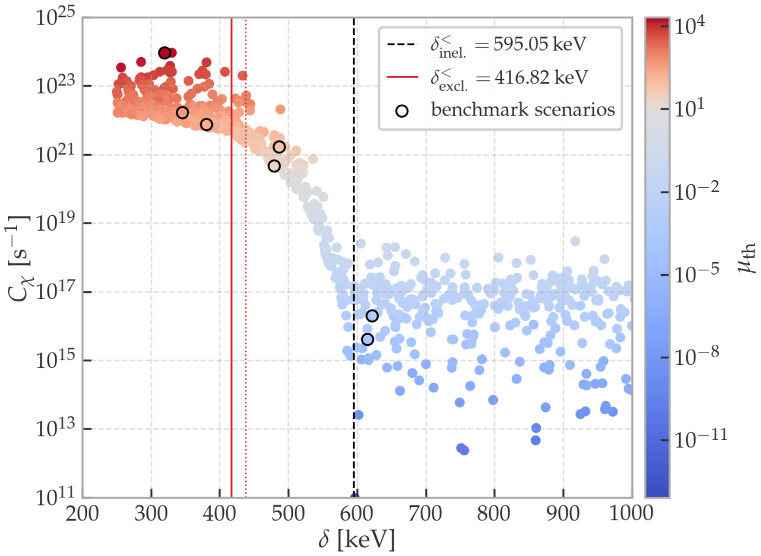

Figure 5.15: The viable scenarios of the Scotogenic Model, in the plane of the combined elastic plus inelastic capture rate C_χ and the mass splitting between the two neutral scalars δ. The colors indicate the predicted signal strength μ_{th}. The dashed and solid lines indicate the mass splitting thresholds of inelastic scattering and scenario exclusion, respectively. The very fine dotted red line indicates the exclusion threshold without accounting for systematic uncertainties. Note that it is only drawn for orientation, and does not match the color scale of the plot. The black circles mark the benchmark scenarios listed in Tab. 5.5.

the mass splitting parameter λ_5, by means of Eq. (4.8):

$$|\lambda_5|^{<}_{\text{excl.}} = \frac{\delta^{<}_{\text{excl.}}}{\left\langle \phi^0 \right\rangle^2} m_{\text{DM}} = 1.375 \times 10^{-8}\, \frac{m_{\text{DM}}}{\text{GeV}}, \tag{5.22}$$

which corresponds to $|\lambda_5| \approx 10^{-5}$ for $m_{\text{DM}} = 10^3$ GeV and $|\lambda_5| \approx 10^{-4}$ for $m_{\text{DM}} = 10^4$ GeV. Due to the total systematic uncertainties being taken into account, this is the most conservative possible value.

Note that the constraining power of this threshold is somewhat limited, because only individual scenarios can be excluded, and not whole parameter space regions (recalling the beginning of Sec. 5.5). A larger scan of the scotogenic parameter space might therefore reveal scenarios that push $|\lambda_5|^{<}_{\text{excl.}}$ towards lower values, i.e. making it weaker. However, as can be seen in various plots throughout the last two chapters, the scan that revealed the viable scenarios does not contain substantial gaps in the relevant parameter space, and a correlation of λ_5 and the signal strength is clearly given. Therefore it can be concluded that the determined threshold can in fact be interpreted as a constraint on the mass splitting parameter λ_5 of the Scotogenic Model.

Model rejection factors

As mentioned above, the MRFs can be calculated with the predicted signal strengths μ_{th} and the upper limits μ_{90} determined in Sec. 5.7. The MRFs are shown for all scenarios in Fig. 5.16, in the plane of the WIMP mass m_{DM} and the absolute value of the mass splitting parameter, $|\lambda_5|$. Shown as well are the λ_5-constraints discussed in the previous paragraph. Because of the extremely large range of predicted signal strengths ($\sim 10^{-14} - 10^4$ over nine years) and the in comparison more or less constant upper limits, the MRF predominantly scales with the inverse μ_{th}. The color scale in Fig. 5.16 is chosen so that scenarios with MRF $\gg 1$ are colored blue, those with MRF < 1 are red, and those MRF ≈ 1 are gray. One can see that the dashed line

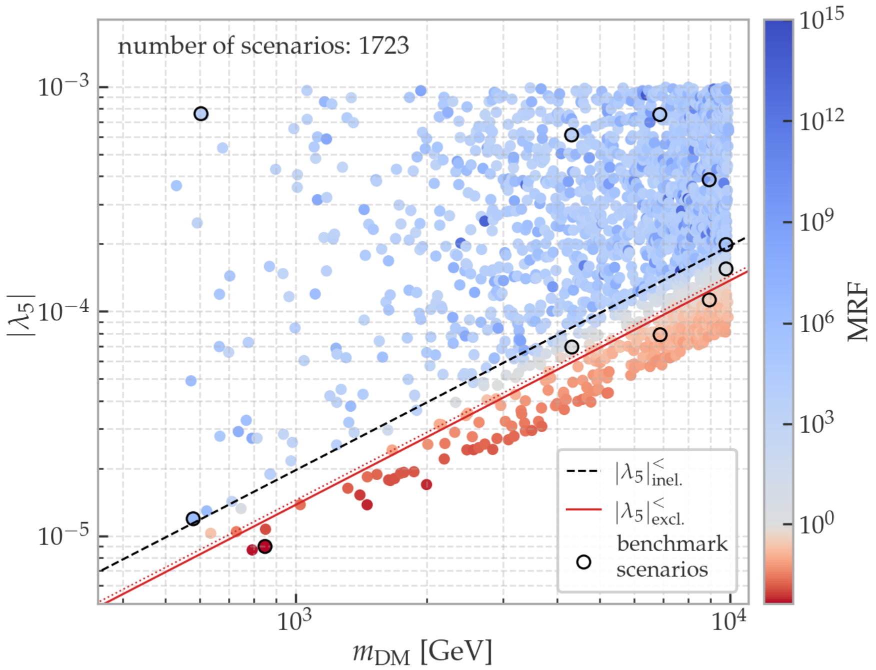

Figure 5.16: The viable scenarios of the Scotogenic Model, in the $|\lambda_5|$ vs. m_{DM} plane. The colors indicate the model rejection factor (MRF), including systematic uncertainties. The dashed and solid lines indicate the mass splitting parameter thresholds of inelastic scattering and scenario exclusion, respectively. The very fine dotted red line indicates the exclusion threshold without accounting for systematic uncertainties. Note that it is only drawn for orientation, and does not match the color scale of the plot. The black circles mark the benchmark scenarios listed in Tab. 5.5.

corresponding to the mass splitting threshold for inelastic scattering very roughly divides the parameter space into blue scenarios and gray-red scenarios, which was observed already in Fig. 5.15. The threshold for scenario exclusion further singles out the majority of red scenarios from the rest of the parameter space. For orientation, the thin dotted red line indicates the exclusion threshold without taking systematic uncertainties into account.

Per definition of the MRF in Eq. (5.16), a scenario with MRF = 1 is excluded with 90 % probability, and scenarios with smaller MRFs are excluded with correspondingly higher probabilities. On the basis of the unblinded data set and the found upper limits, and taking into account the systematic uncertainties, a total of 293 scenarios can be excluded, which corresponds to 67.1 % of the inelastic, and 17.0 % of the total investigated scenarios. (Without accounting for systematic uncertainties, a total of 313 scenarios can be excluded.) No purely elastic scenario can be excluded.

The scenarios colored in a deeper blue towards the upper part of the plot are "out of reach" for IceCube, with sensitivities than can not match the extremely low fluxes at least in the foreseeable future. However, an interesting group of scenarios is formed by those with an MRF only slightly larger than 1. These scenarios are not excluded by this analysis, but could be in potential reach of a followup analysis that has more years of data available or an improved event selection at hand (recalling the energy gap in the effective area in Fig. 5.4 as one possibility for improvent). The threshold for potential future detectability is chosen to be a signal strength one order of magnitude below the upper limit of the respective scenarios. Quantitatively, this regards 72 scenarios located between the two λ_5-threshold lines, 4.2 % of all that have been investigated here.

The remaining 78.8 % of scenarios are considered out of reach for indirect detection with IceCube in the foreseeable future.

In Tab. 5.5, a summary of the results is presented for eleven benchmark scenarios. These scenarios are marked specifically in Figs. 5.15 and 5.16 as well. Listed are six inelastic and five purely elastic scenarios chosen from the whole range of WIMP masses with their corresponding mass splitting parameters λ_5 and mass splittings δ. (From these two quantities the reader can already guess the scenarios that support inelastic scattering, but they are also marked with a gray background.) Listed as well are the test statistic value Λ_0 and the corresponding best estimator of the signal strength μ_{Λ_0} of the unblinded data sample; as well as the pre-unblinding sensitivity, the post-unblinding upper limit, and the MRF.

What has been discussed throughout this section is reflected by the example scenarios in the table: Sensitivities and upper limits are equal for most scenarios, and show a slight decline towards the upper limit for scenarios with smaller WIMP masses. The decline in the upper limit is a result of the non-zero signal strength recovered from the unblinded data sample; whereas under-fluctuations of μ_{Λ_0} result in $\mu_{90} = \bar{\mu}_{90}$. Inelastic scenarios in general obtain smaller MRFs than purely elastic scenarios; all listed scenarios that are excluded are also inelastic (scenarios 0849.4492, 6895.0253 and 8948.6537).

Scenario 0580.5689 (first line) represents an interesting edge case. It does feature inelastic scattering, but is one of the few inelastic scenarios with mass splitting just outside of the range for which a steep increase of the capture rate is observed. The MRF is consequently quite large; even larger than in some elastic cases. In Fig. 5.15, the scenario is shown as one of the two red-circled parameter points to the right of the $\delta^<_{\text{inel.}}$ line. The other one is scenario 9777.3023 (second-to-last line in the table), which does not feature inelastic scattering, despite the slightly smaller mass splitting. To prevent confusion: The $\delta^<_{\text{inel.}}$ threshold marks the mass splitting *below which all scenarios are inelastic*, which does *not* mean there cannot be inelastic scenarios with larger mass splittings. The same holds for $\delta^<_{\text{excl.}}$ in terms of scenario exclusion.

The results of the analysis are further summarized in Tab. 5.6, with the percentage and absolute number of excluded scenarios, the mass splitting thresholds of inelastic scattering and scenario exclusion, and the constraint on the mass splitting parameter λ_5 including systematic uncertainties.

Table 5.5: Analysis results for eleven out of 1,723 benchmark scenarios. Listed are the values of the background test statistic Λ_0, the corresponding best estimator value for the signal strength μ_{Λ_0}, the sensitivity $\bar{\mu}_{90}$, the upper limit μ_{90}, and the MRF; along with the mass splitting δ and the absolute value of the mass splitting parameter, $|\lambda_5|$. The scenario name corresponds to the mass of the respective DM candidate in GeV; gray background color indicates an inelastic scenario. Systematic uncertainties are taken into account.

scenario, m_{DM} [GeV]	$\lvert\lambda_5\rvert \times 10^{-5}$	δ [keV]	Λ_0	μ_{Λ_0}	$\bar{\mu}_{90}$	μ_{90}	MRF
0580.5689	1.2	622.02	4.20×10^{-3}	2.8	68.00	71.32	1.96×10^{6}
0604.9772	76.0	38073.32	3.84×10^{-3}	2.7	75.21	79.50	5.52×10^{3}
0849.4492	0.9	320.05	2.30×10^{-4}	0.7	70.21	70.91	4.79×10^{-3}
4312.8844	61.1	4293.49	0	−4.0	76.37	76.37	2.73×10^{3}
4318.8472	6.9	486.82	0	−0.3	72.35	72.35	2.12
6882.9814	75.3	3318.28	0	−4.6	67.73	67.73	2.11×10^{4}
6895.0253	7.9	345.96	0	−5.2	68.70	68.70	0.15
8941.3663	38.6	1308.23	0	−2.1	60.33	60.33	1.22×10^{9}
8948.6537	11.2	381.00	0	−3.5	59.62	59.62	0.45
9777.3023	19.8	615.32	0	−1.6	57.69	57.69	3.51×10^{5}
9777.3453	15.5	479.52	0	−4.2	58.21	58.21	3.93

Table 5.6: Results of the analysis of 1,723 scotogenic scenarios with nine years of IceCube data. Listed are the percentage and absolute number of excluded scenarios and the mass splitting threshold (MST) for inelastic scattering and scenario exclusion, as well as the constraint of the mass splitting parameter λ_5 below which all investigated scenarios could be excluded. Systematic uncertainties are taken into account.

quantity	**result**
excluded scenarios	17.0 % (293)
MST for inelastic scatteirng	$\delta^{<}_{\mathrm{inel.}} = 595.05\,\mathrm{keV}$
MST for scenario exclusion	$\delta^{<}_{\mathrm{excl.}} = 416.82\,\mathrm{keV}$
constraint on mass splitting parameter	$\lvert\lambda_5\rvert^{<}_{\mathrm{excl.}} = 1.375 \times 10^{-8}\, m_{\mathrm{DM}}/\mathrm{GeV}$

Chapter 6
Summary & outlook

This work presents a theoretical approach to explain the nature of Dark Matter in the form of the Scotogenic Minimal Dark Matter Model, which extends the Standard Model by two new fields, one fermionic singlet and one scalar doublet. The model's Dark Matter candidate is a scalar WIMP, which is stabilized by a global $\mathbb{Z}_2$ symmetry. By scattering off nuclei and being gravitationally captured, scalar Dark Matter can accumulate in the Sun and form an overdensity, in which the rate of Dark Matter annihilation is enhanced. The WIMPs annihilate into Standard Model particle pairs that further decay into neutrinos. This neutrino flux can in principle be measured with neutrino telescopes.

Scalar Dark Matter in the framework of the Scotogenic Model has been studied before; in this work, the effects of an inelastic scattering phenomenology inside the Sun on indirect detection event rates is investigated. It was found that spin-independent inelastic scattering is enabled by a slightly heavier scalar partner to the Dark Matter candidate, provided that the mass splitting between the two particles is small. The mass splitting is governed by the scalar coupling, or mass splitting model parameter λ_5. Inelastic scattering can even dominate the capturing process inside the Sun, in which case a significant boost in the neutrino flux resulting from WIMP annihilation is predicted, bringing the Scotogenic Model in the range of indirect detection experiments.

The investigation of the scotogenic parameter space revealed $1,723$ scenarios that proved viable with regard to theoretical and experimental constraints. The threshold mass splitting for inelastic scattering, valid for the scenarios in this study, could be determined to be $\delta^{<}_{\text{inel.}} = 595.05\,\text{keV}$. In total, 437 scenarios supporting inelastic scattering could be identified.

All $1,723$ scenarios were tested in a maximum likelihood statistical analysis using nine years of IceCube data, with the goal to exclude as many so-far unconstrained scenarios as possible. This study was able to exclude 17 % (or a total of 293) of the scenarios with at least 90 % probability, all them featuring inelastic scattering. A constraint on the mass splitting model parameter could be determined, $|\lambda_5|^{<}_{\text{excl.}} = 1.375 \times 10^{-8}\, m_{\text{DM}}/\text{GeV}$, below which all investigated scenarios are excluded. It was discussed that this threshold has a somewhat limited but justified validity for other scenarios of the Scotogenic Model that have not been studied here.

This study showed that indirect detection experiments can in principle be compatible in the spin-independent scattering realm, which is otherwise dominantly constrained by direct detection experiments. However, many of the considered scenarios are out of reach for IceCube. A small number of not-excluded scenarios was identified that could be probed in a follow-up analysis by means of longer exposure and an improved event selection. Even more scenarios could come in reach with the future large-scale upgrade of the detector, IceCube-Gen2.

A Bayesian point of view?

The special setup of this analysis, especially the way the Scotogenic Model parameter space is sampled in order to identify viable scenarios, calls for a Bayesian statistical analysis method. A Bayesian parameter inference, assuming the experimental constraints as priors, and a Markov-Chain Monte Carlo sampling method could help identify possible likelihood maxima in the parameter space. This would potentially allow for exclusion of whole sections of the parameter space, instead of only individual scenarios. The implementation of such a parameter inference is very complex, not alone because of the many dimensions of the parameter space, and exceeded the scope of this work. A follow-up analysis could pick up the Bayesian approach and deduct improved constraints on the Scotogenic Model.

A gauged Scotogenic Model?

The era of ultra-large-scale neutrino telescopes has been ultimately rang in. There is a high-energy upgrade planned for IceCube, called IceCube-Gen2 [176], a detector eight times the volume of the current configuration; and the low-energy IceCube upgrade [177] will be installed in the upcoming years. Other telescopes are currently being completed, like the KM3NeT experiment, and even more are in the planning phase, for instance the Pacific Ocean Neutrino Experiment (P-ONE) [178] whose 70-string configuration is to be installed at the seafloor in a depth of 2.7 km, off the Pacific coast of Canada; as well as a Chinese initiative called The tRopIcal DEep-sea Neutrino Telescope (TRIDENT) [179], that consists of over a thousand strings in a multi-km wide footprint in its preliminary design.

Indirect detection with neutrino telescopes will continue to play an important role in the quest for finding the nature of Dark Matter; and parameter spaces of minimal models could soon be probed in regions that seemed unthinkable just a few decades ago.

Many models, especially those with simpler field content, have been thoroughly studied already, but inelastic scattering in the Scotogenic Model is living proof that interesting phenomenology sometimes turns up in unexpected places. The scenarios studied in this work were only few out of many possible solutions to the Dark Matter mystery that involve indirect detection, and many models are yet to be investigated with regard to indirect detection neutrino limits.

One such model — of some sorts a modification of the Scotogenic Model — introduces a singlet fermion in combination with a massive vector boson Z' (spoken Z-prime) mediator, which arises naturally from gauging the model under a $U(1)$ (which replaces the global $\mathbb{Z}_2$ symmetry of "our" Scotogenic Model). Such a continuous symmetry is favorable over a discrete $\mathbb{Z}_2$, because it is easily motivated as a residual of some larger, universal symmetry. Different scenarios of this model are currently being studied with the tools developed as a part of this thesis.

Of course, each move towards more complexity has impacts on neutrino event rates, as each modification towards a simplified field content could come at the price of detectability. It will require many more hours, probably years, of inspired collaboration of theoretical and experimental physicists, to stake out the future path of minimal models towards solving the mystery of Dark Matter.

Appendix

A The IceCube coordinate system

The position of celestial objects is often given as a pair of two angles. These coordinates have variable meaning, depending on convention and the frame of reference. For a study that aims at finding signals from a specific point in the sky, it is crucial to understand the conversion between astronomical directions. This section is an attempt to help with some widespread confusion about coordinate systems.

Spherical coordinates

For observations of the night sky, defining the position of astronomical objects in spherical coordinates is a logical choice. Objects are "pinned" to a virtual sphere with a well known origin. *Virtual* because the true distance of the objects is irrelevant; all celestial bodies are simply projected onto one canvas or *firmament* (much like it is depicted in the famous Flammarion Engraving, Fig. A.1).
In general for spherical coordinates, the frame of reference is spanned by the *fundamental plane* and the *primary direction*, see Fig. A.2. A position is given as a pair of angles, which have different names in different spherical coordinate systems.

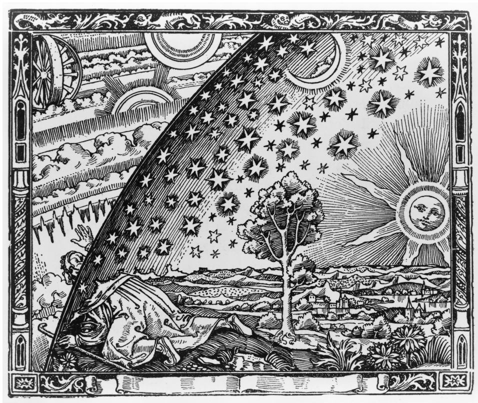

Figure A.1: The Flammarion Engraving. [Unknown artist, public domain]

The geographic coordinate system

Unsurprisingly, coordinates on Earth are given in spherical coordinates. The surface of the Earth is the "virtual" sphere, the Earth's core is the origin, the equatorial line defines the fundamental plane, and the primary direction corresponds to the *Prime Meridian* (the position of which is a historical, political, and completely arbitrary choice). The two angles of measurement are the *latitude* (lat.), measured northward from the equator (meaning southward angles are negative, or fit with an "S"); and the *longitude* (long.), measured eastward from the Prime Meridian.

As a characteristic of spherical coordinate systems, the circles of longitude grow smaller with larger distance to the equator, until they collapse into points at the North and South Poles. Consequently, the longitude seems to have limited meaning for navigation very close to the poles. It can be crucial information though, as the reader will see below.

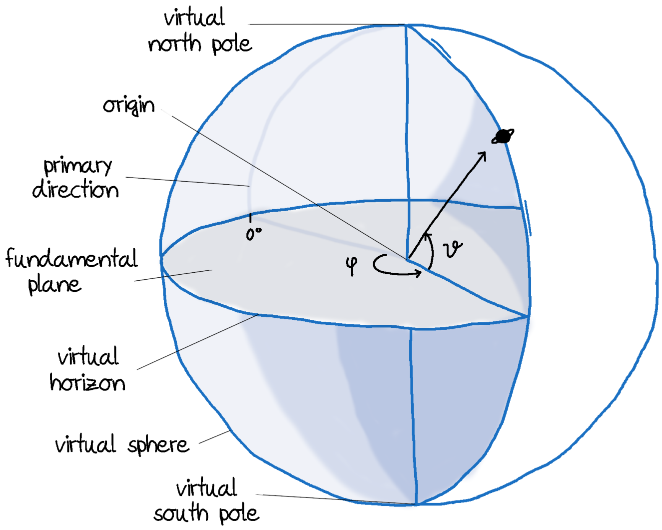

Figure A.2: The principal of spherical coordinates. The position of any object projected onto the virtual sphere is given as a set of two angles φ and ϑ. The primary direction is the semi-circle of $\varphi = 0\,°$ in all spherical coordinates. The circle of $\vartheta = 0\,°$ is up to convention, but usually coincides with the virtual horizon.

The equatorial coordinate system

Charting astronomical objects is usually done with equatorial coordinates, and positions are defined by the two angles of *declination* (Dec) and *right ascension* (RA). Like the geographic system, the equatorial system is geocentric, meaning that the origin lies in the center of the Earth. The fundamental plane is again the equator of the Earth, but it is called the *celestial equator* and is projected onto a sphere which is actually virtual this time. The primary direction is the intersection of the ecliptic (i.e. the plane in which the Earth orbits the Sun) with the celestial equator at the time of the vernal (spring) equinox.[1] Coordinates are conventionally described by angles northward from the celestial equator, which corresponds to declination, and eastward/clockwise from the primary direction, which corresponds to the right ascension.

The equatorial coordinate system does not rotate with the Earth around its axis, keeping sufficiently distant objects fixed and independent from observation time and location on Earth. (Closer objects, for instance in the solar system, still depend on observation time and the observer's location.)

The horizontal coordinate system

The complement to equatorial directions is the horizontal coordinate system, in which the location of an object is expressed by the angles of *altitude (Alt)* and *azimuth (Az)*. By design, the origin is the observer herself, the fundamental plane her horizon on Earth, and the primary direction is the *True North*, i.e. the (shortest!) connection between the virtual horizon and the virtual north pole (which can be found by extending the Earth's axis). Altitude is measured northward from the local horizon, and the azimuth eastward from True North. Obviously, this system depends not only on observation time, but also on the observer's location, so that objects obtain different coordinates for every place on Earth and for any time of the day or night. The practical advantage is that objects are relatively easy to find in the sky, provided that the direction of True North is known.

[1]Technically, the vernal equinox moves as a result of Earth's slow precession around its axis. So equatorial coordinates only make sense in combination with a time, called the *epoch*, of the vernal equinox. The most commonly used epoch is J2000 (Julian year 2000).

The IceCube coordinate system

The IceCube (or I3) coordinate system is a modified horizontal coordinate system. The origin is located in the approximate center of the detector, at an elevation of 883.9 m (approximately 1,500 m underground). The precise location is relative to the geographic South Pole, which is surveyed every year.[2] The approximate location of the origin projected onto the surface of the Earth, given by latitude and longitude, is 89.99 °S, −62.61 °E. The fundamental plane of the I3 coordinate system is the local horizon at this (moving) origin.

One might wonder why the longitude matters at a point so close to the South Pole. Indeed geographically, the longitude is basically irrelevant information. Astronomically however, it is crucial, because the primary direction is True North, and True North is the shortest way to the North Pole. At the South Pole, however, *every* way is the shortest way to the North Pole. Imagine an observer drawing a tight circle of a few meters in diameter around the geographic South Pole, and moving about this circle. True North would always be facing directly away from the center of the circle, changing the azimuth of an object on the virtual sphere by 360 ° for a full revolution, even though the observer had barely moved.

On human scales, it is very impractical to keep track of cardinal directions while being in close proximity to a pole. So "Polies" define their directions by "Grid North" which always points along the Prime Meridian of 0 ° longitude. But Grid North is *not* the primary direction of the I3 coordinate system. Instead, the primary direction is oriented at Grid *East*, i.e. 90 ° eastward from Grid North. Oddly enough, the azimuth angle is measured westward from Grid East. IceCube uses zenith angle instead of altitude, which is measured southward from the perpendicular, instead of northward from the horizon. So, in other words, IceCube breaks with a lot of conventions, which can make an attempt to understand I3 coordinates very difficult.

The following formulae should help with conversion from *any* horizontal system into I3 coordinates:

$$\begin{aligned} \text{zenith}_{\text{I3}} &= 90\,^\circ - \text{altitude}_{\text{hrz}} \\ \text{azimuth}_{\text{I3}} &= \left(90\,^\circ - \text{azimuth}_{\text{hrz}} - \text{longitude}_{\text{ICL}}\right) \mod 360 \end{aligned} \tag{6.1}$$

Fortunately, IceCube data usually comes with the reconstructed directions for every event, already converted into I3 coordinates which account for the current location of the detector relative to the South Pole, so manual conversion is rarely necessary.

[2]The location of the geographic South Pole changes with the movement of the glacier. A sign and marker indicate the precise spot; they are moved to their new position every year on January 1st. On this occasion a new marker is placed, traditionally designed by the winterovers of the previous year. The ceremonial inauguration by the wintersite manager is considered an important event at Amundsen-Scott's and is attended by all station personnel.

B A winterover's anecdote

Since the year 1957, 1,666 people [180] have wintered over at the South Pole. Despite modern technology and infrastructure, South Pole remains the most remote permanent human outpost of our time — the International Space Station included (not only is the ISS closer to society in terms of actual distance, it is also way faster to evacuate in case of emergency). A winter at Pole is therefore a most exclusive experience; one that has changed my view on life, the planet, and everything on it (including this PhD thesis).

From a purely science-motivated point of view, the location of the South Pole for the IceCube detector does not seem to be a particularly good choice. High-end computing equipment *hates* the extreme temperatures and the electrostatics that comes with the not-existing humidity (many expensive things have been fried by a thoughtless touch). Internet connectivity is sparse, and most of the science data has to stay put until the end of each season. And there is a dust layer from volcanic activity thousands of years ago, sitting inside the detector volume and throwing a shadow on a significant number of modules. However, from the standpoint of logistics, the choice of location was quite logical. The South Pole is the only place on Earth with a sufficiently thick ice sheet that also has an infrastructure that allows building something that big. The infrastructure is not constant over the year, though. Only four months, November through February — or "summer" as we call it — are warm enough to supply Amundsen-Scott South Pole Station by airplane or tractor caravan. The other eight months is "winter", where nothing's in and nothing's out. During that time of darkness, only a skeleton crew of around forty people remains on site (compared to around 150 in summer), the so-called *winterovers*, two of which are responsible for keeping IceCube alive and running 24 hours each day.

Figure B.1: The author at South Pole.

When I was IceCube winterover in 2017/18, I got to experience first hand what it means to be a human in Antarctica (specimen shown in Fig. B.1). The very vibrant sensation of ice crystals rapidly forming on my nose-hairs when I first set foot on South Pole station air field is etched into my brain forever, as well as the miserable pain of frost-nipped fingers that had me and several other people crying in the hallways, with nothing much that could be done about it except waiting until the pain goes away. (Pain is a good sign, though — as long as it still hurts, it's not frost-*bitten*, which could lead to amputation.) But not only people suffer in the harsh environment; stuff does, too. Fun fact: Apart from the station's kitchen freezer, the ICL server room, that houses hundreds of machines for IceCube data taking, is the only room on site that has to be actively cooled. When the air conditioning would fail, which used to happen after some of the frequently occurring station-wide power outages, the excess heat of the machines that failed over to battery-power would turn the server room into a sauna within as little as thirty minutes. In an incident like that, my colleague and I would rush out to the ICL (which is about a kilometer away from station), one of us gently ventilating outside air into the room — only for a few seconds at a time — while the other one would try to get the cooling back online before the hardware would take damage from the extreme temperatures. You know, high-performance servers aren't usually graded for neither positive nor negative $60°$ C. (In the following year, the AC failure issue was fixed.)

Despite all the inconveniences and ways to die, South Pole is still a breathtakingly beautiful place. It comes with a unique set of sounds, be it the howling of the wind beneath the station that can drown out all other sounds, or the cracking when you step on the a sastrugi with your moon boots — kind of what I would imagine walking across meringue sounds like. There are special ice formations that develop during winter, with long pointy ends, completely defying the laws of gravity, which make a particularly funny sound when broken off: *Kdunk*. Then again, at other times, South Pole can be extraordinarily quiet, leaving you with nothing but the sound of your own breath inside your balaclava, which can be quite eerie.

One of the main reasons people (including me) want to go to the South Pole, are the Aurora Australis, or Southern Lights. The electrifying phenomenon is almost exclusive to Antarctic winterovers, and worth the risk of a couple frozen toes. An example from my winter (auroras, not toes) is shown in Fig. 2.13.

The IceCube winterovers do an important job for the collaboration, but they're more technicians than physicists. They make sure that the machines are running and the uptime is as high as possible, watching the detector around the clock by means of a sophisticated automatic monitoring system that sends pages to their radios whenever something is off, much like a baby-phone (they make those notorious modem sounds, a recording of which I still use as a ringtone for my phone, probably out of nostalgia); as well as routine work like swapping hard drives and running calibrations. However, even though the data is collected on site, the science happens elsewhere, conducted by the Northern collaboration members in tireless efforts to squeeze out information about our universe. I was privileged and lucky enough to work on both sides. Although, after a year of hands-on work in the icy desert it took me a while to warm up to real physics and data analysis. This thesis is dedicated to these efforts.

Bibliography

[1] Y. Fukuda, et al. (Super-Kamiokande Collaboration), *Evidence for oscillation of atmospheric neutrinos*, Phys. Rev. Lett. 81 (1998) 1562–1567, Preprint (arXiv) hep-ex/9807003, DOI 10.1103/PhysRevLett.81.1562.

[2] Q. R. Ahmad, et al. (SNO Collaboration), *Direct evidence for neutrino flavor transformation from neutral current interactions in the Sudbury Neutrino Observatory*, Phys. Rev. Lett. 89 (2002) 011301, Preprint (arXiv) nucl-ex/0204008, DOI 10.1103/PhysRevLett.89.011301.

[3] J. Oberauer, L. Oberauer, *Neutrinophysik — Grundlagen, Experimente und aktuelle Forschung*, Springer Spektrum, Berlin, Germany, 2019, ISBN 978-3-662-59334-9.

[4] C. Spiering, *Towards High-Energy Neutrino Astronomy. A Historical Review*, Eur. Phys. J. H 37 (2012) 515–565, Preprint (arXiv) 1207.4952, DOI 10.1140/epjh/e2012-30014-2.

[5] R. L. Workman, et al. (Particle Data Group Collaboration), *Review of Particle Physics*, PTEP 2022 (2022) 083C01, DOI 10.1093/ptep/ptac097, URL `https://pdg.lbl.gov/` (accessed 14.11.2022).

[6] A. M. Hillas, *Cosmic Rays: Recent Progress and some Current Questions*, in: Conference on Cosmology, Galaxy Formation and Astro-Particle Physics on the Pathway to the SKA, 2006, Preprint (arXiv) astro-ph/0607109.

[7] M. G. Aartsen, et al. (IceCube Collaboration), *Measurement of the Atmospheric ν_e Spectrum with IceCube*, Phys. Rev. D 91 (2015) 122004, Preprint (arXiv) 1504.03753, DOI 10.1103/PhysRevD.91.122004.

[8] T. K. Gaisser, R. Engel, E. Resconi, *Cosmic Rays and Particle Physics*, Cambridge University Press, Cambridge, United Kingdom, 2016, ISBN 978-0-521-01646-9.

[9] A. Fedynitch, R. Engel, T. K. Gaisser, F. Riehn, T. Stanev, *Calculation of conventional and prompt lepton fluxes at very high energy*, EPJ Web Conf. 99 (2015) 08001, Preprint (arXiv) 1503.00544, DOI 10.1051/epjconf/20159908001.

[10] IceCube collaboration, *nuflux*, URL `https://github.com/icecube/nuflux` (accessed 14.11.2022).

[11] C. A. Argüelles, *NUSQuIDS*, URL `https://github.com/arguelles/nuSQuIDS` (accessed 22.08.2022).

[12] L. Classen, *The mDOM — a multi-PMT digital optical module for the IceCube-Gen2 neutrino telescope*, PhD thesis, Friedrich-Alexander-Universität Erlangen-Nürnberg (2017), URL `https://www.uni-muenster.de/Physik.KP/AGKappes/ag/arbeiten.html` (accessed 14.11.2022).

[13] M. G. Aartsen, et al. (IceCube Collaboration), *Searches for neutrinos from cosmic-ray interactions in the Sun using seven years of IceCube data*, JCAP 02 (2021) 25, Preprint (arXiv) 1912.13135, DOI 10.1088/1475-7516/2021/02/025.

[14] G. L. Fogli, E. Lisi, A. Mirizzi, D. Montanino, P. D. Serpico, *Oscillations of solar atmosphere neutrinos*, Phys. Rev. D 74 (2006) 093004, Preprint (arXiv) hep-ph/0608321, DOI 10.1103/PhysRevD.74.093004.

[15] M. G. Aartsen, et al. (IceCube Collaboration), *Neutrino emission from the direction of the blazar TXS 0506+056 prior to the IceCube-170922A alert*, Science 361 (6398) (2018) 147–151, Preprint (arXiv) 1807.08794, DOI 10.1126/science.aat2890.

[16] M. G. Aartsen, et al. (IceCube, Fermi-LAT, MAGIC, AGILE, ASAS-SN, HAWC, H.E.S.S., INTEGRAL, Kanata, Kiso, Kapteyn, Liverpool Telescope, Subaru, Swift NuSTAR, VERITAS, VLA/17B-403 Collaboration), *Multi-messenger observations of a flaring blazar coincident with high-energy neutrino IceCube-170922A*, Science 361 (6398) (2018) eaat1378, Preprint (arXiv) 1807.08816, DOI 10.1126/science.aat1378.

[17] R. Stein, et al., *A tidal disruption event coincident with a high-energy neutrino*, Nature Astron. 5 (5) (2021) 510–518, Preprint (arXiv) 2005.05340, DOI 10.1038/s41550-020-01295-8.

[18] R. Abbasi, et al. (IceCube Collaboration), *Evidence for neutrino emission from the nearby active galaxy NGC 1068*, Science 378 (6619) (2022) 538–543, DOI 10.1126/science.abg3395.

[19] R. Davis, *A review of the Homestake solar neutrino experiment*, Prog. Part. Nucl. Phys. 32 (1994) 13–32, DOI 10.1016/0146-6410(94)90004-3.

[20] W. Hampel, et al. (GALLEX Collaboration), *Verification tests of the GALLEX solar neutrino detector, with Ge-71 produced in-situ from the beta decay of As-71*, Phys. Lett. B 436 (1998) 158–173, DOI 10.1016/S0370-2693(98)00875-2.

[21] M. Altmann, et al. (GNO Collaboration), *Complete results for five years of GNO solar neutrino observations*, Phys. Lett. B 616 (2005) 174–190, Preprint (arXiv) hep-ex/0504037, DOI 10.1016/j.physletb.2005.04.068.

[22] J. N. Abdurashitov, et al. (SAGE Collaboration), *Measurement of the solar neutrino capture rate with gallium metal. III: Results for the 2002–2007 data-taking period*, Phys. Rev. C 80 (2009) 015807, Preprint (arXiv) 0901.2200, DOI 10.1103/PhysRevC.80.015807.

[23] S. Abe, et al. (KamLAND Collaboration), *Precision Measurement of Neutrino Oscillation Parameters with KamLAND*, Phys. Rev. Lett. 100 (2008) 221803, Preprint (arXiv) 0801.4589, DOI 10.1103/PhysRevLett.100.221803.

[24] C. Grupen, *Astroparticle Physics*, Springer, Berlin, Heidelberg, Germany, 2010, ISBN 978-3-540-27670-8.

[25] B. Aharmim, et al. (SNO Collaboration), *Combined Analysis of all Three Phases of Solar Neutrino Data from the Sudbury Neutrino Observatory*, Phys. Rev. C 88 (2013) 025501, Preprint (arXiv) 1109.0763, DOI 10.1103/PhysRevC.88.025501.

[26] K. Abe, et al. (Super-Kamiokande Collaboration), *Solar Neutrino Measurements in Super-Kamiokande-IV*, Phys. Rev. D 94 (5) (2016) 052010, Preprint (arXiv) 1606.07538, DOI 10.1103/PhysRevD.94.052010.

[27] Y. Abe, et al. (Double Chooz Collaboration), *Improved measurements of the neutrino mixing angle θ_{13} with the Double Chooz detector*, JHEP 10 (2014) 086, Preprint (arXiv) 1406.7763, DOI 10.1007/JHEP02(2015)074, [Erratum: JHEP 02, 074 (2015)].

[28] J. K. Ahn, et al. (RENO Collaboration), *RENO: An Experiment for Neutrino Oscillation Parameter θ_{13} Using Reactor Neutrinos at Yonggwang* Preprint (arXiv) 1003.1391.

[29] F. P. An, et al. (Daya Bay Collaboration), *New measurement of θ_{13} via neutron capture on hydrogen at Daya Bay*, Phys. Rev. D 93 (7) (2016) 072011, Preprint (arXiv) 1603.03549, DOI 10.1103/PhysRevD.93.072011.

[30] K. Abe, et al. (Super-Kamiokande Collaboration), *Atmospheric neutrino oscillation analysis with external constraints in Super-Kamiokande I-IV*, Phys. Rev. D 97 (7) (2018) 072001, Preprint (arXiv) 1710.09126, DOI 10.1103/PhysRevD.97.072001.

[31] M. G. Aartsen, et al. (IceCube Collaboration), *Measurement of Atmospheric Neutrino Oscillations at 6–56 GeV with IceCube DeepCore*, Phys. Rev. Lett. 120 (7) (2018) 071801, Preprint (arXiv) 1707.07081, DOI 10.1103/PhysRevLett.120.071801.

[32] L. Wolfenstein, *Neutrino Oscillations in Matter*, Phys. Rev. D 17 (1978) 2369–2374, DOI 10.1103/PhysRevD.17.2369.

[33] S. P. Mikheev, A. Y. Smirnov, *Resonant amplification of neutrino oscillations in matter and solar neutrino spectroscopy*, Nuovo Cim. C 9 (1986) 17–26, DOI 10.1007/BF02508049.

[34] J. A. Formaggio, G. P. Zeller, *From eV to EeV: Neutrino Cross Sections Across Energy Scales*, Rev. Mod. Phys. 84 (2012) 1307–1341, Preprint (arXiv) 1305.7513, DOI 10.1103/RevModPhys.84.1307.

[35] J. Boger, et al. (SNO Collaboration), *The Sudbury neutrino observatory*, Nucl. Instrum. Meth. A 449 (2000) 172–207, Preprint (arXiv) nucl-ex/9910016, DOI 10.1016/S0168-9002(99)01469-2.

[36] Y. Fukuda, et al. (Super-Kamiokande Collaboration), *The Super-Kamiokande detector*, Nucl. Instrum. Meth. A 501 (2003) 418–462, DOI 10.1016/S0168-9002(03)00425-X.

[37] H. Kolanoski, N. Wermes, *Teilchendetektoren*, Springer Spektrum, Berlin, Heidelberg, Germany, 2016, ISBN 978-3-662-45349-0, DOI 10.1007/978-3-662-45350-6.

[38] I. M. Frank, I. E. Tamm, *Coherent visible radiation of fast electrons passing through matter*, Compt. Rend. Acad. Sci. URSS 14 (3) (1937) 109–114, DOI 10.3367/UFNr.0093.196710o.0388.

[39] A. Roberts, *The Birth of high-energy neutrino astronomy: A Personal history of the DUMAND project*, Rev. Mod. Phys. 64 (1992) 259–312, DOI 10.1103/RevModPhys.64.259.

[40] I. A. Belolaptikov, et al. (BAIKAL Collaboration), *The Baikal underwater neutrino telescope: Design, performance and first results*, Astropart. Phys. 7 (1997) 263–282, DOI 10.1016/S0927-6505(97)00022-4.

[41] E. Andres, et al., *The AMANDA neutrino telescope: Principle of operation and first results*, Astropart. Phys. 13 (2000) 1–20, Preprint (arXiv) astro-ph/9906203, DOI 10.1016/S0927-6505(99)00092-4.

[42] E. Aslanides, et al. (ANTARES Collaboration), *A deep sea telescope for high-energy neutrinos* Preprint (arXiv) astro-ph/9907432.

[43] S. Adrian-Martinez, et al. (KM3Net Collaboration), *Letter of intent for KM3NeT 2.0*, J. Phys. G 43 (8) (2016) 084001, Preprint (arXiv) 1601.07459, DOI 10.1088/0954-3899/43/8/084001.

[44] M. G. Aartsen, et al. (IceCube Collaboration), *The IceCube Neutrino Observatory: Instrumentation and Online Systems*, JINST 12 (03) (2017) P03012, Preprint (arXiv) 1612.05093, DOI 10.1088/1748-0221/12/03/P03012.

[45] M. Ackermann, et al., *Optical properties of deep glacial ice at the South Pole*, J. Geophys. Res. 111 (D13) (2006) D13203, DOI 10.1029/2005JD006687.

[46] R. Abbasi, et al. (IceCube Collaboration), *Low energy event reconstruction in IceCube DeepCore*, Eur. Phys. J. C 82 (9) (2022) 807, Preprint (arXiv) 2203.02303, DOI 10.1140/epjc/s10052-022-10721-2.

[47] R. Abbasi, et al. (IceCube Collaboration), *The Design and Performance of IceCube DeepCore*, Astropart. Phys. 35 (2012) 615–624, Preprint (arXiv) 1109.6096, DOI 10.1016/j.astropartphys.2012.01.004.

[48] R. Abbasi, et al. (IceCube Collaboration), *IceTop: The surface component of IceCube*, Nucl. Instrum. Meth. A 700 (2013) 188–220, Preprint (arXiv) 1207.6326, DOI 10.1016/j.nima.2012.10.067.

[49] M. A. U. Elorrieta, *Development, simulation, and characterisation of a novel multi-PMT optical module for IceCube Upgrade with emphasis on detailed understanding of photomultiplier performance*, PhD thesis, Westfälische Wilhelms-Universität Münster, not yet published.

[50] M. G. Aartsen, et al. (IceCube Collaboration), *Evidence for High-Energy Extraterrestrial Neutrinos at the IceCube Detector*, Science 342 (2013) 1242856, Preprint (arXiv) 1311.5238, DOI 10.1126/science.1242856.

[51] *IceCube Masterclass website*, URL `https://masterclass.icecube.wisc.edu/en/learn/detecting-neutrinos` (accessed 23.05.2022).

[52] R. Abbasi, et al. (IceCube Collaboration), *Detection of astrophysical tau neutrino candidates in IceCube*, Eur. Phys. J. C 82 (11) (2022) 1031, DOI 10.1140/epjc/s10052-022-10795-y.

[53] M. G. Aartsen, et al. (IceCube Collaboration), *Measurement of Atmospheric Tau Neutrino Appearance with IceCube DeepCore*, Phys. Rev. D 99 (3) (2019) 032007, Preprint (arXiv) 1901.05366, DOI 10.1103/PhysRevD.99.032007.

[54] I. N. Bronštein, K. A. Semendjajew, G. Musiol, H. Mühlig, *Taschenbuch der Mathematik*, 7th Edition, Wissenschaftlicher Verlag Harri Deutsch GmbH, Frankfurt am Main, Germany, 2008, ISBN 978-3-817-12007-9.

[55] S. May, *Minimal dark matter models with radiative neutrino masses: From Lagrangians to observables*, Master's thesis, Westfälische Wilhelms-Universität Münster (2020), Preprint (arXiv) 2003.04157.

[56] F. Halzen, A. D. Martin, *Quarks and Leptons: An Introductary Course in Modern Particle Physics*, John Wiley & Sons Ltd., New York, USA, 1984, ISBN 978-0-471-88741-6.

[57] M. Schwartz, *Quantum Field Theory and the Standard Model*, Cambridge University Press, Cambridge, United Kingdom, 2014, ISBN 978-1-107-03473-0.

[58] M. Aker, et al. (KATRIN Collaboration), *Direct neutrino-mass measurement with sub-electronvolt sensitivity*, Nature Phys. 18 (2) (2022) 160–166, Preprint (arXiv) 2105.08533, DOI 10.1038/s41567-021-01463-1.

[59] L. e. Evans, P. e. Bryant, *LHC Machine*, JINST 3 (2008) S08001, DOI 10.1088/1748-0221/3/08/S08001.

[60] J. Schwichtenberg, *Physics from Symmetry*, 2nd Edition, Springer Nature, Cham, Switzerland, 2015, ISBN 978-3-319-66630-3.

[61] G. Aad, et al. (ATLAS Collaboration), *Observation of a new particle in the search for the Standard Model Higgs boson with the ATLAS detector at the LHC*, Phys. Lett. B 716 (2012) 1–29, Preprint (arXiv) 1207.7214, DOI 10.1016/j.physletb.2012.08.020.

[62] Flip Tanedo, *Helicity, Chirality, Mass, and the Higgs*, URL `https://quantumdiaries.org/2011/06/19/helicity-chirality-mass-and-the-higgs/` (accessed 11.08.2022).

[63] N. Aghanim, et al. (Planck Collaboration), *Planck 2018 results. VI. Cosmological parameters*, Astron. Astrophys. 641 (2020) A6, Preprint (arXiv) 1807.06209, DOI 10.1051/0004-6361/201833910, [Erratum: Astron.Astrophys. 652, C4 (2021)].

[64] J. Bekenstein, M. Milgrom, *Does the missing mass problem signal the breakdown of Newtonian gravity?*, Astrophys. J. 286 (1984) 7–14, DOI 10.1086/162570.

[65] S. Profumo, *An Introduction to Particle Dark Matter*, World Scientific Publishing Europe Ltd., London, United Kingdom, 2017, ISBN 978-1-786-34000-9.

[66] A. Liddle, *Einführung in die moderne Kosmologie*, WILEY-VHC Verlag, Weinheim, Germany, 2009, ISBN 978-3-527-40882-5.

[67] A. G. Riess, et al. (Supernova Search Team Collaboration), *Observational evidence from supernovae for an accelerating universe and a cosmological constant*, Astron. J. 116 (1998) 1009–1038, Preprint (arXiv) astro-ph/9805201, DOI 10.1086/300499.

[68] S. Perlmutter, et al. (Supernova Cosmology Project Collaboration), *Measurements of Ω and Λ from 42 high redshift supernovae*, Astrophys. J. 517 (1999) 565–586, Preprint (arXiv) astro-ph/9812133, DOI 10.1086/307221.

[69] F. Zwicky, *On the Masses of Nebulae and of Clusters of Nebulae*, Astrophys. J. 86 (1937) 217–246, DOI 10.1086/143864.

[70] Y. Sofue, V. Rubin, *Rotation curves of spiral galaxies*, Ann. Rev. Astron. Astrophys. 39 (2001) 137–174, Preprint (arXiv) astro-ph/0010594, DOI 10.1146/annurev.astro.39.1.137.

[71] C. Alcock, et al. (MACHO Collaboration), *The MACHO project: Microlensing results from 5.7 years of LMC observations*, Astrophys. J. 542 (2000) 281–307, Preprint (arXiv) astro-ph/0001272, DOI 10.1086/309512.

[72] M. Aker, et al. (KATRIN Collaboration), *Improved Upper Limit on the Neutrino Mass from a Direct Kinematic Method by KATRIN*, Phys. Rev. Lett. 123 (22) (2019) 221802, Preprint (arXiv) 1909.06048, DOI 10.1103/PhysRevLett.123.221802.

[73] M. Lattanzi, R. A. Lineros, M. Taoso, *Connecting neutrino physics with dark matter*, New J. Phys. 16 (12) (2014) 125012, Preprint (arXiv) 1406.0004, DOI 10.1088/1367-2630/16/12/125012.

[74] Gelmini, Graciela and Gondolo, Paolo, *DM Production Mechanisms* (2010) 121–141 Preprint (arXiv) 1009.3690.

[75] A. Boveia, C. Doglioni, *Dark Matter Searches at Colliders*, Ann. Rev. Nucl. Part. Sci. 68 (2018) 429–459, Preprint (arXiv) 1810.12238, DOI 10.1146/annurev-nucl-101917-021008.

[76] G. Aad, et al. (ATLAS Collaboration), *The ATLAS Experiment at the CERN Large Hadron Collider*, JINST 3 (2008) S08003, DOI 10.1088/1748-0221/3/08/S08003.

[77] B. B. Abelev, et al. (ALICE Collaboration), *Performance of the ALICE Experiment at the CERN LHC*, Int. J. Mod. Phys. A 29 (2014) 1430044, Preprint (arXiv) 1402.4476, DOI 10.1142/S0217751X14300440.

[78] S. Chatrchyan, et al. (CMS Collaboration), *The CMS Experiment at the CERN LHC*, JINST 3 (2008) S08004, DOI 10.1088/1748-0221/3/08/S08004.

[79] D. Decamp, et al. (ALEPH Collaboration), *ALEPH: A detector for electron-positron annnihilations at LEP*, Nucl. Instrum. Meth. A 294 (1990) 121–178, DOI 10.1016/0168-9002(90)91831-U, [Erratum: Nucl.Instrum.Meth.A 303, 393 (1991)].

[80] P. A. Aarnio, et al. (DELPHI Collaboration), *The DELPHI detector at LEP*, Nucl. Instrum. Meth. A 303 (1991) 233–276, DOI 10.1016/0168-9002(91)90793-P.

[81] K. Ahmet, et al. (OPAL Collaboration), *The OPAL detector at LEP*, Nucl. Instrum. Meth. A 305 (1991) 275–319, DOI 10.1016/0168-9002(91)90547-4.

[82] B. Adeva, et al. (L3 Collaboration), *The Construction of the L3 Experiment*, Nucl. Instrum. Meth. A 289 (1990) 35–102, DOI 10.1016/0168-9002(90)90250-A.

[83] E. Aprile, et al. (XENON Collaboration), *Design and Performance of the XENON10 Dark Matter Experiment*, Astropart. Phys. 34 (2011) 679–698, Preprint (arXiv) 1001.2834, DOI 10.1016/j.astropartphys.2011.01.006.

[84] E. Aprile, et al. (XENON Collaboration), *The XENON1T Dark Matter Experiment*, Eur. Phys. J. C 77 (12) (2017) 881, Preprint (arXiv) 1708.07051, DOI 10.1140/epjc/s10052-017-5326-3.

[85] R. Bernabei, et al. (DAMA Collaboration), *The DAMA/LIBRA apparatus*, Nucl. Instrum. Meth. A 592 (2008) 297–315, Preprint (arXiv) 0804.2738, DOI 10.1016/j.nima.2008.04.082.

[86] R. Bernabei, et al., *First model independent results from DAMA/LIBRA-phase2*, Nucl. Phys. Atom. Energy 19 (4) (2018) 307–325, Preprint (arXiv) 1805.10486, DOI 10.15407/jnpae2018.04.307.

[87] R. Bernabei, et al., *Improved model-dependent corollary analyses after the first six annual cycles of DAMA/LIBRA-phase2*, Nucl. Phys. Atom. Energy 20 (4) (2019) 317–348, Preprint (arXiv) 1907.06405, DOI 10.15407/jnpae2019.04.317.

[88] J. Amare, et al., *Annual modulation results from three-year exposure of ANAIS-112*, Phys. Rev. D 103 (10) (2021) 102005, Preprint (arXiv) 2103.01175, DOI 10.1103/PhysRevD.103.102005.

[89] G. Adhikari, et al. (COSINE-100 Collaboration), *Three-year annual modulation search with COSINE-100*, Phys. Rev. D 106 (5) (2022) 052005, Preprint (arXiv) 2111.08863, DOI 10.1103/PhysRevD.106.052005.

[90] C. Amole, et al. (PICO Collaboration), *PICASSO, COUPP and PICO - Search for Dark Matter with Bubble Chambers*, in: L. Bravina, Y. Foka, S. Kabana (Eds.), 3rd International Conference on New Frontiers in Physics (ICNFP 2014), Vol. 95, 2015, p. 04020, DOI 10.1051/epjconf/20149504020.

[91] C. Amole, et al. (PICO Collaboration), *Dark matter search results from the PICO-60 CF_3I bubble chamber*, Phys. Rev. D 93 (5) (2016) 052014, Preprint (arXiv) 1510.07754, DOI 10.1103/PhysRevD.93.052014.

[92] R. Abbasi, et al. (IceCube Collaboration), *A Search for Neutrinos from Decaying Dark Matter in Galaxy Clusters and Galaxies with IceCube*, PoS ICRC2021 (2021) 506, Preprint (arXiv) 2107.11527, DOI 10.22323/1.395.0506.

[93] J. A. Hinton (H.E.S.S. Collaboration), *The Status of the H.E.S.S. project*, New Astron. Rev. 48 (2004) 331–337, Preprint (arXiv) astro-ph/0403052, DOI 10.1016/j.newar.2003.12.004.

[94] A. Abramowski, et al. (H.E.S.S. Collaboration), *Search for a Dark Matter annihilation signal from the Galactic Center halo with H.E.S.S*, Phys. Rev. Lett. 106 (2011) 161301, Preprint (arXiv) 1103.3266, DOI 10.1103/PhysRevLett.106.161301.

[95] E. Lorenz (MAGIC Collaboration), *Status of the 17-m MAGIC telescope*, New Astron. Rev. 48 (2004) 339–344, DOI 10.1016/j.newar.2003.12.059.

[96] M. L. Ahnen, et al. (MAGIC, Fermi-LAT Collaboration), *Limits to Dark Matter Annihilation Cross-Section from a Combined Analysis of MAGIC and Fermi-LAT Observations of Dwarf Satellite Galaxies*, JCAP 02 (2016) 039, Preprint (arXiv) 1601.06590, DOI 10.1088/1475-7516/2016/02/039.

[97] W. B. Atwood, et al. (Fermi-LAT Collaboration), *The Large Area Telescope on the Fermi Gamma-ray Space Telescope Mission*, Astrophys. J. 697 (2009) 1071–1102, Preprint (arXiv) 0902.1089, DOI 10.1088/0004-637X/697/2/1071.

[98] G. Bélanger, J. Da Silva, T. Perrillat-Bottonet, A. Pukhov, *Limits on dark matter proton scattering from neutrino telescopes using micrOMEGAs*, JCAP 12 (2015) 036, Preprint (arXiv) 1507.07987, DOI 10.1088/1475-7516/2015/12/036.

[99] T. Kopka, *Parameter-space studies of Dark Matter annihilations in the Sun in the scotogenic minimal model*, Bachelor's thesis, Westfälische Wilhelms-Universität Münster (2021), URL `https://www.uni-muenster.de/Physik.KP/AGKappes/ag/arbeiten.html` (accessed 14.11.2022).

[100] G. Jungman, M. Kamionkowski, K. Griest, *Supersymmetric dark matter*, Phys. Rept. 267 (1996) 195–373, Preprint (arXiv) hep-ph/9506380, DOI 10.1016/0370-1573(95)00058-5.

[101] P. Gondolo, *Phenomenological introduction to direct dark matter detection*, in: 31st Rencontres de Moriond: Dark Matter and Cosmology, Quantum Measurements and Experimental Gravitation, 1996, pp. 41–51, Preprint (arXiv) hep-ph/9605290.

[102] E. Ma, *Verifiable radiative seesaw mechanism of neutrino mass and dark matter*, Phys. Rev. D 73 (2006) 077301, Preprint (arXiv) hep-ph/0601225, DOI 10.1103/PhysRevD.73.077301.

[103] D. Restrepo, O. Zapata, C. E. Yaguna, *Models with radiative neutrino masses and viable dark matter candidates*, JHEP 11 (2013) 011, Preprint (arXiv) 1308.3655, DOI 10.1007/JHEP11(2013)011.

[104] T. Hambye, F. S. Ling, L. Lopez Honorez, J. Rocher, *Scalar Multiplet Dark Matter*, JHEP 07 (2009) 090, Preprint (arXiv) 0903.4010, DOI 10.1007/JHEP05(2010)066, [Erratum: JHEP 05, 066 (2010)].

[105] T. de Boer, R. Busse, A. Kappes, M. Klasen, S. Zeinstra, *New constraints on radiative seesaw models from IceCube and other neutrino detectors*, Phys. Rev. D 103 (12) (2021) 123006, Preprint (arXiv) 2103.06881, DOI 10.1103/PhysRevD.103.123006.

[106] T. de Boer, R. Busse, A. Kappes, M. Klasen, S. Zeinstra, *Indirect detection constraints on the scotogenic dark matter model*, JCAP 08 (2021) 038, Preprint (arXiv) 2105.04899, DOI 10.1088/1475-7516/2021/08/038.

[107] T. de Boer, R. Busse, A. Kappes, M. Klasen, S. Zeinstra, *Neutrino constraints to scotogenic dark matter interacting in the Sun*, in: 55th Rencontres de Moriond on Electroweak Interactions and Unified Theories, 2021, Preprint (arXiv) 2105.05613.

[108] D. Tucker-Smith, N. Weiner, *Inelastic dark matter*, Phys. Rev. D 64 (2001) 043502, Preprint (arXiv) hep-ph/0101138, DOI 10.1103/PhysRevD.64.043502.

[109] P. Agrawal, Z. Chacko, C. Kilic, R. K. Mishra, *A Classification of Dark Matter Candidates with Primarily Spin-Dependent Interactions with Matter* Preprint (arXiv) 1003.1912.

[110] *The user's manual, version 5.0*, D. Barducci, et al. (Feb 12, 2019), URL `https://lapth.cnrs.fr/micromegas/v5.0/manual_5.0.pdf` (accessed 23.02.2022).

[111] F. Staub, *SARAH 4 : A tool for (not only SUSY) model builders*, Comput. Phys. Commun. 185 (2014) 1773–1790, Preprint (arXiv) 1309.7223, DOI 10.1016/j.cpc.2014.02.018.

[112] S. Nussinov, L.-T. Wang, I. Yavin, *Capture of Inelastic Dark Matter in the Sun*, JCAP 08 (2009) 037, Preprint (arXiv) 0905.1333, DOI 10.1088/1475-7516/2009/08/037.

[113] A. Menon, R. Morris, A. Pierce, N. Weiner, *Capture and Indirect Detection of Inelastic Dark Matter*, Phys. Rev. D 82 (2010) 015011, Preprint (arXiv) 0905.1847, DOI 10.1103/PhysRevD.82.015011.

[114] J. Shu, P.-f. Yin, S.-h. Zhu, *Neutrino Constraints on Inelastic Dark Matter after CDMS II*, Phys. Rev. D 81 (2010) 123519, Preprint (arXiv) 1001.1076, DOI 10.1103/PhysRevD.81.123519.

[115] A. Gould, *Resonant Enhancements in Weakly Interacting Massive Particle Capture by the Earth*, ApJ 321 (1987) 571, DOI 10.1086/165653, provided by the SAO/NASA Astrophysics Data System, URL `https://ui.adsabs.harvard.edu/abs/1987ApJ...321..571G`.

[116] *SARAH website*, URL `https://sarah.hepforge.org/` (accessed 13.10.2021).

[117] I. Esteban, M. C. Gonzalez-Garcia, A. Hernandez-Cabezudo, M. Maltoni, T. Schwetz, *Global analysis of three-flavour neutrino oscillations: synergies and tensions in the determination of θ_{23}, δ_{CP}, and the mass ordering*, JHEP 01 (2019) 106, Preprint (arXiv) 1811.05487, DOI 10.1007/JHEP01(2019)106.

[118] J. A. Casas, A. Ibarra, *Oscillating neutrinos and $\mu \to e, \gamma$*, Nucl. Phys. B 618 (2001) 171–204, Preprint (arXiv) hep-ph/0103065, DOI 10.1016/S0550-3213(01)00475-8.

[119] T. Toma, A. Vicente, *Lepton Flavor Violation in the Scotogenic Model*, JHEP 01 (2014) 160, Preprint (arXiv) 1312.2840, DOI 10.1007/JHEP01(2014)160.

[120] A. M. Baldini, et al. (MEG Collaboration), *Search for the lepton flavour violating decay $\mu^+ \to \mathrm{e}^+\gamma$ with the full dataset of the MEG experiment*, Eur. Phys. J. C 76 (8) (2016) 434, Preprint (arXiv) 1605.05081, DOI 10.1140/epjc/s10052-016-4271-x.

[121] U. Bellgardt, et al. (SINDRUM Collaboration), *Search for the Decay mu+ —> e+ e+ e-*, Nucl. Phys. B 299 (1988) 1–6, DOI 10.1016/0550-3213(88)90462-2.

[122] C. Dohmen, et al. (SINDRUM II Collaboration), *Test of lepton flavor conservation in mu —> e conversion on titanium*, Phys. Lett. B 317 (1993) 631–636, DOI 10.1016/0370-2693(93)91383-X.

[123] S. Adrian-Martinez, et al. (ANTARES Collaboration), *Limits on Dark Matter Annihilation in the Sun using the ANTARES Neutrino Telescope*, Phys. Lett. B 759 (2016) 69–74, Preprint (arXiv) 1603.02228, DOI 10.1016/j.physletb.2016.05.019.

[124] M. G. Aartsen, et al. (IceCube Collaboration), *Search for annihilating dark matter in the Sun with 3 years of IceCube data*, Eur. Phys. J. C 77 (3) (2017) 146, Preprint (arXiv) 1612.05949, DOI 10.1140/epjc/s10052-017-4689-9, [Erratum: Eur.Phys.J.C 79, 214 (2019)].

[125] K. Choi, et al. (Super-Kamiokande Collaboration), *Search for neutrinos from annihilation of captured low-mass dark matter particles in the Sun by Super-Kamiokande*, Phys. Rev. Lett. 114 (14) (2015) 141301, Preprint (arXiv) 1503.04858, DOI 10.1103/PhysRevLett.114.141301.

[126] E. Aprile, et al. (XENON Collaboration), *Dark Matter Search Results from a One Ton-Year Exposure of XENON1T*, Phys. Rev. Lett. 121 (11) (2018) 111302, Preprint (arXiv) 1805.12562, DOI 10.1103/PhysRevLett.121.111302.

[127] A. Albert, et al. (ANTARES, IceCube Collaboration), *Combined search for neutrinos from dark matter self-annihilation in the Galactic Center with ANTARES and IceCube*, Phys. Rev. D 102 (8) (2020) 082002, Preprint (arXiv) 2003.06614, DOI 10.1103/PhysRevD.102.082002.

[128] K. Abe, et al. (Super-Kamiokande Collaboration), *Indirect search for dark matter from the Galactic Center and halo with the Super-Kamiokande detector*, Phys. Rev. D 102 (7) (2020) 072002, Preprint (arXiv) 2005.05109, DOI 10.1103/PhysRevD.102.072002.

[129] G. Steigman, B. Dasgupta, J. F. Beacom, *Precise Relic WIMP Abundance and its Impact on Searches for Dark Matter Annihilation*, Phys. Rev. D 86 (2012) 023506, Preprint (arXiv) 1204.3622, DOI 10.1103/PhysRevD.86.023506.

[130] J. Billard, L. Strigari, E. Figueroa-Feliciano, *Implication of neutrino backgrounds on the reach of next generation dark matter direct detection experiments*, Phys. Rev. D 89 (2) (2014) 023524, Preprint (arXiv) 1307.5458, DOI 10.1103/PhysRevD.89.023524.

[131] G. Abbiendi, et al. (OPAL Collaboration), *Search for stable and longlived massive charged particles in e+ e- collisions at s**(1/2) = 130-GeV to 209-GeV*, Phys. Lett. B 572 (2003) 8–20, Preprint (arXiv) hep-ex/0305031, DOI 10.1016/S0370-2693(03)00639-7.

[132] M. Carena, A. de Gouvea, A. Freitas, M. Schmitt, *Invisible Z boson decays at e+ e- colliders*, Phys. Rev. D 68 (2003) 113007, Preprint (arXiv) hep-ph/0308053, DOI 10.1103/PhysRevD.68.113007.

[133] Q.-H. Cao, E. Ma, G. Rajasekaran, *Observing the Dark Scalar Doublet and its Impact on the Standard-Model Higgs Boson at Colliders*, Phys. Rev. D 76 (2007) 095011, Preprint (arXiv) 0708.2939, DOI 10.1103/PhysRevD.76.095011.

[134] E. Lundstrom, M. Gustafsson, J. Edsjo, *The Inert Doublet Model and LEP II Limits*, Phys. Rev. D 79 (2009) 035013, Preprint (arXiv) 0810.3924, DOI 10.1103/PhysRevD.79.035013.

[135] S. Kang, S. Scopel, G. Tomar, *Probing DAMA/LIBRA data in the full parameter space of WIMP effective models of inelastic scattering*, Phys. Rev. D 99 (10) (2019) 103019, Preprint (arXiv) 1902.09121, DOI 10.1103/PhysRevD.99.103019.

[136] E. Aprile, et al. (XENON100 Collaboration), *Implications on Inelastic Dark Matter from 100 Live Days of XENON100 Data*, Phys. Rev. D 84 (2011) 061101, Preprint (arXiv) 1104.3121, DOI 10.1103/PhysRevD.84.061101.

[137] E. Aprile, et al. (XENON Collaboration), *Effective field theory search for high-energy nuclear recoils using the XENON100 dark matter detector*, Phys. Rev. D 96 (4) (2017) 042004, Preprint (arXiv) 1705.02614, DOI 10.1103/PhysRevD.96.042004.

[138] S. Zeinstra, *Minimal models for dark matter and neutrinos masses*, PhD thesis, Westfälische Wilhelms-Universität Münster (2021), to be published at the following website, URL `https://www.uni-muenster.de/Physik.TP/research/publications/theses/klasen.shtml` (accessed 22.11.2022).

[139] X. Chen, et al. (PandaX-II Collaboration), *Exploring the dark matter inelastic frontier with 79.6 days of PandaX-II data*, Phys. Rev. D 96 (10) (2017) 102007, Preprint (arXiv) 1708.05825, DOI 10.1103/PhysRevD.96.102007.

[140] G. Aad, et al. (ATLAS, CMS Collaboration), *Combined Measurement of the Higgs Boson Mass in pp Collisions at $\sqrt{s}$ = 7 and 8 TeV with the ATLAS and CMS Experiments*, Phys. Rev. Lett. 114 (2015) 191803, Preprint (arXiv) 1503.07589, DOI 10.1103/PhysRevLett.114.191803.

[141] M. Lindner, M. Platscher, C. E. Yaguna, A. Merle, *Fermionic WIMPs and vacuum stability in the scotogenic model*, Phys. Rev. D 94 (11) (2016) 115027, Preprint (arXiv) 1608.00577, DOI 10.1103/PhysRevD.94.115027.

[142] W. Porod, *SPheno, a program for calculating supersymmetric spectra, SUSY particle decays and SUSY particle production at e+ e- colliders*, Comput. Phys. Commun. 153 (2003) 275–315, Preprint (arXiv) hep-ph/0301101, DOI 10.1016/S0010-4655(03)00222-4.

[143] W. Porod, F. Staub, *SPheno 3.1: Extensions including flavour, CP-phases and models beyond the MSSM*, Comput. Phys. Commun. 183 (2012) 2458–2469, Preprint (arXiv) 1104.1573, DOI 10.1016/j.cpc.2012.05.021.

[144] *SPheno website*, URL `https://spheno.hepforge.org/` (accessed 14.11.2022).

[145] A. Belyaev, N. D. Christensen, A. Pukhov, *CalcHEP 3.4 for collider physics within and beyond the Standard Model*, Comput. Phys. Commun. 184 (2013) 1729–1769, Preprint (arXiv) 1207.6082, DOI 10.1016/j.cpc.2013.01.014.

[146] P. Gondolo, J. Edsjo, P. Ullio, L. Bergstrom, M. Schelke, E. A. Baltz, *DarkSUSY: Computing supersymmetric dark matter properties numerically*, JCAP 07 (2004) 008, Preprint (arXiv) astro-ph/0406204, DOI 10.1088/1475-7516/2004/07/008.

[147] T. Bringmann, J. Edsjö, P. Gondolo, P. Ullio, L. Bergström, *DarkSUSY 6 : An Advanced Tool to Compute Dark Matter Properties Numerically*, JCAP 07 (2018) 033, Preprint (arXiv) 1802.03399, DOI 10.1088/1475-7516/2018/07/033.

[148] *DarkSUSY website*, URL `http://www.darksusy.org/` (accessed 18.11.2021).

[149] G. Bélanger, F. Boudjema, A. Goudelis, A. Pukhov, B. Zaldivar, *micrOMEGAs5.0 : Freeze-in*, Comput. Phys. Commun. 231 (2018) 173–186, Preprint (arXiv) 1801.03509, DOI 10.1016/j.cpc.2018.04.027.

[150] T. de Boer, *Verifiable dark matter with radiative neutrino masses*, Master's thesis, Westfälische Wilhelms-Universität Münster (2021), to be published at the following website, URL `https://www.uni-muenster.de/Physik.TP/research/publications/theses/klasen.shtml` (accessed 22.11.2022).

[151] M. Blennow, J. Edsjo, T. Ohlsson, *Neutrinos from WIMP annihilations using a full three-flavor Monte Carlo*, JCAP 01 (2008) 021, Preprint (arXiv) 0709.3898, DOI 10.1088/1475-7516/2008/01/021.

[152] E. Bugaev, T. Montaruli, Y. Shlepin, I. A. Sokalski, *Propagation of tau neutrinos and tau leptons through the earth and their detection in underwater / ice neutrino telescopes*, Astropart. Phys. 21 (2004) 491–509, Preprint (arXiv) hep-ph/0312295, DOI 10.1016/j.astropartphys.2004.03.002.

[153] A. Vicente, C. E. Yaguna, *Probing the scotogenic model with lepton flavor violating processes*, JHEP 02 (2015) 144, Preprint (arXiv) 1412.2545, DOI 10.1007/JHEP02(2015)144.

[154] A. Osipowicz, et al. (KATRIN Collaboration), *KATRIN: A Next generation tritium beta decay experiment with sub-eV sensitivity for the electron neutrino mass. Letter of intent* Preprint (arXiv) hep-ex/0109033.

[155] M. Klasen, C. E. Yaguna, J. D. Ruiz-Alvarez, D. Restrepo, O. Zapata, *Scalar dark matter and fermion coannihilations in the radiative seesaw model*, JCAP 04 (2013) 044, Preprint (arXiv) 1302.5298, DOI 10.1088/1475-7516/2013/04/044.

[156] J. F. Navarro, C. S. Frenk, S. D. M. White, *The Structure of cold dark matter halos*, Astrophys. J. 462 (1996) 563–575, Preprint (arXiv) astro-ph/9508025, DOI 10.1086/177173.

[157] M. G. Aartsen, et al. (IceCube Collaboration), *Search for dark matter annihilations in the Sun with the 79-string IceCube detector*, Phys. Rev. Lett. 110 (13) (2013) 131302, Preprint (arXiv) 1212.4097, DOI 10.1103/PhysRevLett.110.131302.

[158] M. Medici, *Search for Dark Matter Annihilation in the Galactic Halo using IceCube*, PhD thesis, University of Copenhagen (2016), URL `https://nbi.ku.dk/english/theses/phd-theses/morten-ankersen-medici/` (accessed 15.11.2022).

[159] M. de With, *Search for neutrinos from annihilating dark matter in galaxies and galaxy clusters with the IceCube detector*, PhD thesis, Humboldt-Universität zu Berlin (2018), URL `https://edoc.hu-berlin.de/handle/18452/20232` (accessed 15.11.2022).

[160] N. Iovine, *Indirect Searches for Dark Matter in the Centre of the Milky Way with the IceCube Neutrino Telescope*, PhD thesis, Université Libre De Bruxelles (2022), URL `https://difusion.ulb.ac.be/vufind/Record/ULB-DIPOT:oai:dipot.ulb.ac.be:2013/340058/Details` (accessed 15.11.2022).

[161] M. G. Aartsen, et al. (IceCube Collaboration), *Characterization of the Atmospheric Muon Flux in IceCube*, Astropart. Phys. 78 (2016) 1–27, Preprint (arXiv) 1506.07981, DOI 10.1016/j.astropartphys.2016.01.006.

[162] K. Leonard DeHolton (IceCube Collaboration), *Atmospheric Neutrino Oscillations with 8 years of data from IceCube DeepCore*, in: The 22nd International Workshop on Neutrinos from Accelerators (NuFact2021), Vol. 402, 2022, p. 062, DOI 10.22323/1.402.0062.

[163] R. Abbasi, et al. (IceCube Collaboration), *A New Search for Neutrino Point Sources with IceCube*, PoS ICRC2021 (2021) 1138, Preprint (arXiv) 2107.08700, DOI 10.22323/1.395.1138.

[164] T. Glauch, *The Origin of High-Energy Cosmic Particles: IceCube Neutrinos and the Blazar Case*, PhD thesis, Technische Universität München (2021), URL `https://mediatum.ub.tum.de/doc/1584755/1584755.pdf` (accessed 14.11.2022).

[165] R. Reimann, *Search for the Sources of the Astrophysical High-Energy Muon-Neutrino Flux with the IceCube Neutrino Observatory*, PhD thesis, RWTH Aachen (2019), URL `http://publications.rwth-aachen.de/record/773297` (accessed 14.11.2022).

[166] R. J. Barlow, *Statistics — A Guide to the Use of Statistical Methods in the Physical Sciences*, John Wiley & Sons Ltd., Chichester, United Kingdom, 1989, ISBN 978-0-471-92295-7.

[167] W. von der Linden, V. Dose, U. von Toussaint, *Bayesian Probability Theory*, Cambridge University Press, Cambridge, United Kingdom, 2014, ISBN 978-1-107-03590-4.

[168] M. Rosenblatt, *Remarks on Some Nonparametric Estimates of a Density Function*, Ann. Math. Statist. 27 (3) (1956) 832–837, DOI 10.1214/aoms/1177728190.

[169] E. Parzen, *On Estimation of a Probability Density Function and Mode*, Ann. Math. Statist. 33 (3) (1962) 1065–1076, DOI 10.1214/aoms/1177704472.

[170] B. W. Silverman, *Density Estimation for Statistics and Data Analysis — Monographs on Statistics and Applied Probability*, Vol. 26, Chapman and Hall, London, United Kingdom, 1986, ISBN 978-0412246203.

[171] R. Busse, *KDE2B: Tool for calculating Gaussian Kernel Density Estimations (KDEs) on 2D bounded data sets*, URL `https://github.com/nechnif/KDE2B` (accessed 22.09.2022).

[172] J. Neyman, E. S. Pearson, *On the Problem of the Most Efficient Tests of Statistical Hypotheses*, Phil. Trans. Roy. Soc. Lond. A 231 (694-706) (1933) 289–337, DOI 10.1098/rsta.1933.0009.

[173] G. C. Hill, K. Rawlins, *Unbiased cut selection for optimal upper limits in neutrino detectors: The Model rejection potential technique*, Astropart. Phys. 19 (2003) 393–402, Preprint (arXiv) astro-ph/0209350, DOI 10.1016/S0927-6505(02)00240-2.

[174] M. G. Aartsen, et al. (IceCube Collaboration), *Measurement of South Pole ice transparency with the IceCube LED calibration system*, Nucl. Instrum. Meth. A 711 (2013) 73–89, Preprint (arXiv) 1301.5361, DOI 10.1016/j.nima.2013.01.054.

[175] M. Rongen (IceCube Collaboration), *Measuring the optical properties of IceCube drill holes*, EPJ Web Conf. 116 (2016) 06011, DOI 10.1051/epjconf/201611606011.

[176] M. G. Aartsen, et al. (IceCube-Gen2 Collaboration), *IceCube-Gen2: the window to the extreme Universe*, J. Phys. G 48 (6) (2021) 060501, Preprint (arXiv) 2008.04323, DOI 10.1088/1361-6471/abbd48.

[177] A. Ishihara (IceCube Collaboration), *The IceCube Upgrade - Design and Science Goals*, PoS ICRC2019 (2021) 1031, Preprint (arXiv) 1908.09441, DOI 10.22323/1.358.1031.

[178] M. Agostini, et al. (P-ONE Collaboration), *The Pacific Ocean Neutrino Experiment*, Nature Astron. 4 (10) (2020) 913–915, Preprint (arXiv) 2005.09493, DOI 10.1038/s41550-020-1182-4.

[179] Z. P. Ye, et al., *Proposal for a neutrino telescope in South China Sea* Preprint (arXiv) 2207.04519.

[180] W. J. Spindler, *Unofficial South Pole statistics and trivia web site*, URL `https://southpolestation.com/` (accessed 01.06.2022).

Acknowledgments

I thank Prof. Dr. Alexander K. for being my advisor for this thesis and throughout most of my scientific career, as well as for the opportunity to study and graduate in his group. Furthermore, I thank Prof. Dr. Michael K. for overseeing the development of “our” Scotogenic Model and the theoretical part of this work, and Priv. Doz. Dr. Karol K. for examining my thesis.

Further acknowledgment goes out to Dr. Sybrand Z. and Thede de B. for productive cooperation in the field of minimal Dark Matter models. I am proud of having been the coding muscle to their theory super brains.

Next, I’d like to express my gratitude to Dr. Klas H. and Dr. Robert H. who reviewed my analysis. Further, to the entire Beyond Standard Model working group for providing the necessary infrastructure, and for interesting and helpful discussions; especially to Jeffrey L. who is working on a similar study and provided many helpful resources, and to Dr. Carlos A. for his invaluable help with statistics; and to Theo G. and Tom S. for helping with data sample processing. I thank the IceCube collaboration for a productive and inclusive work environment, and for the opportunities to see the ends of this world.

I very much enjoyed being a part of the AG Kappes working group. It has always been an odd gang, and I hope it stays that way. Thanks for many hours of coffee breaks, game nights, parking lot BBQs, and innumerable visits to the Mensa am Ring. That reminds me, I also thank the Mensa am Ring for sustaining me for twelve years.
I actually quite like the food, seriously.

A huge thank-you goes out to Willem A., Dr. Lew C., Dr. Daniel G., Michael H., and Dr. Amin I., for taking the time to proof-read this thesis.

I thank my office mate of the last three years, Dr. Lew C., for being a friend and scientific idol since my very first baby steps in astroparticle physics; and for our many doorway conversations about the latest craze in Python. Further praise goes out to my former office mate Michael H. for his invaluable insights into group theory (he somehow manages to break down any abstract mathematical concept into a simple example with farm animals). He has been a beacon of knowledge throughout my entire studies. Then I also thank Volker V., Martin U. and Cristian L., for being there when I was struggling after my year on the Ice.

Last but not least, my sincere gratitude goes to my family for always having my back and for “looking at the pictures, at least, promise!”. And to my fiance Dr. Benjamin E., for luring me away from the desk from time to time for fresh air, nature and
zufällige Spaziergänge (in the outside!).